Tailoring titanium dioxide thin films for photocatalysis and energy efficient glazing via dye-sensitised solar cells

Ann-Louise Anderson

Submitted in partial fulfilment of the requirements of the Degree of Doctor of Philosophy

I, Ann-Louise Anderson confirm that the research included within this thesis is my own work or that where it has been carried out in collaboration with, or supported by others, that this is duly acknowledged below and my contribution indicated. Previously published material is also acknowledged below.

I attest that I have exercised reasonable care to ensure that the work is original, and does not to the best of my knowledge break any UK law, infringe any third party's copyright or other Intellectual Property Right, or contain any confidential material.

I accept that the College has the right to use plagiarism detection software to check the electronic version of the thesis.

I confirm that this thesis has not been previously submitted for the award of a degree by this or any other university.

Signature:

Date: 1st September 2016

Details of collaboration and publications:

A.-L. Anderson, R. Binions, The effect of Brij® surfactants in sol–gel processing for the production of TiO2 thin films, Polyhedron. 85 (2015) 83–92.

A.-L. Anderson, R. Binions, The effect of Tween® surfactants in sol–gel processing for the production of TiO2 thin films. Coatings (2014), 4, (4) 796-809.

A.-L. Anderson, R. Binions, A preferential precursor for photocatalytically active titanium dioxide thin films: Titanium bis-ammonium lactato dihydroxide as an alternative to titanium tetra iso-propoxide. Polyhedron. 118 (2016) 81-90.

Abstract

This thesis focuses on the synthesis and characterisation of titanium dioxide (TiO_2) thin films for photocatalytic applications and use in semi-transparent dye-sensitised solar cells for energy efficient glazing. Several synthetic methods for the production of TiO_2 thin films are explored including sol-gel, aerosol-assisted chemical vapour deposition (CVD) and hybrid combinatorial CVD. For sol-gel processing two different precursors were studied; titanium tetra-isopropoxide (TTIP) and titanium bis-ammonium lactato dihydroxide (TiBALD). Non-ionic surfactants (Tween 20, 40, 60 and Brij 58 and 98) were successfully incorporated into all three methods for the production of TiO_2 thin films modified morphology, microstructure and enhanced functional properties in some cases. All films are fully characterised using scanning electron microscopy, X-ray diffraction, atomic force microscopy, Raman spectroscopy, UV-Vis spectroscopy, contact angle analysis, as well as assessment for photocatalytic performance with resazurin 'intelligent' ink. Photocatalytic performance has been used as an indicator for performance in dye-sensitised solar cells (DSSCs). The best photocatalytic performances with half-lives of up to 2 minutes were obtained for thin films produced with the addition of Brij surfactants.

A selection of thin films were tested in semi-transparent DSSC devices with up to 70% transparency, to determine their overall potential for use as energy-efficient glazing. Three DSSC device configurations were tested, whereby the optimum configuration used N3 "black" dye with a dye loading time of 42 hours in combination with a high performance iodine electrolyte and a platinum counter electrode. The highest power conversion efficiencies (PCE) obtained were within the region of 0.1 – 0.3 %, with the highest PCE of 0.3814 % obtained with a 3-layer TTIP sol-gel derived Brij 58 thin film (0.0006 mol dm^3) which exhibited an short-circuit current of 0.857 mA/cm^2, an open-circuit voltage of 0.71 V and a fill factor of 0.60.

Acknowledgements

My first words of thanks go to my supervisor Dr Russell Binions, for always having the time to offer encouragement, understanding and guidance throughout my PhD, whilst giving me the freedom to try out new things and explore my own ideas. It has been a privilege to be a member of 'Team Binions' and I am grateful for all of the opportunities and fun along the way.

I would like to thank past and present members of the team, with special mentions to Dr Luz Romero-Nunez and Dr Shuqun Chen. I am also particularly grateful to Dr Joe Briscoe for all his guidance with dye-sensitised solar cells. I would like to extend this thanks to all of those that underpin the materials science research at Queen Mary; Dr Rory Wilson for all of the XRD measurements, Dr Russell Bailey for his patient help with AFM and all the technicians in the second floor labs.

I would also like to thank everyone else I have met along the way at Queen Mary, especially my science sister Dr Pelin Yilmaz. In addition, a very special thanks goes to Hazel Kitching for the long standing support in helping me to keep the faith.

I would like to thank my family, especially my dad for instilling me with determination and my mum for giving me the confidence and support that I needed to fulfil my ambitions. Thank you for having patience and understanding throughout my studies and for supporting my decision to continue this far; it would not have been possible without you. Thanks to my brother, John, for always surprising me with enigmatic words of encouragement. In addition, I would like to thank Eily for all the supportive coffees over the years, my cousin Breda for always being there, as well as Mary and Adrian Daly for taking my request for purple potatoes from West Cork seriously.

My final thanks go to Robert, whose love and support have been invaluable from the very start of this journey; your belief in me has made all the difference. My very last thoughts go to my thesis mascot, Mollie, whose presence will never be forgotten and will always be missed.

Table of Contents

Abstract 3

List of Figures 12

List of Tables 29

List of Equations. 33

List of Abbreviations 34

Introduction: Tailoring titanium dioxide thin films for photocatalysis and energy efficient glazing via dye-sensitised solar cells 35

Current Approaches to Solar Glazing 36

Scope of this thesis 37

Fundamentals: 1: Titanium Dioxide-structure, properties and applications 38

1.1. Titanium Dioxide 38

1.1.2 Functional Application: TiO_2 as a photocatalyst 38

1.1.3. Structure and properties: Tailoring TiO_2 for photocatalytic and DSSC applications 41

Fundamentals 1.2: Sol-Gel Technology for thin films 46

1.2.1. Principles of Sol-Gel Dip Coating 47

1.2.2. The Metal Alkoxide Method 48

1.2.3. Preparation of the TiO_2 sol-gel; traditional vs. novel precursors and other modifications 50

1.2.4. Surfactants 51

1.2.5. Non-Ionic Surfactants 52

Fundamentals 1.3: Chemical Vapour Deposition 54

1.3.1. Principles of CVD 55

1.3.2. Thermodynamics, kinetics and mass transport 56

1.3.3. Structure and Morphology of CVD thin films 59

1.3.4. CVD precursors for TiO_2 thin films 61

1.3.5. Variations of CVD 62

1.3.6. Aerosol-Assisted Chemical Vapour Deposition (AACVD) 62
1.3.7. Atmospheric Pressure Chemical Vapour Deposition (APCVD) 64
1.3.8. Hybrid Chemical Vapour Deposition (HCVD) 64
Fundamentals 1.4: Dye-sensitised solar cells 66
1.4.1 Operating mechanism of the DSSC 69
1.4.2. Key efficiency parameters of the DSSC 71
1.4.3 Materials development for semi-transparent DSSCs 73
1.4.3.1 TCO Electrode 73
1.4.3.2 Dyes 73
1.4.3.3 Electrolyte/ Redox mediator 74
1.4.3.4 Nanostructured Metal Oxide electrode (anode) 76
1.4.3.5 TiO_2 electrode preparation 76
1.4.4 Potential for DSSC building integrated photovoltaics 78
Chapter 2: Experimental and Analytical Details 80
2.1. Sol-gel 80
2.1.1. Traditional TiO_2 sol synthesis: Titanium (IV) tetraisopropoxide (TTIP) as precursor 80
2.1.2 Novel TiO_2 sol synthesis: Titanium (IV) bis (ammonium lactate) dihydroxide (TiBALD) as precursor 83
2.1.3. Dip-coating and annealing 83
2.2. Chemical Vapour Deposition Techniques 84
2.2.1. Aerosol-assisted chemical vapour deposition (AACVD) 84
2.2.2. AACVD: Experimental details 84
2.2.3. Hybrid (Aerosol Assisted/Atmospheric Pressure) Chemical Vapour Deposition (HCVD) 86
2.2.4. HCVD Experimental Details 86
2.3. Characterisation and functional property testing 88

2.3.1 Scanning Electron Microscopy (SEM) 88
2.3.12 X-Ray Diffraction (XRD) 89
2.3.13 Raman Spectroscopy 89
2.3.14. Atomic Force Microscopy (AFM) 89
2.3.15. Ultra-Violet/ Visible Spectroscopy 90
2.3.2. Determination of functional properties 90
2.3.21 Contact Angle Measurements 90
2.3.22 Photocatalytic Activity 90
2.3.23 Preparation of resazurin 'intelligent' ink solution 91
2.3.24 Aerosol spray technique for the application of resazurin ink coating 91
2.3.25 Formal Quantum Efficiency/ Formal Quantum Yield 92
Chapter 3: Results: Sol-gel processing of titanium dioxide thin films with two different precursors and the effects of surfactant addition 93
3.1. Introduction 93
3.2. Results: TiO_2 thin films prepared by sol-gel methods 95
3.2.1. Results: Titanium Isopropoxide (TTIP) as precursor with Tween and Brij surfactant addition 96
3.2.1.1. Thin film thickness and particle size 96
3.2.1.21. Thin film morphology: Tween surfactants 99
3.2.1.22. Thin film morphology: Brij surfactants 99
3.2.1.3. Surface roughness 101
3.2.1.4. Influence of annealing temperature and time on morphology and roughness 103
3.2.1.5. Crystalline phase identification of TiO_2 thin films 104
3.2.1.6. Wetting behaviour of thin films 107
3.2.1.7. Photocatalytic activity of thin films produced from TTIP and effects of surfactant addition 107
3.2.1.8. Results tables for sol-gel samples produced from TTIP precursor 111

3.2.1.9 Conclusions: TTIP 116

3.2.2. Results: Titanium Bis-Ammonium Lactato Dihydroxide (TiBALD) as precursor with surfactant addition 116

3.2.2.1. Thin film thickness and particle size 116

3.2.2.2 Surface morphology and particle size 117

3.2.2.3. Thin film morphology: Tween surfactants 118

3.2.2.4. Thin film morphology: Brij surfactants 119

3.2.2.5 Surface Roughness 121

3.2.2.6. Crystalline phase identification of TiBALD prepared TiO_2 thin films 123

3.2.2.8. Results tables for sol-gel samples prepared with TiBALD precursor 125

3.2.2.7 Functional properties of thin films produced from TiBALD and effects of surfactant addition 128

3.2.2.9 Comparison of TiBALD prepared thin films and TTIP prepared thin films 130

3.2.2.9 Conclusions: TiBALD 134

Chapter 4: Results: Aerosol-assisted chemical vapour deposition of titanium dioxide thin films and the effects of surfactant addition 135

4.1 Introduction 135

4.2. Results: TiO_2 thin films prepared by AACVD 136

4.2.1. Results: AACVD of TiO_2 thin films from TTIP precursor with toluene as solvent, modified with Tween and Brij surfactant addition 137

4.2.1.1. Thin film thickness and particle size 137

4.2.1.21. Thin film morphology: Tween surfactants 141

4.2.1.22. Thin film morphology: Brij surfactants 142

4.2.1.3 Surface roughness and wetting properties 143

4.2.1.4 Crystalline phase identification of TiO_2 thin films 147

4.2.1.5. Photocatalytic activity of thin films produced from TTIP with toluene and the effects of surfactant addition 151

4.2.1.6. Conclusions: TTIP precursor with toluene as solvent with surfactant addition 154

4.2.2. Results: Titanium Isopropoxide (TTIP) as precursor with dichloromethane (DCM) as solvent with Tween and Brij surfactant addition 155

4.2.2.1. Thin film thickness and particle size 155

4.2.2.21. Thin film morphology: Tween surfactants 157

4.2.2.22. Thin film morphology: Brij surfactants 158

4.2.2.3 Surface roughness and wetting properties 160

4.2.2.4 Crystalline phase identification of TiO_2 thin films 163

4.2.2.5. Photocatalytic activity of thin films produced from TTIP with DCM and effects of surfactant addition 166

4.2.2.7. Discussion and conclusion: AACVD TiO_2 thin films prepared with toluene as solvent vs DCM as solvent 170

Chapter 5: Results: Hybrid chemical vapour deposition of titanium dioxide thin films and the effects of surfactant addition 174

5.1 Introduction 174

5.2. Results: TiO_2 thin films prepared by HCVD 174

5.2.1. Results: HCVD of TiO_2 thin films from TTIP precursor with ethanol as solvent, modified with Tween and Brij surfactant addition via an aerosol stream 176

5.2.1.10. Thin film morphology: Brij surfactants 176

5.2.1.11. Thin film morphology: Tween surfactants 179

5.2.1.2. Thin film thickness and particle size 180

5.2.1.3 Surface roughness and wetting properties 184

5.2.1.4 Crystalline phase identification of TiO_2 thin films 191

5.2.1.5. Photocatalytic activity of thin films produced by HCVD and the effects of surfactant addition 195

5.3. Discussion on the photocatalytic performance of HCVD thin films in comparison to AACVD and sol-gel prepared films and the effects of surfactant addition 198

Chapter 6: Results: Incorporation of surfactant modified TiO_2 thin films into semi-transparent dye-sensitised solar cells 200

6.1. Introduction 200

6.2 Experimental Methods: DSSC configuration and variations 203

6.2.1. Preparation of the counter electrode (cathode).....203

6.2.1.1. ITO Counter Electrode 203

6.2.1.2. Pt Counter Electrode.....204

6.2.2. Preparation of dye-sensitised TiO_2 thin film working electrode (anode).....205

6.2.3. Device configuration and addition of electrolyte 206

6.3. Results: Incorporation ofTiO_2 thin films into DSSC devices.....208

6.3.1. Performance of DSSC devices prepared using sol-gel thin films derived from TTIP precursor with surfactant addition 209

6.3.1.1. Conclusions: DSSC devices using TiO_2 thin films prepared with TTIP precursor and the effects of surfactant addition 222

6.3.2. Performance of DSSC devices prepared using sol-gel thin films derived from TiBALD precursor with surfactant addition.....223

6.3.2.1 Conclusions: DSSC devices using TiO_2thin films prepared with TiBALD precursor and the effects of surfactant addition.....226

6.3.2. Performance of DSSC devices prepared using AACVD thin films derived from TTIP precursor in solvents of toluene DCM with surfactant addition.....226

6.3.2.1. Conclusions: DSSC devices using TiO_2thin films prepared by AACVD with TTIP precursor and the effects of surfactant addition.....234

6.3.3. Additional investigations into DSSC configurations: natural vegetable dyes.....235

6.3.3.1. Organic anthocyanin dye derived from purple potatoes used as sensitising dye for semi-transparent DSSC 236

6.3.3.2. Purple pigment extraction method.....237

6.3.3.3. Results: DSSC device performance with natural anthocyanin dye derived from purple potato. 238

6.3.4. Additional DSSC configuration investigation: Ionic liquids as electrolytes.....240

6.3.4.1. Ionic liquids including copper oxide nanofluids used as ionic electrolyte for semi-transparent DSSCs.....240

6.3.4.2. Results: DSSC device performance with various ionic liquids used as redox electrolyte 241

6.3.5. Conclusions: use of purple potatoes as a source for natural dye sensitiser and ionic liquids as a replacement for the triiodide redox electrolyte in semi-transparent DSSCs 244

6.4. Discussion and conclusion: Semi-transparent dye-sensitised solar cells 245

7. Conclusions and future work 248

7.1. Overall conclusions 248

7.2. Future Work.....254

8. References.....256

Appendix A. 278

A1. Selection of representative Tauc Plots (used to determine band gap of TiO_2 thin films) 278

A2. Example photographs of wetting behaviour of TiO_2thin films 281

Appendix B.....282

B1- SEM images for sol-gel samples prepared with TTIP and TiBALD 282

Appendix C.....289

Figure A-H: Current (I) –voltage (V) curves showing performance of DSSC devices produced in chapter 6. 289

List of Figures

Chapter 1.		Page Number
Fundamentals 1.1		
Figure 1.1	Schematic representing the photoexcitation of an electron to generate an electron-hole pair, where vb = valence band, cb = conduction band, Eg = bandgap energy.	38
Figure 1.2.	Schematic of photogenerated electron and hole pathways over a semiconductor particle. (Adapted from Linsebigler et al.)[27]	39
Figure 1.3.	Representations of the three forms of TiO2. Reproduced as seen in Dambournet et al, 2010. [29]	40
Fundamentals 1.2.		
Figure 1.2.1.	Schematic of the sol-gel process and possible products. Adapted from reference.[37]	45
Figure 1.2.2.	Schematic of Sol-Gel dip coating process.	47
Figure 1.2.3.	Metal alkoxide SN2 hydrolysis mechanism where X = H and R = alkyl group.	47
Figure1. 2.4 (a) and (b)	(a) Structural representation of a surfactant molecule. **(b)** Micelle structures formed by surfactant molecules. *Adapted from reference*.[51]	51
Figure1. 2.5.	Structure of a typical non-ionic surfactant; polyethylene ethoxylate.	51
Fundamentals 1.3.		
Figure 1.3.1.	Simplified illustration of the main reaction steps in the process of CVD. Adapted from Choy.[3]	54
Figure 1.3.2.	Schematic of three main types of thin film produced by the CVD process. Lines represent orientation of the crystal lattice.	58
Figure 1.3.3.	Three main mechanisms of thin film growth that occur within CVD.	59
Figure 1.3.4.	Schematic of thin film structures obtained by CVD with respect to grain growth. Adapted from reference.[2]	59
Figure 1.3.5.	Schematic showing the various routes that AACVD reactions can undergo to form a thin film. Adapted from reference.[10]	62

Fundamentals 1.4.

Figure 1.4.1.	Schematic of a dye-sensitised solar cell (DSC).	66
Figure 1.4.2.	Chemical structures of Ru-complex dyes used in DSSCs that give cell efficiencies of over 10%. As seen in references,[7,13]	68
Figure 1.4.3.	Diagram representing the energy levels within a DSSC and the basic electron transfer processes as represented by numbers 1-7. The redox potential values shown are based on a DSSC with N3 dye, TiO2 and a I-/I3- redox couple mediator, and are obtained from Hagfeldt et al. [31]	69
Figure 1.4.4.	The DSSC-based PV facade of the Capricorn Haus in Germany, as seen in Pagliaro et al,[21] originally reproduced from Gattermann und Schossig Architekten, who reserve all rights.[73]	78
Chapter 2.		
Figure 2.	Chemical structure of (a) titanium tetra-isopropoxide, TTIP, and (b) titanium bis-ammonium lactate dihydroxide, TiBALD.	79
Figure 2.1.	Schematic diagram of AACVD apparatus.	83
Figure 2.2.	Schematic of hybrid chemical vapour deposition apparatus; a combination between atmospheric pressure CVD and AACVD.	86
Figure 2.3.	Schematic of glass substrate sizes used and areas used for materials characterisation analysis and functional property testing.	87
Figure 2.4.	Schematic of photocatalytic degradation of resazurin dye by TiO2 with glycerol as the sacrificial electron donor.	90
Figure 2.5.	Photographs of the observed colour change of resazurin dye on the surface of TiO_2 thin films as it is degraded to resorufin over a 60 minute period of UV irradiation.	90
Chapter 3. **Figure 3.0.**	Chemical structure of titanium tetra-isopropoxide, TTIP, and titanium bis-ammonium lactate dihydroxide, TiBALD.	93
Figure 3.1.	Schematic visualisation of (a) granular, (b) layered and (c) columnar sol-gel film structures as classified by Schuler et al,[14] and modified from Wang et al.[15]	96
Figure 3.2.	SEM images of TiO_2 produced from TTIP precursor by sol-gel with; no surfactant addition (samples C1-C3) and Tween 60 (T60),Tween 40 (T40) and Tween 20 (T20) addition in concentrations; D = 0.0008 mol dm^3, A = 0.0006 mol dm^3, B = 0.0004 mol dm^3. Numbers represent number of consecutive layers. Films were annealed at 500 °C for 15 mins with a ramp rate of 15°C min^{-1}.	97

Figure 3.3. SEM images showing two layer TiO_2 films produced from TTIP via a non-aqueous sol-gel method without surfactant addition (sample C2) and with Brij 58 and Brij 98 surfactant addition in concentrations A = 0.0006 mol dm^3, B = 0.0004 mol dm^3. Films were annealed at 500 °C for 15 mins with a ramp rate of 15°C min^{-1}. 99

Figure 3.4. AFM 3D representation of thin film surface, shown with average root mean square roughness values determined from measurement of three areas across the thin film surface. (a) C2 (no surfactant), (b) T40 A2 (Tween 40, 0.0006 mol dm^3), (c) T40 B2 (Tween 40, 0.0004 mol dm^3), (d) T20 A2 (Tween 20, 0.0006 mol dm^3), (e) T20 B2 (Tween 20, 0.0004 mol dm^3. 101

Figure 3.5. AFM 3D representation of thin film surface, shown with average root mean square roughness values determined from measurement of three areas across the thin film surface to demonstrate the influence of number of layers. (a) C2 (no surfactant), (b) B58 B1 (Brij 58 0.004 mol dm^3), (c) B58 B2 (d) B58 B3. 102

Figure 3.6. SEM images showing two layer TiO_2 films produced from TTIP with Brij surfactant addition (Brij 58 = B58, Brij 98= B98) in concentrations; A = 0.0006 mol dm^3, B = 0.0004 mol dm^3. Films were annealed at 600 °C for 1= hour with a ramp rate of 15°C min^{-1}. 103

Figure 3.7. XRD for TiO_2 films produced using TTIP precursor without surfactant (Control) and with Tween 60 (T60 A), Tween 40 (T40 A), and Tween 20 (T20 A) in a concentration of 0.006 mol dm^3. Peaks identified as anatase are marked in red, brookite in blue and rutile in black. Peaks denoted with asterisks (*) are assigned to the F:SnO_2 coating of the glass substrate. XRD are normalised for intensity. 104

Figure 3.8. Typical Raman spectrum obtained for all samples. This spectrum was obtained for sample T40 A3 annealed at 500°C for 15 minutes. Peaks match the reference spectra for TiO_2 anatase.[18] 105

Figure 3.9. XRD obtained for TiO_2 films produced using TTIP precursor and addition of Brij 98 surfactant (concentration = 0.0004 mol dm^3). Red line represents the diffraction pattern for a sample annealed at 600°C (1 hour), and blue line represents a sample annealed at 500°C (15 minutes). Peaks identified as anatase are labelled red, brookite blue and rutile in black. Peaks denoted with asterisks (*) are assigned to the F:SnO_2 coating of the glass substrate. XRD are normalised for intensity. 105

Figure 3.10. Normalised absorption curve for determination of photocatalytic half-life (in minutes) for samples prepared with TTIP precursor and Tween surfactants, annealed at 500°C for 15 mins. Control (CT2) represents the TTIP sample prepared without surfactant addition and is used for comparison. 107

Figure 3.11. Normalised absorption curve used to determine photocatalytic half-life (in minutes) for samples prepared with TTIP precursor and Brij surfactants, annealed at 500°C for 15 mins. Control (CT2) represents the TTIP sample prepared without surfactant addition and is used for comparison. 107

Figure 3.12. Bar chart representing the rate of calculated photoactivity for Rz dye molecules degraded s^{-1} cm^2 for each sample type. Concentrations of surfactant; A = 0.0006 mol dm^3 and B = 0.0004 mol dm^3. Samples names with '600' represent samples that were annealed at 600 °C for one hour rather than 500 °C for 15 minutes. Samples are two layer samples. Error bars shown are 5% experimental error. 109

Figure 3.13. SEM images of TiO_2 films produced from titanium bis-ammonium lactato dihydroxide (TiBALD) precursor with no surfactant addition. Films were annealed at 600 °C for 1 hour with a ramp rate of 15°C min-1. Numbers represent number of layers. 117

Figure 3.14 SEM images showing two-layer TiO_2 films produced from TiBALD precursor with Tween® surfactant addition; Tween 60 (T60), Tween 40 (T40) and Tween 20 (T20) in concentrations DT= $8x10^{-4}$ mol dm^3, AT = $6x10^{-4}$ mol dm^3, BT = $4x10^{-4}$ mol dm^3. Films were annealed at 600 °C for 1 hour with a ramp rate of 15°C min^{-1}. 119

Figure 3.15. SEM images showing two-layer TiO_2 films produced from TiBALD precursor with Brij® surfactant addition; Brij 58 (B58) and Brij 98 (B98) in concentrations AT = $6x10^{-4}$ mol dm^3, and B98 BT = $4x10^{-4}$ mol dm^3. Films were annealed at 600 °C for 1 hour with a ramp rate of 15°C min^{-1}. 120

Figure 3.16. AFM 3D surface representation of thin films produced without surfactant (OT 1-3) and with 6 x 10^{-4} mol dm^3 Brij 98 surfactant (CT 1-3), with numbers representing number of consecutive layers. 121

Figure 3.17. Typical XRD patterns for TiO_2 films produced using TiBALD precursor, with and without surfactant addition. Samples are for three-layer samples prepared with Brij 98 surfactant (B98 AT3, $6x10^{-4}$ mol dm^3) (blue line), without surfactant (CT3) (red line), and Tween 20 surfactant (T20 BT3, $4x10^{-4}$ mol dm^3). Peaks identified as anatase are labelled red, brookite blue and rutile black. Peaks denoted with asterisks (*) are assigned to the F:SnO_2 coating of the glass substrate. XRD normalised for intensity. 122

Figure 3.18. Raman spectra of TiO_2 thin film produced from TiBALD precursor. These Raman patterns were typically observed for all samples prepared with TiBALD and modified with surfactant. The samples shown here are for a three layer sample prepared without surfactant (blue), with Tween 60 surfactant (4×10^{-4} mol dm^3) (red), and of Brij 98 surfactant (4×10^{-4} mol dm^3) (green). Raman shifts observed and labelled here correspond to the anatase phase.[1] 123

Figure 3.19. Normalised absorption curve used to determine photocatalytic half-life in minutes for samples prepared with TiBALD precursor and Tween surfactants. Control (CT2) sample represents the TiBALD sample prepared without surfactant addition and is used for comparison. 128

Figure 3.20. Normalised absorption curve used to determine photocatalytic half-life (in minutes) for samples prepared with TiBALD precursor and Tween surfactants. Control (CT2) sample represents the TiBALD sample prepared without surfactant addition and is used for comparison. 128

Figure 3.21. Bar chart representing the rate of calculated photoactivity for Resazurin (Rz) dye molecules degraded s^{-1} cm^{-2} for each sample type. Surfactant concentrations are; A = 0.0006 mol dm^3 and B = 0.0004 mol dm^3. Samples represented here are two layer samples. Error bars shown are 5% experimental error. 129

Figure 3.22. Metal alkoxide SN2 hydrolysis mechanism where M= metal (Ti) X = H and R = alkyl group, as for TTIP precursor, R= $\{CH(CH_3)_2\}_4$. 131

Figure 3.23. **Top:** Hydrolysis mechanism of TiBALD. **Bottom:** Polycondensation reaction of TiBALD to Ti-O-Ti linkages that subsequently undergo nucleation and growth to form titanium dioxide. 132

Chapter 4.
Figure 4.0. Bar chart comparison of the average thin film thickness of thin films prepared by AACVD with TTIP precursor and toluene as solvent, with increasing concentrations of surfactants of different types, indicated by colours. The reactions were run until the entire precursor had been depleted, at a constant gas flow of 1 L min^{-1}. Error bars show the standard deviation. Numbers represent the molar concentration from 0.5 M – 2 M. 137

Figure 4.1. SEM images of TiO_2 thin films produced via AACVD with TTIP as precursor, toluene as solvent, with Tween 20 and Tween 40 surfactant addition in concentrations 0.5 M to 2 M. Films were deposited at 400 °C. 140

Figure 4.2. SEM images of TiO_2 thin films produced via AACVD with TTIP as precursor, toluene as solvent, with Brij 58 and Brij 98 surfactant addition in concentrations 0.5 M to 2 M. Films were deposited at 400 °C. 142

Figure 4.3. XRD for TiO_2 films produced by AACVD using TTIP precursor in toluene solvent, without surfactant (**TTIP Tol**) and with addition of Tween surfactants; **Tween 20** 0.5 M (A T20 0.5 t), 1 M (A T20 1 t), 2 M (A T20 2 t) and **Tween 40**; 0.5 M (A T40 0.5 t), 1M (A T40 1 t), 2 M (A T40 2 t). Peaks identified as anatase phase are marked in red and rutile in black. Peaks denoted with asterisks (*) are assigned to the F:SnO_2 coating of the glass substrate. 146

Figure 4.4. XRD for titanium dioxide films produced by AACVD using TTIP precursor in toluene solvent, without surfactant (TTIP Tol) and with the addition of Brij surfactants in several concentrations; **Brij 58** 0.5 M (A B58 0.5 t), 1 M (A B58 1 t), 2 M (A B58 2 t) and **Brij 98**; 0.5 M (A B98 0.5 t), 1M (A B98 1 t), 2 M (A B98 2 t). Peaks identified as anatase are marked in red and rutile marked in black. Peaks denoted with asterisks (*) are assigned to the F:SnO_{2co}ating of the glass substrate. 147

Figure 4.5. **(a)** Unit cell structure of anatase titanium dioxide, with the lattice planes directed in the (004) plane **(b)** and (101) plane **(c)**. 148

Figure 4.6. **(a**) The truncated tetragonal bipyramid crystal form of anatase TiO_2, showing the (101), (001) and (011) facets as modified from Diebold et al19 **(b**) Crystal representation of TiO2 anatase phase without the 004 plane and with the (004) plane **(c**), modified as seen in Ali et al, whom reserve all rights· Blue circles represent titanium atoms, and red represent oxygen**.** 149

Figure 4.7. **(a)** Schematic to show potential charges on anatase crystal surfaces as a result of increased oxygen concentration in some planes. **(b)** Schematic of potential binding of polar surfactant molecules to specific surfaces of anatase crystal. 149

Figure 4.8. Normalised absorption curve used to determine photocatalytic half-life in minutes for samples prepared by AACVD reaction of TTIP in toluene with addition of Brij surfactants. TTIP Tol sample represents the sample prepared without surfactant addition and is used for comparison. 151

Figure 4.9. Bar chart representing the rate of calculated photoactivity for resazurin dye molecules degraded per second per cm^2 for each AACVD sample type prepared with toluene as solvent. TTIP tol represents the control sample prepared without any surfactant addition. Surfactant types are represented as T20 and T40 for Tween 20 and Tween 40, and B58 and B98 for Brij 58 and Brij 98. Surfactant concentrations are represented by 0.5 (0.5 M), 1 (1 M) and 2 (2 M). Errors are shown as experimental percentage error (5%). Inset picture is a magnified version of the bar chart 152

to show differences between the slower rate samples.

Figure 4.10. Normalised absorption curve used to determine photocatalytic half-life in minutes for samples prepared by AACVD reaction of TTIP in toluene with addition of Tween surfactants. "TTIP Tol" sample represents the sample prepared without surfactant addition and is used for comparison. 153

Figure 4.11. Bar chart comparison of the average film thickness. Films were prepared by AACVD with TTIP precursor and DCM, with increasing concentrations (0.5M to 1M) of Brij and Tween surfactants, different types indicated by different colours. Error bars show standard deviation. TTIP DCM column in black represents the control sample prepared without surfactant addition. 155

Figure 4.12. SEM images of TiO_2 thin films produced via AACVD with TTIP as precursor, dichloromethane (DCM) as solvent, with Tween 20 and Tween 40 in concentrations 0.5 M to 2 M. Films were deposited at 400 °C. 156

Figure 4.13. SEM images of TiO_2 thin films produced via AACVD with TTIP as precursor, dichloromethane (DCM) as solvent, with Brij 58 and Brij 98 surfactant addition in concentrations 0.5 M to 2 M. Films were deposited at 400 °C. 157

Figure 4.13a. Chemical structure of Brij 58 and Brij 98 surfactants, where n = 20.

Figure 4.14. Critical packing parameter of an non-ionic surfactant where V0 is the volume of the hydrophobic tail group, ae is the equilibrium area of the hydrophilic head group and Ic is the chain/tail length. 159

Figure 4.15. Comparison bar chart of average surface roughness of thin films obtained when using a different solvent (Toluene or Dichloromethane) for AACVD with TTIP precursor and surfactant addition, deposited at 400 °C. Surfactants used were Brij 58, Brij 98, Tween 20 and Tween 40 in 0.5 M and 1 M concentrations. 'TTIP' is the control sample prepared without surfactant addition. Errors bars show the standard deviation. 162

Figure 4.16. XRD of TiO_2 films produced by AACVD using TTIP precursor in DCM solvent, without surfactant (**TTIP DCM**) and with Brij surfactants in 0.5 M, 1M and 2M; **Brij 58** (A B58 0.5 d, A B58 1 d, A B58 2 d) and **Brij 98** (A B98 0.5 d, A B98 1 d, A B98 2 d). Peaks identified as anatase are marked in red and rutile in black. Peaks denoted with asterisks (*) are assigned to the F:SnO_2 coating of the glass substrate. XRD normalised for intensity. 163

Figure 4.17. XRD of TiO_2 films produced by AACVD using TTIP precursor in DCM solvent, without surfactant (**TTIP DCM**) and with Tween surfactants in 0.5M, 1M and 2M; **Tween 20** (A T20 0.5 d, AT20 1 d, A T20 2 d) and **Tween 40** (A T40 0.5 d, A T40 1 d, A T40 2 d). Peaks identified as anatase are marked in red and rutile in black. Peaks denoted with asterisks (*) are assigned to the F:SnO_2 coating of the glass substrate. XRD normalised for intensity. 164

Figure 4.18. Bar chart comparing the texture coefficients of different samples prepared with toluene/DCM solvent, with and without the addition of surfactant. Samples were prepared as stated in Fig 4.23. Surfactants used; Brij 58, Brij 98, Tween 2, Tween 40 in 0.5 M and 1 M concentrations. 'TTIP' is the control sample prepared without surfactant addition. 165

figure 4.19. Normalised absorption curve used to determine photocatalytic half-life in minutes for samples prepared by AACVD reaction of TTIP in DCM with addition of Brij surfactants in different concentrations from 0.5 M to 1M. TTIP DCM sample represents the sample prepared without surfactant addition. 166

Figure 4.20. Bar chart representing the rate of calculated photoactivity for resazurin dye molecules degraded per second per cm^2 for each AACVD sample prepared with DCM as solvent. TTIP DCM represents the control sample prepared without surfactant addition. Inset picture shows magnified version of bar chart to show differences between the slower rate samples. 167

Figure 4.21. Normalised absorption curve used to determine photocatalytic half-life in minutes for samples prepared by AACVD reaction of TTIP in DCM with addition of Tween surfactants. TTIP DCM sample represents the sample prepared without surfactant addition and is used for comparison. 168

Figure 4.30(a)(b) Bar chart comparison representing the rate of calculated photoactivity for resazurin dye molecules degraded per second per cm2 for each AACVD sample type prepared with toluene (blue) and DCM (red) as solvent. TTIP represents the control sample prepared without any surfactant addition. Surfactant types are represented as T20 and T40 for Tween 20 and Tween 40. Surfactant concentrations are represented by 0.5 (0.5 M) and 1 (1 M). Error bars show 5% experimental error. (b) Brij prepared samples. 170

Chapter 5.

Figure 5.0. SEM images of TiO_2 thin films produced via HCVD with the surfactant mixture added via aerosol in two forms; Brij surfactant in 1M concentration in a solution of methanol (HB98 1-m) and Brij surfactant 1M concentration in toluene (HB98 1-t). Films were deposited at 550 °C. 175

Figure 5.1. SEM images of TiO_2 thin films produced via HCVD with Brij surfactants added via a methanol solution. Surfactants were added in concentrations of 0.5 M – 2 M as indicated by numbers. Films were deposited at 550 °C. 177

Figure 5.2. SEM images of TiO_2 thin films produced via HCVD with Tween surfactants added via a methanol solution. Surfactants were added in concentrations of 0.5 M – 1 M as indicated by numbers. Films were deposited at 550 °C. 179

Figure 5.3. Bar chart comparison of the average thin film thickness of thin films prepared by HCVD with TTIP precursor and ethanol as solvent, with increasing concentrations of different surfactant mixtures in methanol added via AACVD, indicated by colours. Error bars show the standard deviation. Numbers represent the molar concentration from 0.5 M – 2 M. 180

Figure 5.4.(a) Schematic representation of surfactant size relative to one another with exaggerated representations of head and tail size. 181

Figure 5.4b Schematic of potential micelle formation with non-ionic surfactants and the nucleation/growth of film surrounding them. 183

Figure 5.5. Bar chart to show average surface roughness (nm, root mean square) for TiO_2 thin film samples prepared by hybrid CVD (red) , AACVD with toluene as solvent (light blue) and AACVD with DCM as solvent (dark blue). Error bars show 5% percentage error. 184

Figure 5.6. Bar chart comparison between average particle size (nm) shown with 10% measurement error, and the average RMS surface roughness (nm) shown with standard deviation error. 185

Figure 5.7. Schematic to show the two possible wetting regimes of a droplet on a surface; Cassie-Baxter and Wenzel, with corresponding equations for measuring the contact angle on a rough surface (θr) when the contact angle on a smooth surface is known, where D = pillar diameter, P is pillar pitch, H is pillar height and r is droplet radius. 186

Figure 5.8.1. Cropped SEM images with corresponding contact angles (before° à after °) to the bottom left of each image and surface RMS roughness (nm) to the bottom right of each image. 187

Figure 5.8.2. Worked example for the estimation of wetting regime for HCVD samples. Pillar pitch was estimated at half the pillar (particle) diameter. The height was estimate as an average of RMS surface values, as given in table 5.1. When the left side of the equation is equal to or greater than the height, the sample will follow the Wenzel rather than the Cassie-Baxter regime. 189

Figure 5.11. XRD of TiO_2 films produced by HCVD without surfactant (HCVD) and with Brij surfactants in methanol via aerosol in several concentrations where numbers represent concentration (M); **Brij 58** (H B58 0.5, H B58 1, H B58 2) and **Brij 98** (H B98 0.5, H B98 1, H B98 2). Peaks identified as anatase are marked in red, brookite in blue and rutile in black. Peaks denoted with asterisks (*) are assigned to the F:SnO_2 coating of the glass substrate. XRD normalised for intensity. 192

Figure 5.11. XRD of TiO_2 produced by HCVD without surfactant (APCVD) and with Tween surfactants in methanol via aerosol in several concentrations where numbers represent concentration (M); **Tween 20 (**H T20 0.5,H T20 1) and **Tween 40** (H T40 0.5, H T40 1). Peaks identified as anatase are marked in red, brookite in blue and rutile in black. Peaks denoted with asterisks (*) are assigned to the F:SnO_2 coating of the glass substrate. XRD normalised for intensity. 193

Figure 5.12. Comparison of average crystallite size (nm) for thin films prepared by hybrid CVD (red), AACVD with toluene (light blue) and AACVD with DCM (black). 193

Figure 5.13. Comparison of texture coefficient in the (004) plane of anatase phase thin films produced by hybrid CVD (red), AACVD with toluene (light blue) and AACVD with DCM (black). 193

Figure 5.14. Normalised absorption curves for determination of photocatalytic half-life (minutes) for samples prepared by hybrid CVD reactions with and without the addition of Brij surfactants. HCVD represents the films prepared without surfactant and is used for comparison. 0.5, 1 and 2 represent the concentration (M) of surfactant that was used to make the films. 195

Figure 5.15. Normalised absorption curves for determination of photocatalytic half-life (minutes) for samples prepared by hybrid CVD reactions with and without the addition of Tween surfactants. HCVD represents the films prepared without surfactant and is used for comparison. 0.5 and 1 represent the concentrations (M) of surfactant. 1966

Figure 5.16. Bar chart representing the calculated rate of photoactivity for the degradation of resazurin dye s^{-1} cm^2 for each sample prepared by hybrid CVD with and without surfactant addition. APCVD represents the sample prepared without any surfactant addition. Error bars show standard deviation. 196

Figure 5.17.a. Bar chart to compare the photoactivity rates of thin films prepared by hybrid CVD (red), AACVD (blue) and sol-gel (black). Rates are shown as rate of photodegradation of resazurin dye s^{-1} cm^2. APCVD, AA tol, AA DCM and TTIP and TiBALD represent the samples prepared by each method without surfactant addition. 202

Figure 5.17. b. Enlarged version of fig 5.18(a) for better comparison between sample sets. Bar chart here is as above, comparing the photoactivity rates of thin films prepared by hybrid CVD (red), AACVD (blue) and sol-gel (grey). Errors shown are 5% experimental error. 203

Chapter 6.

Figure 6.1. Product details of the DSSC technology produced by Glass 2 Energy Ltd for building integrated photovoltaic (BIPV) window facades. Glass 2 Energy reserve all rights to this information and pictures which have been reproduced in this thesis with full permission.[2] 201

Figure 6.2. Schematic of the semi-transparent dye sensitised solar cell configuration, where the counter electrode is either indium doped tin oxide (ITO) glass or fluorine doped tin oxide (FTO) glass with a layer of finely dispersed platinum is deposited, the electrolyte is a ionic redox electrolyte, the monoadsorbed dye is that which is adsorbed onto the TiO_2 thin film which is deposited onto the FTO glass directly. 203

Figure 6.3. (a)(b)(c) **6.3.(a)** Schematic of the dye solar cell active area in red, and the dimensions of the TiO_2 anode. The blue box represents the area of the anode which is left uncovered by the sealing gasket in order to make an electrical contact for connecting the device together and making performance. **6.3 (b)** Schematic of dye sensitised solar cell configuration, and photo of a typical DSSC under illumination. 206

Figure 6.4. Current-Voltage (IV) curve for the DSSC device a1 showing 0.0131 % PCE efficiency, highlighted in blue in table 6.2. This was prepared in configuration 1 as detailed above, with a 2 layer control TiO_2 thin film produced by sol-gel with TTIP precursor and no surfactant addition. 209

Figure 6.5. Current-Voltage (IV) curve for the DSSC device A11 showing 0.0073 % PCE efficiency, highlighted in blue in table 6.3. This was prepared in configuration 1 as detailed above, with a 3 layer TiO_2 thin film produced by sol-gel with TTIP precursor and Brij 98 surfactant addition in 0.0004 mol dm^3 concentration. 210

Figure 6.5a Representative transmission (%) spectra for DSSC devices prepared in configuration 1, with DSSC performance values given in tables 6.2-6.3. 211

Figure 6.6. Current-Voltage (IV) curves for the DSSC devices prepared in configuration 1.5, with a platinum counter electrode showing enhanced performance compared to the ITO electrode as in figures 6.4 and 6.5. IV curves here are for (a) A14, DSSC with 0.1429 % PCE efficiency, prepared with a sol-gel film made with TTIP precursor and Brij 58 surfactant in a concentration of 0.0006 mol dm^3, and (b) A16, DSSC with 0.2257 % PCE efficiency, prepared with a sol-gel film made from TTIP precursor and Brij 98 surfactant in ca concentration of 0.0004 mol dm^3, as highlighted in blue in table 6.4. 213

Figure 6.7. Current-Voltage (IV) curves for the DSSC devices prepared in configuration 2, with 42 hours dye soaking time, HI-30 Iodolyte (high performance electrolyte) and a platinum counter electrode. IV curves here are for (a) DSSC with 0.1792 % PCE efficiency (b) DSSC with 0.1134 % PCE efficiency and (c) DSSC with 0.1193 % PCE efficiency, as shown in table 6.5. 215

Figure 6.7a Representative transmission (%) spectra for DSSC devices prepared in configuration 2. Devices shown here are A17 and A19, control thin film devices as described in figure 6.7 above. 216

Figure 6.8. Current-Voltage (IV) curves for the DSSC devices prepared in configuration 2, with 42 hours dye soaking time, HI-30 Iodolyte (high performance electrolyte) and a platinum counter electrode. IV curves here are for (a) A26- DSSC with 0.3814 % PCE efficiency (b) A28- DSSC with 0.3721 % PCE efficiency (c) A30-DSSC with 0.3303 % PCE efficiency and (d) A23- DSSC with 0.2484 % efficiency as shown in table 6.6. 218

Figure 6.8a Representative transmission (%) spectra for DSSC devices prepared in configuration 2. Devices shown here are A26, A22, A29 and A24, Brij 58/Brij 98 thin film devices as described in figure 6.8 and table 6.6. 218

Figure 6.9. Current-Voltage (IV) curves for the DSSC devices prepared in configuration 2, with 42 hours dye soaking time, HI-30 Iodolyte (high performance electrolyte) and a platinum counter electrode. IV curves here are for (a) DSSC with 0.1689 % PCE efficiency (b) DSSC with 0.3749 % PCE efficiency (c) DSSC with 0.2396 % PCE efficiency and (d) DSSC with 0.3392 % efficiency as shown in table 6.7. 221

Figure 6.10 Representative transmission (%) spectra for DSSC devices prepared in configuration 2. Devices shown here are A50, A47, A54 and A52, Brij 58/Brij 98 thin film devices as described in figure 6.8 and table 6.9. 237

Figure 6.11 Current-Voltage (IV) curves for the DSSC devices prepared from AACVD films in configuration 1, with corresponding optical % transmission plots. Configuration 1= 24 hours dye soaking time, triiodide electrolyte and an ITO counter electrode. IV curves here are for (a) DSSC with 0.004 % PCE efficiency (b) DSSC with 0.0021 % PCE efficiency (c) 211

DSSC with 0.011 % PCE efficiency as shown in tables 6.10-6.12.

Figure 6.12 Representative transmission (%) spectra for DSSC devices prepared in configuration 1.5, with 24 hours dye soaking time, triiodide electrolyte and platinum counter electrode. Devices shown here are A73, A75, A77 and A78, Tween 20/ Tween 40 thin film devices as described in figure 6.13 and table 6.14. 231

Figure 6.13 (ab). Current-Voltage (IV) curves for the optimum DSSC devices prepared with AACVD thin films, in configuration 2, with 42 hours dye soaking time, HI-30 Iodolyte (high performance electrolyte) and a platinum counter electrode. IV curves here are for (a) DSSC with 0.0337 % PCE efficiency (b) DSSC with 0.0295 % PCE efficiency as shown in table 6.15. (c) % transmission plot for sample A79 (d) % transmission plot for sample A83. 233

Figure 6.14 As seen and modified from the review by Calogero et al,[3] of whom reserve all rights. Chart to show progression of DSSC performance using different vegetable based natural dyes. Data on the right shows state-of-the-art vegetable dye-based DSSC efficiency (2015), all data references found within this reference.[3] 235

Figure 6.15 Photographs of washed purple potatoes (a), sliced for freeze drying (b), and undergoing filtering after hydrolysis steps to produce purple dye. 236

Figure 6.16 Current-Voltage (IV) curves for TiO_2 thin film devices prepared with 3 layer "control" thin films (prepared without surfactant) and ruthenium dye sensitiser (A1, A4, A5 and A6) compared to that prepared with anthocyanin dye derived from purple potatoes (A85). DSSC devices were prepared in configuration 1, with 24 hours dye soaking time, triiodide electrolyte and an indium-doped tin oxide counter electrode. %PCE efficiency are given in each IV curve for comparison. 238

Figure 6.17 Photographs of DSSC devices prepared with ionic liquids; (a) shows a non-sealed DSSC prepared with CB-1a ionic liquid showing a light green colour, (b) shows a sealed DSSC prepared with CB-8 with a dark blue hue owing to the presence of cobalt in the ionic liquid. 244

Appendix A

A1 Selection of representative Tauc Plots (used to determine band gap of TiO_2 thin films) 277-279

A2 Typical photographic example of wetting behaviour of TiO_2 thin films before and after UV irradiation. Film sample shown here was prepared with Tween 60 surfactant ($6x10^{-4}$ mol dm^3) 280

Appendix B **SEM images for sol-gel samples prepared with TTIP and TiBALD**

B1 SEM images of samples prepared by sol-gel with TTIP as precursor, with no surfactant addition. Numbers represent the number of layers. Samples were annealed at 500°C for 15 minutes. 281

B2 SEM Images of samples prepared by sol-gel with TTIP as precursor and decreasing concentrations of Tween® 60 surfactant. T60 D= $8x10^{-4}$ mol dm^3, T60 A= $6x10^{-4}$ mol dm^3, T60 B=$4x10^{-4}$ mol dm^3. Numbers represent the number of layers. Samples were annealed at 500°C for 15 minutes. 281

B3 SEM Images of samples prepared by sol-gel with TTIP as precursor and decreasing concentration of Tween® 40 surfactant. T40 A= $6x10^{-4}$ mol dm^3, T40 B=$4x10^{-4}$ mol dm^3. Numbers represent the number of layers. Samples were annealed at 500 °C for 15 minutes. 282

B4 SEM Images of samples prepared by sol-gel with TTIP as precursor and decreasing concentration of Tween® 20 surfactant. T20 A= $6x10^{-4}$ mol dm^3, T20 B=$4x10^{-4}$ mol dm^3. Numbers represent the number of layers. Samples were annealed at 500 °C for 15 minutes. 282

B5 SEM Images of samples prepared by sol-gel with TTIP as precursor and decreasing concentration of Brij® 98 surfactant. B98 A= $6x10^{-4}$ mol dm^3, B98 B=$4x10^{-4}$ mol dm^3. Numbers represent the number of layers. Samples were annealed at 500 °C for 15 minutes. 283

B6 SEM Images of samples prepared by sol-gel with TTIP as precursor and decreasing concentration of Brij® 98 surfactant. B98 A= $6x10^{-4}$ mol dm^3, B98 B=$4x10^{-4}$ mol dm^3. Numbers represent the number of layers. Samples were annealed at 600 °C for 1 hour. 284

B7 SEM Images of samples prepared by sol-gel with TiBALD as precursor and decreasing concentration of Tween® 60 surfactant. T60 DT = $8x10^{-4}$ mol dm^3, T60 AT = $6x10^{-4}$ mol dm^3, T60 BT = $4x10^{-4}$ mol dm^3. Numbers represent the number of layers. Samples were annealed at 600 °C for 1 hour. 285

B8 SEM Images of samples prepared by sol-gel with TiBALD as precursor and decreasing concentration of Tween® 40 surfactant. T40 AT = $6x10^{-4}$ mol dm^3, T40 BT = $4x10^{-4}$ mol dm^3. Numbers represent the number of layers. Samples were annealed at 600 °C for 1 hour. 286

B9 SEM Images of samples prepared by sol-gel with TiBALD as precursor and decreasing concentration of Tween® 20 surfactant. T20 AT = $6x10^{-4}$ mol dm^3, T20 BT = $4x10^{-4}$ mol dm^3. Numbers represent the number of layers. Samples were annealed at 600 °C for 1 hour. 286

B10 SEM Images of samples prepared by sol-gel with TiBALD as precursor and decreasing concentration of Brij 58 and Brij 98 surfactant. AT = $6x10^{-4}$ mol dm^3, BT = $4x10^{-4}$ mol dm^3. Numbers represent the number of layers. Samples were annealed at 600 °C for 1 hour. 287

Appendix C	**Current (I) –voltage (V) curves showing performance of DSSC devices produced in chapter 6.**	288
A	**A1-** TTIP Control 2 (2)/ Triiodide/ N3 dye 24 hrs/ ITO CE	
	A2- TTIP Control 4 (2)/ Triiodide/ N3 dye 24 hrs/ ITO CE	
	A3- TTIP Control 7 (2)/ Triiodide/ N3 dye 24 hrs/ ITO CE	
	A4- TTIP Control 1 (3)/ Triiodide/ N3 dye 24 hrs/ ITO CE	
	A5- TTIP Control 2 (3)/ Triiodide/ N3 dye 24 hrs/ ITO CE	
	A6- TTIP Control 3 (3)/ Triiodide/ N3 dye 24 hrs/ ITO CE	292
	A7- TTIP B98 B-4 (2)/ Triiodide/ N3 dye 24 hrs/ ITO CE	
	A8- TTIP B98 B-8 (2)/ Triiodide/ N3 dye 24 hrs/ ITO CE	
	A9- TTIP B98 B-8 (3)/ Triiodide/ N3 dye 24 hrs/ ITO CE	
	A10- TTIP B98 B-0 (3)/ Triiodide/ N3 dye 24 hrs/ ITO CE	
	A11- TTIP B98 B-1 (3)/ Triiodide/ N3 dye 24 hrs/ ITO CE	
B	**A12-** TTIP B58 A-2 (2)/ Triiodide/ N3 dye 42 hrs/ Pt CE	
	A13- TTIP B58 A-7 (2)/ Triiodide/ N3 dye 42 hrs/ Pt CE	
	A14- TTIP B58 A-5 (3)/ Triiodide/ N3 dye 42 hrs/ Pt CE	
	A15 - TTIP B58 A-7 (3)/ Triiodide/ N3 dye 42 hrs/ Pt CE	
	A16- TTIP B98 B-3 (3)/ Triiodide/ N3 dye 42 hrs/ Pt CE	293
	A17- TTIP Control 4 (2)/ Iodolyte/ N3 dye 42 hrs/ Pt CE	
	A18- TTIP Control 7 (2)/ Iodolyte/ N3 dye 42 hrs/ Pt CE	
	A19- TTIP Control 9 (3)/ Iodolyte/ N3 dye 42 hrs/ Pt CE	
C	**A23-** TTIP B98 B-1 (2)/ Triiodide/ N3 dye 42 hrs/ Pt CE	
	A24- TTIP B98 B-4 (2)/ Triiodide/ N3 dye 42 hrs/ Pt CE	
	A25- TTIP B98 B-3 (2)/ Triiodide/ N3 dye 42 hrs/ Pt CE	
	A26 - TTIP B58 A-8 (3)/ Triiodide/ N3 dye 42 hrs/ Pt CE	
	A27- TTIP B58 A-2 (3)/ Triiodide/ N3 dye 42 hrs/ Pt CE	
	A28- TTIP B58 A-4 (3)/ Iodolyte/ N3 dye 42 hrs/ Pt CE	294
	A29- TTIP B98 B-3 (3)/ Iodolyte/ N3 dye 42 hrs/ Pt CE	
	A30- TTIP B98 B-8 (3)/ Iodolyte/ N3 dye 42 hrs/ Pt CE	
	A31- TTIP B98 B-5 (3)/ Iodolyte/ N3 dye 42 hrs/ Pt CE	
	A32- TTIP T20 B-1 (2)/ Iodolyte/ N3 dye 42 hrs/ Pt CE	
	A33- TTIP T20 B-4 (2)/ Iodolyte/ N3 dye 42 hrs/ Pt CE	

D

A34- TTIP T20 B-0 (2)/ Iodolyte/ N3 dye 42 hrs/ Pt CE

A35- TTIP T40 B-4 (2)/ Iodolyte/ N3 dye 42 hrs/ Pt CE

A36- TTIP T40 B-7 (2)/ Iodolyte/ N3 dye 42 hrs/ Pt CE

A37 - TTIP T40 B-3 (2)/ Iodolyte/ N3 dye 42 hrs/ Pt CE

A38- TTIP T40 B-6 (2)/ Iodolyte/ N3 dye 42 hrs/ Pt CE

A39- TTIP T40 B-5 (2)/ Iodolyte/ N3 dye 42 hrs/ Pt CE

295

A40- TTIP T20 B-6 (3)/ Iodolyte/ N3 dye 42 hrs/ Pt CE

A41- TTIP T20 B-7 (3)/ Iodolyte/ N3 dye 42 hrs/ Pt CE

A42- TTIP T40 B-5 (3)/ Iodolyte/ N3 dye 42 hrs/ Pt CE

A43- TTIP T40 B-7 (3)/ Iodolyte/ N3 dye 42 hrs/ Pt CE

A44- TTIP T40 B-3 (3)/ Iodolyte/ N3 dye 42 hrs/ Pt CE

E

A45- TTIP T40 B-9 (3)/ Iodolyte/ N3 dye 42 hrs/ Pt CE

A46- TTIP T40 B-8 (3)/ Iodolyte/ N3 dye 42 hrs/ Pt CE

A47- TiBALD B58 AT-8 (2)/ Iodolyte/ N3 dye 42 hrs/ Pt CE

A48 - TiBALD B58 AT-6 (2)/ Iodolyte/ N3 dye 42 hrs/ Pt CE

A49- TiBALD B58 AT-5 (3)/ Iodolyte/ N3 dye 42 hrs/ Pt CE

A50- TiBALD B58 BT-1 (3)/ Iodolyte/ N3 dye 42 hrs/ Pt CE

296

A51- TiBALD B58 BT-7 (3) / Iodolyte/ N3 dye 42 hrs/ Pt CE

A52- TiBALD B98 BT-7 (2)/ Iodolyte/ N3 dye 42 hrs/ Pt CE

A53- TiBALD B58 BT-5 (2)/ Iodolyte/ N3 dye 42 hrs/ Pt CE

A54- TiBALD B58 AT-7 (3)/ Iodolyte/ N3 dye 42 hrs/ Pt CE

A55- TiBALD B58 AT-1 (3)/ Iodolyte/ N3 dye 42 hrs/ Pt CE

F

A56- TiBALD B98 BT-1 (1)/ Iodolyte/ N3 dye 42 hrs/ Pt CE

A57- TiBALD B98 BT-2 (3)/ Iodolyte/ N3 dye 42 hrs/ Pt CE

A58- AACVD Tol (1)/ Triiodide/ N3 dye 24 hrs/ ITO CE

A59 - AACVD Tol (2)/ Triiodide/ N3 dye 24 hrs/ ITO CE

A60- AACVD B98 0.5 t (1)/ Triiodide/ N3 dye 24 hrs/ ITO CE

297

A61- AACVD B98 0.5 t (2)/ Triiodide/ N3 dye 24 hrs/ ITO CE

A62- AACVD B98 0.5 t (3)/ Triiodide/ N3 dye 24 hrs/ ITO CE

A63- AACVD B98 1 t (1)/ Triiodide/ N3 dye 24 hrs/ ITO CE

A64- AACVD B98 1 t (2)/ Triiodide/ N3 dye 24 hrs/ ITO CE

A65- AACVD B98 1 t (3)/ Triiodide/ N3 dye 24 hrs/ ITO CE

A66- AACVD B58 0.5 t (1) Triiodide/ N3 dye 24 hrs/ ITO CE

G **A67-** AACVD B58 0.5 t (2) Triiodide/ N3 dye 24 hrs/ ITO CE

A68- AACVD B58 0.5 t (3) Triiodide/ N3 dye 24 hrs/ ITO CE

A69- AACVD B58 1 t (1) Triiodide/ N3 dye 24 hrs/ ITO CE

A70 - AACVD B58 1 t (2) Triiodide/ N3 dye 24 hrs/ ITO CE

A71- AACVD B58 1 t (3) Triiodide/ N3 dye 24 hrs/ ITO CE

A72- AACVD T20 0.5 t (1)/ Triiodide/ N3 dye 24 hrs/ Pt CE 298

A73- AACVD T20 0.5 t (2)/ Triiodide/ N3 dye 24 hrs/ Pt CE

A74- AACVD T20 1 t (1)/ Triiodide/ N3 dye 24 hrs/ Pt CE

A75- AACVD T20 1 t (1)/ Triiodide/ N3 dye 24 hrs/ Pt CE

A76- AACVD T40 0.5 t (1)/ Triiodide/ N3 dye 24 hrs/ Pt CE

A77- AACVD T40 0.5 t (2)/ Triiodide/ N3 dye 24 hrs/ Pt CE

H **A78-** AACVD T40 0.5 t (3)/ Triiodide/ N3 dye 24 hrs/ Pt CE

A79- AACVD B98 0.5 t (1)/ Iodolyte/ N3 dye 42 hrs/ Pt CE

A80- AACVD B98 0.5 t (2) Iodolyte/ N3 dye 42 hrs/ Pt CE

A81- AACVD B98 0.5 t (3) Iodolyte/ N3 dye 42 hrs/ Pt CE

A82- AACVD B98 1 t (1) Iodolyte/ N3 dye 42 hrs/ Pt CE

A83- AACVD B58 1 t (1) /Iodolyte/ N3 dye 42 hrs/ Pt CE 299

A84- AACVD B58 1 t (2) /Iodolyte/ N3 dye 42 hrs/ Pt CE

A85- TTIP Control 3/ Triiodide/ Purple potato dye/ ITO CE

A86- TTIP B58 A-3/ CB-1a/ N3 dye 24 hrs/ ITO CE

A87- TTIP B58 A-3/ CB-1a/ N3 dye 24 hrs/ ITO CE

A88- TTIP B58 B-2/ CB-3a/ N3 dye 24 hrs/ ITO CE

I **A89-** TTIP B98 B-2/ CB-3a/ N3 dye 24 hrs/ ITO CE

A90- TTIP B98 A-3/ CB-3a/N3 dye 24 hrs/ ITO CE

A91- TTIP B98 A-3/ CB-3a/ N3 dye 24 hrs/ ITO CE

A92- TTIP B98 B-2/ CB-4/ N3 dye 24 hrs/ ITO CE

A93- TTIP B98 B-3/ CB-5/ N3 dye 24 hrs/ ITO CE 300

A94- TTIP B98 A-2/CB-6/ N3 dye 24 hrs/ ITO CE

A95- TTIP B98 A-2/ CB-7/ N3 dye 24 hrs/ ITO CE

A96- TTIP B98 A-2/ CB-8/ N3 dye 24 hrs/ ITO CE

List of Tables

Chapter 1		Page Number
Table 1. 1	Basic physical and chemical properties of titanium dioxide phases	40
Table 1.2.	Partial charges (δ) of the metal (M) in alkoxide complexes. Values as seen in Pierre.[5]	48
Table 1.3.	Examples of single and dual source precursors used for the CVD of titanium dioxide thin films.	60
Chapter 2.		
Table 2.1.	Sol-gel details: surfactant name, corresponding sol name/ precursor used with relevant concentration of surfactants added (mol/ dm^3) and subsequent annealing time and temperature.	80
Table 2.2.	Details of the non-ionic surfactants investigated in sol-gel with common name in coloured rows, followed by chemical name/synonyms, approximate molecular weights and the chemical formula with structure.	81
Table 2.3.	AACVD details: surfactant name, corresponding sample name and solvent used with concentration of surfactant added (mol/ dm^3) and deposition temperature.	84
Chapter 3.		
Table 3.1.	Sol-gel sample names with relevant surfactant types and concentrations added, as well as annealing temperature and time. Samples were produced in duplicate, with 1, 2 and 3 layer samples produced for each sol-gel type.	94
Table 3.2.	Results for TTIP prepared samples with and without the addition of Tween 60 surfactant, where D= 0.008 mol dm^3, A= 0.006 mol dm^3, B = 0.004 mol dm^3. Sample C represent control samples prepared without surfactant. Numbers represent the number of layers. Samples were annealed at 500°C for 15 minutes. Formal quantum efficiency (FQE) is the number of dye molecules degraded per incident photon, whereas the formal quantum yield (FQY) is the number of dye molecules degraded per absorbed photon.	110
Table 3.3.	Results for samples prepared using TTIP precursor with addition of Tween 20 and Tween 40, A= 0.006 mol dm^3, B = 0.004 mol dm^3. Sample C represents control samples prepared without surfactant. Numbers represent the number of layers. Samples were annealed at 500°C for 15 minutes. FQE is the number of dye molecules degraded per incident photon, and FQY is the number of dye molecules degraded per absorbed photon.	111

Table 3.4.	Results for samples prepared using TTIP precursor with addition of Brij 58 and Brij 98, in two concentrations, A= 0.006 mol dm^3, B = 0.004 mol dm^3. Sample C represents the sample prepared without surfactant. Numbers represent the number of layers. Samples were annealed at 500°C for 15 minutes. Values denoted with an asterisk (*) are samples that showed agglomerated particles in SEM images. FQE is the number of dye molecules degraded per incident photon, and FQY is the number of dye molecules degraded per absorbed photon.	112
Table 3.5.	Results for samples prepared using TTIP precursor with addition of Brij 58 and Brij 98, in two concentrations, A= 0.006 mol dm^3, B = 0.004 mol dm^3. Sample C represents the control sample prepared without surfactant. Numbers represent the number of layers. Samples were annealed at 600°C for 1 hour. Values denoted with an asterisk (*) are samples that showed agglomerated particles in SEM images. FQE is the number of dye molecules degraded per incident photon, and FQY is the number of dye molecules degraded per absorbed photon.	113
Table 3.6.	Results table for samples prepared using TiBALD precursor with addition of Tween 60 in three concentrations DT = 0.0008 mol dm^3, A= 0.0006 mol dm^3, B = 0.0004 mol dm^3. Tween 40 and Tween 20, in two concentrations, A and B. Sample C represents the control sample prepared without surfactant. Numbers represent the number of layers. Samples were annealed at 600°C for 1 hour. Values denoted with an asterisk (*) are samples that showed agglomerated particles in SEM images. FQE is the number of dye molecules degraded per incident photon, and FQY is the number of dye molecules degraded per absorbed photon.	124
Table 3.7.	Results table for samples prepared using TiBALD precursor with addition of Brij 58 and Brij 98, in two concentrations, A= 0.0006 mol dm^3, B = 0.0004 mol dm^3. Sample C represents the control sample prepared without surfactant. Numbers represent the number of layers. Samples were annealed at 600°C for 1 hour. FQE is the number of dye molecules degraded per incident photon, and FQY is the number of dye molecules degraded per absorbed photon.	126

Chapter 4.

Table 4.0.	Surfactant name, corresponding sample name and solvent used with concentration of surfactant added (mol/ dm^3) and deposition temperature.	135
Table 4.1.	Surfactant types with their molecular weight, density, critical micelle concentration (CMC) and hydrophilic-lypophilic balance (HLB).	138
Table 4.2.	Results for samples prepared by AACVD using TTIP in toluene with the addition of surfactant in the precursor solution. Three concentrations of surfactant were used, 0.5 M to 2 M. Sample C represents the control sample prepared without surfactant. Samples were deposited 400°C until all of the precursor solution was depleted.	145

Table 4.3.	Results for samples prepared by AACVD using TTIP in DCM with the addition of surfactant in the precursor solution. Three concentrations of surfactant were used, 0.5 M to 2 M. Sample C represents the control sample prepared without surfactant. Numbers represent the number of layers. Samples were deposited at annealed at 400°C until all of the precursor solution was depleted.	160
Table 4.4.	Summary table to show the samples exhibiting the fastest photocatalytic degradation rates for resazurin dye and the respective data for each sample that contributes to the enhancement performance observed. Green highlighted values are the highest photocatalytic rates observed. Yellow highlighted areas are an indication of which properties of the material may have contributed to the enhanced photocatalytic performance.	171
Chapter 5.		
Table 5.0.	HCVD details: Surfactant name, corresponding sample name and concentration of surfactant added (mol/ dm^3) and deposition temperature.	174
Table 5.1.	Results for samples prepared by HCVD using TTIP with ethanol in combination with the addition of surfactant in a methanol solution. Three concentrations of surfactant were used, 0.5 M to 2 M. Sample 'HCVD' represents the control sample prepared by hybrid CVD without surfactant. Samples were deposited at 550°C until all of the surfactant solution was depleted.	189
Chapter 6.		
Table 6.1.	Surfactant types and concentrations used to prepare TiO_2 thin films by sol-gel, with corresponding TiO_2 sample name and precursor used.	208
Table 6.2.	DSSC device performance for sol-gel TiO_2 thin films prepared with TTIP precursor, without surfactant addition in configuration 1. Power conversion efficiency (PCE, %) values highlighted blue are the best PCE values obtained within a group of devices prepared with the same type of TiO_2 thin film in a specific configuration.	209
Table 6.3.	DSSC device performance for sol-gel TiO_2 thin films prepared with TTIP precursor and Brij 98 surfactant in 0.0004 mol dm^3 concentrations. Power conversion efficiency (PCE, %) values highlighted blue are the best PCE values obtained within this group of devices.	210
Table 6.4.	DSSC device performance for sol-gel TiO_2 thin films prepared with TTIP precursor and Brij 58 in 0.0006 mol dm^3 concentrations (A) and Brij 98 in 0.0004 mol dm^3 concentrations (B). PCE, % values highlighted blue are the best PCE values obtained within this group.	212
Table 6.5.	DSSC device performance for sol-gel TiO_2 thin films prepared with TTIP precursor without surfactant addition. Power conversion efficiency (PCE, %) values highlighted yellow are for those showing optimum performance (> 0.1 %)and blue for the best PCE values obtained within a group of devices prepared with the similar TiO_2 thin film types.	214

Table 6.6.	DSSC device performance for sol-gel TiO_2 thin films prepared with TTIP precursor and Brij 58 and Brij 98 surfactants in concentrations A (0.0006 mol dm^3) and B (0.0004 mol dm^3). Power conversion efficiency (PCE, %) values highlighted yellow are for those showing optimum performance (> 0.1 %)and blue for the best PCE values obtained within this group of devices.	217
Table 6.7.	DSSC device performance for sol-gel TiO_2 thin films prepared with TTIP precursor and Tween 20 and Tween 40 surfactants in concentration B (0.0004 mol dm^3). Power conversion efficiency (PCE, %) values highlighted yellow are for those showing optimum performance (> 0.1 %)and blue for the best PCE values obtained within this group of devices.	220
Table 6.8.	DSSC performance of sol-gel TiO_2 thin films prepared with TIBALD precursor and Brij 58 surfactant in concentrations A (0.0006 mol dm^3) and B (0.0004 mol dm^3). The highest power conversion efficiency (PCE, %) value obtained within this group is highlighted blue.	222
Table 6.9.	DSSC performance of sol-gel TiO_2 thin films prepared with TIBALD precursor and Brij 98 surfactant in concentrations A (0.0006 mol dm^3) and B (0.0004 mol dm^3). The highest power conversion efficiency (PCE, %) values obtained within this group are highlighted blue.	223
Table 6.10.	DSSC performance of AACVD TiO_2 thin films prepared with TTIP precursor and toluene as solvent with no surfactant addition.	226
Table 6.11.	DSSC performance of AACVD TiO_2 thin films prepared with TTIP precursor, toluene as solvent and Brij 98 surfactant in concentrations of 0.5 M and 1M . The highest power conversion efficiency (PCE, %) value obtained within this group is highlighted blue.	227
Table 6.12.	DSSC performance of AACVD TiO_2 thin films prepared with TTIP precursor, toluene as solvent and Brij 58 surfactant in concentrations of 0.5 M and 1 M. The highest power conversion efficiency (PCE, %) value obtained within this group is highlighted blue.	229
Table 6.13.	DSSC device performance for AACVD TiO_2 thin film prepared with TTIP precursor, toluene as solvent and Tween 20 surfactant in concentrations of 0.5 M and 1 M. The highest power conversion efficiency (PCE, %) value obtained within this group is highlighted blue.	230
Table 6.14.	DSSC performance of AACVD TiO_2 thin films prepared with TTIP precursor, toluene as solvent and Tween 40 surfactant in concentrations of 0.5 M and 1 M. The highest power conversion efficiency (PCE, %) value obtained within this group is highlighted blue.	230
Table 6.15.	DSSC performance of AACVD TiO_2 thin films prepared with TTIP precursor, toluene as solvent and Brij 58 or Brij 98 surfactants in concentrations of 0.5 M and 1. The highest power conversion efficiency (PCE, %) values obtained within this group are highlighted blue.	232

Table 6.16.	DSSC performance of sol-gel TiO_2thin film prepared with TTIP precursor and no surfactant addition, tested with an organic anthocyanin dye derived from purple potatoes.	237
Table 6.17.	Table of compositions for the 7 ionic liquids tested as ionic electrolytes in dye-sensitised solar cells. Abbreviations for precursors and details of categories are listed below.	240
Table 6.18.	DSSC performance of sol-gel TiO_2 thin films prepared with Brij 58 and Brij 98 surfactants in concentrations A (0.0006 mol dm^3) and B (0.0004 mol dm^3. Numbers in TiO_2 sample name (2 or 3) represent number of thin film layers. Power conversion efficiency (PCE, %) values and fill factor (FF) values highlighted yellow are the best PCE/ FF values obtained for these devices.	242

List of Equations.

Equations 1.1- 1.9	Overall equations of the process of photocatalysis with titanium dioxide	38-39
Equation 2.0-2.2	Sol-gel hydrolysis process for metal-alkoxide precursor	47
Equation 3.0.	Arrhenius Law	56
Equation 3.1.	Reynolds number (simplified)	57
Equation 3.2.	Knusden number	57
Equations 4.1-4.6	Reaction equations of processes occuring within a DSSC	68-69
Equation 4.7.	Overall solar energy-to-electric power conversion efficiency	70
Equation 4.8.	Fill Factor	70
Equation 4.9.	Incident Photon to Current Conversion Efficiency (IPCE)	71
Equation 5.0.	Light Harvesting Efficiency (LHE)	71
Equation 5.1.	Beer-Lambert Law	71
Equation 6.0.	Formal Quantum Efficiency (FQE)	91
Equation 6.1.	Formal Quantum Yield (FQY)	91
Equation 7.0.	Wenzel regime	186

List of Abbreviations

AACVD	Aerosol-Assisted Chemical Vapour Deposition
Acac	Acetylacetone
APCVD	Atmospheric Pressure Chemical Vapour Deposition
AFM	Atomic Force Microscopy
BIPVs	Building Integrated Photovoltaics
B58	Brij® 58 surfactant
B98	Brij® 98 surfactant
CB	Conduction Band
CE	Counter electrode
CVD	Chemical Vapour Deposition
DCM	Dichloromethane
DSSC	Dye-sensitised Solar Cell
EACVD	Electric Field Assisted Chemical Vapour Deposition
FTO	Fluorine-doped tin oxide
HCVD	Hybrid Chemical Vapour Deposition
HES	High Energy Solar Radiation
IR	Infra-red
ITO	Indium-doped tin oxide
IV	Current-Voltage
LPCVD	Low-Pressure Chemical Vapour Deposition
MOCVD	Metal Organic Chemical Vapour Deposition
Pt	Platinum
PV	Photovoltaic
PVD	Physical Vapour Deposition
Rf	Resofurin
Rz	Resazurin
RMS	Root Mean Square
SA	Surface Area
SEM	Scanning Electron Microscopy
TiBALD	Titanium Bis-Ammonium Lactato Dihydroxide
TTIP	Titanium Isopropoxide
TCO	Transparent conduction oxide
TTIP	Titanium Isopropoxide
T20	Tween® 20 surfactant
T40	Tween® 40 surfactant
T60	Tween® 60 surfactant
VB	Valence Band
XRD	X-ray Diffraction

Introduction: Tailoring titanium dioxide thin films for photocatalysis and energy efficient glazing via dye-sensitised solar cells

The energy efficiency, sustainability and environmental impact of buildings are a growing concern for the modern world. There is increasing acceptance of the environmental and health concerns related to the use of fossil fuels for energy production and their subsequent role in climate change, which is placing greater demands on policy makers and industry to shift to a zero-carbon energy supply. These issues coupled with the escalating cost and demand for energy in buildings is putting pressure on building legislators to increase the energy efficiency and sustainability of new buildings whilst reducing the impact on the environment. As a result, more pressure is being placed on manufacturers to design buildings which are not only energy efficient, but also incorporate their own renewable energy supply.

In contemporary buildings windows play an important aesthetic as well as functional role, where the trend for high-rise, glazed office buildings is evident around the world regardless of climate. Taller buildings offer the benefits of higher density over a smaller ground space, which in densely populated cities offers a distinct advantage. Windows in such buildings come with several advantages; a much desired (and needed) view of the outside world, added passive solar heat gain which can be beneficial in colder climates and reduction in electric lighting required due to natural light access. However, disadvantages such as heat loss, thermal and visual discomfort due to glare, and increased need for air-conditioning in warmer climates due to solar heat gain often outweigh these benefits, especially when energy efficiency is concerned.[4] Windows typically account for about 30-50% of transmission losses within a building envelope, and as a result the extensive use of windows can dramatically increase the subsequent energy demands of a building. [5] Increased heating or cooling is often then required to maintain a comfortable internal environment for occupants. It is for this reason that many advanced window systems now utilise so called 'energy efficient' glazing in the form of low emissivity (low E) coatings, spectrally selective thin films (heat mirrors) or absorbing glass.[6] However increasing research interest is focusing on moderating window glazing so that it offers not only energy efficiency, but also energy generation, as the demand for energy independent buildings increases.

One of the most attractive options to incorporate renewable energy into buildings is through the use of building-integrated photovoltaics (BIPVs). Solar energy is often considered

the cleanest and most abundant renewable energy option,[7] and with the sun's irradiation to earth producing around 10,000 times more energy than that required for daily use by mankind, it is considered by many to be the most viable option to meet demand.[8] It seems both a natural and logical step that research into BIPVs should aim to combine with energy efficient glazing, to develop energy efficient solar glazing which can both *conserve* and *generate* energy for use within the building.

Current Approaches to Solar Glazing

The incorporation of solar glazing into high-rise office buildings is a particularly attractive opportunity for architects and building manufacturers, potentially satisfying both the aesthetic desires of the former with the energy requirements of the latter, whereby entire façades of buildings could be used for solar power generation. However, to function as a normal window, solar glazing needs to retain some element of transparency, and as a result the system must sacrifice its ability to utilise light from the visible part of the solar spectrum.[9] Therefore it is understandable that solar glazing will inherently have a low efficiency compared to traditional BIPV materials, however, solar glazing offers the advantage of being suitable for coverage over a much larger area on a building, in a much more aesthetically pleasing way.

For solar glazing to become a truly practical and realistic alternative, power conversion efficiency of the system must be optimised, in addition, it should be low cost, semi-transparent and easy to manufacture.[10] Ideally solar glazing should be manufactured in-line utilising existing technologies, such as chemical vapour deposition (CVD) or sputtering, which are already in use within the glazing industry. Importantly, there is a significant balance to be found whereby transparency of the solar glazing is optimised without compromising power conversion efficiency. Another important consideration is the life-span of the technology, whereby organic photovoltaics are unsuitable for applications in buildings due to their short life-time.[11]

Currently there is a vast array of research into developing next generation materials for BIPVs that do not rely on the conventional single p-n junction, that are called 'third-generation' photovoltaics. For solar glazing however, the challenge of producing a photovoltaic that can act as a window as well as a solar harvesting device is still on-going. The most successful approaches have utilised dye-sensitised solar cells (DSSCs)[12,13] and organic photovoltaics (OPVs).[14–16] These approaches are particularly suitable as they meet all criteria whereby they use relatively low cost materials and their manufacture can be easily scaled up to an industrial level.

More recently, microstructured perovskite solar cells have experience a huge surge in research interest, and specifically for their potential to be integrated into windows.[10,17] However, as with DSSCs and OPVs, perovskite solar cells have been subject to intense scrutiny in terms of their potential stability under 'real-life' conditions for outdoor applications in windows.[18]

Scope of this thesis

This thesis aims to explore the use of titanium dioxide (TiO_2) thin films in semi-transparent dye-sensitised solar cells (DSSCs) for application in energy efficient glazing in windows. The methods used to produce TiO_2 thin films will be applicable to scale-up within industry, whereby the use of surfactants will be explored for modifying and optimising thin films for both self-cleaning photocatalytic and DSSC applications.

Fundamentals: 1: Titanium Dioxide-structure, properties and applications

1.1. Titanium Dioxide

The discovery of photocatalytic water splitting under ultraviolet (UV) light using titanium dioxide (TiO_2) as an electrode in 1972 by Fujishima and Honda sparked a worldwide surge in research into use of TiO_2 as a photocatalyst. [19,20] Not only did this discovery push the use of TiO_2 beyond the scope of its main commercial application as a pigment in paints, toothpastes and sunscreens, but it spawned a broad range of subsequent applications ranging from self-cleaning, antimicrobial thin-film coatings to environmental photocatalysts, gas sensors and, as for the subject of this thesis, as electrodes in dye-sensitised solar cells (DSSCs).[21–24]

Focus on enhancing the performance of TiO_2 materials for these applications has driven research at the nanoscale, whereby the control of composition, size and shape of TiO_2 nanoparticles has enabled the resulting morphology and composition of the material to be specifically tailored to suit its application. As a result, production of TiO_2 in the form of nanorods, nanowires and nanocrystalline thin films has been achieved using various controlled deposition methods including sol-gel[25] and hydrothermal routes,[26] as well as vapour deposition methods such as chemical vapour deposition (CVD),[27] physical vapour deposition[28] and more recently, aerosol-assisted CVD[29] and electric field assisted CVD.[30]

1.1.2 Functional Application: TiO_2 as a photocatalyst

Photocatalysts such as TiO_2 are commonly used for environmental remediation applications, such as in the degradation of organic pollutants,[31] treatment of contaminated waste water,[32] and also for the production of clean hydrogen fuel via water splitting. [33] A photocatalyst can be defined as a material which absorbs light to accelerate a chemical reaction, whereby the photocatalyst is subsequently regenerated. A semiconductor photocatalyst such as TiO_2 absorbs light with photon energies greater than or equal to its band gap energy ($h\nu \geq E_g$,) to excite an electron from the valence band (vb) into the conduction band (cb), leaving behind a hole (h^+). This can be represented by equation (1.1) and is also shown schematically in figure 1.2. Each polymorph of TiO_2 has a different band gap energy, thereby requiring different wavelengths of light for excitation of an electron whereby anatase (E_g = 3.20 eV) has a larger band gap than

rutile (E_g = 3.02 eV), which absorb 380 and 410 nm of light respectively.[34] Consequently, only ultraviolet light (about 5% of incident solar irradiation) is active for the photoexcitation process in pure TiO_2. [35] This has encouraged a wide variety of research into the doping of TiO_2 photocatalysts using metal ions to increase light absorption in the visible range. [36–40]

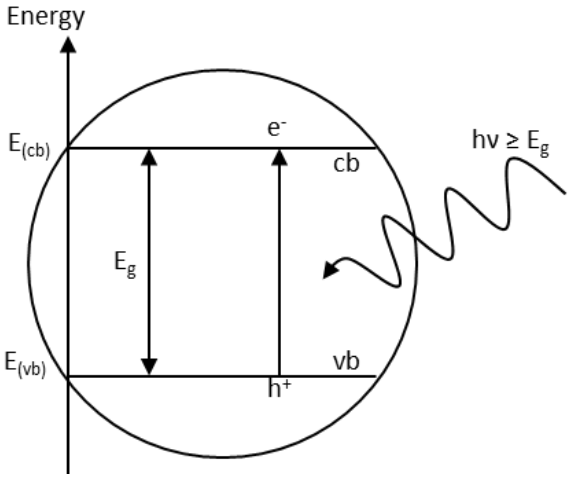

Figure 1.1: Schematic representing the photoexcitation of an electron to generate an electron-hole pair, where vb – valence band, cb – conduction band, E_g –bandgap energy).

Following initial charge separation, the photogenerated electron (e^-) and hole (h^+) can succumb to a variety of different fates. Recombination, as in Equation 1.2, (Fig. 1.2, (e)) may reduce the overall rate of photocatalysis. Alternatively, the electron and hole (charge carriers) may migrate via diffusion (Fig. 1.1.2 (b, c, d)) to then undergo reactions near or on the catalyst surface. However, recombination can take place within the bulk and also at the surface of semiconducting materials such as TiO_2 due to the presence of photoinduced intrinsic or extrinsic trapping sites. [41,42] As a result, charge carriers that migrate to the surface can be trapped by intrinsic subsurface energy traps as in equations 1.3 and 1.4.

$$TiO_2 + h\nu \rightarrow e^-_{cb} + h^+_{vb} \qquad \textbf{Equation 1.1}$$

$$e^-_{cb} + h^+_{vb} \rightarrow TiO_2 + h\nu + (\text{heat}) \qquad \textbf{Equation 1.2}$$

$$Ti^{IV} - O^{2-} - Ti^{IV} + h^+_{vb} \rightarrow Ti^{IV} - O^{\bullet-} - Ti^{IV} \qquad \textbf{Equation 1.3}$$

$$Ti^{IV} + e^-_{cb} \rightarrow Ti^{III} \qquad \textbf{Equation 1.4}$$

$$h^+_{vb} + D \rightarrow D^+ \qquad \textbf{Equation 1.5}$$

$$e^-_{cb} + A \rightarrow A^- \qquad \textbf{Equation 1.6}$$

Despite these competing reactions, if the electrons and holes that drift to the surface do not recombine (Fig 1.1.2. d), interfacial electron transfer can occur with the adsorbed acceptors (A) and donor molecules (D) on the surface via oxidation or reduction (Equations 1.5 and 1.6, Fig 1.1.2. b, c).[43]The reaction of these photogenerated electrons and holes in titanium dioxide with adsorbed species on the surface can result in the formation of reactive species such as superoxide ions ($O_2^{\bullet-}$) and hydroxyl radicals ($OH^{\bullet}$).[34] The presence of absorbed oxygen, water and hydroxide have found to be an advantage to the photocatalysis process, whereby absorbed oxygen acts as an electron trap, thereby producing oxygen radicals which can prevent recombination of charge carriers (Equation 1.7).[42] Absorbed water or hydroxides however, can act as hole traps resulting in the formation of hydroxyl radicals which can then participate in photocatalytic reactions on the surface. (Equations 1.8 and 1.9)[44]

$$e^-_{cb} + O_{2\,(abs)} \rightarrow O_2^- \qquad \textbf{Equation 1.7}$$

$$h^+_{vb} + H_2O_{(ads)} \leftrightarrow H^+_{(ads)} + OH^{\bullet}_{(ads)} \qquad \textbf{Equation 1.8}$$

$$h^+_{vb} + OH^-_{(ads)} \leftrightarrow OH^{\bullet}_{(ads)} \qquad \textbf{Equation 1.9}$$

A summary of the processes in photocatalysis are shown below in Figure 1.1.2.

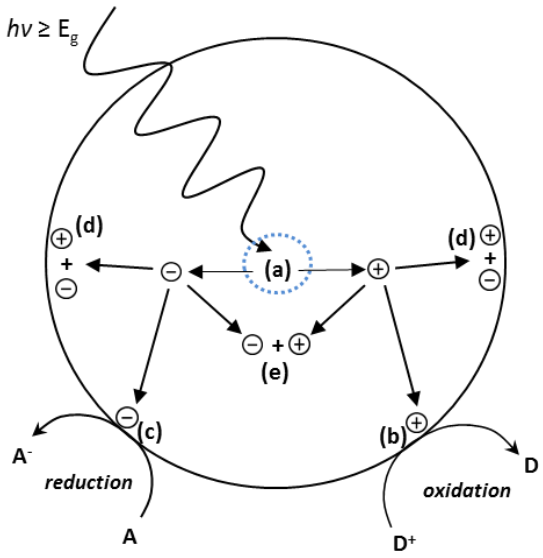

(a) Generation of an electron, ⊖, and hole ,⊕, from light
(b) Oxidation of the adsorbed donor species (D)
(c) Reduction of adsorbed acceptor species (A)
(d) Recombination at the catalyst surface
(e) Recombination in the bulk

Figure 1.1.2. Schematic of photogenerated electron and hole pathways over a semiconductor particle. (Adapted from Linsebigler et al.)[45]

1.1.3. Structure and properties: Tailoring TiO_2 for photocatalytic and DSSC applications

TiO_2 exists naturally in three semiconducting polymorphs; anatase, rutile and brookite, whereby rutile is the most thermodynamically stable phase at all temperatures and pressures up to 60 kbar.[46] Each structural polymorph is built upon the connection of TiO_6 octehedra, as shown in figure 1.1.3. The anatase phase only consists of edge-sharing octahedra, whereas rutile and brookite contain both corner-sharing and edge-sharing configurations. [47]

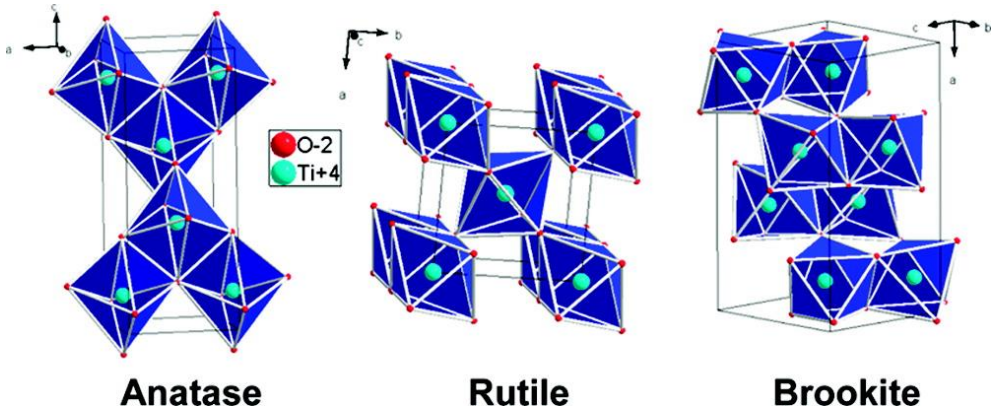

Figure 1.1.3. Representations of the three forms of TiO_2. Reproduced as seen in Dambournet et al, 2010. [47]

Despite all polymorphs of TiO_2 being non-toxic, chemically inert and durable to extended use as photocatalyst, anatase is often the phase of choice for photocatalytic applications whereby it offers the greatest efficiency.[48] The basic physical properties of the three phases of TiO_2 are shown in table 1, with information adapted from references. [43,49]

Table. 1.1. Basic physical and chemical properties of titanium dioxide phases

Phase	Crystal Structure	Refractive Index	Band Gap Energy (eV)	Thermal stability
Anatase	Tetragonal	2.56	3.2	Phase change to Rutile typically at 500 – 800 °C.
Rutile	Tetragonal	2.95	3.02	Most stable
Brookite	Orthorhombic	2.81	3.14	Metastable

As the photocatalytic activity of TiO_2 is directly related to its crystal properties; such as size and surface area of particles, presence of defects as well as phase and composition of the material, it is understandable that a significant amount of research has focused on preferentially obtaining anatase in TiO_2 syntheses.[50–54] It has been found that the difference in Gibbs free energy between the three polymorphs of TiO_2 is relatively small (between 4-20 kJ/mole) which suggests that the anatase and brookite phases are almost as stable as rutile at normal temperatures and pressures.[46]

There have been a wide variety of studies focused on the use ofTiO_2 as a photocatalyst, including how to modify its structure and properties to enable increased photocatalytic performance. TiO_2 has a photonic efficiency of less than 10% for most degradation processes, and current research has focused on improving the efficiency of TiO_2 through several methods. It is now possible to tailor TiO_2 photocatalysts for specific applications through optimisation of the material synthesis to obtain specific structural and chemical properties (1), narrowing of TiO_2's wide indirect bandgap to harness a larger portion of light from the solar spectrum (2) and surface sensitisation of TiO_2 via chemisorbed/physisorbed dyes/metal complexes (3).

(1) Optimising the synthesis of TiO_2

The TiO_2 synthesis can be tailored to produce a specific combination of characteristics in the resulting material, through altering the method used, such as sol-gel, hydrothermal, powder based, or thin film and also through treatments applied, such as different calcination temperatures, additives etc. The efficiency of the resultant photocatalyst is determined by the crystalline structure (anatase), particle size, pore size, density of OH groups, surface acidity, number and nature of trap sites (lattice and surface) within the material.[46] Generally the performance of all catalyst materials benefit from a high surface area which enables a greater concentration of active sites per square metre, leading to a higher overall reactivity. Thus, the smaller the particle size, the larger the surface area, and the higher the expected activity. [55]

Investigations into the effect of TiO_2 particle size on phase stability and transformations within the material have confirmed that the relative stability of each phase can be dependent on the particle size itself, whereby anatase is most thermodynamically favourable at particles sizes less than 11 nm, brookite is most stable between 11 and 35 nm and rutile is most stable at sizes greater than 35 nm. [56] The optimal particle size for photocatalytic TiO_2 has been referenced as between 10-15nm,[57] and this is due to the ability of the smaller anatase particles to accelerate the

diffusion of electrons and holes to the surface (as the distance is smaller) and to thereby inhibit electron-hole recombination through charge carrier trapping.[58] In addition, with a smaller particle size the overall surface area to volume ratio of the material is increased, thereby creating a larger surface area for the reactants to be in contact with TiO_2 and for the photocatalytic reaction to occur.

The type of synthetic method used and the presence of dopants can also encourage phase transformations within TiO_2. In particular, the presence of lattice and surface defects can encourage the anatase to rutile phase conversion, whereby an increase in surface defects enhances the transformation to rutile because these defects act as nucleation sites to form larger particles. As a result, in photocatalytic applications, defects can act as trapping sites for electrons and holes leading to recombination, therefore reducing the photocatalytic activity if there is no driving force for separation. [46,59]

(2) Narrowing TiO_2 bandgap to harness a larger portion of light from the solar spectrum

As the wide indirect bandgap of TiO_2 (3.2 eV) is only activated by radiation with wavelengths below 385 nm (accounting for only 5% of the solar spectrum) another tactic used to increase TiO_2 photocatalytic performance is to narrow the bandgap various metal dopants. Extrinsic doping with metals (such as Fe, Cu and V) and non-metals (such as N, S and C) has been studied in an effort to harness energy from the visible portion of the solar spectrum.[60]

(3) Surface sensitisation using dyes/metal complexes

Dye sensitisers or metal complexes can be chemisorbed or physisorbed on the surface of TiO_2 to enable increased efficiency of the excitation processes in the material. The use of a sensitiser expands the used wavelength range through excitation of the sensitiser followed by an electron transfer between the excited dye and the semiconductor conduction band. Depending on the redox environment, the dye is then able to donate or receive an electron, improving electron-hold separation in the material.[46]

State-of-the-art photocatalytic performance for TiO_2 thin films is typically benchmarked against Pilkington NSG Activ^{TM}, which is the world's first commercially available self-cleaning glass. Activ^{TM} is produced by an atmospheric pressure chemical vapour deposition (APCVD) technique

which is controlled to produce a 15 nm thick layer of TiO_2 on the surface of float glass,[61] and it has been measured under laboratory conditions to exhibit a photocatalytic efficiency of 2.7 x 10^{11} molecules s^{-1} cm^{-2} for the degradation of resazurin 'intelligent' ink.[60] Part of the difficulty in evaluating the photocatalytic performance of TiO_2 lies in the fact that within academic literature there are a wide variety of methods used to assess photocatalysis depending on the type of TiO_2 to be tested, whereby there are a very limited number of methods suitable for assessing thin films. Those methods suitable for thin film analysis include primarily stearic acid,[62,63] alongside more recent photocatalyst indicator inks in the form of redox dyes methylene blue (MB), resorufin (Rf), resazurin (Rz) and 2,6-dichloroindophenol (DCIP).[61]

For DSSC applications, similar properties as those required for photocatalytic applications are desired, such as small particle size, large surface area and reduced defects as described above. Therefore it can be suggested that photocatalytic performance can be used as an indication as to whether a thin film will perform well within a DSSC device, as the mechanisms of electron transfer through the film are similar; recombination needs to be kept to a minimum and increased surface area enables better absorption of light to kick-start the reaction. For DSSCs, anatase TiO_2 is once again favoured as the semiconducting material owing to its wide band gap energy of 3.2 eV (vs 3.02 eV for rutile). The major breakthrough for DSSCs came in 1991 when a mesoporous electrode with a high internal surface area was used.[64] This enabled an increased adsorption of dye sensitiser, meaning greater adsorption of light and increased electron injection into the TiO_2 thin film. Anatase TiO_2 has a greater photoactive potential than other phases such as rutile and brookite, meaning that it absorbs light only below 388 nm within the correct wavelengths for excitation, and so it is invisible to most of the solar spectrum, thus reducing the recombination rate of photo injected electrons as in the DSSC. [65–67] The optimum TiO_2 thin film for DSSCs is typically regarded as a porous thin film electrode, with a thickness of between 10-20µm, and particle sizes around 20 nm.[68]

Therefore, for the use of TiO_2 as an effective photocatalyst or as a semiconductor in DSSCs, there are a wide variety of characteristics that need to be considered and controlled, in addition to the overall structural properties of the TiO_2 catalyst. The surface area, porosity, pore size and distribution are of great importance for DSSC application, whereby the sensitisation of the thin film enables greater dye adsorption and thus greater light absorption and electron injection into the TiO_2 conduction band. [69] These characteristics are also very important for photocatalytic

applications, whereby the increased surface area due to small particle size and increased porosity means a larger surface area for the photocatalytic reaction to take place.

There has been extensive research focused on sol-gel methods for the preparation of TiO_2 photocatalysts and for DSSC applications, [65,69–85] as they offer a simple and efficient route to transparent nanostructured TiO_2 thin films whereby carefully controlling the hydrolysis of the titania precursor and the subsequent reaction conditions allows for the control of particle morphology, crystallite size, film thickness and the transformation between anatase and rutile phases.[58,86–89] As a result, this thesis will look at sol-gel processing in chapter 1 as a starting point for the production of photocatalytically active TiO_2 thin films for DSSC applications.

Fundamentals 1.2: Sol-Gel Technology for thin films

The sol-gel process is a wet chemical technique that enables substrates to be coated with thin films of unique compositions and properties which cannot often be obtained through other processing methods. Sol-gel coating systems have been extensively studied since the 1950's, with significant emphasis on the preparation of single oxide optical coatings such as TiO_2 and SiO_2. Bulk sol-gel processes utilising the alkoxide route were first introduced in 1971 by Dislich,[90] and since then research in this area has flourished as materials produced via this technique typically exhibit excellent homogeneity and high purity, whereby unique structures can be produced at low reaction temperatures, making this process useful for a wide range of applications.[77] Indeed, the sol-gel process allows for the microstructure of the deposited film to be directly controlled, an advantage which is often not possible with standard vapour-phase methods.[80] The main aspects of sol-gel chemistry and the application of sol-gel derived materials are described in detail in a number of reviews and books.[91–95] An overview of the use of sol-gel processing for the production of TiO_2 thin films will be given here.

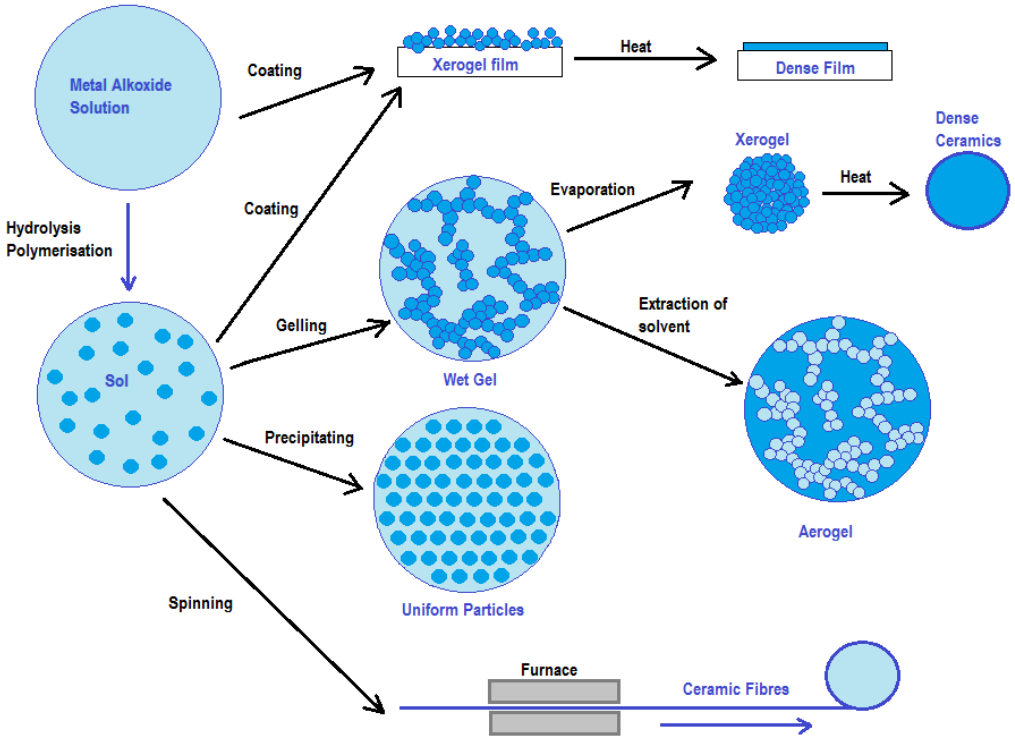

Figure 1.2.1 Schematic of the sol-gel process and possible products. Adapted from reference.[96]

The fundamental process of sol-gel involves the formation of a colloidal solution with 1-100nm sized particles, called a 'sol', which is subsequently formed into an integrated network or 'gel'. Thin films can be produced at this stage by spin-coating or dip-coating, followed by subsequent conversion to dense ceramic thin films with further drying and heat treatment.[97] Otherwise, complete polymerisation of the sol occurs when the solvent is lost through evaporation and the liquid sol becomes a solid gel. A schematic of the sol-gel process and the various products that can be produced via sol-gel technology is shown in Figure 1.2.1.

1.2.1. Principles of Sol-Gel Dip Coating

The dip coating method is one of the most popular wet-chemical techniques for producing metal oxide thin films. Unlike the similar method of spin coating, it does not require any specialised apparatus. A substrate is dipped into a sol-gel solution containing the chemical precursor and then gently withdrawn at a controlled rate. The thickness of the resulting thin film is a result of the balancing of forces at the stagnation point on the liquid surface. A faster withdrawal rate pulls more fluid up onto the substrate surface before it has time to flow back into the solution, thus creates thicker films. The thickness is also affected by fluid viscosity, density and surface tension.

Dip coating allows a thin film to be coated on both sides of the substrate, which is advantageous as it reinforces the effect of the coating and also reduces the number of coatings required. It is most often used for producing oxide thin film coatings over large areas such as on bulk glass.[98] Other substrates can be used as long as they withstand the required curing temperature of around 500°C. Thin films of up to 1µm can be deposited with a single coating, and several additional layers can be subsequently added. As sol-gel derived precipitates are typically amorphous in nature, they require further heat treatment to induce crystallisation. This heat treatment usually involves the calcination process, which frequently gives rise to particle agglomeration, grain growth and induced phase transformations.[77] Alternatively, hydrothermal treatments can be used to promote crystallisation at milder temperatures.

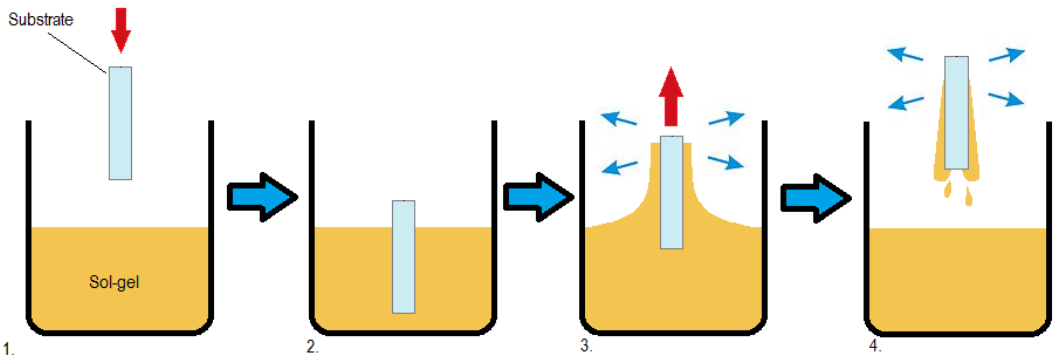

Figure 1.2.2. Schematic of Sol-Gel dip coating process.

1.2.2. The Metal Alkoxide Method

The most commonly used sol-gel synthesis for the production of TiO_2 thin films is the metal alkoxide method. The reaction mechanism for this process is shown in three stages below, whereby the metal alkoxide precursor (M= e.g. Si, Ti, Zr, Al etc., R = alkyl ligands) is rapidly hydrolysed to the corresponding hydroxide or oxide (equation 2.0) with a hydroxlyated species, represented here as water. This species is then polycondensed (equation 2.1-2.3) to form a new phase (M-O-M) in the form of a metal oxide sol gel:

$M(OR)_n + {}_nH_2O \rightarrow M(OH)_n + {}_nROH$ (hydrolysis) **Equation 2.0**

$M(OH)_n + M(OR)_n \rightarrow M\text{-}O\text{-}M + {}_nROH$ (alcohol condensation) **Equation 2.1**

$M(OH)_n + M(OH)_n \rightarrow M\text{-}O\text{-}M + H_2O$ (water condensation) **Equation 2.2**

During hydrolysis the alkoxy groups (OR) are replaced by hydroxo ligands (OH) or oxo ligands (O). The by-products in (2.0) and (2.1) are aliphatic alcohols which are removed by volatilization. These reactions can be summarised with an associative S_N2 mechanism as shown in figure 1.2.3 below, where X represents hydrogen.[99]

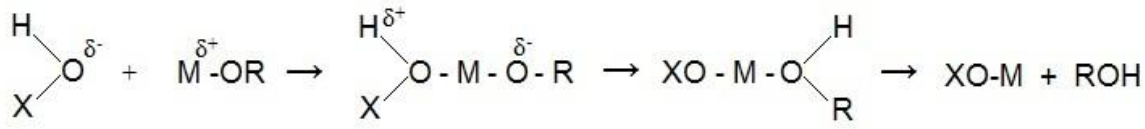

Figure 1.2.3. Metal alkoxide S_N2 hydrolysis mechanism where X = H and R = alkyl group.

The relative rates of the first two steps in this mechanism strongly affect the resulting structure and properties of the metal oxides produced. In addition, other factors which can influence the

products include; the reactivity of the metal alkoxide used, the pH and temperature of the reaction medium, the water to alkoxide molar ratio, the nature of the solvent and the addition of any additives.[77,92] As a result, metal alkoxides are often tailored to allow for a specific rate of hydrolysis to be achieved. [100]

The kinetics of this metal alkoxide hydrolysis step has been shown to be very fast for most metal cations, whereby the electronegative alkoxide groups makes the metal centre highly prone to nucleophilic attack by water. Therefore, the more electrophilic metal centre as well as the larger and thus the more stereolabile coordination sphere results in a higher hydrolytic susceptibility. This difference can be explained using the partial charge model, whereby an alkoxide with the formula $M(OR)_z$ undergoes hydrolysis if:

(1) The metal M is an electrophile ($\delta(M) > 0$) *(see table 1.2 for exemplar partial charges δ(M) of metals)*
(2) The oxygen is a nucleophile ($\delta(O) < 0$)
(3) The leaving group (usually an alcohol or water molecule) can attain a positive partial charge thus enabling it to leave the intermediate structure.

Table 1.2. Partial charges *(*δ) of the metal (M) in alkoxide complexes. Values as seen in Pierre.[92]

Alkoxide	δ(M)
$Zr(OEt)_4$	+0.65
$Ti(OEt)_4$	+0.63
$VO(OEt)_3$	+0.46
$Si(OEt)_4$	+0.32

When the steric bulk of the metal alkoxide is increased, as in titanium alkoxide precursors, e.g. $Ti(OR)_4$ where R = ^{i}Pr or ^{t}Bu, monomeric species are reported.[101] Such metal alkoxides are advantageous for this process because they are volatile and therefore can be readily purified by distillation, producing very pure oxide products. However, owing to the high coordination number of the central metal atom, which is higher than its corresponding valency, coordination expansion occurs within the compound. As a result, metal alkoxides can be regarded as Lewis acids, whereby titanium alkoxides ($Ti(OR)_4$) react vigorously with water to produce ill-defined titanium-oxo/hydroxo precipitates. This means that chemical additives are often utilised to slow

down the hydrolysis reaction and enable more control over the resulting products. Additives such as acetylacetone, a stabilising agent, and acetic acid are frequently used to obtain transparent titania based sols, without the ill-defined precipitates previously mentioned.

1.2.3. Preparation of the TiO_2 sol-gel; traditional vs. novel precursors and other modifications

As discussed, the typical route to a TiO_2 sol-gel involves the hydrolysis of a titanium alkoxide precursor, utilising water to form a Ti-OH species and the corresponding alcohol. Titanium alkoxide precursors are often used, such as titanium isopropoxide ($Ti(OCH(CH_3)_2)_4$, (TTIP). However, due to the high reactivity of the Ti-OH species, hydrolysis often occurs quickly and exothermically without control, leading to undesirable consequences such as the precipitation of particles with uncontrolled shape and size. As a result it is necessary to find ways to slow down this process with greater control. There are several strategies that have been used to slow down this hydrolysis step, including changing the nature of the organic group, e.g. alkoxides with primary organic groups such as n-butoxides are less sensitive to hydrolysis than secondary ones such as isopropoxides. Another strategy is to increase the coordination number of the metal, thereby hindering its attack from water and the subsequent formation of the metal hydroxyl (M-OH) bond. In addition, it is possible to decrease the functionality of the precursor via partial substitution of the OR ligands with anionic ligands, such as carboxylates or β-diketonates, whereby the subsequent bonds that are formed are less susceptible to hydrolysis.

Alternatively, where precursors such as TTIP are used, non-aqueous sol-gel methods have been developed using acetic acid to modify the molecular structure of the titania precursor in the presence of an alcoholic solvent.[69,70,102] This non-aqueous route encourages the initial replacement of the titania alkoxy groups with acetate groups to form an alcohol. The alcohol then undergoes esterification with acetic acid to release water as a by-product. The water released through esterification or through the direct condensation of the acetate-bonded titanium initiates a slower hydrolysis reaction with much more control. In addition to this, it has been found that the addition of acetylacetone (acac) as a chelating agent can decrease the reactivity and further stabilise the sol for a longer period of time before precipitation occurs.[71] Another recent strategy utilises a novel titanium dioxide sol-gel precursor, called Titanium(IV) bis(ammonium lactato) dihydroxide (TiBALD), which has been investigated by Pelentridou et al,[103] with the advantage that TiBALD is stable at ambient temperatures in neutral solutions meaning that it can be

condensed in a controlled manner, thus it is an ideal precursor for the preparation of nanocrystalline titanium dioxide thin films.

In addition, an increasingly popular strategy to control the growth of metal oxide particles in the metal-alkoxide sol-gel method is through the addition of surfactants and polymer templates to the precursor sol-gel solution,[58,74,83,104,105] or through utilisation of the reverse micelle process.[106] Templating allows for the fine structure of a material to be controlled whereby a sacrificial template such as an organic membrane, like cellulose, acts as a support around which the final material can be built before it is removed. This technique is typically used for the preparation of materials that require a specific outer and predetermined inner structure.[105] The most common method to prepare highly porous materials with a specific pore structure and size is to use surfactants and block copolymers which act as pore directing agents within the sol-gel.

1.2.4. Surfactants

Surfactants are organic compounds which are amphiphilic, meaning that they contain both a hydrophilic and hydrophobic component, often referred to as the "polar head" and "non-polar tail". When a surfactant is dissolved within a solvent, the presence of the hydrophobic group distorts the solvent structure, increasing the free energy of the system. As a result, the surfactant spontaneously orients itself in such a way that the contact between the solvent and the hydrophobic group is minimised, thereby decreasing the free energy of the system.[107] For this reason, the surfactant is often regarded as a "spacer" within the sol-gel solution. Another method to minimise the contact between the solvent and the hydrophobic group is for aggregation of the surfactant molecules into structures such as spheres, cylinders or sheets, whereby the hydrophobic group faces the interior of the aggregate structure, and the hydrophilic groups face the exterior, in contact with the solvent. These structures are called micelles, and they alter the properties of the solution phase of the material.

There are several classifications of surfactants that can be used in materials processing including anionic, cationic, zwitterionic and non-ionic surfactants. The use of surfactants in sol-gel processing is a commonplace strategy for the direct control of particle size and shape during the growth phase for the enhancement of resulting properties.[73,83] Due to their amphiphilic nature, surfactants act as pore-directing agents that can enable the production of highly porous materials with specific pore size and structure. For sol-gel processes, ionic surfactants have been

investigated and shown to have limited potential for the preparation of porous TiO_2 thin films because they bind electrostatically to the product, whereby they cannot be easily removed through extraction or heat treatment methods post production.[69] As a result, this has led to increased interest in the use of non-ionic chain surfactants such as Tween® 20, Tween® 80 and Triton™ X-100.[69,70,106,108]

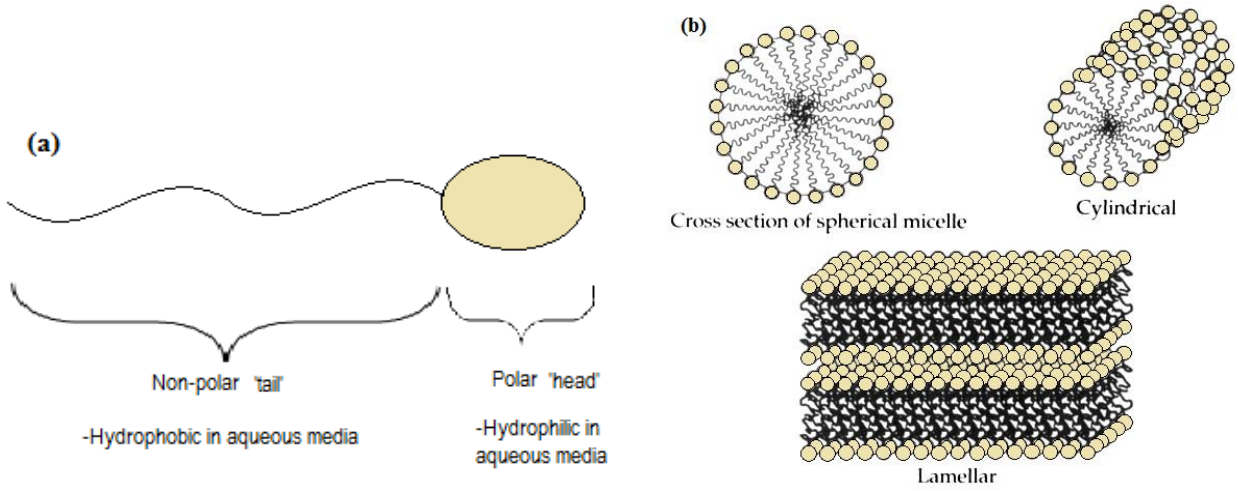

Figure 1.2.4(a) Structural representation of a surfactant molecule. **(b)** Micelle structures formed by surfactant molecules. *Adapted from reference*.[51]

1.2.5. Non-Ionic Surfactants

Non-ionic chain surfactants have been used widely for sol-gel processing owing to their distinct advantages over other types of surfactant molecules. As suggested by the name, in non-ionic surfactants, the surface-active part of the molecule bears no apparent ionic charge, and in addition, there is also no added sulphur or nitrogen groups present that may interfere with resulting particle formation in thin film synthesis. The most common type of non-ionic surfactants used are variations of polyethylene ethoxylates, with the common structure shown in figure 1.2.5.

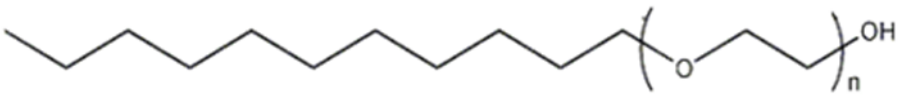

Figure 1.2.5. Structure of a typical non-ionic surfactant; polyethylene ethoxylate.

For the production of TiO_2 thin films, a wide variety of non-ionic surfactants have been used in sol-gel processing including Brij® surfactants,[70,73] Pluronic triblock copolymers such as P123 and

F127, [73,83,109,110] Triton variations such as X-100, [103,111] and Tween surfactants.[69,112] Two families of non-ionic surfactants will be investigated in this thesis; Brij and Tween, owing to their infrequent yet promising uses in sol-gel literature.[69,70]

Brij surfactants are di-block copolymers that have been shown to enable control of pore size and uniformity in mesoporous titania, as well as enhancement of photocatalytic activity.[113,114] Brij 58 has been used as an efficient structuring agent to prepare 2D-hexagonal TiO_2 mesoporous thin films by dip-coating, using $TiCl_4$ as precursor in a water/alcohol medium.[115] Brij 35 has been used with TTIP to produce TiO_2 nanoparticles that are a mixture of anatase and brookite.[116] In addition, Brij 98 has been used in combination with cetyl trimethyl ammonium bromide (CTAB) to produce mesoporous TiO_2 with a high specific surface area (SBET=279.0m^2g^1).[117]

Tween surfactants are polysorbate derivatives often used as detergents or emulsifiers for a variety of domestic as well as pharmaceutical applications owing to their non-toxicity and stability. The use of Tween surfactants in sol-gel processing however has enabled a variety of improvements over titanium dioxide thin films produced without the addition of surfactant, such as increased thin film thickness,[112] enhanced porosity[69] and improved photocatalytic activity.[58]

Chapter 3 will discuss the addition of two Brij surfactants with polyether chains of different lengths; 58 and 98; and three Tween surfactants of different polysorbate lengths; 20, 40 and 60 in different concentrations in sol-gel processing for the production of TiO_2 thin films. The subsequent microstructure and functional properties of TiO_2 thin films are reported.

Fundamentals 1.3: Chemical Vapour Deposition

There are a variety of methods used to deposit thin films onto a substrate, including physical vapour deposition techniques such as molecular beam epitaxy and sputtering. For glazing applications, chemical vapour deposition (CVD) is by far the most favourable method, allowing for the production of high quality, uniform films with little or no contamination. The CVD process involves chemical reactions between gaseous precursors; that occur either on or near a heated substrate, whereby the substrate can be metal, glass or silica wafer. The result is a solid film deposit on the substrate surface, and because this deposition occurs at the atomic level, materials with high purity can be produced, enabling control over the resulting properties of the film at the nanoscale. As a result, CVD can be used to produce single or multi-layer films, as well as composite materials and complex nanostructures for use in an array of applications, such as in the electronics industry for semiconductor devices and also in the glazing industry for windows. The unique advantages of CVD are that it can be used to produce multiple thin films, coat large surface areas, and that it is a non-line-of-sight technique, meaning that CVD deposits films with a high level of conformity on topographically complex surfaces that are generally not possible with techniques such as sputtering or PVD.

The use of CVD for the deposition of large-scale coatings on glass for window applications extends back to the 1960s where an important development in the history of CVD occurred through the introduction of 'on-line' CVD architectural coatings by Pilkington (now NSG Group). Such coatings are deposited on a very large scale in a continuous process, by atmospheric pressure CVD (detailed in section 1.3.7), directly onto the float glass as it is passing through the production line. By application of this coating directly to the glass while it is already on the manufacturing line, production costs are massively reduced, enabling economies of scale and production that are not possible with other 'off-line' techniques such as sputtering.[118] As a result of these developments, a whole range of glazing technologies are now possible through the on-line CVD process, including low thermal emissivity coatings (fluorine doped tin oxide glass ($F:SnO_2$)) to prevent heat loss through windows, as well as self-cleaning coatings (TiO_2) to remove dirt from the window surface.

1.3.1. Principles of CVD

Chemical vapour deposition combines many scientific and engineering processes, including thermodynamics, plasma physics, kinetics, fluid dynamics, and chemistry, of which some basic principles will be outlined here, but are discussed in greater detail in references. [118,119] CVD thin films are formed as a result of chemical reactions between precursors that occur homogeneously within the gas phase and/or heterogeneously on the substrate surface. This process is initiated most commonly by thermal activation, whereby heating the precursors and/or the substrate to high temperatures (>400°C) enables the necessary reactions to occur. The basic factors that control CVD are the thermodynamics and kinetics of the precursor chemistry, the processing parameters (reactor temperature, pressure and chemical precursor activity), the dynamics of heat and mass transport, in addition to the physics of surface adsorption and crystal growth of the thin film.

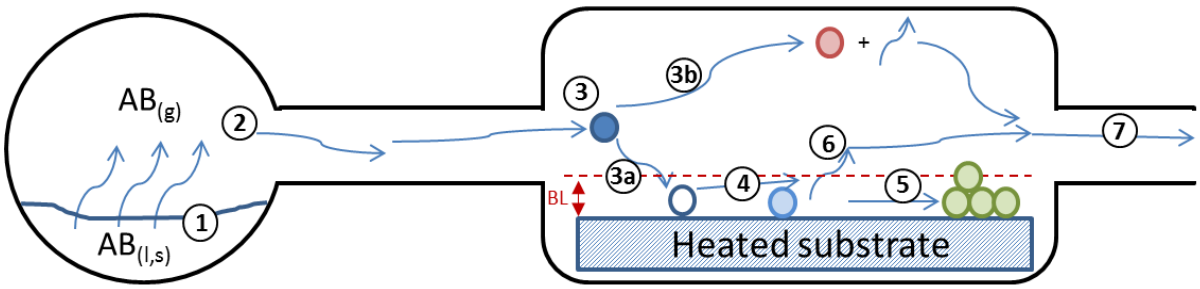

Figure 1.3.1. Simplified illustration of the main reaction steps in the process of CVD. Adapted from Choy.[120]

The process of CVD involves a series of gas-phase and surface reactions that are summarised in figure 1.3.1 and in the following key steps:

1. Active gaseous precursors are generated from solid or liquid precursors.
2. Gaseous precursor species are transported to the reaction chamber by a carrier gas, typically N_2.
3. Gas phase reactions occur between the precursor species to form reactive intermediate species that can then undergo two fates depending on the temperature:

(a) **Heterogeneous reaction:** At temperatures below the decomposition temperature of the reaction intermediates, the intermediate species undergo diffusion or convection across

the boundary layer. The boundary layer (BL) is a thin layer close to the substrate surface as shown in figure 1.3.1. These intermediates subsequently undergo steps 4-7.

(b) **Homogeneous reaction:** At temperatures higher than the decomposition temperature of the reaction intermediates, homogeneous gas phase reactions can occur as the intermediates undergo subsequent decomposition and/or chemical reactions forming powders and volatile by-products. Any powder that forms is collected on the substrate surface where it may act as a crystallisation centre. The by-products are carried away from the deposition chamber by the carrier gas stream. The film deposited in this way often exhibits poor adhesion to the substrate.

4. Adsorption of the gaseous reaction species onto the heated substrate initiates a heterogeneous reaction to occur at the gas-solid interface (i.e. on the heated substrate surface), forming a deposited material and by-products.
5. The deposited material can diffuse along the surface of the substrate until it reaches a crystallisation growth site, where nucleation and growth of the film can occur.
6. Gaseous by-products are removed from the boundary layer by either diffusion or convection.
7. Any unreacted gaseous precursor species and by-products are carried away from the deposition chamber by the carrier gas stream.

Often CVD processes are specifically tailored to follow just one of the two reaction pathways (homogeneous or heterogeneous) depending on the desired film, whereby a combination of both homogenous and heterogeneous reaction typically results in porous coatings.[120] However, as CVD is not a 'macro-scale' process, it is difficult to measure, monitor and control the deposition process directly to obtain a specific outcome. This is because the individual molecules reacting within a CVD system cannot be individually measured, monitored or controlled, as several reactions occur simultaneously without direct control. As a result, the uniformity, quality and repeatability for a given thin film process is determined through previous experience with that particular system, whereby the control strategies for CVD are developed through extensive experimentation, modelling and material analyses.[118]

1.3.2. Thermodynamics, kinetics and mass transport

CVD is a complex chemical system where reactions tend to be non-equilibrium and the process is determined by reaction kinetics and mass transport phenomena. The process of CVD is

initially governed by thermodynamics, which is the driving force of the reaction that determines whether the reaction is going to proceed, followed by the kinetics, which determines the rate of the reaction. In typical thermal CVD, where the process operates at elevated temperatures, it is this increased temperature that acts as the driving force of the reaction, whereby the Gibbs free energy of the reaction (ΔG_r) will be negative. The increased temperature encourages heat transfer between chemical reactants in the gas phase and also on the substrate surface, which then react to form a solid deposit (thin film) which is more thermodynamically stable than the precursor, and to any gaseous by-products. Therefore, film growth can be initially classified as limited by the substrate temperature, temperature and pressure within the reactor as well as the composition chemistry of reactants in the gas-phase.

However, at low substrate temperatures the rate of film growth is limited by the kinetics, which refers to the chemical reactions occurring between precursors in the gas-phase, on the substrate surface or those undergoing chemisorption or desorption. This is often called *kinetic growth or surface reaction rate limited* control, whereby the rate of thin film deposition increases exponentially with substrate temperature. The rate of deposition typically follows Arrhenius law as shown in equation 3.0:

$$\textit{Deposition Rate} = A \exp(-E_A / RT) \qquad \textbf{Equation 3.0}$$

Where A is a constant, E_A is the apparent activation energy, R is the gas constant and T is the deposition temperature.

At higher substrate temperatures, typically above 1350 °C, the kinetic processes occurring become so rapid that the deposition becomes limited by the diffusion of the active gaseous species through a boundary layer to the deposition surface, thus the speed at which the precursor reagents are delivered to the reactor and to the substrate surface. This means that the growth rate becomes almost independent of the temperature, and the film growth becomes *mass transport* or *diffusion* limited.

The mass transport phenomena within a CVD system can include (i) fluid (or flow) dynamics, e.g. the fluid flow, mass transfer and heat transfer of the precursor into the reactor, and (ii) mass transport of precursors near to the substrate surface and diffusion through the boundary layer.

Considerations of the fluid dynamics and mass transport within a CVD system can be used to understand how the control parameters such as reactor temperature, pressure, gas flow rate, density of gas supplied can affect the overall performance of the system, in particular the uniformity of the film coating produced.

CVD systems typically follow one of two types of fluid dynamics; molecular or continuum. In the molecular flow regime, the mean free path (l) of a gas molecule is relatively large (> 5 cm). The mean free path length (l) is the average distance travelled by a gas molecule before collision with another molecule occurs. This molecular flow regime is generally found in low pressure chemical vapour deposition (LPCVD) systems. In contrast, continuum flow regimes are more typically observed in atmospheric pressure chemical vapour deposition (APCVD) systems where the mean free path of a gas molecule is short as several gas phase collisions readily occur. In such continuum flow regimes, the system can be modelled as a fluid. Thus basic fluid mechanics concepts can be used to describe the fluid dynamic in the system and the mass transfer occurring in the gas phase. The fluid flow in a CVD process is characterised by several dimensionless parameters including the Reynolds number (Re) and the Knudsen number (k_n) as shown in equations 3.1 and 3.2:

$$\mathrm{Re} = \frac{pu}{\mu} \qquad \textbf{Equation 3.1}$$

The Reynolds number (Re) relates the mass density (p) and flow density (u) to the viscosity (μ) and defines the limit between the laminar (Re <100) and turbulent (Re >2100) flow regimes. Most CVD reactors operate with laminar flow, due to the typically low precursor flow rate used. [120] The Knudsen number defines the limits between laminar, intermediate and molecular flow, and is the ratio between the mean free path (λ) and reactor dimensions (d) perpendicular to the direction of flow, as shown in equation 3.2:

$$k_n = \frac{\lambda}{d} \qquad \textbf{Equation 3.2}$$

When $k_n > 1$ in a reactor, gas molecules are just as likely to strike the reactor surface as another gas molecule, and the system is functioning under the molecular flow regime. This flow is a result of the random orientation of molecules, and typically occurs in low pressure systems where there is a pressure gradient. If $k_n < 1$ in a reactor, then the gas molecules are convected through the system by other molecules in the carrier gas flow, and the system is said to be functioning

under the continuum flow regime. This flow type is a result of the precursor molecules diffusing from the bulk gas flow to the substrate surface due to a concentration gradient, and is typically observed in high pressure systems.

1.3.3. Structure and Morphology of CVD thin films

The properties of a thin film produced by CVD are directly related to the nature of its structure, which can be controlled by the deposition conditions such as substrate temperature, reactor pressure and gas phase composition of precursors. Thin films produced by CVD tend to fall within one of three main categories; amorphous, epitaxial or polycrystalline, as represented schematically and explained categorically in figure 1.3.2. This thin film morphology is determined by the surface diffusion and nucleation reactions that occur during deposition, and thus can be easily influenced by typical CVD process parameters such as substrate temperature, which can affect the film growth rate and the resulting film morphology.

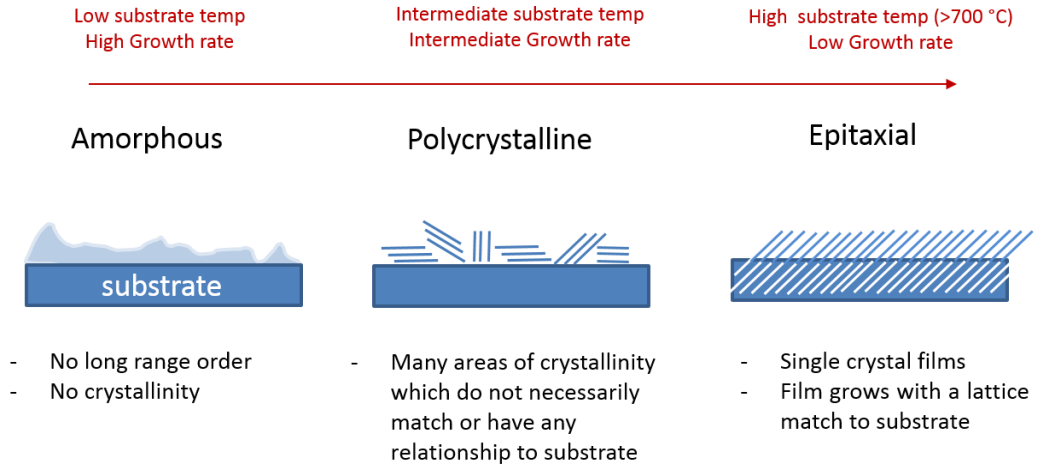

Figure 1.3.2. Schematic of three main types of thin film produced by the CVD process. Lines represent orientation of the crystal lattice.

In addition, the growth mechanism of a thin film can vary widely depending on the process parameters used. There are many different types of growth mechanism for thin films prepared by CVD, of which the three main types include layer-by-layer growth (Volmer-Webber), island growth (Van Der Meerwe) and mixed growth, a combination of both layer-by-layer and island growth (Stranski-Kastanov). The growth mechanism is determined by the strength of bonding between the substrate and film, or between the film and film. For example, if the bonding between the film and substrate is stronger than the film-film bonds that form then layer-by-layer

growth is favoured. If the bonds within the film (film-film bonds) are stronger, then island growth occurs. A combination of growth mechanisms occurs when both bond types have similar strength.[118]

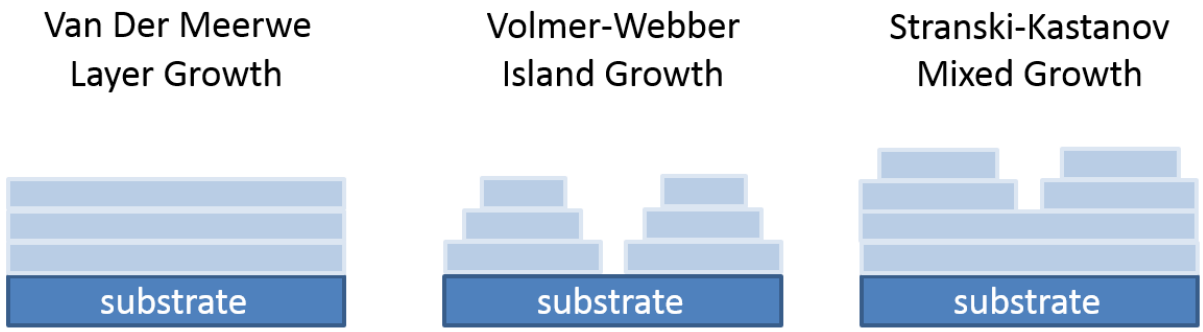

Figure 1.3.3. Three main mechanisms of thin film growth that occur within CVD.

The structure of a CVD film can be classified further into three major types depending on grain growth, as shown schematically in figure 1.3.4. (adapted from reference[119]). In zone A, the film structure consists of columnar grains with domed tops, whereas in zone B the structure is also columnar but the top edges of the columns are randomly faceted and angular. Zone C consists of fine accost grains, which are equiaxed, meaning that the crystal grains have approximately the same axis size.

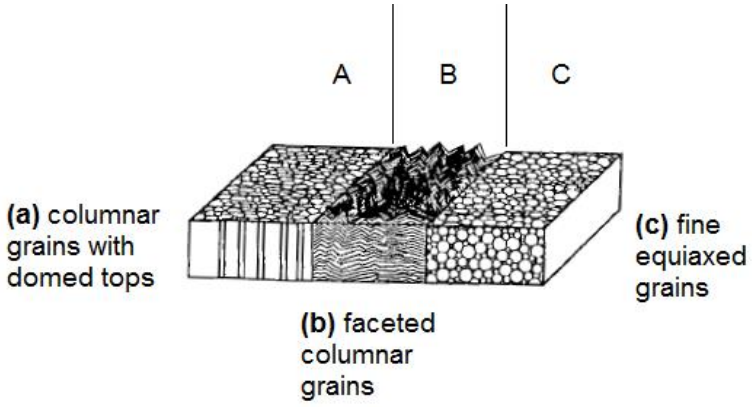

Figure 1.3.4. Schematic of thin film structures obtained by CVD with respect to grain growth. Adapted from reference.[119]

Typically, this microstructure depends on the material type being deposited, whereby metallic thin films, such as TiO_2, tend to form more crystalline deposits, typically of the columnar type structure as in zones A and B. As expected the crystal size and structural growth of grains depends on the deposition conditions, especially temperature.

1.3.4. CVD precursors for TiO_2 thin films

There are several types of precursors used for CVD including metals, metal hydrides, halides, halohydrides and metal organic compounds. Generally metalorganic precursors are preferred as they enable lower reaction and deposition temperatures to be used and are less toxic and pyrophoric than halides and hydrides.[120] The ideality of a precursor for a given CVD process is governed by the following basic characteristics as originally summarised by Pierson:[119]

- Stability at room temperature
- Volatility; should be sufficiently volatile at low temperatures to prevent condensation of the precursor in gas lines on the way to the reactor chamber
- Ability to undergo clean reactions near or on the substrate surface, with little or no side reactions
- Purity

There are two main types of precursors used in CVD, classified as either single source or dual source. As the name implies, single source precursors contain all the required elements to form the desired product within one individual precursor material, enabling direct stoichiometric control. Dual source precursors contain more than one individual precursor, whereby the combination of precursors occurs either as a gas phase or surface reaction. For the preparation of titanium dioxide thin films, both single source and dual source precursors have been studied, with some common examples shown in table 1.3.

Table 1.3. Examples of single and dual source precursors used for the CVD of titanium dioxide thin films.

Single Source Precursor	Dual Source Precursor
$Ti(OiPr_2)_4$ (TTIP)	$TiCl_4 + H_2O$
$Ti(OEt)_4$	$Ti(OiPr_2)_4 + EtOH$

It is generally accepted that the presence of the readymade fragment of the material to be deposited, such as the O-Ti-O linkage, in the source molecule accelerates the kinetics of thin film growth, and thus a single source precursor such as TTIP would enable this.

1.3.5. Variations of CVD

The process of CVD has evolved to encompass a wide range of variations to the original technique. Some commonly used variations of CVD include metal-organic CVD (MOCVD), low pressure CVD (LPCVD), atmospheric pressure CVD (APCVD), plasma enhanced CVD (PECVD), liquid injection CVD and aerosol assisted CVD (AACVD).

For the production of TiO_2 thin films, CVD processes with TTIP are traditionally favoured, whereby photocatalytically active thin films have been produced in addition to TiO_2 films for gas sensing applications. [22,29,30,63] The AACVD and APCVD methods are often the most popular, offering relatively facile setup and other advantages described in the upcoming sections.

1.3.6. Aerosol-Assisted Chemical Vapour Deposition (AACVD)

AACVD is a variant of the CVD process based on the use of an aerosol precursor, and has been concisely reviewed by Hou and Choy in 2006,[121] and more recently by Marchand et al in 2013.[122] The main distinction between AACVD and conventional CVD is the method by which the precursor is delivered to the substrate. In conventional CVD delivery, the precursor is generally evaporated from a bubbler or entrained in a gas stream. However, in aerosol assisted CVD, a precursor is dissolved in a solvent to form a solution from which a 'mist' is then generated, typically using a piezoelectric humidifying device. This atomises the chemical precursor into finely divided sub-micrometre liquid droplets (an aerosol), which can then be transported to the reaction chamber by a flow of carrier gas. In the reaction chamber, the solvent evaporates as the aerosol reaches the substrate surface, due to the increased temperature, thereby leaving the precursor to either adsorb directly onto the substrate surface, or decompose in the gas phase to form intermediates that are then adsorbed onto the substrate surface. Further decomposition and heterogeneous reactions leads to the deposition of a thin film. A schematic demonstrating the possible routes a precursor undergoes during the AACVD process is shown in figure 1.3.5.

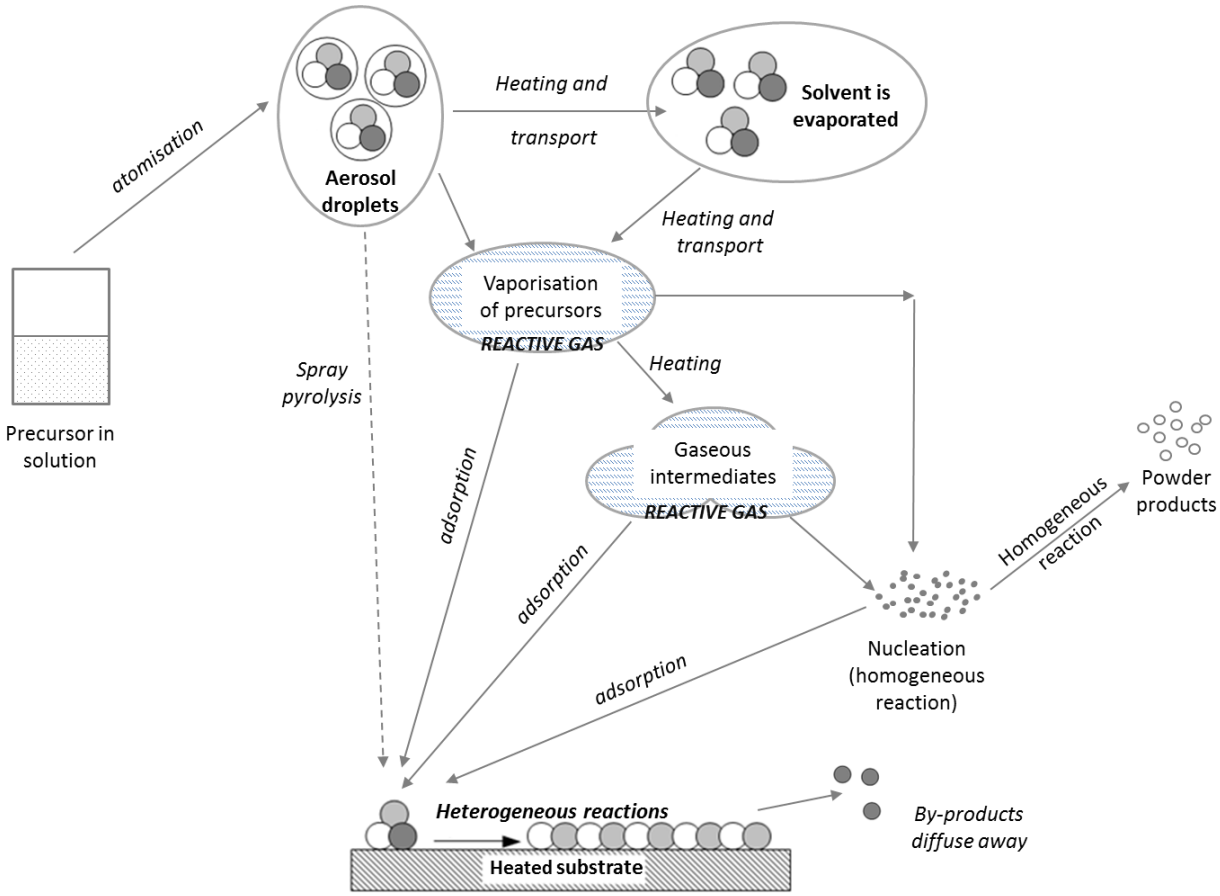

Figure 1.3.5. Schematic showing the various routes that AACVD reactions can undergo to form a thin film. Adapted from reference.[123]

There are several advantages of AACVD over traditional routes, including low cost owing to the simplicity of the apparatus used, whereby a vacuum system or specialised CVD chamber is not required, as the reaction can occur at atmospheric pressure in an open environment. This potential cost reduction is an important consideration when designing CVD systems for the industrial scale production of thin films coatings, and is particularly beneficial for coating float glass for window glazing. In addition, the delivery of the CVD precursor by an aerosol enables a high mass transport rate compared to conventional low pressure CVD methods, leading to a higher rate of film deposition.[121] Furthermore, as AACVD commonly uses single source precursors that are dissolved in a solvent, volatility of the precursor is not an issue as with conventional vapour deposition methods, and it is also much easier to control the proportions of precursor in the solution rather than in the gas phase, thus there is greater stoichiometric control over the resulting products. The deposition of films by AACVD can also occur rapidly at relatively low temperatures owing to the small diffusion distances between the reactants and intermediates.[122]

However, AACVD does have some disadvantages for the production of thin films including poor adhesion to the substrate surface, defects such as pin holes which occur due to gas phase reactions and the deposition of large particles. As a result, AACVD can often lead to the production of powdery films. Furthermore, AACVD is often considered as having poor repeatability, owing to the nature of gas flow during the process, which is turbulent and thus the flow is not identical in each repeated deposition. Also, the use of organic solvents can often lead to increased carbon content in the thin film, due to the decomposition of the solvent and subsequent incorporation during deposition.

1.3.7. Atmospheric Pressure Chemical Vapour Deposition (APCVD)

Atmospheric pressure CVD (APCVD) is one of the most widely used variants of CVD as it can run using a single precursor, or multiple precursor sources. This opens up a breadth of opportunities for producing doped materials or composites. As mentioned, APCVD is already used in the glazing industry for the deposition of films onto float glass for windows. APCVD is generally performed at atmospheric pressure, however the name can refer to any CVD process that operates between atmospheric pressure and 10^{-3} atmospheres. This means that complicated vacuum or plasma equipment is not required, and thus APCVD is a cheaper alternative to other methods such as LPCVD and PECVD.

The main disadvantage of APCVD is that it relies on heat to transform the precursor into the gas phase so that it can travel to the reaction chamber. As a result, this limits the choice of precursors that can be used in APCVD in comparison with more accessible techniques such as AACVD. Titanium dioxide thin films have been deposited using APCVD in numerous studies, including with $TiCl_4$ and ethyl acetate to produce films for photocatalytic water oxidation applications,[124] $TiCl_4$ and ethyl acetate with carbon disulphide for sulfur-doped TiO_2 antimicrobial films,[125] and further in studies where TTIP precursor has been compared with $TiCl_4$, with the conclusions that TTIP was found to produce anatase rather than rutile films.[126]

1.3.8. Hybrid Chemical Vapour Deposition (HCVD)

Hybrid chemical vapour deposition (HCVD) is a relatively new technique, first reported by Binions et al in 2008,[127] which shows great potential for producing thin films that exhibit similar characteristics to those produced by APCVD, such as good adhesion, mechanical robustness, uniformity and coverage, but with the versatility afforded by AACVD. The HCVD method

involves combining the aerosol-assisted and atmospheric pressure CVD systems by directing an aerosol gas flow into the reaction chamber at the same time as the atmospheric pressure reaction gas flow. This enables the mixing of two different precursor streams within the reaction chamber, thus enabling the incorporation of materials or additives that would not normally be introduced together, such as preformed nanoparticles and non-volatile chemicals. Experimental details and an illustration of HCVD is given in chapter 2.2.4.

HCVD has been successfully used for the gold-doping of vanadium dioxide thin films through the reaction of vanadyl acetylacetonate with auric acid in methanol, [127] whereby gold-doped vanadium dioxide thin films are an attractive material for optical switching. This method has also been used to produce nanocomposite thin films through the incorporation of preformed metal oxide nanoparticles such as titanium dioxide and cerium oxide into a vanadium dioxide matrix.[128] The resulting thin films produced showed potential application in energy saving coatings and self-cleaning coatings when applied to glass. In principle, any combination of matrix material and nanoparticles/additives could be used in HCVD to produce a variety of multifunctional thin films or composite materials, thus opening up a whole new area of CVD experimentation.

Fundamentals 1.4: Dye-sensitised solar cells

The dye-sensitised solar cell (DSSC) has been a continually attractive method for converting solar energy to electricity ever since the seminal paper published by Gratzel and O'Regan in 1991.[64] The DSSC is regarded as a 'third generation' photovoltaic, following first generation solar cells based on silicon wafers and second generation thin-film technologies such as amorphous silicon, copper indium gallium selenide (CIGS), cadmium telluride (CdTe) and polycrystalline silicon solar cells.[129] Despite being the most commercially available and widely used solar cells, both first and second generation PV technologies have their disadvantages, including limited availability of starting materials combined with energy intensive and often challenging manufacturing processes.[130]

Third generation solar cells such as DSSCs are still widely regarded as in the research phase and have had limited commercial application. However, DSSCs offer a technically and economically credible alternative to the solar technologies mentioned, especially for architectural applications. The DSSC is a promising route to low cost energy production owing to its inexpensive and abundant starting materials, simple fabrication, easy scale-up ability, architectural/environmental compatibility and good performance under any atmospheric condition and low light irradiance.[131] Unlike competing solar technologies, DSSCs can also offer semi-transparency and multi-colour options, a factor which is widely underrated, especially for the field of building-integrated photovoltaics (BIPVs).

A DSSC is a thin-layer solar cell formed as a sandwich arrangement between two transparent conducting oxides (TCO) electrodes, often fluorine-doped tin oxide (FTO, F:SnO_2) glass, where one electrode- the working electrode- is coated with a dye-sensitised thin film of TiO_2. (Figure 1.4.1). The operation of the DSSC differs from conventional p-n junction solar cells as the optical absorption and charge-generating functions are separated into two dissimilar constituents; the photosensitive dye and the n-type nanocrystalline TiO_2 respectively. In a conventional solar cell, it is the semiconductor that performs both of these functions. In a DSSC, the photovoltaic effect is produced at the interface between a redox electrolyte and the dye-sensitised TiO_2 film when a platinum counter electrode is added to complete the electrochemical cell.[132] For semi-transparent DSSCs it is more common for a counter electrode of glass with an FTO or ITO (Indium-doped tin oxide layer) to be used, with a very thin layer of platinum added on the counter electrode as a catalyst, especially if the cell is to offer transparency.

TiO_2 is a wide band gap semiconductor, meaning that it has a band gap larger than 2 eV (typically 3.2 eV for anatase TiO_2) and so can operate at higher temperatures and voltages compared to conventional silicon. However, on its own TiO_2 cannot absorb visible light, and so in the DSSC it is the photosensitisers (e.g. organic dyes) that are adsorbed onto the TiO_2 surface that act as visible light absorbers. This results in the excitement of electrons that are then injected into the conduction band of the TiO_2 semiconductor electrode.[133,134] The TiO_2 (anatase) nanocrystalline thin film electrode forms the core of the system, where it is then placed in contact with a redox electrolyte or an organic hole conductor. Other semiconductors such as ZnO[135] and Nb_2O_5[136] have also been investigated but TiO_2 is still commonly favoured, as it is the most-well known material for DSSCs and is non-toxic, inexpensive, and easily obtainable. Films are typically made to approximately 10µm thickness, with nanoparticles of 10-30nm in diameter and a general film porosity of 50-60%.[137] The thin film is deposited onto a transparent conducting oxide (TCO) on a glass or plastic substrate.

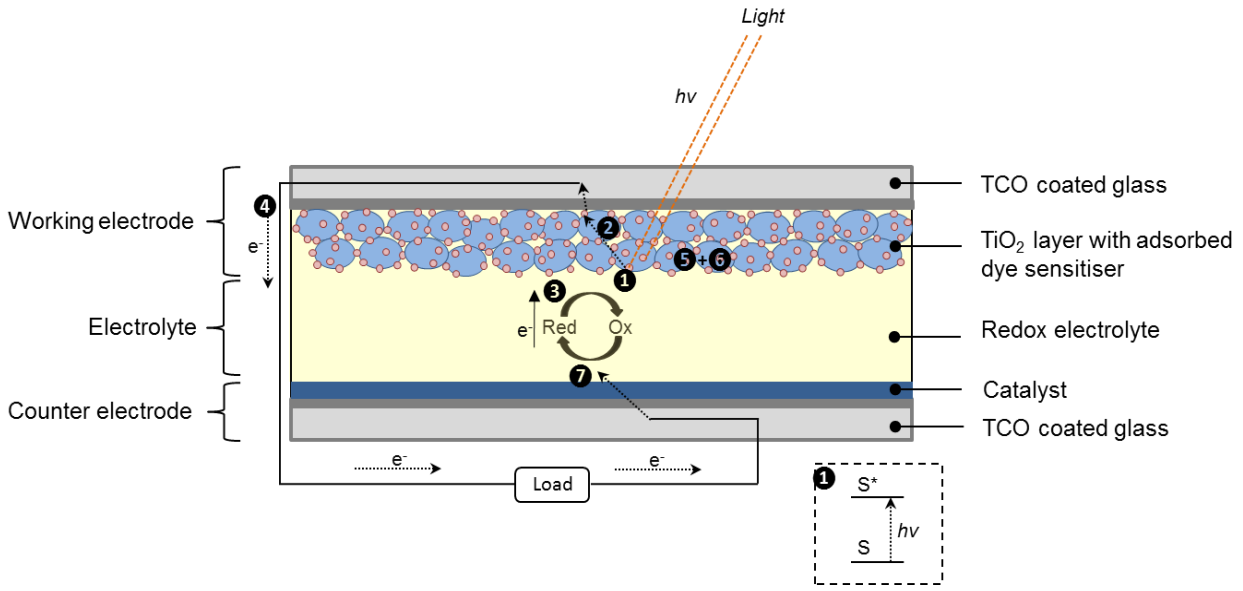

Figure 1.4.1. Schematic of a dye-sensitised solar cell (DSSC).

The sensitisation of wide band gap oxide semiconductor materials with dyes that can absorb visible light has been extensively studied since the late nineteenth century where they were of interest in the development of photography.[134] However, early studies of DSSCs produced low light-harvesting efficiencies (LHE) resulting in low photon-to-current conversion efficiencies. This was because the devices used smooth semiconductor surfaces such as single crystal and polycrystalline materials for the photoelectrodes. Smooth surfaces have a lower surface area,

resulting in less dye adsorption onto the surface. Attempts to increase the LHE by adding multilayers of dyes were generally unsuccessful. In addition, the first organic dyes used were typically unstable with a narrow absorption range for visible light, which also contributed to poor solar cell performance. In order to improve the LHE and overall performance of these devices, research was focused on developing photoelectrodes with larger surface areas, by increasing the roughness factor (rf) of the surface, and additionally by synthesising dyes with wider absorption ranges.

The standard DSSC (Figure 1.4.1) now consists of a working electrode made from a nanocrystalline mesoporous layer of TiO_2 coated onto a TCO substrate, typically fluorine-doped tin oxide ($F:SnO_2$) glass. The most commonly used photosensitiser is a trimeric ruthenium complex, which results in the DSSC having a bright red-pink hue**.** A variety of different colours ranging from blue, red and green can also be obtained by changing the type of dye used, where organic[138] and inorganic dyes have been used successfully.[139,140] The counter electrode usually consists of finely divided platinum deposited on a TCO, with the space between the two electrodes then filled with an organic electrolyte containing a redox mediator, typically a triiodide complex in a low viscosity organic solvent, e.g. acetonitrile. [141]

It was the seminal paper published in *Nature* by Grätzel and O'Regan in 1991 that reported the above described DSSC design. This new design resulted in a dramatic increase in device efficiency due to the mesoporous TiO_2 structure, whereby the high internal surface area enabled more dye to be absorbed onto the surface, and therefore more light harvested and injected into the TiO_2 for charge transport. [133] Efficiencies of 7-8%[142] were reported for this new design, which was a great improvement on previous attempts which demonstrated conversion yields well below 1%.[143,144] It was also found that through the use of the trimeric ruthenium complex as a photosensitiser with TiO_2, a much greater stability was possible with a turnover of 5×10^6 cycles measured.[145,146] This was shortly followed by the use of the N3 dye on nanocrystalline TiO_2 electrodes which gave even better efficiency around 10% in 1993.[147] These efficient ruthenium complex photosensitisers are capable of absorbing in the wide visible and near-IR regions of light from 400-800/900 nm. Some commonly used Ru-complexes are shown in figure 1.4.2.[134]

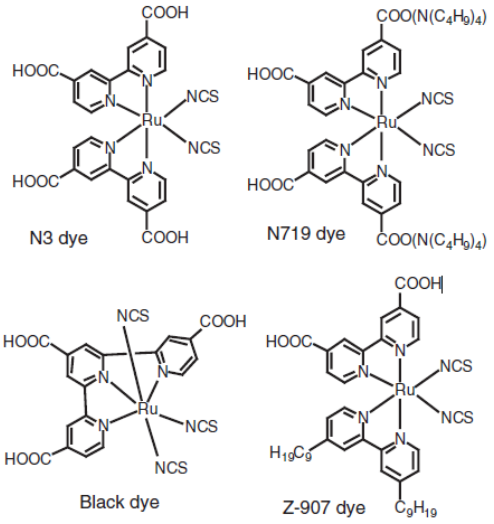

Figure 1.4.2. Chemical structures of Ru-complex dyes used in DSSCs that give cell efficiencies of over 10%. As seen in references.[134,140]

Since then, the efficiency of the DSSC has been improved incrementally through various combinations of nanoporous electrode structures including nanotubes and nanowires,[65] optimized Ru-complex dyes,[148–150] and improved electrolyte compositions.[151–154] Currently the best solar conversion efficiencies obtained for the DSSC are in the range of 11-12%; 11.9% for those DSSCs commercially manufactured by Sharp[155] and a maximum of 12.3% for those produced at lab scale.[156]

1.4.1 Operating mechanism of the DSSC

Exposure of the dye-sensitised solar-cell assembly to visible light leads to a sequence of reactions that are numbered in figure 1.4.1 and shown in more detail in figure 1.4.3. Light absorption occurs at the anode (the working electrode), whereby the dye sensitiser molecules, S, absorb light to form an electronically excited state, S^* as in reaction 1:

(1)	$S + h\nu \rightarrow S^*$	*Photoexcitation*	**Eqn 4.1**
(2)	$S^* \rightarrow S + h\upsilon'$	*Emission*	**Eqn 4.2**
(3)	$S^* \rightarrow S^+ + e^-_{cb}$	*Electron Injection*	**Eqn 4.3**

After photoexcitation, the dye molecule in the excited state decays back down to the ground state (emission, (2)) or undergoes oxidative quenching, injecting electrons into the conduction band of TiO_2 (electron injection, (3)).

Following injection into the conduction band, the electrons travel through the mesoporous network of TiO_2 particles until they reach the back-collector electrode of the TCO where they then pass through the external circuit to the counter electrode. Almost simultaneously the oxidised dye becomes rapidly reduced to its ground state by the redox electrolyte donor (typically iodide) as in step (4).

(4) $2S^+ + 3I^- \rightarrow 2S + I_3^-$ *Regeneration of dye* **Eqn 4.4**

If there is no redox electrolyte to intercept the dye and rapidly reduce it from an oxidised state (S^+) to ground state, recombination with electrons in the titania layer can occur, (5) resulting in no measurable photocurrent observed from the cell.

(5) $S^+ + e^- (TiO_2) \rightarrow S$ *Recombination* **Eqn 4.5**

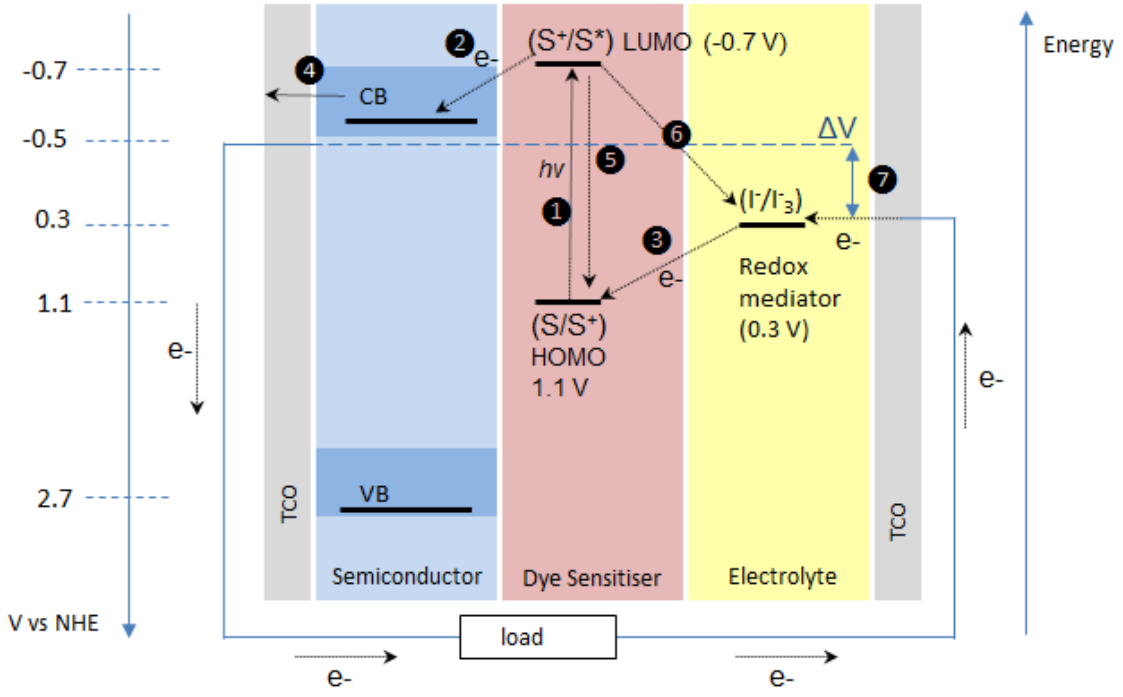

Figure 1.4.3. Diagram of the energy levels within a DSSC and the basic electron transfer processes as represented in equations 1-7. The redox potential values shown are based on a DSSC with N3 dye, TiO_2 and a I^-/I_3^- redox couple mediator, and are obtained from Hagfeldt et al.[157]

If recombination does not occur, the electrons travelling around through the external circuit reach the counter electrode where they then reduce the oxidised electrolyte (Iodide, I^- (6)). This regeneration of the sensitiser by iodide intercepts the recapture of a conduction band electron by the oxidised dye. The I_3^- ions formed through the oxidation of I^- ions diffuse a short distance (<50 μm) through the electrolyte to the cathode, which is coated with a thin layer of platinum catalyst, where the regenerative cycle is completed by electron transfer to reduce I_3^- to I^-.[137]

(6) $I^-_3 + 2e^- \rightarrow 3I^-$ *Regeneration of electrolyte* **Eqn 4.6**

The entire sequence of electron transfer reactions can therefore be described as cyclic owing to the role of the dye and the redox mediator (I^-/I^-_3). As a consequence, the overall effect when the dye solar cell is illuminated with sunlight, is that excitation of the dye prompts this series of chain reactions to occur, where electrons are driven through the external circuit to produce a photocurrent which thereby corresponds to direct conversion of sunlight to electricity, without any permanent chemical transformation.

1.4.2. Key efficiency parameters of the DSSC

The characterisation of DSSC performance depends on a number of experimentally determined parameters, such as the photocurrent and photopotentials measured in darkness and under illumination. The overall solar energy-to-electric power conversion efficiency (η/ PCE) for a DSSC is given in equation 4.7, with the following measurements; J_{sc}- short-circuit current density under irradiation, V_{oc}- open-circuit photovoltage, FF- fill factor of the cell, and P_{in}- the incident light intensity.

$$\eta = \frac{(J_{sc}\, V_{oc}\, FF)}{P_{in}}$$ **Equation 4.7**

The fill factor is defined by the ratio of the maximum power (P_{max}) of the solar cell per unit area divided by the V_{oc} and J_{sc} (Equation 4.1) and can take values 0<1.

$$FF = P_{max}/(J_{sc}\, V_{oc})$$ **Equation 4.8**

The V_{oc} value is determined by the energy gap between the Fermi level of the TiO_2 electrode, which is located near to the conduction band edge potential (Ecb), and the redox potential of I^-/I_3^-

in the electrolyte. (Figure 1.4.1). The TiO_2 electrode Ecb value and the redox potential of I^-/I_3^- are estimated to be -0.5 and 0.4V respectively, versus the normal hydrogen electrode (NHE).[137] Therefore for DSSCs with a TiO_2 electrode and the I^-/I_3^- redox mediator, the maximum V_{oc} obtainable is expected to be approximately 0.9V. State of the art optimised DSSCs currently exhibit V_{oc} values ranging from 0.75 to 0.85 V.[134]

Another fundamental measurement for DSSC evaluation is the incident photon to current conversion efficiency (IPCE). The IPCE value is the photocurrent density generated in the external circuit under monochromatic illumination (single wavelength source of light) of the DSSC, divided by the photon flux landing on the cell.[137] The IPCE can be calculated as a function of wavelength from the following equation (4.2) where *e* is the elementary charge:

$$\text{IPCE} = \frac{J_{sc}(\lambda)}{e\Phi(\lambda)} = 1240 \frac{(J_{sc}(\lambda)\ [\text{A cm}^{-2}]}{\lambda\ [\text{nm}]\ P_{in}(\lambda)\ [\text{W cm}^{-2}]} \qquad \textbf{Equation 4.9}$$

The short-circuit current density under irradiation (J_{sc}) is determined by the product of light-harvesting efficiency (LHE), charge injection efficiency (ϕ_{inj}), and charge collection efficiency of the injected electrons at the back contact (η_c). The LHE is given by equation 4.3, where T is transmittance and A is absorbance.

$$\text{LHE} = 1 - T = 1 - 10^{-A} \qquad \textbf{Equation 5.0}$$

The LHE is determined by the absorption coefficient of the dye-sensitised electrode, which depends on the concentration of adsorbed dye, the extinction coefficient of the sensitiser and the TiO_2 electrode thickness. This is governed by the Beer-Lambert Law, which is described as the linear relationship between absorbance and the concentration of an absorbing species, as shown in equation 4.4.

$$A = \varepsilon\ b\ c \qquad \textbf{Equation 5.1}$$

Where A is the measured absorbance, ε is the wavelength-dependent molar absorptivity coefficient with units of $M^{-1}\ cm^{-1}$, b is the path length and c is the analyte concentration.

1.4.3 Materials development for semi-transparent DSSCs

Dye-sensitised solar cells have many components that require individual optimisation and there is a broad range of very thorough reviews on DSSC technology to which the reader is referred for detailed information on the development of each DSSC component,[131,157,158] including reviews focused on dye development using porphyrin sensitisers,[159] natural pigment sensitisers, [160] gel polymer electrolytes,[161] in addition to current life cycle assessments of DSSC modules now at the scale up stage.[162] With such a breadth of research and technological development available it is beyond the scope of this thesis to review all recent literature on DSSC technology here. As such, a review of important developments along with those that can be specifically applicable to the preparation of semi-transparent dye-sensitised solar cells will be described here.

A semi-transparent DSSC similar to that described in figure 1.4.1 has been used for a prototype solar glazing panel with a quoted 60% transparency, analysed as a nine-unit solar cell 'electric' window by Park et al, producing an open circuit voltage (V_{oc}) of 5.7 V for the panel, and V_{oc} of 0.64 V for a single solar cell. This measurement is not far from the optimum range for open circuit voltage, taking into account the cell is semi-transparent and therefore not utilising all wavelengths of light.[12]

1.4.3.1 TCO Electrode

The substrate for the TiO_2 photoelectrode is typically glass coated with a transparent conducting oxide (TCO). A TCO with low sheet resistance and high transparency enables high solar cell performance. Low sheet resistance enables voltage losses within the electrode to be minimised, whereby the high transparency enables the amount of light passing through to the active sensitised TiO_2 layer to be maximised. The most commonly used TCO materials are Fluorine-doped tin oxide (FTO) and Indium-doped tin oxide (ITO), owing to their low resistance at ambient temperatures. Typically for the counter electrode, platinum is finely divided as a film to coat the TCO counter electrode, in order to provide a catalyst for electrolyte regeneration.

1.4.3.2 Dyes

The dye component of the DSSC has been optimised over the years through the variation of the metal centre, ligands and other substituent groups within the transition-metal complexes. As a result, mononuclear and polynuclear dyes based on metals such as Ru^{II},[163–165] Os^{II},[166–168] Pt^{II},

[169,170] Re^{I},[171] Cu^{I},[172] and Fe^{I},[173] have been implemented within DSSC devices. As well as transition-metal complexes, a variety of different organic molecules have been investigated, including indoline, coumarin and hemicyanine, as well as other conjugated donor-acceptor organic dyes and porphyrin and phthalocyanine dyes.[140]

As a fundamental element in the DSSC, the photosensitising dyes used within these devices need to conform to a number of essential design requirements for the cell to function effectively. The dye must be able to bind strongly to the semiconductor surface by means of an anchoring group, whereby carboxylic or phosphonic acid groups are typically used. For efficient electron transfer to occur between the excited dye and the conduction band (CB) of the semiconductor, the excited state level of the photosensitiser should be higher in energy than the conduction band edge of the n-type semiconductor (for n-type DSSCs).

However for p-type DSSCs, the HOMO level of the photosensitiser needs to have a more positive potential than the valence band (VB) level of the p-type semiconductor. In addition, the oxidised state level of the photosensitiser needs to be more positive than the redox potential of the electrolyte to allow dye regeneration to occur, as shown by the redox potential values in figure 1.4.3. The dye must be able to absorb light with absorption bands in the visible or near-IR region, preferably covering a broad range of wavelengths. The molecular structure of the dye should be optimised to avoid unfavourable dye aggregation on the semiconductor surface. Co-adsorbers that prevent aggregation can also be added. These dye aggregates (H- and J-aggregates) can also be controlled in order to improve the performance compared with a monomer dye layer, as described in the following reference.[174] Furthermore, electron transfer from the dye to the semiconductor must be rapid in comparison with decay to the ground state of the dye. The photosensitiser should also have photostability as well as electrochemical and thermal stability. Through acknowledgement of these characteristics, many different types of photosensitisers have been developed for use in DSSCs, including metal complexes,[175] porphrins,[159,176] phthalocyanines[177] and metal-free organic dyes.[132,178]

1.4.3.3 Electrolyte/ Redox mediator

There are several types of electrolytes which can be used within the DSSC, including traditional liquid redox electrolytes, gel and polymer electrolytes[161] and ionic liquid electrolytes.[179] In addition to these, there are several additives which can be introduced to modify and enhance the

performance of the electrolyte, as well as alternative redox couples that have been investigated. Both solid organic and inorganic hole conductors have also been used. The most common electrolyte used in DSSCs constitutes of an I^-/I_3^- ion mixture which allows the transfer of electrons between the sensitisers and the counter electrode. Usually iodide mixtures of LiI, NaI, KI, tetralkylammonium iodide (R_4NI), and imidazolium-derivative iodides are used, with varying concentrations of 0.1-0.5 M and 0.05-0.1 M I_2 dissolved in non-protonic organic solvents.[134] Nitrile solvents such as acetonitrile etc. are often used as the organic solvent in the DSSC owing to their low viscosity, which is an important characteristic as this affects the ionic conductivity in the electrolyte, and corresponding DSSC performance.[180] Solvents with a low viscosity allow for a high ionic conductivity; however they tend to have high vapour pressure resulting in difficulties sealing them for long term use.

Despite considerable research interest, the need for an electrolyte has long been the main limitation for the DSSC, where concerns over the DSSCs long term chemical stability has resulted in limited practical development within industry. This is due to the organic dye and redox electrolyte combination that often limit the DSSC stability under real-life conditions.[181] For use in solar glazing, these issues with stability must be addressed to enable commercial viability. In particular, the liquid electrolyte which usually consists of an iodide/tri-iodide redox couple poses the problem of solvent leakage, low durability and corrosion within the DSSC.[179] In attempt to combat these problems, many research groups have focused on substituting the liquid electrolyte for other materials, with the main alternatives being either solid or quasi-solid (QS) inorganic or organic hole-transporting materials, such as gel electrolytes prepared by ionic liquids or by the solidification of liquids,[161] and polymer electrolytes.[182]

It is this research interest in alternative electrolytes for DSSCs that has spawned a large area of research centred around solid-state dye sensitised solar cells (ssDSSC). The solid hole transporting materials used in ssDSSCs typically exhibit small molecular size (~2nm), high solubility and an amorphous structure that enables good impregnation of the photoanode mesopores.[183,184] At present, the most efficient and widely used organic hole conductors are spiro-OMeTAD (2,2',7,7'-tetranis-(N,N-di-p-methoxyphenyl-amine)9,9'-spirobifluorene)[185] and bis-EDOT (bis-ethylenedioxythiophene)[186], with efficiencies of 6.08% and 6.1% respectively. [184] For a more detailed description and analysis of the ssDSSC and other variants of DSSC technology the reader is referred to the recent reviews by Upadhyaya et al[158] and Hardin et al.[187]

1.4.3.4 Nanostructured Metal Oxide electrode (anode)

The major breakthrough in the development of DSSCs in 1991[142] was the use of a mesoporous TiO_2 electrode with a high internal surface area, to support the monolayer of sensitiser.[137] The mesoporous electrode increased the surface area of the TiO_2, whereby a surface with a high roughness factor (rf) adsorbs more dye. As a result, the porous electrodes developed by Graetzel et al, prepared from TiO_2 nanoparticles (~10-30 nm), enabled an actual surface area of >1000 cm^2, i.e. a 1 cm^2 TiO_2 film (10 µm thickness).[134] The increased surface area enables more sensitising dye to be adsorbed so that electrons can be injected into the TiO_2 film, towards the TCO back collecting electrode and thus around the external circuit. The absorption coefficient of the sensitiser determines the ideal surface area and thickness of the electrode; however the optimal thickness is also limited by the electron diffusion length. Typically, a porous electrode with an optimal thickness of 10-20µm, consisting of around 20 nm sized TiO_2 particles is the optimum configuration for sufficient adsorption of the most commonly used dyes.

TiO_2 is still the material of choice as it offers the highest efficiencies, but many other oxide systems have been studied, such as ZnO, SnO_2 and Nb_2O_5. The reader is referred to the references for recent reviews on the development of DSSC nanostructured metal oxide electrodes.[65,188–190] Over the past decade there has been extensive investigation into optimisation of the nanostructured electrode morphology, resulting in a wide range of nanostructures being studied, ranging from random nanoparticle assemblies to organized nanotube arrays and single-crystalline nanorods. The use of nanorods and nanotubes was specifically investigated for improved, more directional charge transport and an improved pore filling of the hole conductor materials used in the solid-state DSSC. A short overview on the development of the nanostructured TiO_2 electrode and preparation techniques will be discussed here.

1.4.3.5 TiO_2 electrode preparation

As described in section 1.1, TiO_2 is a stable, nontoxic oxide with a high refractive index (n = 2.4-2.5) which has a widespread use as a pigment in paints, toothpastes, sunscreens and self-cleaning materials. Anatase is the favoured phase for use in DSSCs as it has a larger band gap than other phases of TiO_2 (3.2 eV vs. 3.0 eV for rutile) and a higher conduction band edge energy (E_{cb}), thereby leading to a higher Fermi level and V_{oc} in DSSCs for the same conduction band electron concentration.[137] In addition, through a comparative study of rutile and anatase DSSCs, Park et

al. found similar V_{oc} values were obtained, however a higher conduction band edge, E_{cb} was found in the anatase DSSC (0.1-0.2 eV) where the observed photocurrent was lower for rutile by approximately 30%.[191] This reduced photocurrent was attributed to the larger particle sizes present within the rutile electrode, whereby it was estimated that the resulting surface area of the rutile film was at least 25% lower than that of the anatase film. The authors suggested that the difference in the J_{sc} values between the rutile and anatase prepared DSSCs was thereby due to their lower internal surface area, which resulted in less dye sensitiser adsorption on the film surface. There has been significant development in the range of methods used for the synthesis of new anatase nanostructures for DSSCs, including nanoparticles, nanorods, nanotubes, nanosheets and mesoporous materials such as aerogels and photonic materials. Such methods include sol-gel, hydrothermal, solvothermal, chemical vapour deposition, physical vapour deposition and electrodeposition.

The most common method for preparing TiO_2 nanoparticles for use in DSSCs is the sol-gel process, through the hydrolysis of Ti(IV) alkoxides such as titanium isopropoxide (TTIP) and titanium butoxide (TBT) as described in section 1.2. The hydrolysis and condensation kinetics of the reaction are carefully controlled in order to obtain monodispersed TiO_2 particles of the desired size (10-30 nm). These nanoparticles are typically formulated into a paste with polymer additives and deposited onto the TCO substrate using doctor blading or screen printing techniques.[137] The resultant film is then sintered in air at 450-550°C to remove organic components and to generate an electrical connection between the nanoparticles. The thickness of the film can be controlled during the screen-printing process by modifying the screen mesh size and repeating the process (multiple printing) to obtain a thicker film. In addition to film thickness, film porosity also needs to be controlled, with a porosity of 50-60% desirable. This enables redox ions in the electrolyte to penetrate the film, interact with the adsorbed dye and diffuse back to the electrode effectively. Porosity of the film is controlled during the sintering process by the addition of a polymer such as polyethylene glycol (PEG) and ethyl cellulose (EC) into the TiO_2 colloidal solution.[75] High porosity leads to less interconnection between the particles and a decrease in charge collection efficiency.[192] Such thin films produced by doctor blading or screen printing are typically opaque, and thus ideal for maximum absorbance of light, however unsuitable if a semi-transparent DSSC is desired. Methods for producing semi-transparent TiO_2 thin films avoid the formation of a paste by using sol-gel dip coating or CVD methods as described in chapters 1.2 and 1.3 respectively.

1.4.4 Potential for DSSC building integrated photovoltaics

In comparison with other building integrated photovoltaic (BIPV) products that have reached the commercialisation stage, solar glazing materials can be considered as still in their infancy. A state-of-the-art review by Jelle et al[8] on BIPV products includes several appendices on current BIPV modules available on the market, including those for solar glazing applications to which the reader is referred.

As one of the main criteria of solar glazing (in addition to good transparency) is to enable a sufficient energy offset for the entire building, studies have shown that buildings which incorporate solar glazing technology can exhibit overall electricity consumption reductions of up to 55% compared to standard single glazed windows.[193–195] Solar glazing BIPVs not only enable sustainable generation of electricity, they also offer a reduction in solar heat gain, and therefore less air-conditioning requirements within a building.[195]To become widely used as BIPVs, solar glazing must generate low cost electricity, of which the DSSC is ideally positioned, due to the relatively inexpensive materials used for its manufacture (glass, titania film, dye, electrolyte). The DSSC offers several potential benefits for window glazing in addition to its low cost and inexpensive materials; the DSSC has the ability to perform well under any atmospheric condition and under low irradiance, meaning that the DSSC is an ideal candidate for solar glazing in high-rise office buildings and glass facades in cities where light is often low due to crowding. Preparation of the TiO_2 thin film by sol-gel or chemical vapour deposition methods further lowers the cost of the DSSC as a potential BIPV, whereby typical silicon BIPVs require very expensive vacuum equipment for their manufacture. The semi-transparent DSSC also offers multi-colour options, which along with stable performance at high temperatures under non-standard solar incidence angles/irradiation, make it a potentially high-value addition to new builds in the future.

A clear demonstration of these assumptions has recently emerged from the ColorSol consortium in Germany, where solar PV glass based on DSSC technology have been manufactured/installed and its performance subsequently compared to traditional amorphous silicon solar cells. The results showed that the cost of electricity generated by the DSSC is lower than the silicon analogue (4 €/Wp vs 6 €/Wp), whereby the elegance of the coloured glass façade is easily observed as in figure 1.4.4. [196]

Figure 1.4.4. The DSSC-based PV facade of the Capricorn Haus in Germany, as seen in Pagliaro et al,[65] originally reproduced from Gattermann und Schossig Architekten, who reserve all rights.[196]

Despite the potential of the DSSC, to date there is very limited availability to buy such cheaper BIPV modules based on thin film or PV technologies such as DSSC, organic photovoltaics or perovskite solar cells commercially. This is because despite their promising efficiencies and good visible transparency, these technologies are still too juvenile to demonstrate their stability over a longer time period under real-life conditions. Aside from the fine balance of enhancing transparency without diminishing power conversion, enhancing stability is the main issue to be addressed to enable the development of a solar glazing product based on these technologies that is suitable for market. Future research into the technologies mentioned should aim to target this issue of stability, as well as to increase understanding and development of the materials used within these devices.

In spite of the challenges facing solar glazing research, increasing commercial interest into emerging semi-transparent photovoltaics is continually driving the sector forward. Building manufacturers and architects are beginning to use transparent BIPV modules such as that shown in figure 1.4.4, with pleasing aesthetic results, whereby the demand and desirability for solar glazing is growing. If the issues regarding stability can be properly addressed, then it seems highly likely that solar glazing will have a place in buildings of the future.

Chapter 2: Experimental and Analytical Details

2.1. Sol-gel

A modified, non-aqueous metal alkoxide sol-gel method was used to produce TiO_2 thin films from two different precursors; titanium isopropoxide (TTIP) shown in figure 2a, which is a traditional precursor used frequently for the production of titanium dioxide thin films, and the more novel precursor, titanium bis-ammonium lactate dihydroxide (TiBALD) shown in figure 2b which has been used sparingly in literature for the production of titania sol-gels. [103] The effect of surfactant addition and concentration using five different types of non-ionic surfactants (Brij 58, Brij 98, Tween 20, Tween 40, Tween 60) was explored and the results discussed in chapter 3. The Tween® and Brij® surfactants are composed of poly(oxyethylene) ether neutral, polar heads and hydrophobic tails that are oxyethylene polymers.[197] Chemical details of the surfactants used are given in table 2.2.

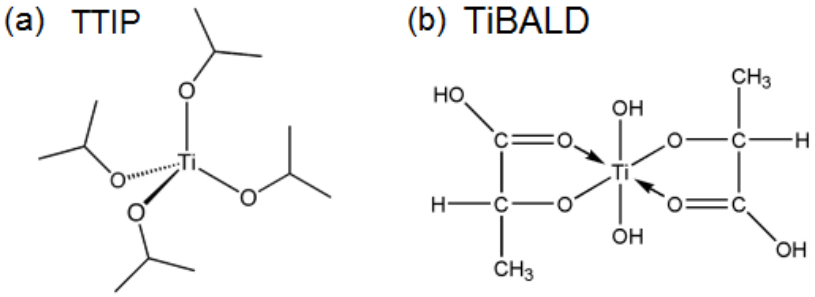

Figure 2. Chemical structure of (a) titanium tetra-isopropoxide, TTIP, and (b) titanium bis-ammonium lactate dihydroxide, TiBALD.

2.1.1. Traditional TiO_2 sol synthesis: Titanium (IV) tetraisopropoxide (TTIP) as precursor

All chemicals were purchased from Sigma Aldrich and used without further purification.
A variety of surfactant types and concentrations were explored, as listed in table 2.2, to determine which modifications enabled the production of thin films with the desired properties. There concentrations were chosen as a previous study by Choi et al,[69] had used similar concentrations which led to improved photocatalytic properties of the subsequent materials, and so these concentrations were scaled down for use in this investigation. The optimum surfactant type and concentrations were then used to produce extra samples for DSSC testing. In the initial

TTIP study, a selection of samples were further heat treated by annealing in air for an extra hour at 600 °C to determine if this improved crystallinity of the thin film samples.

To prepare the TiO_2 sol, the surfactant was dissolved in isopropanol (69 ml, 99.7%) with vigorous stirring until a homogeneous suspension was obtained. Acetylacetone (0.61 ml, 99%) was then added dropwise to this solution with continuous stirring. Acetylacetone acts as a stabilising agent to help control the speed of the hydrolysis and subsequent condensation reactions. Titanium (IV) tetraisopropoxide (TTIP, 6 ml, 99.999% trace metals basis) was then added dropwise to this solution containing the surfactant, with continuous stirring. The resulting transparent pale yellow solution was left to stir for 30 min, after which acetic acid was added (6.86 ml, 99.7%) dropwise and the solution was stirred for a further 30 min. The sol was then ready to use immediately for dip coating of the substrates to prepare thin films. The molar ratio of surfactant/TTIP/Acetylacetone/Isopropanol/Acetic Acid was R: 0.2: 0.06: 9: 0.04, where the surfactant concentration R was varied from 0–0.0008 mol dm^3 (Table 2.1). This range was chosen in order to investigate the mimumum amount of surfactant that could be added to sol-gel in order to produce an enhanced performance, this was scaled down from previous work by Stathatos et al reported in literature.[69] Sols were typically transparent, homogeneous and stable, varying in colour from yellow to orange.

Table 2.1. Sol-gel details: surfactant name, corresponding sol name/ precursor used with relevant concentration of surfactants added (mol/ dm^3) and subsequent annealing time and temperature.

Surfactant used	Sol-gel sample name/ precursor		Concentration of Surfactant (mol/dm^3)	Annealing temperature + time *(Ramp rate: 15°C min^{-1})*
	TTIP	TALH		
Nil	TTIP Tol	TTIP DCM	0	
				TTIP:
Brij 58	B58 A	B58 AT	0.0006	500 °C / 15 mins ***and*** 600 °C / 1 hr
	B58 B	B58 BT	0.0004	**TALH:** 600 °C / 1 hr
Brij 98	B98 A	B98 AT	0.0006	
	B98 B	B98 BT	0.0004	
Tween 20	T20 A	T20 AT	0.0006	
				TTIP:
	T20 B	T20 BT	0.0004	500 °C / 15 mins
Tween 40	T40 A	T40 AT	0.0006	
	T40 B	T40 BT	0.0004	**TALH**: 600 °C / 1 hr
Tween 60	T60 D	T60 DT	0.0008	
	T60 A	T60 AT	0.0006	
	T60 B	T60 BT	0.0004	

Table 2.2. Details of the non-ionic surfactants investigated with common name in coloured rows, followed by chemical name/synonyms, approximate molecular weights and the chemical formula with structure.

Brij 58	
Polyethylene glycol hexadecyl ether: (Polyoxyethylene (20) cetyl ether) **~ 1124**	**$C_{16}H_{33}(OCH_2CH_2)_{20}OH$** 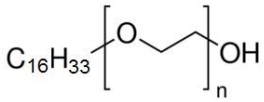
Brij 98 (Brij O20)	
Polyethylene glycol family: Polyoxyethylene (20) oleyl ether **~1150**	**$C_{18}H_{35}(OCHCH)_nOH$ (n~20)** 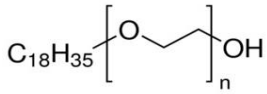
Tween 20	
Polysorbate surfactant: Polyoxyethylene- (20) sorbitan monolaurate **~ 1227**	**$C_{58}H_{114}O_{26}$** 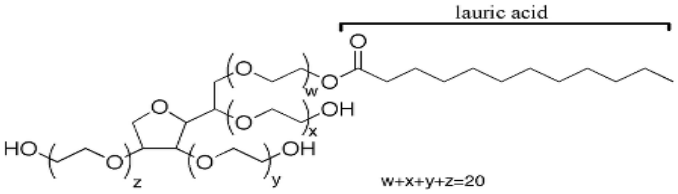
Tween 40	
Polysorbate surfactant: Polyoxyethylene-(40) sorbitan monopalmitate **~ 1277**	**$C_{62}H_{123}O_{26}$** 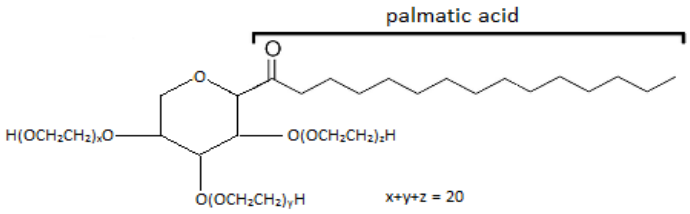
Tween 60	
Polysorbate surfactant: Polyoxyethylene- (60) sorbitan monostearate **~ 1311**	**$C_{64}H_{126}O_{26}$** 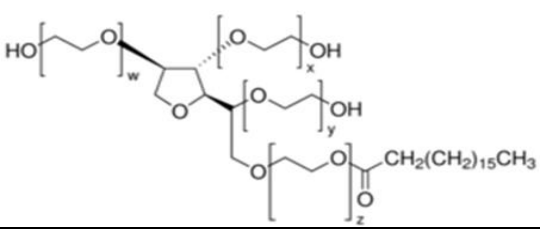

2.1.2 Novel TiO_2 sol synthesis: Titanium (IV) bis (ammonium lactate) dihydroxide (TiBALD) as precursor

The same surfactant types and concentrations were used as with the TTIP precursor, with sol names as shown in table 2.1. The increase in post-synthesis annealing time and temperature to 600°C for 1 hour was found to beneficial in improving crystallinity of samples and was thus used for all TiBALD samples prepared. The TiBALD sol-gel was prepared by dissolving the relevant surfactant type and concentration in ethanol (50ml) with vigorous stirring until a homogeneous suspension was obtained, after which acetylacetone (4ml) was added dropwise. Titanium(IV) bis(ammonium lactato) dihydroxide (TiBALD, 4.14 ml) was then added dropwise to the solution with continuous stirring. A minimum quantity of nitric acid (conc, 0.4-2ml) was added dropwise to the solution until the solution turned from cloudy to clear yellow, after which the sol was immediately ready for dip coating with substrates. The molar ratio of surfactant/TALH/Acetylacetone/Ethanol was **R: 0.2: 0.06: 9**, whereby the surfactant concentration **R** was varied from 0- 0.0008 mol dm^3. The resulting sol-gel solutions were typically transparent, homogeneous and stable, varying in colour from yellow to orange.

2.1.3. Dip-coating and annealing

The TiO_2 thin films were prepared using homemade dip-coating apparatus whereby glass substrates (F-SnO_2 coated, 1.5 cm/2 cm x 6 cm , Pilkington-NSG) were dipped into the sol and removed at a controlled speed of 2.8 cm min^{-1}. For each sol, samples were produced with 1-3 layers by repeating the number of consecutive dips into the sol. After each layer was added, the substrates were left in a fume hood for 30 minutes to allow for full evaporation of the solvent. After completion of dip-coating, substrates were left overnight under a fume hood to evaporate any remaining solvent, and then annealed using a Carbolite Type 301 programmable furnace. The TTIP derived samples were annealed at 500°C for 15 minutes with a ramp rate of 288.15 K min^{-1} (15°C min^{-1}). To explore the effects of annealing time and temperature on the resulting crystallinity and properties of thin films produced, a selection of additional TTIP derived samples with Brij surfactant were produced and annealed at 600 °C for 1 hour. Samples produced from TiBALD were all annealed at 600°C for 1 hour with a ramp rate of 288.15 K min^{-1} (15°C min^{-1}).

2.2. Chemical Vapour Deposition Techniques

2.2.1. Aerosol-assisted chemical vapour deposition (AACVD)

The apparatus and procedure described here was used for the production of all films described in chapter 4. Nitrogen (99.99 %) was obtained by BOC and used as supplied as carrier gas for all experiments. Thin films were deposited onto fluorine-doped tin oxide glass substrates (4.5 cm x 15 cm x 0.3 cm, FTO, Tec 15® Pilkington-NSG) using the CVD apparatus shown in figure 2.1. The substrate was placed inside the cold-wall reaction chamber on top of a graphite block containing a Whatman heating cartridge, controlled by a Pt-Rh thermocouple. The graphite block was preheated to 400 °C and the substrate left at this temperature for at least 10 minutes prior to each reaction to ensure a stable deposition temperature. Before each reaction substrates were cleaned in deionised water in an ultrasonic bath for 5 minutes, followed by washing with acetone and ethanol.

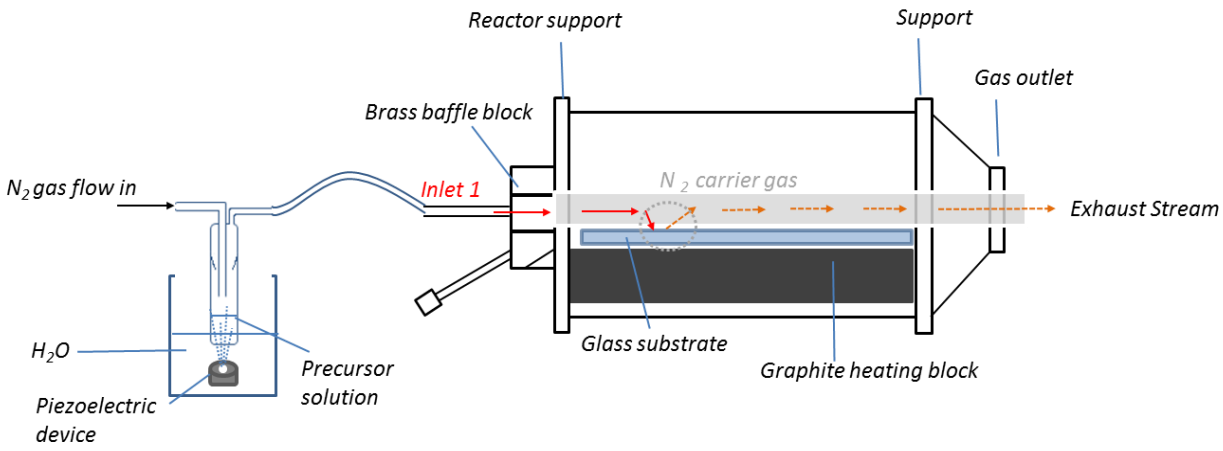

Figure. 2.1. Schematic diagram of AACVD apparatus.

2.2.2. AACVD: Experimental details

For the precursor solution, either toluene or dichloromethane (10 ml) were used as a solvent, and the effects of surfactant addition in the concentrations shown in table 4 were studied. When a surfactant was used, it was added to the solvent in concentrations of 0.5 M, 1 M and 2 M equivalent to titanium tetraisopropoxide (TTIP) precursor, and left to stir for at least ten minutes before the addition of the TTIP (0.5 ml) precursor. These concentrations were chosen to explore the effects of surfactant addition on the AACVD process, and were chosen as as relevant

equivalents to follow on from those concentrations used in the sol-gel experiments described above in chapter 2.1.2. The sample names and the relevant concentrations used are shown in table 2.3. The resulting solution was left to stir for at least 10 minutes before addition to the bubbler. When the substrate had reached the desired temperature of 400 °C, the precursor solution was decanted into the bubbler under constant N_2 gas flow. As shown in figure 2.1, the bubbler was held about 1- 2cm over the piezoelectric humidifying device in a beaker of deionised water for generation of the aerosol precursor mist. The carrier gas of nitrogen then transports the precursor mist directly into the reaction chamber through inlet 1. Depositions were repeated at least four times in order to confirm reproducibility of the system and to produce enough samples for use in DSSCs.

Table 2.3. AACVD details: surfactant name, corresponding sample name and solvent used with concentration of surfactant added (mol/ dm^3) and deposition temperature.

Surfactant used	Sample Name / Solvent		Concentration of Surfactant (mol/dm^3)	Deposition temperature *(Ramp rate: 15°C min^{-1})*
	Toluene	Dichloromethane		
Nil	TTIP Tol	TTIP DCM	0	
Brij 58	AB58 0.5 t	AB58 0.5 d	0.5	
	AB58 1 t	AB58 1 d	1	
	AB58 2 t	AB58 2 d	2	
Brij 98	AB98 0.5 t	AB98 0.5 d	0.5	
	AB98 1 t	AB98 1 d	1	**Substrate temperature:** 400 °C **Gas Flow rate:** 1L/min^{-1}
	AB98 2 t	AB98 2 t	2	
Tween 20	AT20 0.5 t	T20 0.5 d	0.5	
	AT20 1 t	T20 1 d	1	
	AT20 2 t	T20 2 d	2	
Tween 40	AT40 0.5 t	T40 0.5 d	0.5	
	AT40 1 t	T40 1 d	1	
	AT40 2 t	T40 2 d	2	

2.2.3. Hybrid (Aerosol Assisted/Atmospheric Pressure) Chemical Vapour Deposition (HCVD)

The apparatus and procedure described here was used for the production of all films described in chapter 5. Hybrid CVD uses a combination of atmospheric pressure CVD (APCVD) and AACVD as described above. For hybrid CVD as described in this thesis, both inlet 1 and 2 of the brass baffle block are used, as shown in figure 2.2. Inlet 1 is connected to the APCVD rig, whereby addition of the titania precursor and ethanol solvent occurs through heated gas lines by flow of nitrogen. Inlet 2 is then used to incorporate other additives, or dopants into the system by means of an aerosol mist as described above in 2.2.2.

2.2.4. HCVD Experimental Details

All gas handling lines, regulators and flow valves in the APCVD apparatus were made of stainless steel with ¼" internal diameter, except for the mixing chamber inlet and the exhaust line from the apparatus that measured ½" in diameter. The nitrogen gas was preheated by passing along the lengths of the gas lines before reaching the bubblers and the mixing chamber. The temperature of the gas lines was maintained at a constant temperature of 150 °C using Eurotherm heat controllers and monitored by Pt-Rh thermocouples. The gas flow was monitored using flow meters at a constant flow of 1 L/min^{-1} for all gas lines. The precursors of TTIP and ethanol were stored in separate steel bubblers and heated to appropriate temperatures (150 °C for TTIP, 65 °C for ethanol). The bubblers were heated using a heating jacket and preheated for at least ten minutes prior to the beginning of the reaction. These temperatures were used based on the boiling point of the precursor, whereby the value chosen is about 20 °C less than boiling point. The graphite block was heated to 550 °C for all coatings produced. When the lines, bubblers and graphite block had reached the desired temperature, the system was left for a further ten minutes for temperature regulation. Then the entry valves from lines 1 and 2 into the bubblers were opened, enabling nitrogen gas to pass through the bubbler resulting in the vaporised precursors to become entrenched in the gas flow. The exit valves from the bubblers were opened quickly in order to enable this gas flow to exit and be transported to the mixing chamber, and then through inlet 1 to the reaction chamber. (Figure 2.2). Failure to open these valves quickly could result in pressure building up in the system, and so these steps were conducted quickly for safety in each reaction. As with AACVD, the exhaust gases from the reactor were vented directly into the extraction system of a fume hood.

For the addition of surfactants or dopants, an initial solution of surfactant/dopant in methanol (10ml) was prepared and left to stir for ten minutes. Inlet 2 was used to transport this mixture into the reaction chamber as required. As soon as the vaporised precursors from the bubblers were allowed to flow into the mixture chamber and thus into the reactor, the piezoelectric device was switched on immediately to enable the generation of a surfactant mist which is carried through to the reactor with constant nitrogen gas flow at 1 L/min^{-1}. Each reaction was then allowed to run as a whole for one minute, after which all bubbler valves were closed; beginning with the exit valves, and then the entry valves, and then the piezoelectric device was switched off to prevent any further addition of surfactant/dopant. Plain line flow of nitrogen was left on while the heating of the graphite block was switched off and the substrate was left to cool.

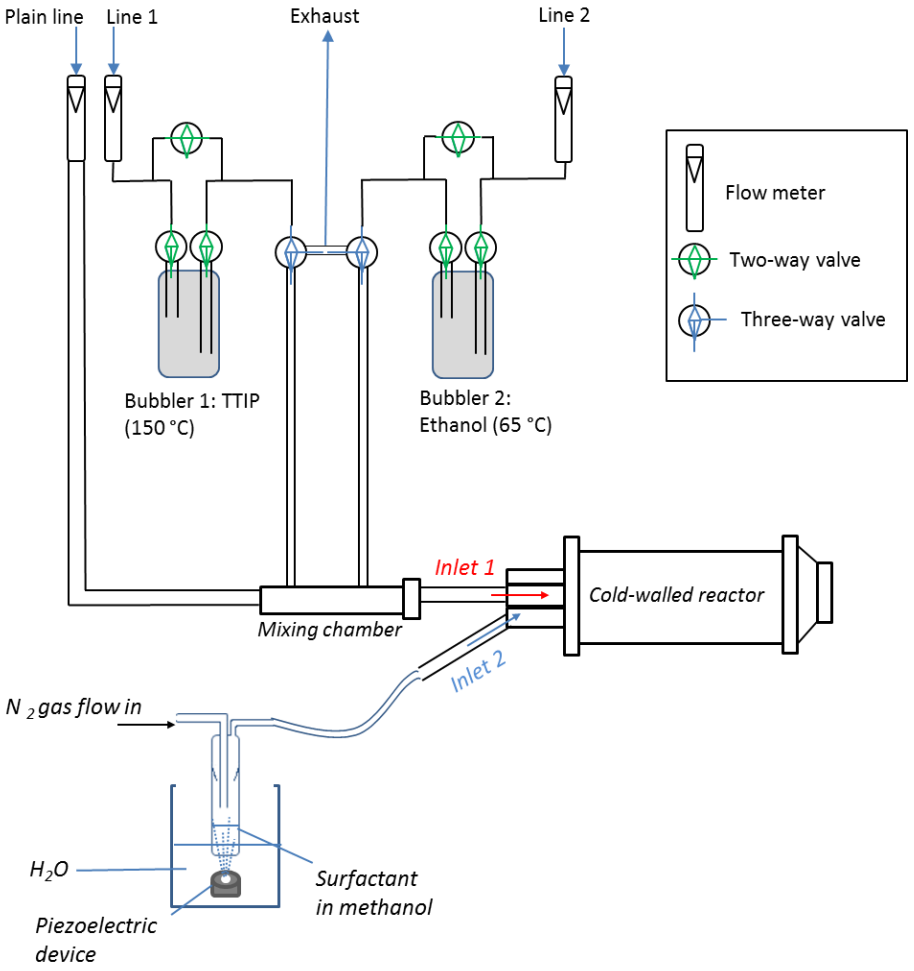

Figure 2.2. Schematic of hybrid chemical vapour deposition apparatus; a combination between atmospheric pressure CVD and AACVD.

2.3. Characterisation and functional property testing

After cooling, all thin films samples were wrapped in tin foil and stored at room temperature. Glass substrate sizes used are shown in figure 2.3. Areas denoted in red, labelled (a) were typically reserved for photocatalytic testing and for use in dye-sensitised solar cell devices, however each sample area was not tested more than twice for once, and repeat samples for DSSCs were used, i.e. a sample used for photocatalytic testing was not then used for DSSC testing. Areas denoted in orange and labelled (b) were used for all other analysis. For analysis by SEM, AFM and XRD, each sample was cut into small squares (approx. 1 cm x 1 cm or 2 cm x 2 cm respectively). For analysis by Raman spectroscopy, UV/Vis spectroscopy and contact angle measurements, samples were cut into larger squares (approx. 4 cm x 4 cm).

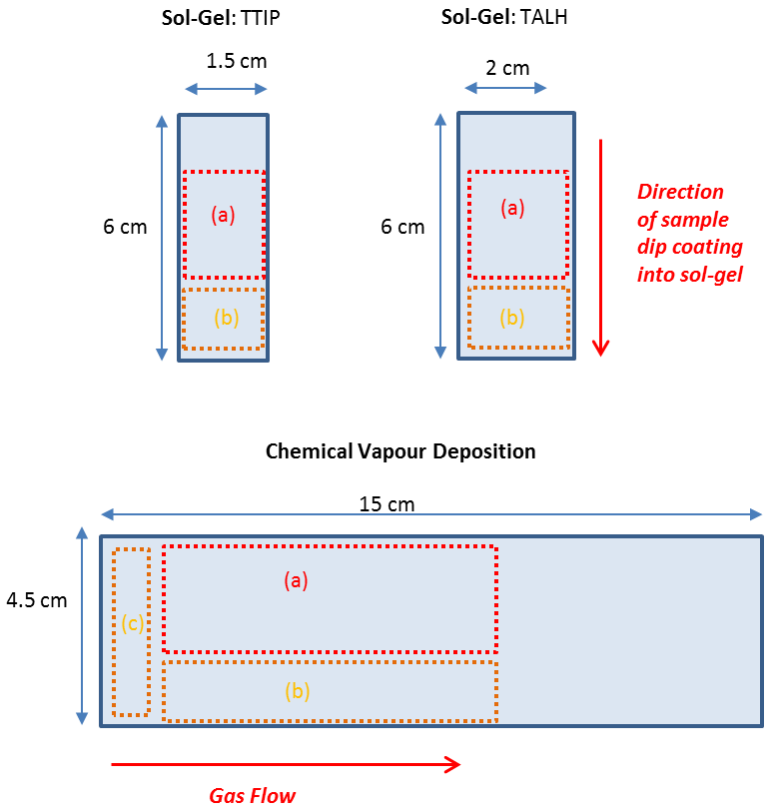

Figure 2.3. Schematic of glass substrate sizes used and areas used for materials characterisation analysis and functional property testing.

2.3.1 Scanning Electron Microscopy (SEM)

SEM was used to investigate thin film microstructure, surface morphology, and thin film thickness. SEM images were produced using an FEI Inspect F Scanning Electron Microscope at a

working distance of 10-12 mm, with an accelerating voltage of 10 eV. The degrees of magnification used ranged between x 10,000 and x 40,000. Thin film thickness was measured using sample cross sections, whereby the average was obtained using measurements from two cross sections from each sample type. ImageJ 1.48[198] software was used to determine the average particle size from SEM images.

2.3.12 X-Ray Diffraction (XRD)

X-ray diffraction was conducted with gratitude by Dr. Rory Wilson (QMUL), and was used to determine the crystalline phases of the TiO_2 thin films. XRD was performed using a Panalytical X'Pert Pro diffractometer in a glancing angle ($\alpha = 3°$) mode using a CuKα X-ray source (Kα1 = 0.1540598 nm; Kα2 = 0.15444260 nm.) The diffraction patterns were collected over 10°–70° with a step size of 0.03° and a step time of 1.7 $s \cdot point^{-1}$.

2.3.13 Raman Spectroscopy

Raman was used for further determination of crystalline phases and impurities. A Renishaw InViva™ Raman microscope equipped with a 1800 $line \cdot mm^{-1}$ grating and a LaserPhysics argon–ion laser (514.5 nm) was used. The Raman system was calibrated using silicon at the start of each set of experiments.

2.3.14. Atomic Force Microscopy (AFM)

Surface roughness and associated analysis of the films was completed using Atomic Force Microscopy NT-MDT NTEGRA in semi-contact mode imaging performed under ambient conditions in air using silicon tips (Acta-20-Appnano ACT tapping mode with aluminium reflex coating, Nanoscience instruments) with a resonant frequency of 300 KHz and a spring constant of 40 $N.m^{-1}$. A scan resolution of 255 lines per sample with an area size of 10 x 10 µm was used. Images were processed and analysed using the offline software Nova 1.0.26.1443 from which root mean square roughness (RMS) values were determined. RMS values are quoted as an average value from the analysis of at least three random areas across the centre of the sample substrate.

2.3.15. Ultra-Violet/ Visible Spectroscopy

Transmission and absorption measurements were carried out to determine the optical properties of the thin films. Spectra were recorded between 300 and 2500 nm using a Perkin Elmer Lambda 950 UV/Vis Spectrometer. The direct and indirect band gap of each sample was then determined using transmission data and the Tauc method.[199]

2.3.2. Determination of functional properties

2.3.21 Contact Angle Measurements

Contact angle measurements were used to determine the hydrophilicity of thin film surfaces, by measuring the contact angle of deionised water before and after 30 minutes of UV irradiation with a 254 nm UV lamp (2 × 8 W-254 nm Tube, Power: 32 W), and a Goniometer Kruss DSA100 drop shape analyser.

2.3.22 Photocatalytic Activity

The photocatalytic activity of thin films was assessed using resazurin 'intelligent ink' as initially developed by Mills et al. [200] Resazurin ink undergoes a photo-reduction mechanism under UV irradiation. Upon photo-excitation of the titanium dioxide thin film, electrons and holes migrate to the film surface. Glycerol within the ink solution acts as an excess sacrificial electron donor, which reacts with the surface holes to stabilise surface electrons and prevent recombination processes as shown in figure 2.4. These surface electrons subsequently reduce the Resazurin dye (royal blue) to Resorufin (pink) in a two electron proton process, whereby the Resorufin is then further reduced to bleached intermediates by additional reduction cycles, and the ink turns colourless. [201] A picture of the observed colour change over a UV irradiation time period of 60 minutes is shown in figure 2.5.

Samples were prepared for testing by washing in acetone and then isopropanol for 5 minutes each in an ultrasonic bath. Samples were left to air dry and then resazurin ink solution was applied evenly to the thin film surface using an aerosol spray gun, in a method initially reported by Kafizas et al.[201] The photo-induced degradation of resazurin ink was monitored using UV-Vis spectroscopy using a Perkin Elmer Lambda 35 UV-Vis spectrometer measuring absorbance between 300-700 nm, before and after illumination of the samples with 365 nm UV irradiation.

Samples were irradiated at a constant distance of 15 cm with a 365 nm UV lamp (2 x 8W– 365 nm Tube, Power: 32 W).

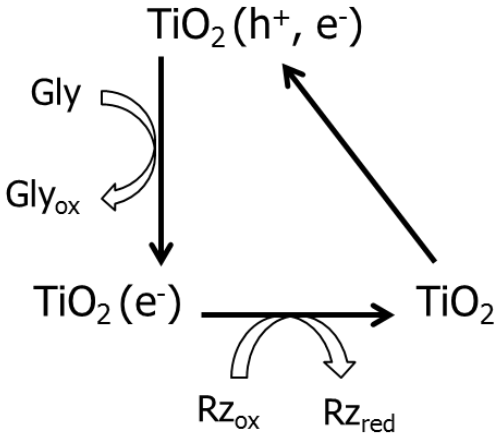

Figure 2.4. Schematic of photocatalytic degradation of resazurin dye by TiO_2 with glycerol as the sacrificial electron donor.

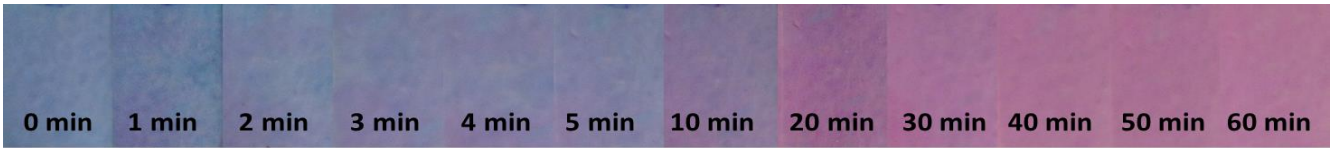

Figure 2.5. Photographs of the observed colour change of resazurin dye on the surface of TiO_2 thin films as it is degraded to resorufin over a 60 minute period of UV irradiation.

2.3.23 Preparation of resazurin 'intelligent' ink solution

Glycerol (99.6%), hydroxyethyl cellulose [average Mv ¼ 90 000, where Mv is the viscosity-average molecular weight; this average is determined by viscosity measurements as quoted by Sigma Aldrich], resazurin (92%) were all purchased from Sigma-Aldrich and used as supplied. The 'intelligent' ink was composed of resazurin (4 mg) dye in an aqueous solution (40 ml) with glycerol (0.3 g) and hydroxylethyl cellulose (3 g). Solutions were stirred vigorously for 50 minutes and then left to age for 24 hours in the dark before use.

2.3.24 Aerosol spray technique for the application of resazurin ink coating

Substrates to be coated were attached to a sheet of paper mounted vertically on a wall inside a fume hood. A Clarke Gravity Fed Pro Spray Gun (Model No. PGF14) was used to apply the ink

using a constant flow of Nitrogen. The gun was held at a constant distance of at least 50 cm from the substrate surface and a thin coating of ink was applied by spraying horizontally from left to right in even motions. This process was repeated several times until a blue coating of resazurin ink was visible on the substrate surface. The samples were then removed and placed in the dark for 15mins to allow the coating to dry before analysis.

2.3.25 Formal Quantum Efficiency/ Formal Quantum Yield

Photocatalytic activity measurements are often represented using normalised results; however in this thesis we have adopted an improved method for representing photocatalytic performance to enable results to be compared quantitatively.[202] This will enable improved analysis of to what extent the addition of surfactants has enhanced the functional properties of the thin films. Results are represented as formal quantum efficiency (FQE), as shown in equation 6.0. The incident photon flux for the 365 nm UV lamp used for all experiments in this thesis was calculated to be 4.34×10^{15} photons $cm^{-2}\ s^{-1}$. Results have also been expressed in terms of formal quantum yield (FQY) (equation 6.1). The photon flux and photon absorption for each film was determined using a homemade UV digital radiometer for 365 nm radiation.

$$\textbf{FQE} = \frac{\text{rate of reaction (molecules degraded/cm}^{-2}\ \text{s}^{-1})}{\text{incident photon flux (photon cm}^{-2}\ \text{s}^{-1})} \qquad \textbf{Equation 6.0}$$

$$\textbf{FQY} = \frac{\text{rate of reaction (molecules degraded/cm}^{-2}\ \text{s}^{-1}}{\text{number of photons absorbed by film}} \qquad \textbf{Equation 6.1}$$

Chapter 3: Results: Sol-gel processing of titanium dioxide thin films with two different precursors and the effects of surfactant addition

3.1. Introduction

Sol-gel processing is widely used for the production of metal oxide thin films due to its many advantages over other deposition methods. Sol-gel offers versatility, experimental simplicity and the ability to directly control particle growth at the molecular level. The addition of surfactants and block copolymers is a particularly attractive route to modifying thin film properties as these additives are typically low cost, readily available and can be introduced with ease into the sol-gel process at low quantities to produce a range of desired effects. There are several types of surfactants that can be used within sol-gel processing as discussed in section 1.4.

Sol-gel is often the method of choice for the preparation of titanium dioxide thin films, and there has been a vast array of research into the effects of different additives, dopants and Ti-precursors on the resulting thin film properties. A concise review of TiO_2 sol-gel syntheses and applications by Macwan et al is referenced here.[25] Studies on the use of surfactants in TiO_2 sol-gel processing are particularly well documented, especially regarding the use of non-ionic surfactants such as those within the Triton-X[203203], Brij,[70] Tween[112] and Pluronic branded families.[204] Research has found that the use of these surfactants can enable the fine-tuning of thin film morphology as well as the resulting TiO_2 particle and crystallite size. These structural changes have been linked to enhanced photocatalytic activity for dye degradation compared to thin films produced without surfactants.[69,70] However with such an array of different branded surfactants available, and a wide variation within each brand type, e.g. Triton X- 100/ X-144/ X-405, Tween 20/40/60/80, Brij 35/52/56/58/93/98 etc., there have been no comparative studies (to the authors knowledge) of how these subtle variations within brands affect the resulting thin film properties and functional performance. This chapter focuses on investigating these effects with Tween and Brij surfactants. Three types of Tween surfactant; Tween 20, 40 and 60 are used in comparison with two types of Brij surfactant; Brij 58 and 98.

Traditional sol-gel methods employ a titanium alkoxide precursor such as titanium isopropoxide (TTIP) or titanium butoxide. However these precursors are highly sensitive to moisture, whereby the hydrolysis stage within the sol-gel process often occurs quickly without control, leading to

the precipitation of TiO_2 particles with uncontrolled shape and size. A novel oxy-carboxylate precursor, titanium(IV) bis (ammonium lactato) dihydroxide (TiBALD), which is stable in water, has been studied infrequently in literature since its introductory use for the preparation of TiO_2 thin films by Möckel et al in 1999.[205] Due to the solubility and stability of TiBALD in neutral aqueous mediums it can be condensed in a controlled manner at ambient temperatures, thus making it an ideal precursor for the preparation of nanocrystalline titanium dioxide thin films.[206]

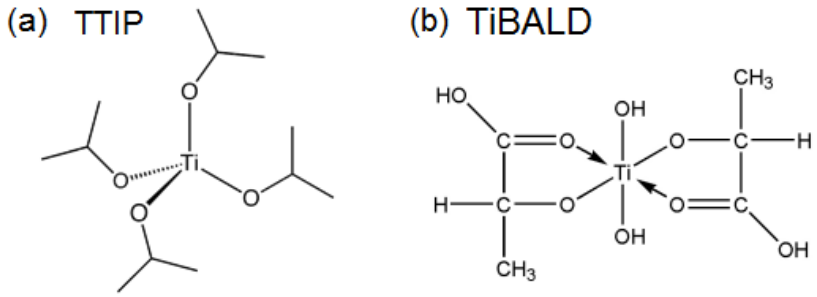

Figure 3.0. Chemical structure of titanium tetra-isopropoxide, TTIP, and titanium bis-ammonium lactate dihydroxide, TiBALD.

Research by Pelentridou et al[207] has shown that TiBALD can produce TiO_2 thin films with a fine nanocrystalline structure that have an improved rate of photodecolorisation for the commonly studied azo dye, basic blue-41, in comparison with traditional TTIP derived films. This enhanced photodecolorisation activity was attributed to an increased surface area and thereby an increased dye absorption in the TiBALD derived films, resulting in better photocatalytic performance. However, such solution based methods require special modified spectrophotometer cells to enable monitoring of the reaction *insitu,* and although useful for assessing a small number of films this method is labour intensive and realistically cannot be applied to the simultaneous analysis of larger numbers of films for reproducible analysis.[201] In contrast, resazurin (Rz) 'intelligent ink', as formulated by Mills et al,[61] follows a rapid photo-reductive mechanism that provides an alternative method for the measure of photocatalytic activity, which is specifically designed for reproducibility with thin film samples. The results herein use this intelligent ink with application by an aerosol-spray method as a measure of photocatalytic activity, whereby several samples of each type have been assessed.[208] As yet there have been no comparative studies to the authors' knowledge of the use of TiBALD precursor with surfactants to produce TiO_2 thin films, and so this chapter looks to address this, and compare the performance of TiBALD derived TiO_2 thin films with those prepared from the traditional TTIP precursor.

Table 3.1. Sol-gel sample names with relevant surfactant types and concentrations added, as well as annealing temperature and time. Samples were produced in duplicate, with 1, 2 and 3 layer samples produced for each sol-gel type.

Surfactant used	Sol-gel sample name/ precursor		Concentration of Surfactant (mol/dm^3)	Annealing temperature + time *(Ramp rate: 15°C min^{-1})*
	TTIP	**TiBALD**		
Nil	TTIP C	TiBALD C	0	**TTIP:** 500 °C / 15 mins ***and*** 600 °C / 1 hr **TiBALD:** 600 °C / 1 hr
Brij 58	B58 A	B58 AT	0.0006	
	B58 B	B58 BT	0.0004	
Brij 98	B98 A	B98 AT	0.0006	
	B98 B	B98 BT	0.0004	
Tween 20	T20 A	T20 AT	0.0006	**TTIP:** 500 °C / 15 mins **TiBALD**: 600 °C / 1 hr
	T20 B	T20 BT	0.0004	
Tween 40	T40 A	T40 AT	0.0006	
	T40 B	T40 BT	0.0004	
Tween 60	T60 D	T60 DT	0.0008	
	T60 A	T60 AT	0.0006	
	T60 B	T60 BT	0.0004	

3.2. Results: TiO_2 thin films prepared by sol-gel methods

All films produced from both precursors were optically transparent, covered the entire surface area of the glass that was dipped, and showed evidence of birefringence. All films were robust and passed the scotch tape test. Films all exhibited a band gap between 3.1-3.3 eV as calculated by the Tauc method,[199] corresponding to anatase phase TiO_2.Some representative tauc plots are given in Appendix A. A selection of non-ionic surfactants were added in varying concentrations, between 0–0.0008 mol dm^3. This range was chosen in order to investigate the minimum amount of surfactant that could be added to sol-gel in order to produce an enhanced performance, this was scaled down from previous work by Stathatos et al reported in literature.[69] The addition of surfactant was found to modify the thin film thickness, morphology, particle size, surface

roughness, wetting properties and photocatalytic performance of the films produced, as will be discussed in the following sections.

3.2.1. Results: Titanium Isopropoxide (TTIP) as precursor with Tween and Brij surfactant addition

3.2.1.1. Thin film thickness and particle size

The addition of Tween and Brij surfactants was found to increase the average thin film thickness with variations observed depending on the surfactant type and concentration used as well as the number of consecutive layers applied. The average film thickness for each sample prepared is shown in data tables 3.2-3.5 in section 3.2.1.8. The film thickness increased with increasing number of layers, as expected as this increases the number of layers of TiO_2 on the surface. The samples produced without surfactant showed average thin film thicknesses of 40, 80 and 90 nm for one, two and three layer samples respectively. The addition of Tween 60 (T60) was found to induce the greatest increase in thickness depending on the concentration used, whereby these samples showed variations ranging from 90-120 nm, 120-180 nm and 190-240 nm for the one, two and three layer samples. The addition of Tween 40 (T40) and Tween 20 (T20) were also found to increase the average film thickness as shown in table 3.3. The addition of Brij surfactants was found to result in a smaller increase in thin film thickness, with thin film thicknesses for two layer films ranging from 110-210 nm, as shown in tables 3.4 and 3.5.

The increase in thin film thickness due to surfactant addition can be explained by the role of the surfactant during processing. The surfactant acts as a spacer, orienting around growing titania particles, resulting in a more viscous solution. Upon dipping, this increased viscosity is transferred as a thicker individual layer onto the glass substrate due to surface tension. As more layers are then added, consecutive layers become thicker as they nucleate with underlying layers to form an overall thicker film. Schuler et al[209] has described the microstructure of sol-gel films in terms of a "structural zone model" as shown in figure 3.0. This model enables a prediction of the type of microstructural features in thin films that can be produced with an increasing number of layers. The Schuler model shows that the intrinsic grain size of the material is closely related to the corresponding single layer thickness. In a thin film which has a large individual single layer thickness, as within this study where the individual thickness of the layers has been

increased by surfactant addition, there is likely to be multiple nucleation sites within the material and so smaller grain sizes. This favours the granular structure growth as shown in figure 3.1 (a).

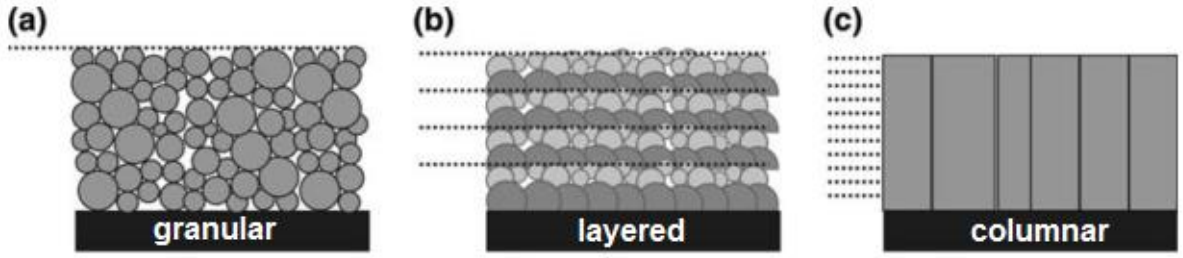

Figure 3.1. Schematic visualisation of (a) granular, (b) layered and (c) columnar sol-gel film structures as classified by Schuler et al,[209] and modified from Wang et al.[210]

This granular structure correlates with the wide range of particle sizes observed for all samples prepared, whereby most samples ranged between 40-300nm, as for the sample produced without surfactant. The addition of Tween surfactant was found to slightly decrease this particle size range, e.g. two layer sample prepared with T40 (A2) had a particle range of 40-200 nm. The particle size range was increased by the addition of Brij surfactants, with ranges typically observed between 25-355 nm. (Table 3.4). The average particle size was found to decrease with surfactant addition, e.g. sol-gel samples produced without surfactant exhibit an average particle size of 130, 130 and 40 nm for one, two and three layer films respectively, whereas samples produced with T20 (A1-A3) show decreased particle sizes of 40, 25, and 40 nm respectively, and for Brij 58 (B58 B) 35, 45 and 40 nm for one, two and three layers. These observations correlate with the granular model, whereby the surfactant stunts the growth of TiO_2 particles during the sol-gel growth stage, resulting in smaller crystallites forming, and smaller average particle formation as a result when crystallites grow together to form particles. The XRD patterns observed for these sol-gel films showed limited crystallinity and so determination of the actual crystallite size by the Scherrer equation was not possible.

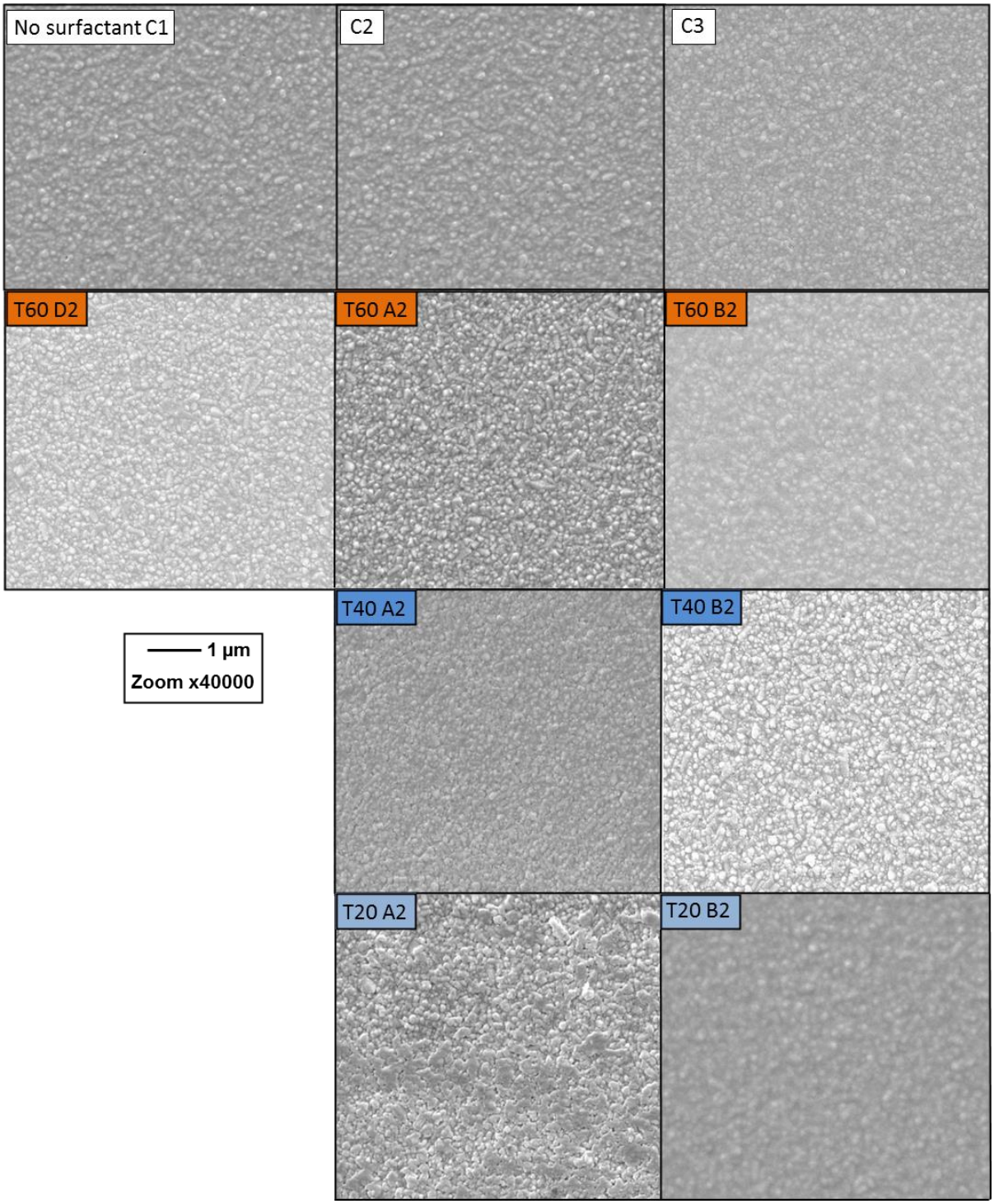

Figure 3.2. SEM images of TiO_2 produced from TTIP precursor by sol-gel with; no surfactant addition (samples C1-C3), and Tween 60 (T60),Tween 40 (T40) and Tween 20 (T20) addition in concentrations; D = 0.0008 mol dm^3, A = 0.0006 mol dm^3, B = 0.0004 mol dm^3. Numbers represent number of consecutive layers. Films were annealed at 500 °C for 15 mins with a ramp rate of 15°C min^{-1}.

3.2.1.21. Thin film morphology: Tween surfactants

Figure 3.2 shows the SEM images of thin films produced using TTIP precursor with and without Tween surfactant addition, and figure 3.3 shows the SEM images produced with TTIP and Brij surfactants. The SEM images for samples C1-C3 show that the thin film morphology undergoes subtle changes as the number of layers are increased from 1-3, whereby increased agglomeration and reduced particle definition is observed in sample C3. For this reason, only 2 layer sample SEM pictures are shown in this chapter, with full SEM images of all samples produced with multiple layers are shown for reference in Appendix 1. The addition of Tween surfactant was found to affect the thin film morphology by producing films with smaller, more angular TiO_2 particles. In comparison to the thin films produced without surfactant, sample C, those films produced with the addition of Tween 60 surfactant, (T60 D, A, B) and Tween 40 (T40 A-B) show greater particle uniformity, less agglomeration and greater particle definition (figure 3.2.) Tween 20 was found to induce areas of agglomeration within the thin film such as that observed for sample T20 A2; however a reduced particle size on average was observed. During the growth phase of sol-gel processing, surfactants act as pore-directing agents, enabling greater control over the size and shape of the Titania particles as they grow, whereby more angular particles can be produced due to the surfactant obstructing particle growth in some directions. More angular TiO_2 particles are beneficial to the overall thin film properties as it increases the resulting surface area to volume ratio of the thin film, thus enhancing photocatalytic and wetting properties, as discussed in sections 3.2.1.5 and 3.2.1.4 respectively.

3.2.1.22. Thin film morphology: Brij surfactants

The addition of Brij surfactants in the sol-gel process was found to enable greater control of the resultant morphology in the TiO_2 thin films produced, as seen in figure 3.3, whereby in comparison to the thin films produced without surfactant, sample C2, those films produced with the addition of Brij surfactants show increased uniformity, less agglomeration and greater particle definition. The addition of Brij 98 surfactant, which has the heavier molecular mass of the two Brij surfactants investigated, produced slightly larger, more angular TiO_2 particles with an average particle size that ranged from 25-50 nm, with more areas of particle agglomeration observed in comparison to those samples produced by Brij 58, which were more spherical with much smaller average particle sizes ranging from 35-45 nm. This data is shown in table 3.4 in section 3.2.1.8. As mentioned, the role of the surfactant as a pore-directing agent during sol

formation results in differences in the particle growth depending on the concentration and weight of the surfactant used. The heavier Brij surfactant (Brij 98) surrounds the growing TiO_2 particles during the growth stage within the sol, leading to the production of more irregular, angular TiO_2 particles compared to Brij 58 prepared samples, due to the obstruction of the surfactant as the particle grows. This angularity and irregularity in TiO_2 particles is beneficial to the overall thin film properties as it increases the resultant surface to volume ratio of the thin film.

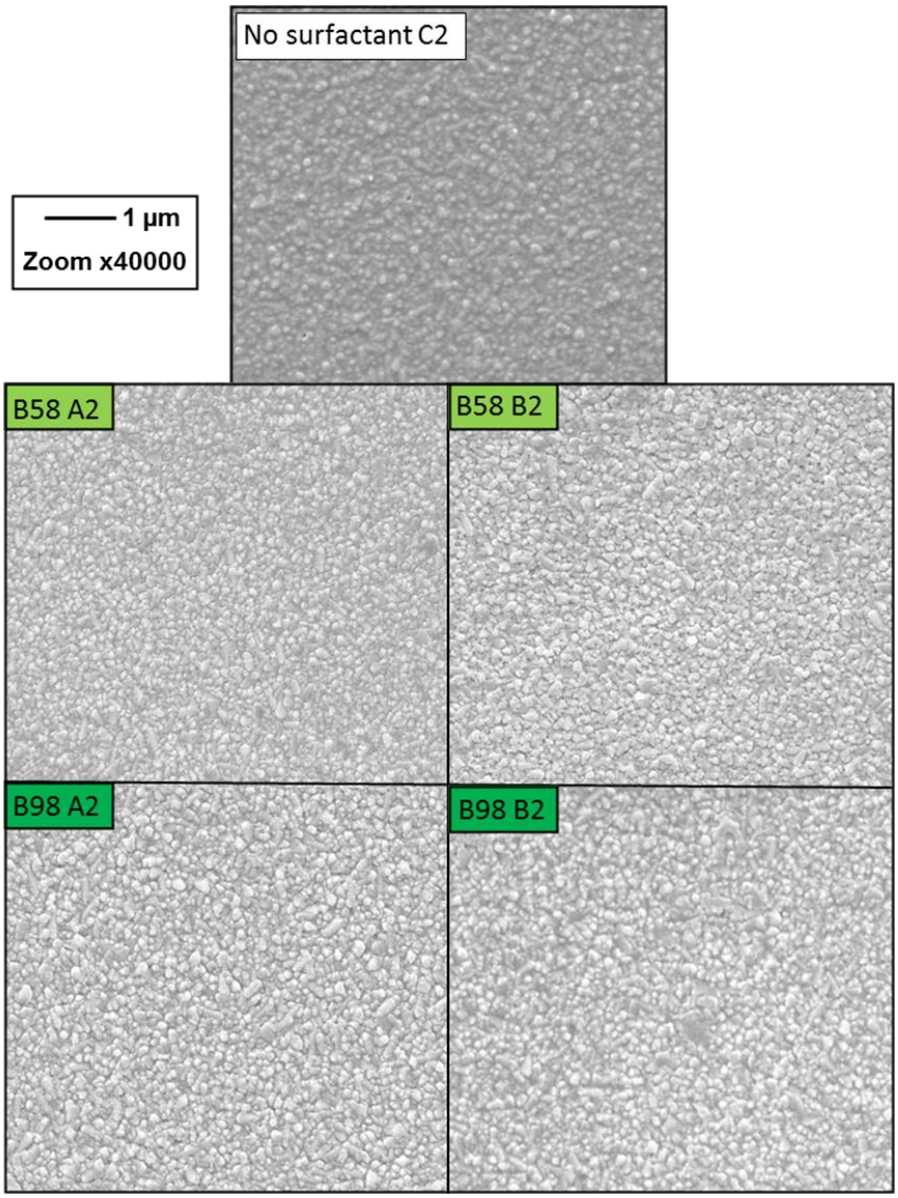

Figure 3.3. SEM images showing two layer TiO_2 films produced from TTIP via a non-aqueous sol-gel method without surfactant addition (sample C2) and with Brij 58 and Brij 98 surfactant addition in concentrations A = 0.0006 mol dm^3, B = 0.0004 mol dm^3. Films were annealed at 500 °C for 15 mins with a ramp rate of 15°C min^{-1}.

3.2.1.3. Surface roughness

Surfactant addition was found to found to increase the root mean square (RMS) surface roughness of thin films by up to 170 nm, e.g. sample C2 (produced without surfactant) shows an average RMS roughness of 14 nm, compared with sample T20 B2 (produced with 0.0004 mol dm^3 of Tween® 20) which has an average surface roughness of 183 nm (tables 3.2-3.5, section 3.2.1.8). Generally Tween surfactants were found to result in greater RMS values compared to Brij surfactant prepared films. The large increase in surface roughness is a result of the morphological changes within the thin film that have been described, whereby the particles produced with surfactant are smaller and also more angular in shape due to the surfactant obstruction during the sol-gel growth phase.

Furthermore, when the concentration of the surfactant is decreased from $6x10^{-4}$ mol dm^3 to $4x10^{-4}$ mol dm^3, as in samples A to B for Tween 20, the RMS generally increases. Sample T20 B exhibits the highest surface roughness observed for all samples produced, with 293 nm observed for the three layer film (T20 B3). This observation is also seen for samples produced with Brij 58 and Brij 98, whereby an increased RMS roughness is observed with surfactant addition, which is increased with the smaller concentration used. For example, the higher concentration two layer film produced with Brij 58 (B58 A2) has a RMS value of 33 nm, whereas that produced with the reduced concentration, (B58 B2) has a RMS value of 95 nm. This observation can be explained by the role of the surfactant during the TiO_2 particle growth phase. When the surfactant concentration is reduced, as from sample T40 A2 to T40 B2 in SEM images in figure 3.2, the particles during the growth phase of sol-gel formation are less restricted in their growth, meaning they can grow larger and more spherical. This is reflected in the particle sizes, whereby sample T40 A2 has an approximate particle size range of 40-200 nm, whereas T40 B2 (lower concentration) has a particle size range of 40-320 nm. This variation in particle size results in a rougher surface observed as a whole, as shown in the 3D representations of thin film surfaces in figure 3.4.

Brij surfactants were also found to induce increased surface roughness, with a maximum surface roughness of 110 nm observed for sample B98 B2, prepared with the lower concentration of Brij 98. Again the observation of increased roughness with lower concentration of surfactant was observed (table 3.4.) Furthermore, the different variants of Brij surfactant used have an effect on the surface roughness of the resulting deposited thin film, whereby there is an increase in root

mean square surface roughness when using the heavier Brij 98 surfactant. This surfactant is larger in size and so occupies more space surrounding the titania particles as they grow, leading to more irregular and angular particles when the surfactant is removed during the annealing stage. For example, sample B58 A2 (Brij 58, 0.0006 mol dm^3) has a root mean square surface roughness of 33 nm compared to sample B98 A2 (Brij 98, 0.0006 mol dm^3) which has a root mean square surface roughness of 92 nm, this is accompanied by a reduction in average particle size from 35 nm to 50nm. A 3D representation of the thin film surface roughness of samples produced with increasing number of layers, with and without Brij 58 surfactant is shown in figure 3.5.

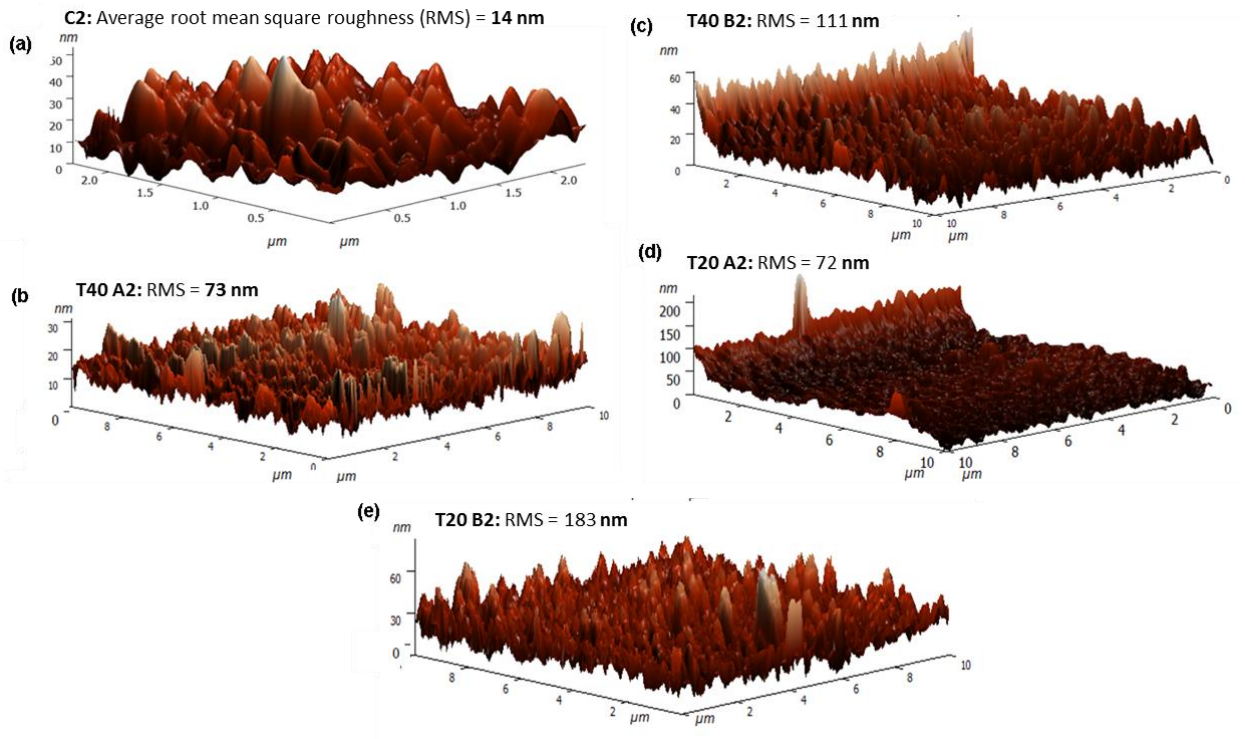

Figure 3.4. AFM 3D representation of thin film surface, shown with average root mean square roughness values determined from measurement of three areas across the thin film surface. (a) C2 (no surfactant), (b) T40 A2 (Tween 40, 0.0006 mol dm^3), (c) T40 B2 (Tween 40, 0.0004 mol dm^3), (d) T20 A2 (Tween 20, 0.0006 mol dm^3), (e) T20 B2 (Tween 20, 0.0004 mol dm^3)

The effect of number of layers on the root mean square surface roughness of the thin films does not have a consistent trend between samples, as seen in the data tables 3.2-3.5 in section 3.2.1.8. Typically increasing the number of layers would be expected to increase the surface roughness of samples due to irregular adhesion between layers where different sized particles are placed on top of one another. However, most samples show a decrease in surface roughness from single

layer to third layer, e.g. sample B58 B1 (90 nm), B58 B2 (95 nm), and B58 B3 (81 nm). This is likely to be the result of particles agglomerating between layers as they adhere to one another, leading to a smoother top surface overall.

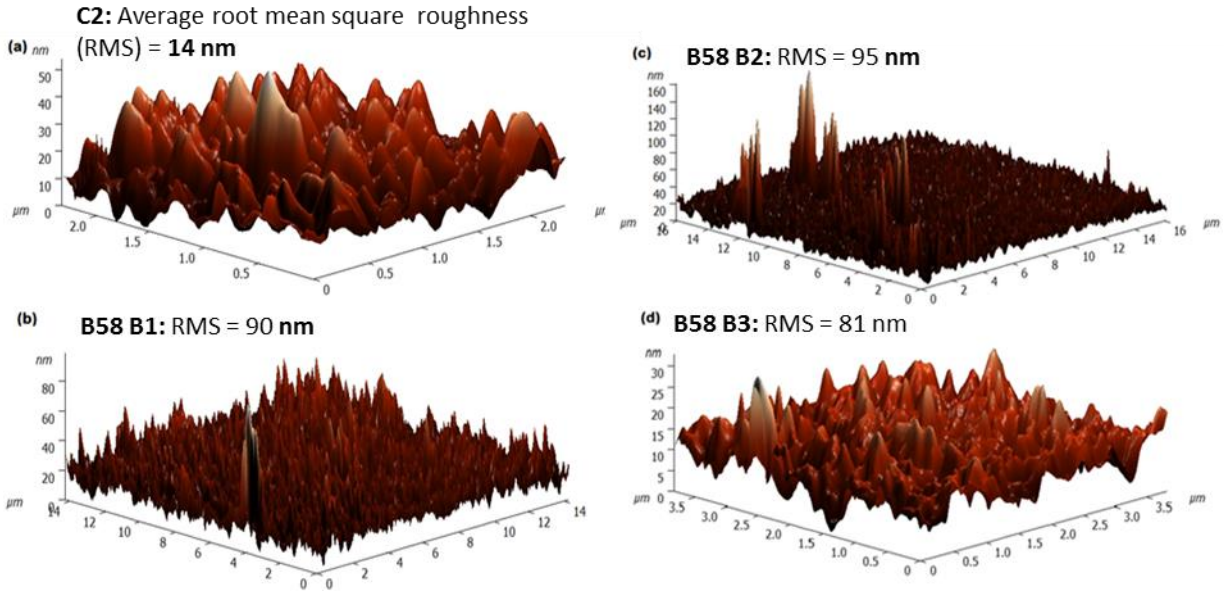

Figure 3.5. AFM 3D representation of thin film surface, shown with average root mean square roughness values determined from measurement of three areas across the thin film surface to demonstrate the influence of number of layers (a) C2 (no surfactant), (b) B58 B1 (Brij 58 0.0004 mol dm^3), (c) B58 B2 (d) B58 B3.

3.2.1.4. Influence of annealing temperature and time on morphology and roughness

The increase in annealing temperature and time from 500 °C for 15 minutes to 600 °C for 1 hour was investigated for the thin films produced with Brij surfactants. This modification to annealing conditions was found to affect the thin film morphology in different ways depending on the type of surfactant used. Brij 58 surfactant was found to produce thin films with more agglomeration and less particle definition as the annealing time and temperature was increased, whereas the morphology of the thin films produced with Brij 98 was observed to show larger, more angular particles, as shown through comparison of figure 3.3 and 3.6. This is a result of the evaporation of organic content, including the removal of the surfactants. During the annealing stage the films become more dense and the particles more pronounced. However, some samples such as sample B58 B2 600 shows increased particle agglomeration, due to the low concentration and light weight of the Brij 58 surfactant used, which is evaporated with the rest of the organic content

during the annealing stage, resulting in shrinkage of the thin film and increased particle agglomeration between layers.

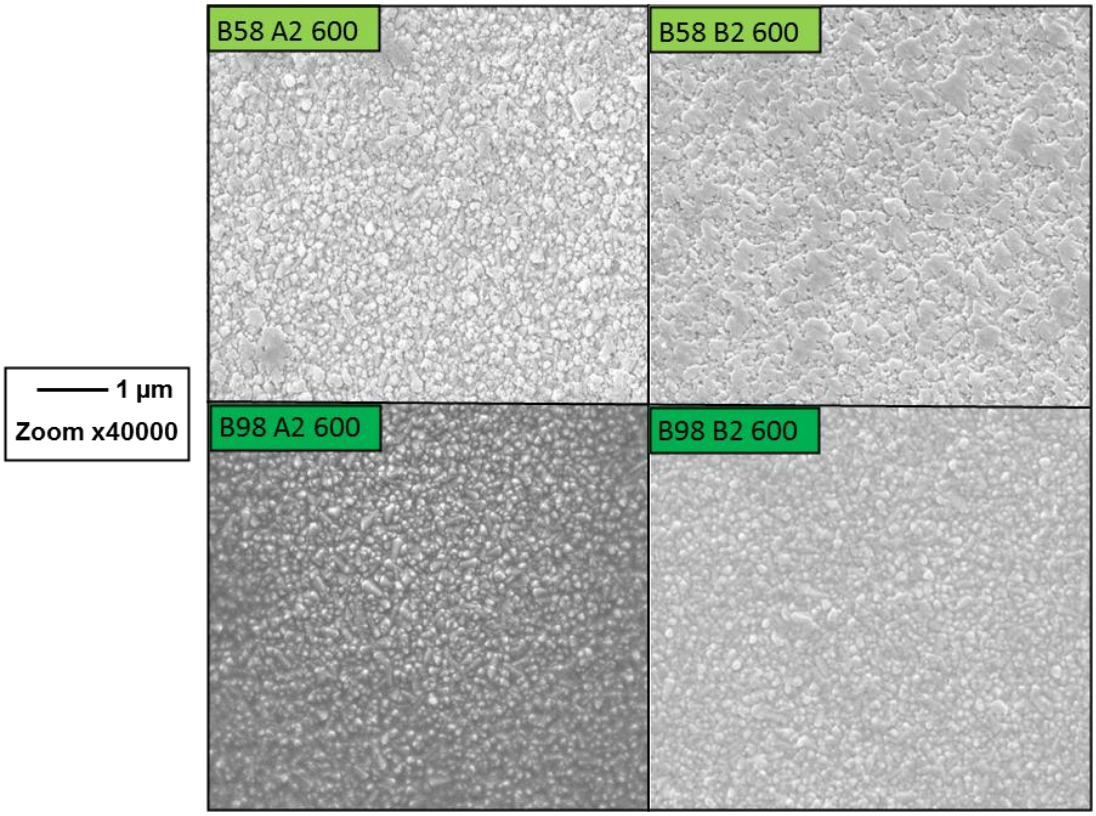

Figure 3.6. SEM images showing two layer TiO_2 films produced from TTIP with Brij surfactant addition (Brij 58 = B58, Brij 98= B98) in concentrations; A = 0.0006 mol dm^3, B = 0.0004 mol dm^3. Films were annealed at 600 °C for 1= hour with a ramp rate of 15°C min^{-1}.

3.2.1.5. Crystalline phase identification of TiO_2 thin films

The XRD diffraction patterns of the TiO_2 thin films deposited on F:SnO_2 coated glass substrates with and without Tween surfactant addition are shown in figure 3.7, and for Brij surfactants figure 3.9. The TiO_2 thin films deposited were thinner than the F:SnO_2 layer (~400 nm) so breakthrough to the substrate was observed for all samples. The samples exhibited diffraction peaks representing a mixture of anatase, the preferred crystal phase in the [101] plane, as well as rutile, which is the more thermodynamically stable phase and was present in the [211] plane. The presence of the brookite phase was also observed in the [121], [221] and [203] planes. This mixture of phases is commonly observed in the production of TiO_2 derived thin films[29,211] and it is believed that the sol-gel method described herein has resulted in the production of largely amorphous TiO_2 thin films which are poorly detected by XRD. For further determination of the

TiO_2 phase, Raman spectroscopy was used, whereby a typical spectrum observed for all Tween and Brij prepared samples is shown in figure 3.8. All samples gave strong Raman bands centred at 147, 395, 513 and 642 cm^{-1}, with a weaker band centred at 198 cm^{-1}, all of which are attributable to anatase titanium dioxide indicating that whilst there is poor long range order, anatase predominates over a short range.[1]

The higher annealing time and temperature was investigated in order to increase the crystallinity of the thin films produced. As a result of this modification, the thin films produced from the extended annealing period were found to exhibit more intense peaks in the corresponding XRD patterns, as shown in figure 3.9. Of particular interest is the increased peak intensity in the [101] plane, which corresponds to the anatase phase. It is believed that the increased preferential orientation in this plane results in an enhanced photocatalytic performance as discussed later in 3.2.1.5. This increased crystallinity is in agreement with literature studies whereby the anatase peak is found to be preferential in thin films that are annealed at temperature up to 600 °C, after which rutile becomes the predominant crystalline phase.[212]

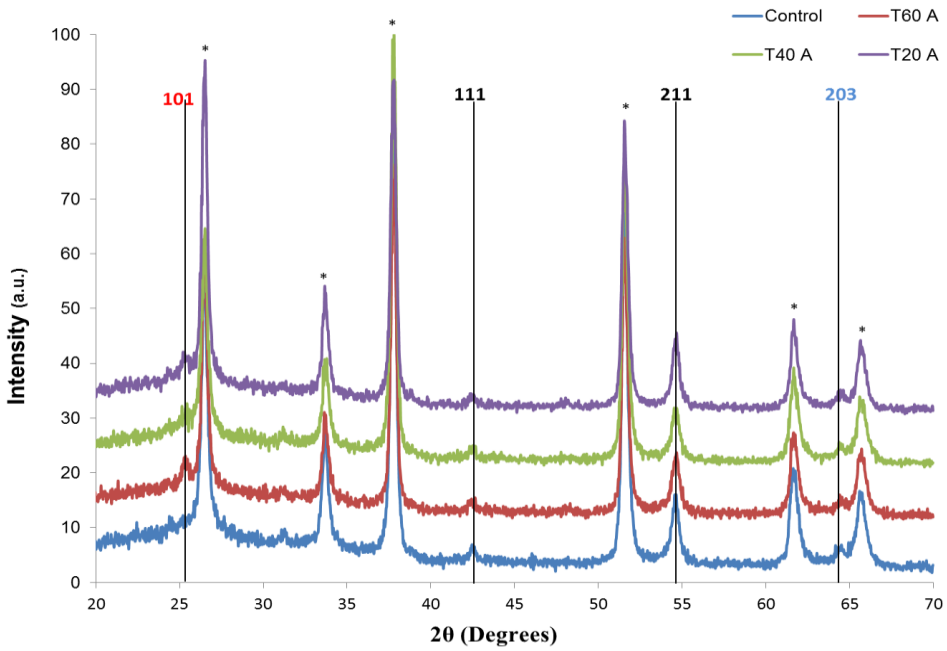

Figure 3.7. XRD for TiO_2 films produced using TTIP precursor without surfactant (Control) and with the addition of Tween 60 (T60 A), Tween 40 (T40 A), and Tween 20 (T20 A) surfactants in a concentration of 0.006 mol dm^3. Peaks identified as anatase are marked in red, brookite in blue and rutile in black. Peaks denoted with asterisks (*) are assigned to the F:SnO_2 coating of the glass substrate. XRD are normalised for intensity.

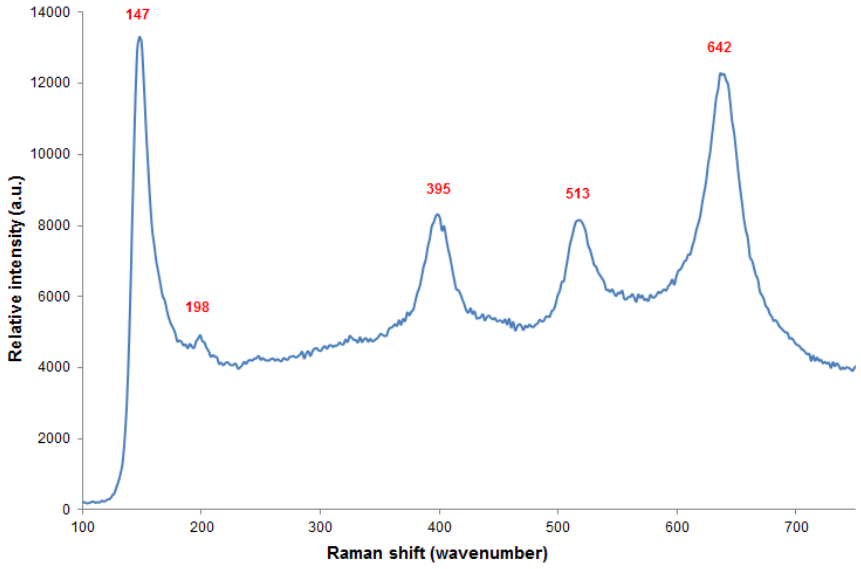

Figure 3.8. Typical Raman spectrum obtained for all samples. This spectrum was obtained for sample T40 A3 annealed at 500°C for 15 minutes. Peaks match the reference spectra for TiO_2 anatase.[1]

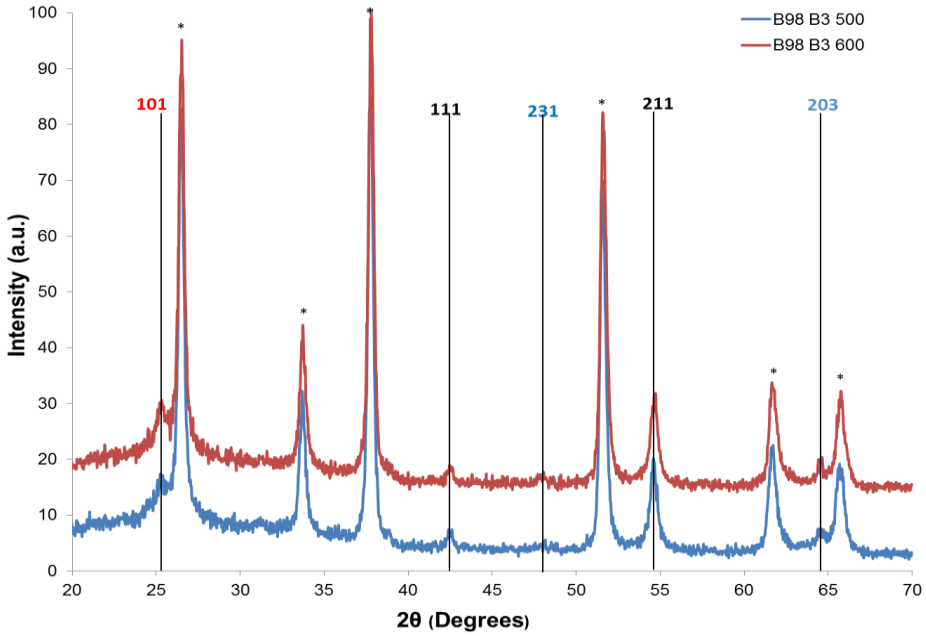

Figure 3.9. XRD obtained for TiO_2 films produced using TTIP precursor and addition of Brij 98 surfactant (concentration = 0.0004 mol dm^3). Red line represents the diffraction pattern for a sample annealed at 600°C (1 hour), and blue line represents a sample annealed at 500°C (15 minutes). Peaks identified as anatase are labelled red, brookite blue and rutile in black. Peaks denoted with asterisks (*) are assigned to the F:SnO_2 coating of the glass substrate. XRD are normalised for intensity.

3.2.1.6. Wetting behaviour of thin films

All TiO_2 thin film samples produced exhibited UV induced hydrophilicity in varying degrees, as seen by the reduction in contact angle of deionised water on the TiO_2 surface after 30 minutes UV irradiation shown in tables 3.2-3.5. Photos of water droplets on the surface of each film were used to measure the contact angle, as shown in figure A2 in appendix A. Some samples that were produced with surfactant exhibited super hydrophilicity whereby the contact angle dropped to below 5° after UV irradiation, such as many two layer samples, e.g. those produced with Brij 58, Brij 98 and Tween 20 (Tables 3.2-3.5, section 3.2.1.8). The increased hydrophilicity of thin films after UV treatment can be attributed to the changes in morphology and increased surface area to volume ratio produced within thin films due to the addition of surfactant during sol-gel processing, as described previously.

3.2.1.7. Photocatalytic activity of thin films produced from TTIP and effects of surfactant addition

The sol-gel derived thin films were all found to be active photocatalysts for the degradation of resazurin intelligent ink, as shown in tables 3.2-3.5. Initial studies of photocatalytic activity were assessed by normalizing UV-Vis absorption results for the degradation of resazurin dye, represented as a half-life in minutes and shown as degradation curves in figures 3.10 and 3.11, with values shown in tables 3.2-3.4, section 3.2.1.8. However due to the nature of normalised results, this form of representation has made comparison between different data sets difficult. A significant limitation with the use of resazurin ink and the normalization method is that the photocatalytic efficiency values obtained are only truly reliable for the first 1-2 minutes of UV irradiation. This is owing to the observation that after 2 minutes of UV irradiation, the absorption curves often exhibit a sudden increase in absorption value, apparent as a fluctuation in the degradation curve as seen in figure 3.10, and more noticeably for sample B58 B2 shown in figure 3.11. These fluctuations in absorption are due to the mechanism by which the ink film is degraded. Often an initial 'top' layer of ink molecules are reduced quickly upon UV irradiation, resulting in a reduced absorbance reading where the ink has been degraded, this top layer then collapses to uncover a layer beneath which has not been exposed to UV light and thus not degraded, causing an increased absorbance reading for resazurin to be recorded when the second measurement is made. Several attempts have been made to try to avoid these fluctuations in absorption measurement such as increased thin film drying time, however as this is an inherent

issue with the "intelligent ink" method used, the only option has been to repeat experiments and obtain an indicative photocatalytic average.

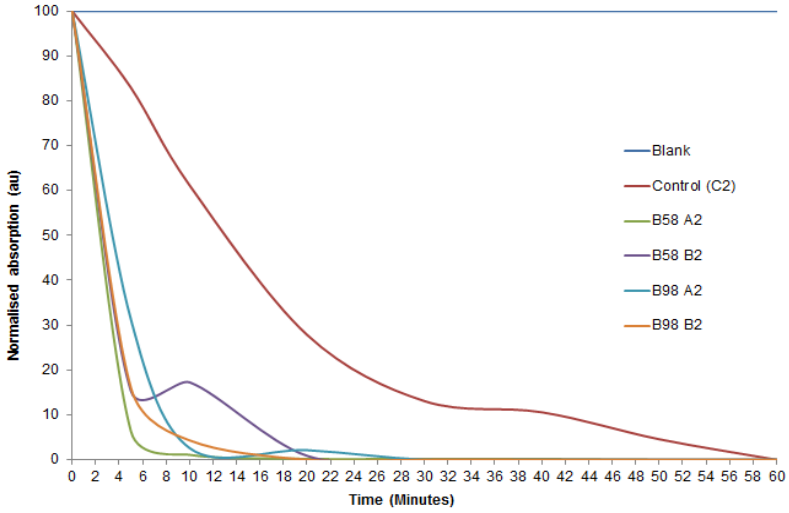

Figure 3.10. Normalised absorption curve for determination of photocatalytic half-life (in minutes) for samples prepared with TTIP precursor and Tween surfactants, annealed at 500°C for 15 mins. Control (CT2) represents the TTIP sample prepared without surfactant addition and is used for comparison.

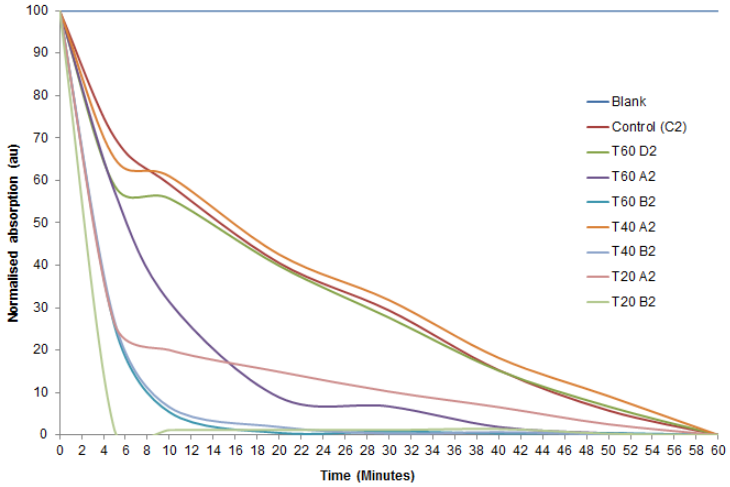

Figure 3.11. Normalised absorption curve used for determination of photocatalytic half-life (in minutes) for samples prepared with TTIP precursor and Brij surfactants, annealed at 500°C for 15 mins. Control (CT2) represents the TTIP sample prepared without surfactant and is used for comparison.

The calculated rate of photoactivity (dye molecules degraded per second per cm^2) is regarded as a more reliable comparison of photocatalytic performance, whereby the calculated value enables greater precision in comparing values. This method uses the maximum and minimum value of

absorbance value obtained to calculate a value which is representative of the photocatalytic performance, thereby ignoring any fluctuations that are measured due to the problem of the incomplete degradation of ink as described above. In contrast, the normalized values are quoted as half-lives which are estimated from a dye degradation curves. Along with formal quantum efficiency (FQE) and formal quantum yield (FQY), this calculated rate of photoactivity is favoured in the following discussions, although the normalized adsorption curves are still shown as figures (3.10 and 3.11) for comparison.

Thin films produced with the addition of Tween 60 surfactant, as shown in table 3.2, were found to show little or no significant enhancement to photocatalytic activity compared to the films produced without surfactant. For example, the average calculated rate of photoactivity for two layer thin films produced without surfactant was found to be 1.76×10^{12} dye molecules degraded per second per cm^2 (s^{-1} cm^{-2}), whereas the two layer thin films prepared with Tween 60 showed rates of 7.01×10^{11} (T60 D2), 2.00×10^{12} (T60 A2), and 1.80×10^{12} (T60 B2) dye molecules degraded s^{-1} cm^{-2}. The highest concentration of Tween 60 (0.0008 mol dm^3) as for sample T60 D2, was found to reduce the photocatalytic activity from 1.76×10^{12} dye molecules degraded s^{-1} cm^{-2} to 7.01×10^{11}, whereby this reduced photoactivity is attributed to a wider particle size range 40-400 nm for the T60 D2 sample, rather than a 40-300 nm particle size range for the sample produced without surfactant. The samples produced with a reduced Tween 60 concentration (samples A2 and B2) show only a small improvement from 1.76×10^{12} for sample produced without surfactant, compared with 2.00×10^{12} (T60 A2), and 1.80×10^{12} (T60 B2). For these reasons, Tween 60 has not been studied in great detail in this thesis. In addition, only a small variation in photocatalytic activity was observed between samples of differing number of layers, and so only the two-layer sample was analysed for each sample type.

The addition of Tween 40, Tween 20, Brij 58 and Brij 98 were all found to enhance the photocatalytic activity of TiO_2 thin films, as shown in table 3.3-3.5 and figure 3.10, 3.11 and 3.12. The fastest rates were observed for samples prepared in the higher concentration, e.g. (0.0006 mol dm^3) of Brij 58 and Brij 98 (samples B58 B and B98 B), with rates of 2.95×10^{12} (dye molecules degraded s^{-1} cm^{-2}) and 2.96×10^{12} respectively, versus plain sample, 1.76×10^{12}. These high photocatalytic degradation rates can be attributed to a combination of factors whereby the addition of the surfactant has produced thin films with highly angular, small particles of TiO_2

with a rough morphology (fig 3.2), hydrophilicity observed after UV irradiation and increased RMS surface roughness (95 nm and 110 nm respectively) (see table 3.4).

The addition of Tween 40 and Tween 20 surfactants in some were also found to increase the photocatalytic activity, as seen in figure 3.10, with the highest rate observed for sample T40 B2, with a rate of 2.24 x 10^{12} dye molecules degraded s^{-1} cm^{-2}. The only Tween sample to show a reduction in performance is that prepared using Tween 20 in the low concentration, e.g. Tween 20 B2 (0.0004 mol dm^3), rate is 1.20 x 10^{12} dye molecules degraded s^{-1} cm^{-2}, whereas the sample produced without surfactant exhibited a rate of 1.76 x 10^{12} dye molecules degraded s^{-1} cm^{-2}. This can be attributed to the morphology of the sample, whereby from the SEM images in figure 3.1 it can be seen that there is a lack of definition in particles, in addition to a wide particle size range observed between 40- 240 nm.

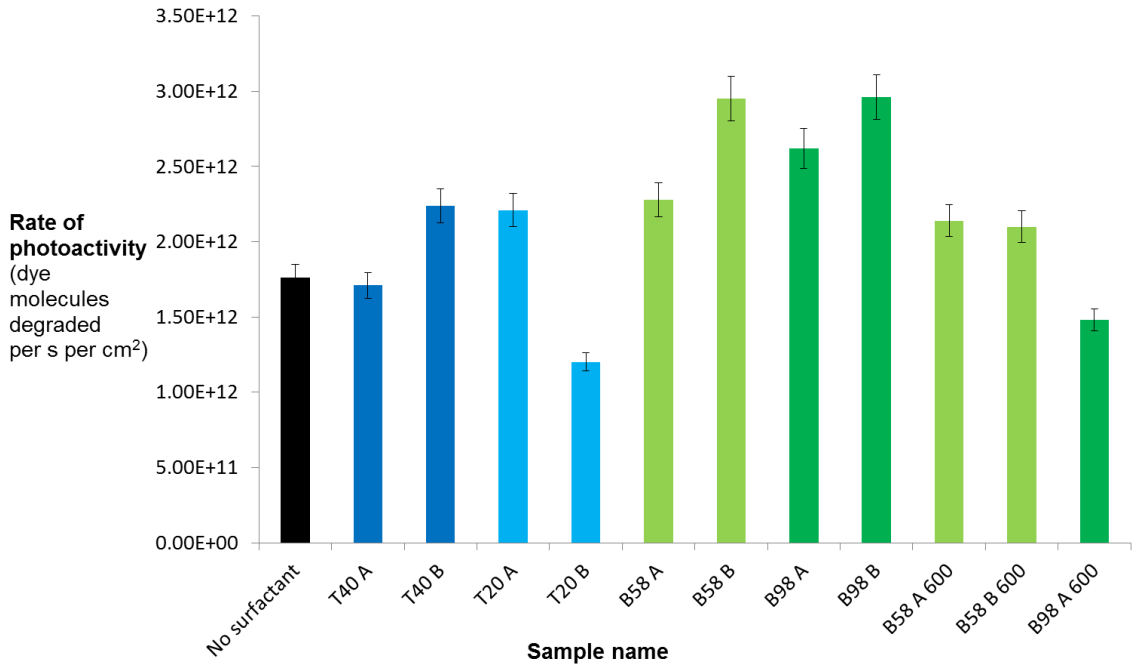

Figure 3.12. Bar chart representing the rate of calculated photoactivity for Rz dye molecules degraded s^{-1} cm^2 for each sample type. Concentrations of surfactant; A = 0.0006 mol dm^3 and B = 0.0004 mol dm^3. Samples names with '600' represent samples that were annealed at 600 °C for one hour rather than 500 °C for 15 minutes. Samples are two layer samples. Error bars are shown with 5%experimental error.

3.2.1.8. Results tables for sol-gel samples produced from TTIP precursor

Table 3.2. Results for TTIP prepared samples with and without the addition of Tween 60 surfactant, where D= 0.0008 mol dm^3, A= 0.0006 mol dm^3, B = 0.0004 mol dm^3. Sample C represent control samples prepared without surfactant. Numbers represent the number of layers. Samples were annealed at 500°C for 15 minutes. Formal quantum efficiency (FQE) is the number of dye molecules degraded per incident photon, whereas the formal quantum yield (FQY) is the number of dye molecules degraded per absorbed photon.

Sample name	Contact angle (°) before UV irradiation	Contact angle (°) after UV irradiation	Approx. particle size range (nm)	Average thin film thickness (nm)	Photocatalytic half-life for Rz degradation (mins)	Calculated rate of photoactivity (Rz dye molecules degraded s^{-1} cm^{-2})	Formal quantum efficiency (FQE)	Formal quantum yield (FQY)
C1	38	14	40- 200	40	13	2.20×10^{12}	5.08×10^{-4}	4.61×10^{-2}
C2	50	7	30- 300	80	12	1.76×10^{12}	4.05×10^{-4}	3.89×10^{-2}
C3	39	7	40- 300	90	11	2.84×10^{12}	6.50×10^{-4}	7.12×10^{-2}
T60 D1	46	9	40- 200	120	13	4.18×10^{11}	9.62×10^{-5}	1.08×10^{-2}
T60 D2	52	8	40- 400	130	11	7.01×10^{11}	1.62×10^{-4}	1.55×10^{-2}
T60 D3	24	17	40-500	240	14	5.77×10^{11}	1.33×10^{-4}	1.30×10^{-2}
T60 A1	33	7	30- 200	120	19	2.09×10^{12}	4.81×10^{-4}	5.22×10^{-2}
T60 A2	46	8	40-200	120	11	2.00×10^{12}	4.61×10^{-4}	4.18×10^{-2}
T60 A3	41	20	200-600	210	12	4.90×10^{11}	1.13×10^{-4}	1.08×10^{-2}
T60 B1	46	14	20-40	90	15	2.12×10^{12}	4.88×10^{-4}	5.14×10^{-2}
T60 B2	33	12	40-200	185	15	1.80×10^{12}	4.14×10^{-4}	4.04×10^{-2}
T60 B3	71	73	40- 200	190	12	3.81×10^{11}	8.77×10^{-5}	8.40×10^{-3}

Table 3.3. Results for samples prepared using TTIP precursor with addition of Tween 20 and Tween 40, A= 0.0006 mol dm^3, B = 0.0004 mol dm^3. Sample C represents samples prepared without surfactant. Numbers = number of layers. Samples were annealed at 500°C for 15 minutes. FQE is the number of dye molecules degraded per incident photon, and FQY is the number of dye molecules degraded per absorbed photon.

Sample name	Contact angle (°) before UV irradiation	Contact angle (°) after UV irradiation	Average particle size (nm)	Approx. particle size range (nm)	Average RMS surface roughness (nm)	Average thin film thickness (nm)	Photocatalytic half- life for Rz degradation (mins)	Calculated rate of photoactivity (dye molecules degraded s^{-1} cm^{-2})	Formal quantum efficiency (FQE)	Formal quantum yield (FQY)
C1	38	14	40	40-200	15	40	13			
C2	50	7	30	30-300	14	80	12	1.76×10^{12}	4.05×10^{-4}	3.89×10^{-2}
C3	39	7	45	40-300	17	90	11			
T40 A1	49	5	40	30-200	53	180				
T40 A2	52	9	25	40-200	73	170	10	1.71×10^{12}	3.93×10^{-4}	4.60×10^{-2}
T40 A3	62	8	40	40-300	193	210				
T40 B1	45	4	40	40-200	149	200				
T40 B2	37	6	35	40-320	111	110	7	2.24×10^{12}	5.13×10^{-4}	6.21×10^{-2}
T40 B3	62	56	25	80-200	115	190				
T20 A1	37	6	40	40-200	42	110				
T20 A2	37	3	25	40-200	72	160	3	2.21×10^{12}	5.08×10^{-4}	5.52×10^{-2}
T20 A3	47	5	40	80-280	52	180				
T20 B1	34	8	40	40-240	116	120				
T20 B2	37	4	35	40-240	183	210	3	1.20×10^{12}	2.77×10^{-4}	2.74×10^{-2}
T20 B3	34	5	25	40-200	293	220				

Table 3.4. Results for samples prepared using TTIP precursor with addition of Brij 58 and Brij 98, in two concentrations, A= 0.0006 mol dm^3, B = 0.0004 mol dm^3. Sample C represents the sample prepared without surfactant. Numbers represent the number of layers. Samples were annealed at 500°C for 15 minutes. Values denoted with an asterisk (*) are samples that showed agglomerated particles in SEM images. FQE is the number of dye molecules degraded per incident photon, and FQY is the number of dye molecules degraded per absorbed photon.

Sample name	Contact Angle (°) before UV irradiation	Contact angle (°) after UV irradiation	Average particle Size (nm)	Approx. particle size range (nm)	Average RMS surface roughness (nm)	Average thin film thickness (nm)	Photocatalytic half- life for Rz degradation (mins)	Calculated rate of photoactivity (dye molecules degraded s^{-1} cm^{-2})	Formal quantum efficiency (FQE)	Formal quantum yield (FQY)
B58 A1	38	7	40	25-355	23	70				
B58 A2	27	3	35	25-320	33	90	2	2.28×10^{12}	5.25×10^{-4}	6.11×10^{-2}
B58 A3	43	14	35	25-355 *	14	120				
B58 B1	38	4	35	30-355	90	75				
B58 B2	28	2	45	30-355	95	80	2	2.95×10^{12}	6.81×10^{-4}	6.35×10^{-2}
B58 B3	49	7	40	30-370	81	90				
C2	50	7	30	30-300	14	80	12	1.76×10^{12}	4.05×10^{-4}	3.89×10^{-2}
B98 A1	32	5	45	35-390 *	85	45				
B98 A2	43	3	50	25-355	92	65	3	2.62×10^{12}	6.02×10^{-4}	5.18×10^{-2}
B98 A3	35	6	35	30-355 *	85	90				
B98 B1	50	<1	25	25-355	83	60				
B98 B2	50	4	50	25-390	110	80	3	2.96×10^{12}	6.83×10^{-4}	9.77×10^{-2}
B98 B3	50	4	40	25-390	50	90				

Table 3.5. Results for samples prepared using TTIP precursor with addition of Brij 58 and Brij 98, in two concentrations, A= 0.0006 mol dm^3, B = 0.0004 mol dm^3. Sample C represents the control sample prepared without surfactant. Numbers represent the number of layers. Samples were annealed at 600°C for 1 hour. Values denoted with an asterisk (*) are samples that showed agglomerated particles in SEM images. FQE is the number of dye molecules degraded per incident photon, and FQY is the number of dye molecules degraded per absorbed photon.

Sample name	Contact Angle (°) before UV irradiation	Contact angle (°) after UV irradiation	Average particle Size (nm)	Approx. particle size range (nm)	Average RMS surface roughness (nm)	Average thin film thickness (nm)	Photocatalytic half- life for Rz degradation (mins)	Calculated rate of photoactivity (dye molecules degraded s^{-1} cm^{-2})	Formal quantum efficiency (FQE)	Formal quantum yield (FQY)
B58 A1 600	42	11	55	30-260	56	70				
B58 A2 600	34	4	45	30-390	39	80	2	2.14×10^{12}	4.9×10^{-4}	7.6×10^{-3}
B58 A3 600	45	5	45	30-370	23	290				
B58 B1 600	37	4	30	25-195 *	65	60				
B58 B2 600	42	5.41	30	15-290 *	44	75	6	2.10×10^{12}	4.8×10^{-4}	7.5×10^{-3}
B58 B3 600	40	4	30	15-355 *	10	100				
B98 A1 600	51	6	110	30-390	205	70				
B98 A2 600	41	<1	105	25-390	234	60	3	1.48×10^{12}	3.4×10^{-4}	3.3×10^{-2}
B98 A3 600	33	21	60	30-320 *	139	70				
B98 B1 600	37	6	40	25-355	145	90				
B98 B2 600	28	4	60	30-355	148	70	3	2.01×10^{12}	4.6×10^{-4}	4.4×10^{-2}
B98 B3 600	50	5	80	30-320	75	80				

The Brij samples annealed at 600°C/1 hour showed slightly reduced photoactivity compared to the samples of the same surfactant type and concentration annealed at the lower temperature and time (500°C/15 min) as seen in figure 3.10. Due to its effect on electronic band structure and surface characteristics, the crystal structure is one of the major determining factors in the effective photoactivity of titanium dioxide. X-ray diffraction (XRD) provides an effective means of determining the crystal phase and crystallinity, and as these samples exhibited increased crystallinity within the 101 anatase plane, it was assumed that increased photocatalytic activity would be observed. However these samples show reduced photoactivity due to the increased agglomeration within thin films as observed in SEM images in figure 3.5 and the increased average particle sizes of up to 105 nm (sample B92 A2 600). These morphological changes are due to the extended annealing time, whereby the removal of increased organic content has resulted in film shrinkage and agglomeration of particles into larger, more spherical particles with reduced surface area. These factors result in a lower surface area for dye absorption and photocatalytic degradation to take place, thus lowering the observed rate of photoactivity.

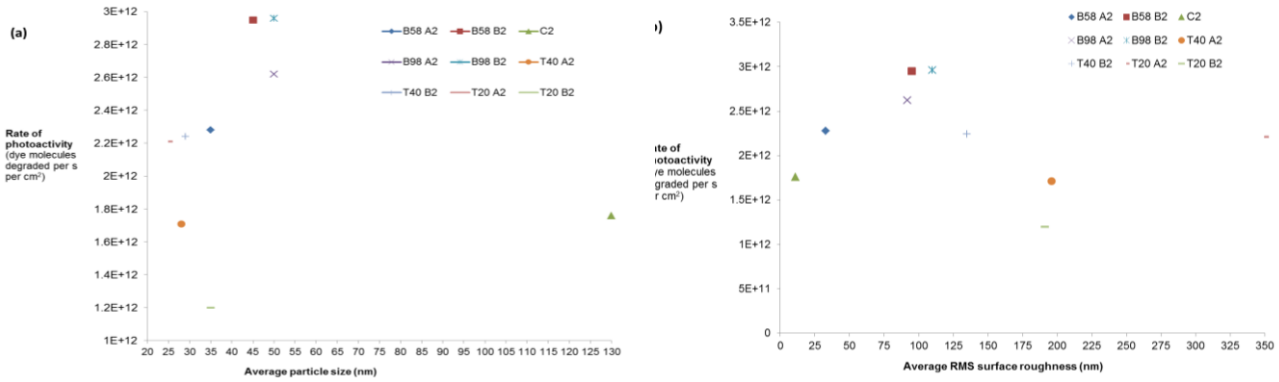

Figure 3.12.(a)(b) Scatter plot comparisons for TiO_2 thin films produced by sol-gel with TTIP precursor and surfactant addition. **(a)** Average particle size (nm) vs rate of photoactivity **(b)** Average root mean square (RMS) roughness (nm) vs rate of photoactivity.

Scatter plots to demonstrate the relationship between average particle size (nm) and average root mean square (RMS) surface roughness (nm) and average rate of photoactivity have been plotted in figure 3.12 (a) (b). These plots show there is a relationship between these properties of the thin film and the resulting photoactivity, whereby an increased average particle size results in an increased rate of photoactivity up to a maximum of ~45-50nm, after which a reduction in rate is

observed (e.g. sample C2 in figure 3.12 (a) which shows an average particle size of 130 nm and an average rate of 1.76 x 10^{12} molecules degraded per s per cm^2. Similarly, increased RMS surface roughness results in an increased rate of photoactivity up to RMS values of ~90-110 nm, after which the rate of photoactivity decreases with increased RMS surface roughness.

3.2.1.9 Conclusions: TTIP

Thin films of photocatalytically active titanium dioxide thin films were deposited using a non-aqueous modified sol gel method and TTIP precursor. The sols were modified using two different Brij and Tween surfactants in differing concentrations. The films have been fully characterised using SEM, XRD, Raman spectroscopy and UV/Vis, and the photocatalytic activity of the films was assessed using an intelligent dye-ink test. It was found that the half-life of the dye could be reduced from 12 minutes to 3 minutes with the addition of some surfactants, whereby the photoactivity has been improved, from a rate of 1.76 x 10^{12} (dye molecules degraded s^{-1} cm^{-2}) to a maximum of 2.96 x 10^{12} as observed for sample B98 B2 prepared with Brij 98 surfactant in a concentration of 0.0004 mol dm^3. This increased photoactivity has been attributed to a higher surface roughness (110 nm RMS) and reduced particle sizes, indicating a greater surface area for catalysis to occur upon.

3.2.2. Results: Titanium Bis-Ammonium Lactato Dihydroxide (TiBALD) as precursor with surfactant addition

3.2.2.1. Thin film thickness and particle size

Transparent TiO_2 thin films of varying uniformity were produced and all films showed good adherence to the substrate after annealing, passing the scotch tape test. The average thin film thickness was measured using side-on SEM images, showing a variation from 130-1905 nm depending on the type and concentration of surfactant added to the initial sol-gel as well as the number of layers applied. The thinnest sample (T60 AT 1) was a one-layer sample produced using 6 x 10^{-4} mol dm^3 of Tween 60 surfactant, whereas the thickest film (B58 BT 3) was a three-layer sample produced from 6 x 10^{-4} mol dm^3 of Brij 58 surfactant. Addition of surfactant was found to increase the thin film thickness, as also seen with the TTIP prepared samples studied in 3.2.1. This increase in thickness due to surfactant addition was particularly noticeable for multiple layer samples, whereby thin film thickness was increased from an average of 305 nm

(two-layer sample produced without surfactant; CT 2) to 625, 890, 1375, 500, 475, 485 nm for two layer samples prepared with Tween surfactants (samples T60 AT2, T60 BT 2, T40 AT2, T40 BT 2, T20 AT2, and T20 BT2 respectively. The same trend was observed with Brij surfactants, e.g. 940, 395, 515, 815 nm for samples AT 2, BT 2, CT 2 and DT 2 respectively (Table 3.6 and 3.7.) This increase in thin film thickness is due to the role of the surfactant during the gelation stage of sol-gel development. As described previously, during this stage, the surfactant coordinates around the growing titania particles resulting in a more viscous solution. When the substrate is dipped into the sol-gel, a thicker layer is left on the substrate upon removal, resulting in individually thicker TiO_2 layers. As a result, the samples produced with surfactant are on average much thicker, and those produced with the highest concentrations of surfactant produce thicker films, e.g. sample B58 BT3 1905 nm, and B98 AT3 1600 nm.

3.2.2.2 Surface morphology and particle size

Scanning Electron Microscope (SEM) images showed that the use of TiBALD precursor rather than TTIP precursor produced thin films with much greater particle definition, with an overall smaller particle size and shape (figure 3.20 vs 3.1). In addition, the variation of surfactant type and concentration added during processing influenced the resulting morphology of the titania thin films produced, along with the number of layers applied. The addition of subsequent layers resulted in more cracking and agglomeration within the thin film due to the coalescence of particles between layers and the evaporation of excess solvent resulting in shrinkage. This is particularly noticeable through the comparison of two and three-layer samples, whereby three-layer samples show increased agglomeration and reduced definition of particles (Figure 3.13, 3.14 and 3.15).

The average particle size of thin films produced with TiBALD precursor varied between 25-30 nm for samples prepared without surfactant (CT), to 10-15 nm for samples prepared with Brij 98 surfactant (B98 AT2). The addition of surfactant with the TiBALD precursor was found to result in a reduction in particle size, owing to the role of surfactant during the growth phase as described previously, and for differences in the decomposition mechanism as will be discussed later in 3.2.2.8.

3.2.2.3. Thin film morphology: Tween surfactants

Figure 3.14 shows the SEM images of thin films produced using TiBALD precursor with Tween surfactant addition, with figure 3.13 showing SEM images for films prepared without surfactant. The SEM images for samples CT1-CT3 show that the thin film morphology undergoes subtle changes as the number of layers are increased from 1-3, whereby some increased agglomeration and reduced particle definition is observed in sample C3. For this reason, only 2 layer sample SEM pictures are shown in this chapter, with full SEM images of all samples produced with multiple layers are shown for reference in Appendix 1.

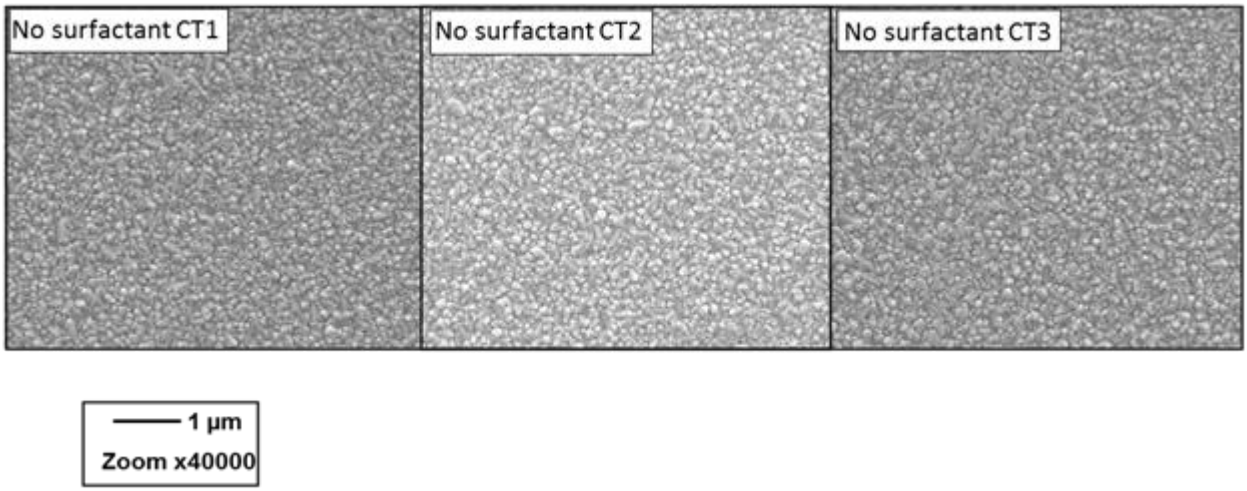

Figure 3.13. SEM images of TiO_2 films produced from titanium bis-ammonium lactato dihydroxide (TiBALD) precursor with no surfactant addition. Films were annealed at 600 °C for 1 hour with a ramp rate of 15°C min^{-1}. Numbers represent number of layers.

The addition of Tween surfactant was found to enhance the thin film morphology by encouraging subtle changes within the thin film (figure 3.14), including the production of slightly smaller, more angular TiO_2 particles. In comparison to the thin films produced without surfactant, as in 3.13, those films produced with the addition of Tween 60 surfactant, (T60 D, A, B) show greater particle uniformity, with a smaller approximated particle size range varying from a maximum of 30-280 nm compared to 30-390 nm for the samples prepared without surfactant. Some cracking and shrinkage is observed due to the higher annealing temperature used (600 ºC, 1 hour) as for T60 AT 2 and T20 BT 2. The use of Tween 40 and Tween 20 surfactant with TiBALD precursor was found to induce a morphology of smaller, more angular TiO_2 particles with reduced agglomeration, whereby the average particle size was found to be 10-15 nm for samples T40/T20

AT and BT. This smaller particle size is due to the role of the surfactant as a pore-directing agent, as previously described.

3.2.2.4. Thin film morphology: Brij surfactants

The addition of surfactant in the TiBALD sol-gel solution produced thin films with greater morphological definition (figure 3.15), with a general reduction in particle size, as seen with the addition of Tween surfactants. In particular, samples prepared with the minimum concentration of surfactant, (4×10^{-4} mol dm^3) showed a reduction in particle size compared to samples produced without surfactant, (10-20 nm vs 25- 30 nm). For example, a single layer sample produced from TiBALD without surfactant (CT), showed an average particle size of 30 nm, whereas a single layer sample produced with 4×10^{-4} mol dm^3 of Brij 98 (BT) showed an average particle size of 10 nm, and that produced with 4×10^{-4} mol dm^3 of Brij 58 (BT) showed an average particle size of 20 nm. This reduction in particle size can be attributed to the role of surfactant during the sol-gel growth phase, whereby the surfactant orients itself around the growing titania and stunts the growth of larger particles.

The SEM images showed that the variation of surfactant type and concentration added during processing influenced the resulting morphology of the titania thin films produced. The number of layers applied also affected the morphology of thin films, whereby the addition of subsequent layers resulted in more cracking and agglomeration due to the coalescence of particles between layers and the evaporation of excess solvent resulting in shrinkage. This is particularly noticeable through the comparison of two and three-layer samples, whereby samples T60 AT2 and T20 BT2 in figure 3.14 and samples B58 AT2/ BT2 have areas of cracking in the film to show underlying layers, whereas the three-layer sample as shown in figure 3.13 shows increased agglomeration and reduced definition of particles.

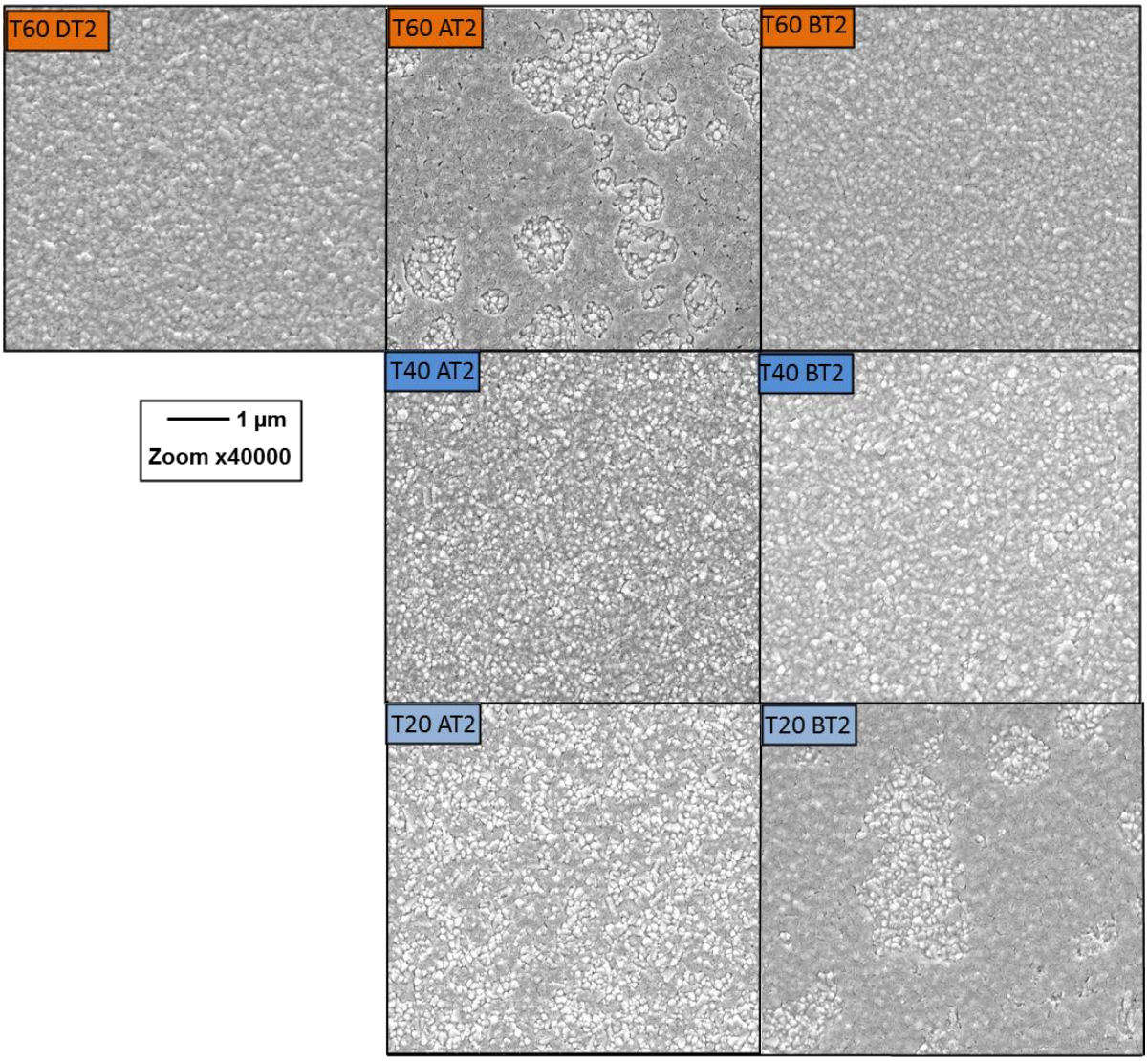

Figure 3.14. SEM images showing two-layer TiO_2 films produced from TiBALD precursor with Tween® surfactant addition; Tween 60 (T60), Tween 40 (T40) and Tween 20 (T20) in concentrations DT= $8x10^{-4}$ mol dm^3, AT = $6x10^{-4}$ mol dm^3, BT = $4x10^{-4}$ mol dm^3. Films were annealed at 600 °C for 1 hour with a ramp rate of 15°C min^{-1}.

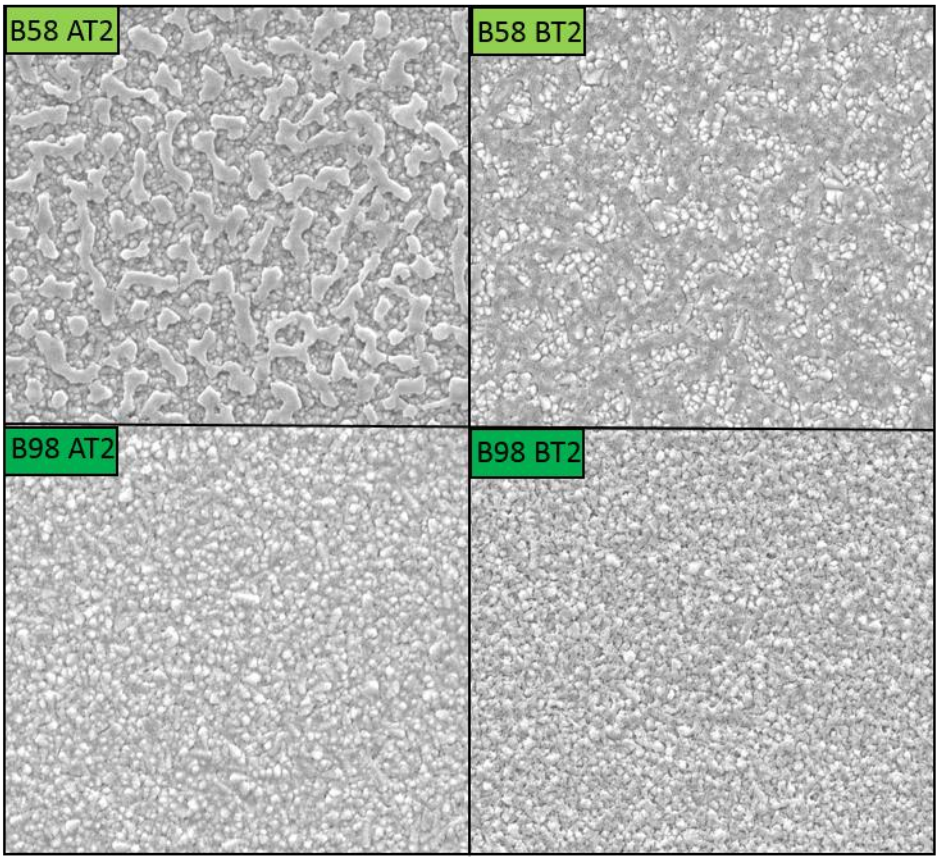

Figure 3.15. SEM images showing two-layer TiO_2 films produced from TiBALD precursor with Brij® surfactant addition; Brij 58 (B58) and Brij 98 (B98) in concentrations AT = $6x10^{-4}$ mol dm^3, and B98 BT = $4x10^{-4}$ mol dm^3. Films were annealed at 600 °C for 1 hour with a ramp rate of 15°C min^{-1}.

3.2.2.5 Surface Roughness

The surface roughness of thin films was measured using atomic force microscopy, whereby an average root mean square (RMS) roughness value was determined for each sample type using RMS values obtained for three randomly selected areas of each sample. The samples analysed varied in roughness from a minimum of 15 nm RMS as for sample T60 DT 3, prepared with Tween 60 surfactant in the highest concentration (8×10^{-4} mol dm^3), with three layers applied; up to a maximum of 216 nm RMS for sample CT 2 produced without surfactant. In contrast to the samples studied in section 3.2.1, the addition of surfactant was found to reduce the average surface roughness, rather than increase it as observed for TTIP samples. However, the samples produced from TiBALD precursor are overall rougher than those prepared from TTIP precursor, as shown in tables 3.6-3.7. The TTIP samples show average RMS values of 15, 14, 17 nm for the 1, 2 and 3 layer samples prepared without surfactant, (table 3.6) whereas the TiBALD samples produced without surfactant show RMS values of 119, 216 and 137 nm for 1, 2 and 3 layer films

respectively. In addition, it can be seen from tables 3.6 and 3.7 and figure 3.16 that as the number of layers within the thin film sample is increased from one to two, the surface roughness slightly increases, with the two layer samples generally exhibiting the highest RMS values, followed by a slight decrease with the three layer samples. This can be attributed to the gelation of individual layers between dipping, due to the particles agglomerating between layers resulting in a smoother top surface overall for the three layer samples.

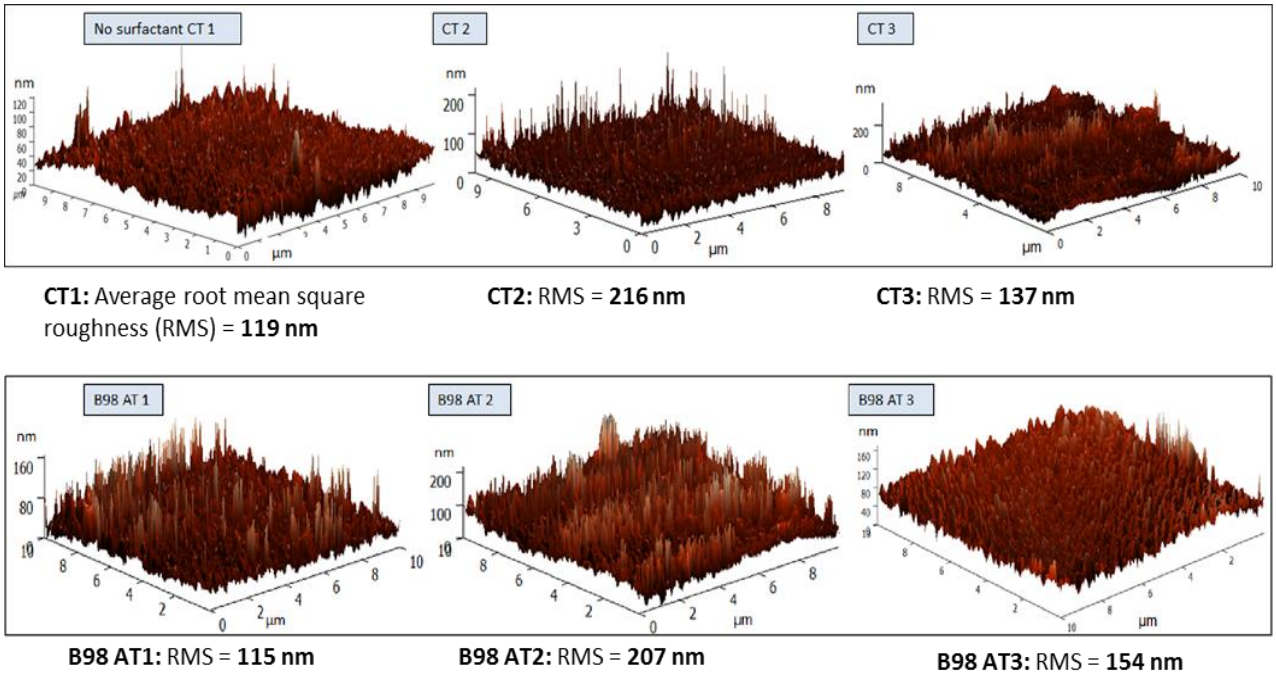

Figure 3.16. AFM 3D surface representation of thin films produced without surfactant (CT 1-3) and with 6 x 10^{-4} mol dm^{-3} Brij 98 surfactant (CT 1-3), with numbers representing number of consecutive layers.

AFM analysis has also revealed a difference in surface topography between the TiBALD samples produced with and without surfactant, whereby samples produced without surfactant (CT 1-3) show a RMS range of 119 -216 nm, depending on the number of film layers. Study of the topographical images in figure 3.16 shows that for the sample prepared without surfactant (CT 1-3) only certain areas across the film surface show these high peaks representing increased RMS roughness of up to 200 nm, thereby indicating that the RMS average has been shifted to a higher value due to the extreme values across the surface. The example shown in figure 3.16 shows a typical topography observed for samples prepared with TiBALD and surfactant, here the example shown is for B98 AT 1, prepared with Brij 98 surfactant in the minimum concentration (4 x 10^{-4} mol dm^{3}). The samples prepared with surfactant show a continual sharp directed growth in the vertical plane that can be observed across the surface, minimising with the addition of a

third layer. The surfactant controls the growth of particles during the sol-gel process, whereby the surfactants align with the growing titanium dioxide particles to result in directed vertical growth and a higher resultant surface roughness.

3.2.2.6. Crystalline phase identification of TiBALD prepared TiO_2 thin films

A representative selection of XRD diffraction patterns of the TiBALD prepared TiO_2 thin films deposited on F: SnO_2 coated glass substrates with and without surfactant addition are shown in figure 3.17 below. As the TiO_2 thin films deposited were thinner than the F: SnO_2 layer (~400 nm), significant breakthrough to the substrate was observed for all samples. The samples exhibited diffraction peaks representing a mixture of anatase, the preferred crystal phase in the [101] plane, in addition to rutile; the more thermodynamically stable phase which was observed in the [211] plane. The presence of brookite was also observed in the [121], [221] and [203] planes.

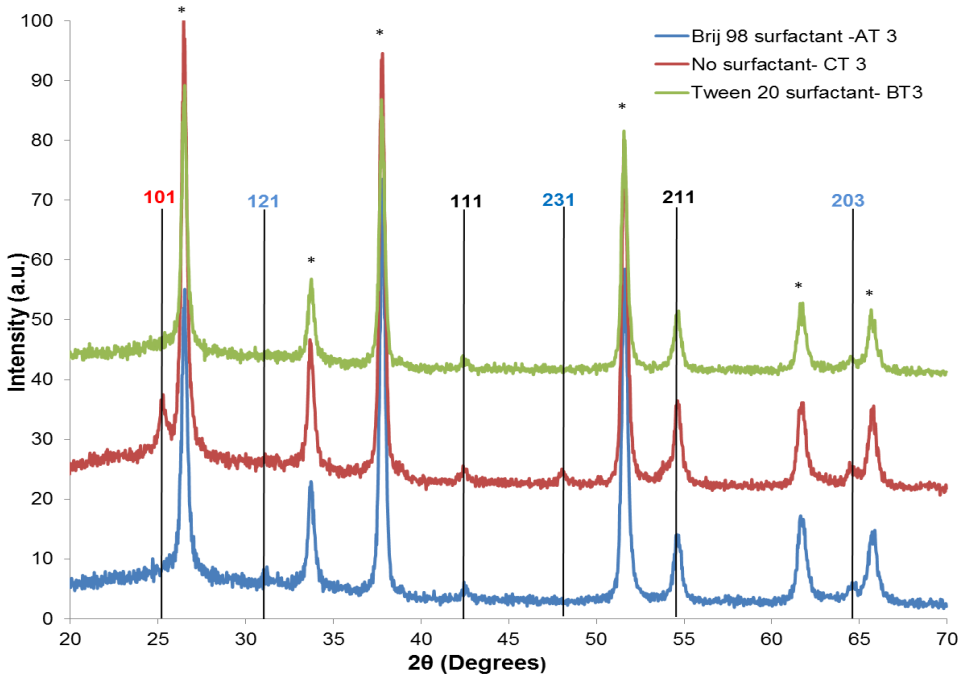

Figure 3.17. Typical XRD patterns for TiO_2 films produced using TiBALD precursor, with and without surfactant addition. Samples are for three-layer samples prepared with Brij 98 surfactant (B98 AT3, $6x10^{-4}$ mol dm^3) (blue line), without surfactant (CT3) (red line), and Tween 20 surfactant (T20 BT3, $4x10^{-4}$ mol dm^3). Peaks identified as anatase are labelled red, brookite blue and rutile black. Peaks denoted with asterisks (*) are assigned to the fluorine-doped tin oxide coating of the glass substrate. XRD are normalised for intensity.

This mixture of phases is commonly observed in the production of TiO_2 derived thin films[29,211] and it is believed that the sol-gel method described herein has resulted in the production of largely amorphous TiO_2 thin films which are poorly detected by XRD. For further determination of the TiO_2 phase, Raman spectroscopy was used, whereby a typical spectrum observed for samples prepared without surfactant, and with Tween and Brij surfactant are shown in figure 3.18. All samples gave strong Raman bands centred at 147, 395, 513 and 642 cm^{-1}, with a weaker band centred at 198 cm^{-1}, all of which are attributable to anatase titanium dioxide indicating that whilst there is poor long range order, anatase predominates over a short range in these TiBALD prepared thin films.[1]

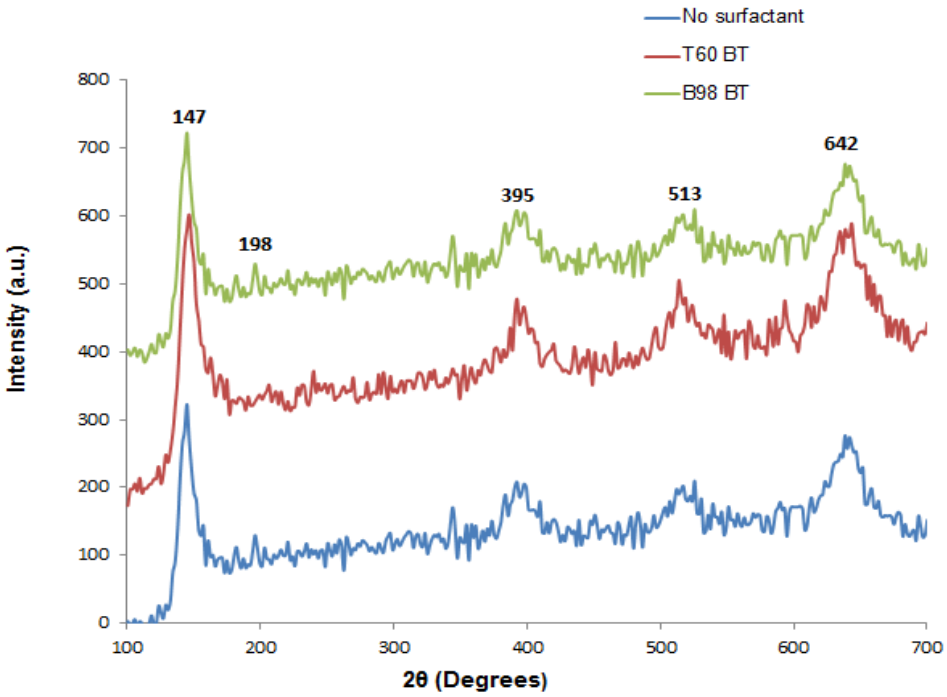

Figure 3.18. Raman spectra of TiO_2 thin film produced from TiBALD precursor. These Raman patterns were typically observed for all samples prepared with TiBALD and modified with surfactant. The samples shown here are for a three layer sample prepared without surfactant (blue), with Tween 60 surfactant (4×10^{-4} mol dm^3) (red), and of Brij 98 surfactant (4×10^{-4} mol dm^3) (green). Raman shifts observed and labelled here correspond to the anatase phase.[1]

3.2.2.8. Results tables for sol-gel samples prepared with TiBALD precursor

Table 3.6. Results table for samples prepared using TiBALD precursor with addition of Tween 60 in three concentrations DT = 0.0008 mol dm^3, A= 0.0006 mol dm^3, B = 0.0004 mol dm^3. Tween 40 and Tween 20, in two concentrations, A and B. Sample C represents the control sample prepared without surfactant. Numbers represent the number of layers. Samples were annealed at 600°C for 1 hour. Values denoted with an asterisk (*) are samples that showed agglomerated particles in SEM images. FQE is the number of dye molecules degraded per incident photon, and FQY is the number of dye molecules degraded per absorbed photon.

Sample Name	Contact Angle (°) before UV irradiation	Contact angle (°) after UV irradiation	Average particle Size (nm)	Approx. particle size range (nm)	Average thin film thickness (nm)	Average RMS surface roughness (nm)	Photocatalytic half- life for Rz degradation (mins)	Calculated rate of photoactivity (dye molecules degraded s^{-1} cm^{-2})	Formal quantum efficiency (FQE)	Formal quantum yield (FQY)
T60 DT 1	43.72	<1	20	30-220	415	20				
T60 DT 2	51.18	<1	20	30-170	310	18	4	7.26×10^{12}	1.12×10^{-3}	1.52×10^{-1}
T60 DT 3	35.85	<1	15	30-220	790	15				
T60 AT 1	22.08	9.06	15	30-170	130	41				
T60 AT 2	21.77	<1	10	30-280	625	61	6	8.80×10^{12}	2.03×10^{-3}	1.72×10^{-1}
T60 AT 3	19.66	<1	20	30-390	2030	18				
T60 BT 1	38.14	<1	15	55-170	870	58				
T60 BT 2	34.85	<1	20	30-280	890	62	4	2.69×10^{12}	6.19×10^{-4}	9.45×10^{-2}
T60 BT 3	32.53	<1	15	55-170	635	41				
CT 1	49.06	<1	30	30-330	270	119				
CT 2	19.40	<1	25	30-390	305	216	3	9.52×10^{12}	2.19×10^{-3}	2.98×10^{-1}
CT 3	28.75	<1	30	30-390	795	137				

T40 AT 1	27.74	<1	15	30-170	300	50				
T40 AT 2	40.81	<1	15	30-220	1375	71	3.5	6.44×10^{12}	1.48×10^{-3}	2.45×10^{-1}
T40 AT 3	43.40	<1	10	55-390	860	50				
T40 BT 1	47.00	3.85	10	30-280	190	69				
T40 BT 2	40.89	2.88	10	30-390	500	61	3	6.35×10^{12}	1.46×10^{-3}	1.80×10^{-1}
T40 BT 3	44.04	3.32	10	30-330	470	69				
T20 AT 1	24.55	<1	10	30-330	440	85				
T20 AT 2	14.64	<1	15	30-280	475	71	2	5.12×10^{12}	1.18×10^{-3}	1.90×10^{-1}
T20 AT 3	16.91	<1	10	30-330	630	16				
T20 BT 1	29.23	<1	10	30-390	435	121				
T20 BT 2	37.68	<1	10	30-330	485	21	3	4.47×10^{12}	1.03×10^{-3}	1.66×10^{-1}
T20 BT 3	41.14	2.26	10	30-390	1845	12				

Table 3.7. Results table for samples prepared using TiBALD precursor with addition of Brij 58 and Brij 98, in two concentrations, A= 0.0006 mol dm^3, B = 0.0004 mol dm^3. Sample C represents the control sample prepared without surfactant. Numbers represent the number of layers. Samples were annealed at 600°C for 1 hour. FQE is the number of dye molecules degraded per incident photon, and FQY is the number of dye molecules degraded per absorbed photon.

Sample Name	Contact Angle (°) before UV irradiation	Contact angle (°) after UV irradiation	Average Particle Size (nm)	Average film thickness (nm)	Average Root Mean Square (RMS) Roughness (nm)	Photocatalytic half- life for Rz degradation (mins)	Rate of Rz reduction (dye molecules degraded s^{-1} cm^{-2})	Formal quantum efficiency (FQE)	Formal quantum yield (FQY)
CT 1	49.06	<1	30	270	119				
CT 2	19.40	<1	25	305	216	3	9.52×10^{12}	2.19×10^{-3}	2.98×10^{-1}
CT 3	28.75	<1	30	795	137				
B58 AT 1	12.19	<1	20	180	124				
B58 AT 2	25.48	<1	20	940	83	4	5.26×10^{12}	1.21×10^{-3}	1.40×10^{-1}
B58 AT 3	20.11	<1	20	900	109				
B58 BT 1	15.63	1.67	10	465	98				
B58 BT 2	14.07	<1	20	395	89	3.5	8.38×10^{12}	1.93×10^{-3}	1.80×10^{-1}
B58 BT 3	12.56	<1	10	1905	85				
B98 AT 1	1.90	<1	30	270	115				
B98 AT 2	10.53	<1	30	515	207	2.5	7.79×10^{12}	1.80×10^{-3}	1.56×10^{-1}
B98 AT 3	8.59	<1	15	730	154				
B98 BT 1	16.42	<1	15	165	98				
B98 BT 2	14.75	<1	10	815	174	3	8.98×10^{12}	2.07×10^{-3}	2.96×10^{-1}
B98 BT 3	12.89	<1	10	1600	151				

3.2.2.7 Functional properties of thin films produced from TiBALD and effects of surfactant addition

All samples produced showed an indirect band gap of 3.2 eV, which was calculated via the Tauc method, thereby indicating anatase as the predominant crystalline phase of titanium dioxide produced.[199] It is generally regarded that in order to produce a TiO_2 material with high photocatalytic activity, there are many structural parameters that must be considered, such as particle size, crystalline phase, surface morphology and surface area.[213] A reduced particle size within a thin film increases the surface area to volume ratio and is often identified as the reason for improved functionality within a thin film such as increased hydrophilicity and enhanced photocatalytic performance properties. All samples produced with TiBALD precursor exhibited superhydrophilicty. This was observed by a decrease in the measured water contact angle after 30 minutes UV irradiation, whereby all thin film surfaces showed a contact angle as low as <1°.

These results show that despite the smaller particle size, photocatalytic performance has not always improved as expected. The samples with the smallest average particle size of 10 nm, such as T20 BT 2 and T40 BT 2 (Tween 20/ Tween 40, 4×10^{-4} mol dm^3) and B98 BT2 (Brij 98, 4×10^{-4} mol dm^3) exhibited slower rates of photocatalytic activity (4.47×10^{12}, 6.35×10^{12} and 8.98×10^{12} dye molecules degraded s^{-1} cm^{-2}, respectively) compared to the sample prepared without surfactant, CT 2, which showed the fastest rate of all samples tested; 9.52×10^{12} dye molecules degraded s^{-1} cm^{-2}. The increased photocatalytic activity observed for CT2 is likely to be a result of the increased surface roughness in the sample, whereby CT 2 shows a large average root mean square roughness of 216 nm, compared to just 61 nm for T40 BT 2 and 21 nm for T20 BT 2. Increased surface roughness on a thin film surface increases the surface area for adsorption of dye molecules to the surface and therefore more sites upon which a photocatalytic reaction can occur. In addition, as CT 2 is the only sample to show the presence of all three TiO_2 crystalline phases via XRD (figure 3.17), it can be suggested that the presence of crystalline anatase has enhanced the photocatalytic performance.

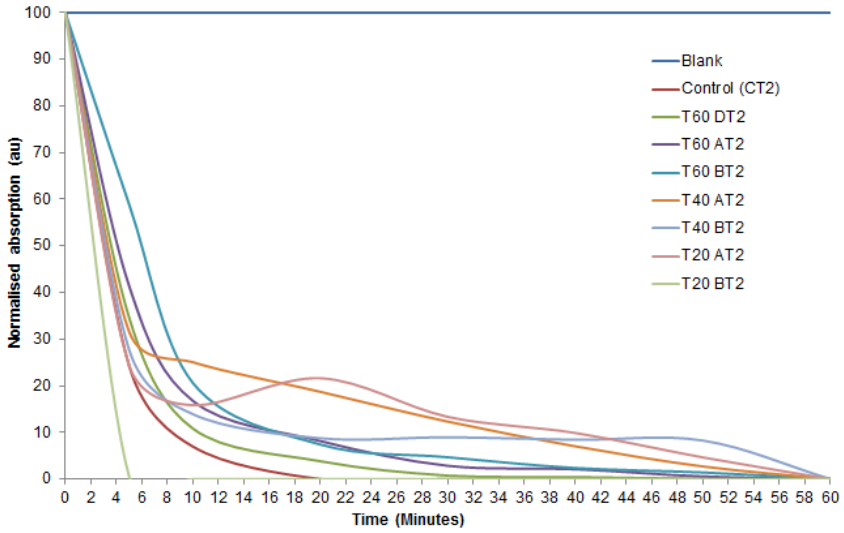

Figure 3.19. Normalised absorption curve used to determine photocatalytic half-life in minutes for samples prepared with TiBALD precursor and Tween surfactants. Control (CT2) sample represents the TiBALD sample prepared without surfactant addition and is used for comparison.

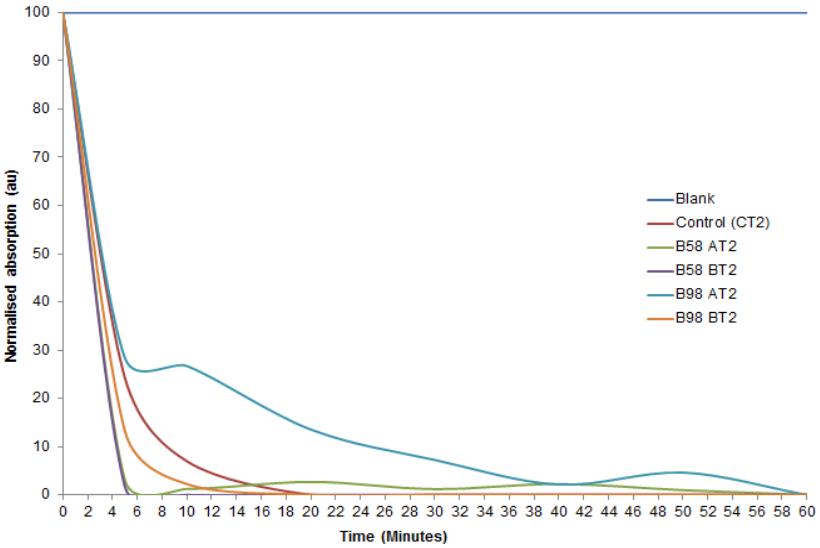

Figure 3.20. Normalised absorption curve used to determine photocatalytic half-life (in minutes) for samples prepared with TiBALD precursor and Tween surfactants. Control (CT2) sample represents the TiBALD sample prepared without surfactant addition and is used for comparison.

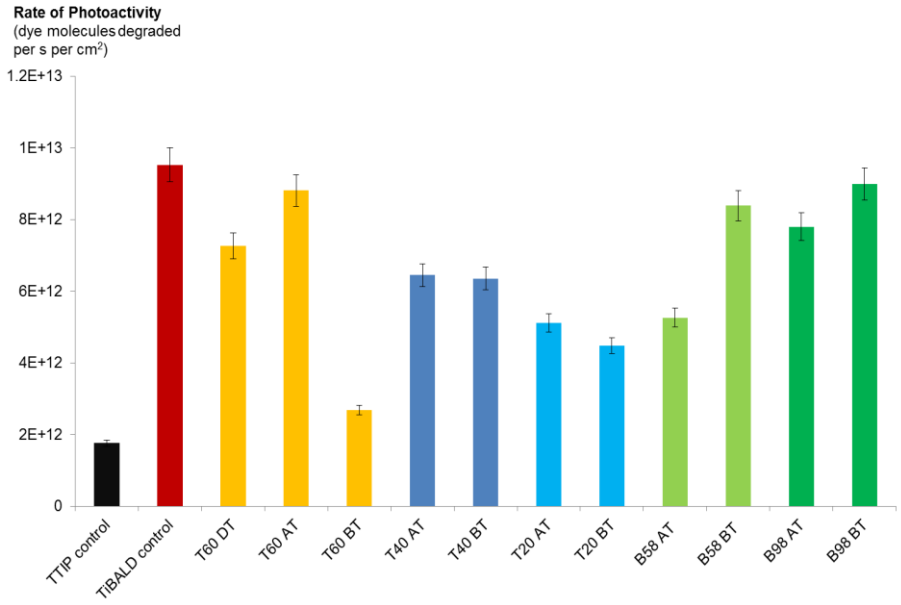

Figure 3.21. Bar chart representing the rate of calculated photoactivity for Resazurin (Rz) dye molecules degraded s^{-1} cm^{-2} for each sample type. Surfactant concentrations are; A = 0.0006 mol dm^3 and B = 0.0004 mol dm^3. Samples represented here are two layer samples. Error bars shown are 5% experimental error.

3.2.2.9 Comparison of TiBALD prepared thin films and TTIP prepared thin films

The use of the TiBALD precursor has been found to greatly increase the thin film thickness compared to films prepared using the traditional precursor, TTIP. The use of TiBALD as an alternative precursor has produced films that are up to five times thicker; 270 nm (TiBALD; CT 2) vs. 40 nm (TTIP C2) for a single layer film prepared without surfactant, as shown in section 3.2.2.8, tables 3.6- 3.7. The average thin film thickness of films prepared from TiBALD precursor showed a variation from 165-1905 nm depending on the type and concentration of surfactant added to the initial sol-gel as well as the number of layers applied. The TiBALD thin films prepared without surfactant showed an average thickness of 270, 305 and 795 nm for the 1, 2 and 3 layer films respectively. In comparison to the TTIP prepared films, which showed average thicknesses of 40, 80 and 90 nm for the 1, 2 and 3 layer films, it can be concluded that the TiBALD precursor produces thicker films overall, which can be attributed to the decomposition mechanism of the individual precursors, as will be discussed further below.

The addition of surfactants was found to further increase thin film thickness to a maximum of 465 nm for a single layer film (prepared from TiBALD precursor with Brij 58 (4×10^{-4} mol dm^3) surfactant) and up to 940 nm for a three-layer film (prepared from TiBALD and Brij 58 (6×10^{-4} mol dm^3) surfactant). Furthermore, the average particle size has been reduced by the use of TiBALD precursor compared to the traditional TTIP precursor, with a reduction in average particle size from 30-45 nm for TTIP prepared films to 25-30 nm for TiBALD prepared films. The addition of surfactant was found in some cases to reduce this particle size even further, e.g. to as low as 10 nm for the TiBALD film prepared with Brij 58 (4×10^{-4} mol dm^3) surfactant (1 and 3 layer). In addition, average surface roughness (root mean square) has been increased from a range of 9-17 nm (TTIP prepared films) to 119-216 nm (TiBALD prepared films) for the films produced without surfactant, whereby surfactant addition with TiBALD precursor was found to produce equally rough films within the ranges of 83-207 nm (table 3.6).

Of main interest in the discussion of these morphological and structural changes when using TiBALD precursor rather than TTIP are the effects that these variations have had on the functional properties of the TiBALD prepared thin films, whereby the rate of average photoactivity for the degradation of resazurin dye has been increased from 1.76×10^{12} dye molecules degraded s^{-1} cm^{-2} as for TTIP (C2) to 9.52×10^{12} dye molecules degraded s^{-1} cm^{-2} for TiBALD (CT 2). The addition of surfactant has been found to slightly hinder this photocatalytic performance, thereby suggesting that in future studies the role of the surfactant with TiBALD may be unnecessary.

The variations observed between the thin films produced using the two precursors; TTIP and TiBALD can be attributed to the differing decomposition mechanisms of hydrolysis and gelation that occur during the sol-gel preparation. It has been widely studied that TTIP follows the metal alkoxide SN2 mechanism as shown in figure 3.22, with three stages; hydrolysis, water condensation and alcohol condensation/polycondensation to form a new phase of metal oxide species, XO-M (or HO-Ti for TTIP) (Figure 3.20).[99] However, due to the high reactivity of the Ti-OH species that is formed from TTIP during this process, hydrolysis often occurs quickly and exothermically without control, leading to undesirable consequences such as the precipitation of titania particles with uncontrolled shape and size. Typically, non-aqueous routes are used to slow down the initial hydrolysis stage, whereby

the titania alkoxy groups are encouraged to be initially replaced by acetate groups to form an alcohol, in the absence of a water species.[69,70,74] The alcohol then undergoes esterification with acetic acid to release water as a by-product. It is this water that is released through esterification or through the direct condensation of the acetate-bonded titanium that then initiates a slower hydrolysis reaction with much more control.

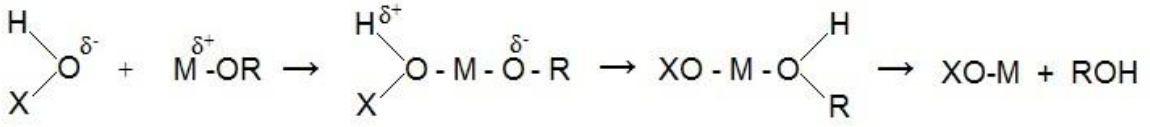

Figure 3.22. Metal alkoxide SN2 hydrolysis mechanism where M= metal (Ti) X = H and R = alkyl group, as for TTIP precursor, R= $\{CH\ (CH_3)_2\}_4$.

In comparison to this, the TiBALD precursor is an ammonium titanium lactate complex, which is stable in aqueous mediums at ambient temperatures. Despite the stability of TiBALD it has been used in very few sol-gel studies for the preparation of titanium dioxide thin films.[205,207,214] Although such previous studies have shown the production of crystalline TiO_2 thin films with discussion relating to the microstructural and morphological effects on the photoactivity of the materials produced, there has been little comparison of how the TiBALD decomposition mechanisms compare to that of TTIP in order to produce this range of different properties. Recent discussions have focused on hydrothermal methods for elucidating the structure of TiBALD as a precursor, and using it to understand the mechanisms of anatase and rutile particle growth, without focus on how this could affect thin film formation.[215,216]

As mentioned, the different physical properties of the precursors result in different decomposition mechanisms, and so the sol-gel reaction of the TiBALD precursor requires a strong acid to initiate hydrolysis, as shown in the proposed mechanism in figure 3.23. The acid catalyses the hydrolysis of the Ti-O linkages within the TiBALD precursor to release the lactate group and form Ti-O-Ti linkages that then undergo subsequent nucleation and growth to form TiO_2 particles.

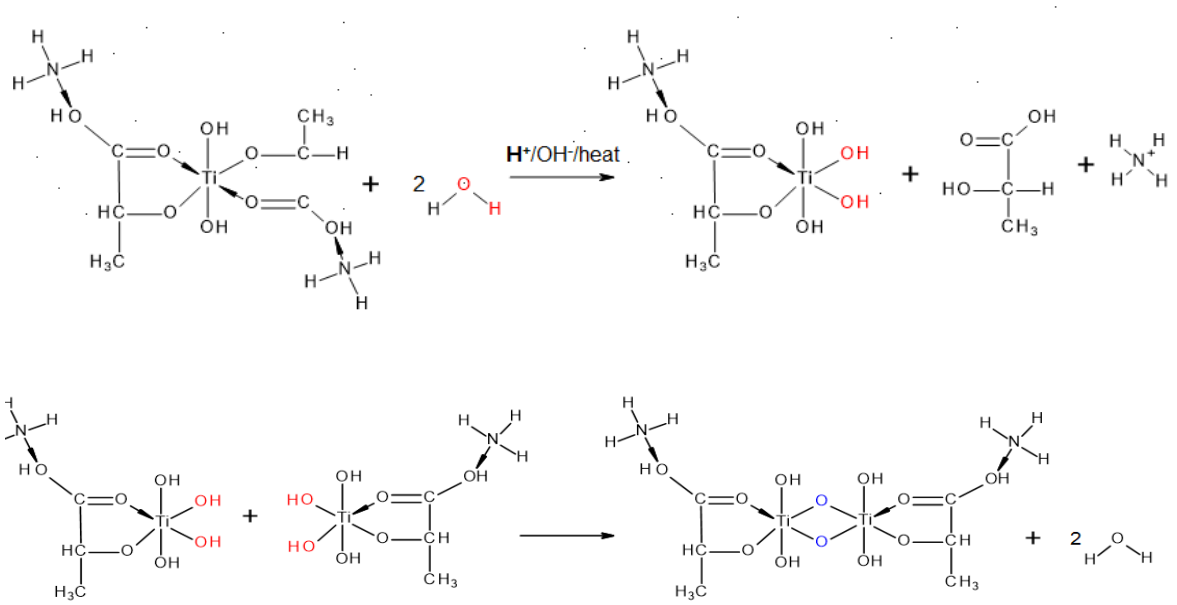

Figure 3.23. Top: Hydrolysis mechanism of TiBALD. **Bottom:** Polycondensation reaction of TiBALD to Ti-O-Ti linkages that subsequently undergo nucleation and growth to form titanium dioxide.

In discussion of the decomposition of TiBALD, Mockel et al[205] have hypothesised that a layer of lactic acid is potentially adsorbed onto the surface of the particles during this process. Our study herein has found that the use of TiBALD has resulted in the formation of smaller average particle sizes (30-45 nm for TTIP prepared films vs 25-30 nm for TiBALD prepared films) and so we can suggest that if this layer of lactic acid does indeed form, it could potentially play a role in hindering the growth of TiO_2 particles; an effect which is then enhanced by surfactant addition. Indeed, surfactants are shown to hinder the growth of the average TiO_2 particle size further to as low as 10-15 nm (sample DT prepared with Brij 98 (4×10^{-4} mol dm^3), table 2. Despite the fact that the reduced particle size observed with TiBALD prepared samples does not result in an increased photoactivity for the degradation of resazurin dye, this small particle size range may be useful for other applications where a reduced particle size is desired. Further studies are required to determine whether reducing the annealing temperature from 600 °C to 500°C enables a reduction in particle size without inducing the anatase-to-rutile transformation which has been observed here. As TiO_2 particles of < 25nm in size are usually attributed to anatase phase,[217] it can be concluded that TiBALD precursor is more likely to produce thin films of anatase phase than TTIP

precursor, and so should be used as a favoured precursor for the preparation of photocatalytically active titanium dioxide thin films.

3.2.2.9 Conclusions: TiBALD

Thin films of photocatalytically active titanium dioxide were deposited using TiBALD as an alternative precursor to TTIP described in section 3.2.1. The effects of surfactant addition was explored for the same surfactant types and concentrations as in section 3.2.1, and the results characterised and analysed using SEM, XRD, Raman spectroscopy and UV/Vis. It was found that although the TiBALD prepared films exhibited higher photocatalytic activities compared to the TTIP prepared films, the addition of surfactant was found to in fact hinder the photocatalytic performance of the thin films. The highest photoactivity was observed for the TiBALD sample prepared without surfactant, exhibiting a rate of 9.52 x 10^{12} (dye molecules degraded s^{-1} cm^{-2}), which is a great enhancement on the similar film prepared without surfactant with TTIP, showing a rate of just 1.76 x 10^{12} (dye molecules degraded s^{-1} cm^{-2}). This enhanced photoactivity has been attributed to the increased film thickness, surface roughness and superhydrophilicity observed in the TiBALD prepared samples.

Chapter 4: Results: Aerosol-assisted chemical vapour deposition of titanium dioxide thin films and the effects of surfactant addition

4.1 Introduction

Aerosol-assisted CVD is a particularly versatile technique for the production of modified TiO_2 thin films. The advantage of this technique for thin film modification lies in the use of an initial precursor solution where the reactants are dissolved in a solvent from which an aerosol is then generated. As a result, the precursor does not need to have specific volatility, and any type of additive could be potentially incorporated into the precursor solution to coordinate with the precursor material as long as it dissolves within the solvent. This has resulted in a broad range of research into the modification of AACVD TiO_2 thin films through the incorporation of additional metal atoms,[202,218,219] either as a method for doping, or forming a composite thin film with the aim to increase absorption of light in the visible range, as seen with gold and niobium.[218,220]

However, the use of more common additives, such as surfactants and templating agents that are widely studied in sol-gel synthesis of thin films, have seen little use in AACVD methods. To the authors' knowledge, there appears to be as yet no published reports on the use of surfactant additives in the production of TiO_2 thin films prepared by AACVD. Kaye et al,[221] have investigated the use of such additives to control the morphology of zinc oxide (ZnO) thin films produced by AACVD, resulting in a range of interesting morphological properties, which are easily encouraged through the use of the surfactant cetyltrimethylammonium bromide (CTAB). Unlike more traditional CVD routes, AACVD offers this unique opportunity where a surfactant additive can be easily introduced into the precursor solution so that it can interact with the precursor or nucleating crystal to directly control of influence morphology of the thin film produced. As a result, this opens up a range of opportunities for tailoring thin films for particular applications, where a specific morphology is desirable.

This chapter focuses on investigating the effect of surfactants in AACVD processing for the production of TiO_2 thin films for photocatalytic applications and for use in semi-transparent dye-solar cells. AACVD is investigated as a method within this thesis as it has the potential

to be scaled up for larger substrate areas within the glazing industry. Following on from the results in chapter 3, the surfactant types and concentrations that showed the most promising photocatalytic performance are investigated. The effects of surfactant addition on a well-studied AACVD route to TiO_2 thin films is investigated, with the use of two different solvents; toluene and dichloromethane (DCM), with Brij and Tween surfactants. Changing the solvent used provides an opportunity to study the potential "solvophobic" effect that can occur with the use of surfactants in non-aqueous media, rather than the micellization effects that occur in aqueous solutions.[222] As TTIP hydrolyses readily in water, non-aqueous solvents; toluene and dichloromethane are used. Both have different polarity indexes, which will result in different growth mechanisms of the thin film, which will be discussed in combination with the surfactant effects within this chapter.

Table 4.0. Surfactant name, corresponding sample name and solvent used with concentration of surfactant added (mol/ dm^3) and deposition temperature.

Surfactant used	Sample Name / Solvent		Concentration of Surfactant (mol/dm^3)	Deposition temperature *(Ramp rate: 15°C min^{-1})*
	Toluene	Dichloromethane		
Nil	TTIP Tol	TTIP DCM	0	
Brij 58	AB58 0.5 t	AB58 0.5 d	0.5	
	AB58 1 t	AB58 1 d	1	
	AB58 2 t	-	2	
Brij 98	AB98 0.5 t	AB98 0.5 d	0.5	
	AB98 1 t	AB98 1 d	1	**Substrate temperature:** 400 °C **Gas Flow rate:** 1L/min^{-1}
	AB98 2 t	-	2	
Tween 20	AT20 0.5 t	AT20 0.5 d	0.5	
	AT20 1 t	AT20 1 d	1	
	AT20 2 t	-	2	
Tween 40	AT40 0.5 t	AT40 0.5 d	0.5	
	AT40 1 t	AT40 1 d	1	
	AT40 2 t	-	2	

4.2. Results: TiO_2 thin films prepared by AACVD

All films produced by AACVD covered the entire surface area of the glass, showing evidence of birefringence which indicates a variation in thin film thickness across the film surface. Birefringence forms through a combination of turbulent gas flow and due to the

temperature gradient across the reactor, where some parts may be hotter or cooler, thus encouraging increased (or decreased) film growth in certain areas. Some carbon incorporation was observed, particularly for those films produced with high concentration of surfactant. All films were robust and passed the scotch tape test. Films all exhibited a band gap of 3.2-3.3 eV as calculated by the Tauc method,[199] corresponding to anatase phase TiO_2. Some representative tauc plots are given in appendix A. The addition of surfactant into the AACVD precursor solution was found to modify the thin film thickness, morphology, particle size, surface roughness, wetting properties and photocatalytic performance of the films produced, as will be discussed in the following sections.

4.2.1. Results: AACVD of TiO_2 thin films from TTIP precursor with toluene as solvent, modified with Tween and Brij surfactant addition

4.2.1.1. Thin film thickness and particle size

The thin films were produced from TTIP precursor with and without surfactant addition, whereby the reaction was run until the entire precursor had been depleted, under a constant gas flow of 1 L min^{-1}, with a constant substrate temperature of 400 °C. The films produced without surfactant showed an average film thickness of 810 nm, as measured through side-on SEM images, on at least three samples. The addition of surfactant was found to modify this average thickness considerably, depending on the surfactant type and concentration used, whereby the thinnest average film thickness was 250 nm as observed for the film produced with the addition of Tween 20 surfactant in a 2 M concentration. In contrast, the thickest average film thickness was 3350 nm, produced from the addition of Brij 98 surfactant in the lowest concentration of 0.5 M. The addition of Tween 40 surfactant was found to reduce the average thin film thickness from 810 nm as for the no surfactant prepared film to 620 nm (0.5 M), 545 nm (1 M) and 605 nm (2M), whereas the addition of Tween 20 in high concentration (2M) was found to produce the thinnest film of all the samples (250 nm). A bar chart for comparison of thin film thicknesses vs concentration and type of surfactant added is shown in figure 4.0.

A potential explanation for the observed reduction in film thickness with the addition of some surfactants could be due to the different molecular weights of the surfactants used and the effect that these heavier surfactants have on the film growth process. As described in

chapter 1 section 2.4, surfactants can form a variety of micelle-type structures within solution, owing to the polar head and non-polar tail within the molecule, as long as they are above the critical micelle concentration (CMC). The critical micelle concentration is defined as the concentration of surfactants above which micelles form and all additional surfactants added to the system form micelles.[223] As shown by table 4.1, the surfactant concentrations used within this study are more than the CMC, thus it is assumed that micelles are formed in all aqueous solutions.

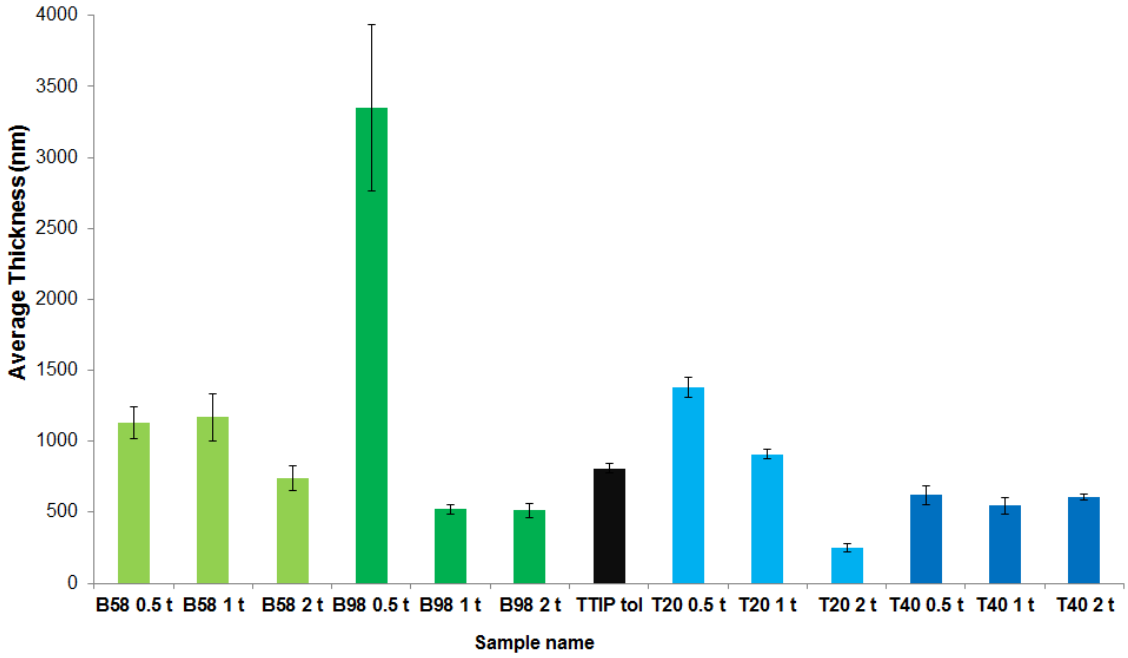

Figure 4.0. Bar chart comparison of the average thin film thickness of thin films prepared by AACVD with TTIP precursor and toluene as solvent, with increasing concentrations of surfactants of different types, indicated by colours. The reactions were run until the entire precursor had been depleted, at a constant gas flow of 1 L min^{-1}. Error bars show the standard deviation. Numbers represent the molar concentration from 0.5 M – 2 M.

Heavier surfactants are likely to interact differently with the TTIP precursor molecule during thin film growth to inhibit the deposition of a thick film. The Tween surfactants have a higher molecular weight compared to the Brij surfactants as shown in table 4.1, where Tween 20 = ~1228 g/mol, Tween 40 = ~1277 g/mol vs. Brij 58 = ~1124 g/mol, Brij 98 = ~1150 g/mol. As the concentration of surfactants used here is relatively low, the system is

most likely to contain simple surfactant species, such as monomers and basic surfactant aggregates (micelles), rather than more elaborate structures that typically form at higher surfactant concentrations. Tween surfactants are actually regarded as emulsifying surfactants, whereby they have the tendency to form larger aggregates called mesophases where one or two dimensions of the structure is highly extended. As micelles are too small to scatter significant quantities of light, solutions with surfactant micelles appear transparent, whereas solutions with surfactant mesophases are typically opaque.[224] All precursor solutions remained transparent throughout the AACVD deposition process, thus indicating that no such complex aggregates were formed, or that the TTIP precursor had undergone precipitation.

As a result the surfactant micelles would surround the TTIP precursor and solvent in the aqueous solution before they are carried to the reaction chamber as a fine aerosol droplet. After this droplet lands upon the heated substrate, the surfactant is coordinated to the TTIP precursor in a micelle type structure thus stunting and blocking the growth of TiO_2 particles on the surface, producing a thinner, more compact film due to the restricted growth. With heavier surfactant (thus larger) micelles surrounding the TTIP precursor it is believed that the resulting growth of the film is inhibited as nucleation sites are prohibited from joining up due to the presence of the surfactant. As a result, smaller crystallites of TiO_2 also form, and the resulting film is thinner as the growth mechanisms are blocked by the presence of the surfactant.

Table 4.1. Surfactant types with their molecular weight, density, critical micelle concentration (CMC) and hydrophilic-lypophilic balance (HLB).[225–229]

Surfactant Name	**Molecular Weight** *(g/mol)*	**Density** *(kg/m^3)*	**Critical Micelle Concentration (CMC)** *(mM)*	**Hydrophilic-Lipophilic Balance (HLB)**
Brij 58	~1124	*Solid*	0.080	15.7
Brij 98	~1150	*Solid*	0.025	15.0
Tween 20	~1228	1095	0.060	16.7
Tween 40	~1277	1080	0.027	15.6

Furthermore, this argument can be extended to explain why the addition of higher concentrations of surfactant (particularly 2 M concentrations) was found to reduce the

average thin film thickness from 810 nm for films produced without surfactant to as low as 250 nm as for Tween 20 (2 M), 515 nm as for Brij 98 (2 M), 605 nm as for Tween 40 (2 M) and 740 nm for Brij 58 (2 M). The phase behaviour of more concentrated surfactant solutions is complex and strongly influenced by the molecular geometry of the surfactant.[230] With a higher concentration of surfactant, surfactant solutions are in instantaneous equilibrium with respect to micelle, or other structure formation, whereby the conditions (such as degree of dilution, or temperature of the solution) can affect the structures that form.[224] As a result, with higher concentrations of surfactant these blocking effects may be enhanced due to the formation of larger surfactant aggregates within the higher temperatures of the reactor chamber, and further stunting of thin film nucleation and growth occurs.

The hydrophilic-lipophilic balance of a surfactant is a measure of the degree to which the molecule is hydrophilic or hydrophobic (lipophilic). This method was originally developed by Griffin in 1949 whereby the scale ranges from 1-20,[231] with lower HLB values (<10) indicating more hydrophobic (lipophilic) molecules, and higher HLB values (>10) indicating more hydrophilic molecules. A high HLB value indicates a large percentage of polar head groups, whereby the surfactant behaves in a dominantly hydrophilic way. These type of surfactants will readily partition into any aqueous phases present.[229] As the surfactants used within this study have relatively high HLB values, it is assumed that they behave in a hydrophilic way and thus help to solubilise the solution.

The particle size for the thin films produced was determined as an average value by analysing SEM images with Image J software. As can be seen in the SEM images shown in figure 4.1, for the addition of Tween surfactant, and in figure 4.2 for the addition of Brij surfactant, most of the particles produced are not perfectly cylindrical or particularly elliptical, and as a result this measurement of average particle size is taken only as a guide to the rough size of particles in order to make a comparison between films produced. The addition of surfactant was found to reduce the average particle size, from 110 nm for the film produced with TTIP and toluene without surfactant addition, to as low as 30 nm for the sample produced with Tween 40 surfactant in a 0.5 M concentration. The only film to show an increase in average particle size was observed for the film produced with Brij 58 surfactant in a high concentration of 2 M. This film is also the only film produced to show only rutile phase present, whereby rutile films typically exhibit a much larger particle size. The reasons for reduced particle sizes with the addition of surfactant have been discussed in

chapter 3 extensively, whereby the same explanations can be given here. The coordination of the surfactant with the TTIP precursor molecule means that the growth of the TiO_2 particle is stunted, resulting in a smaller average particle size.

4.2.1.21. Thin film morphology: Tween surfactants

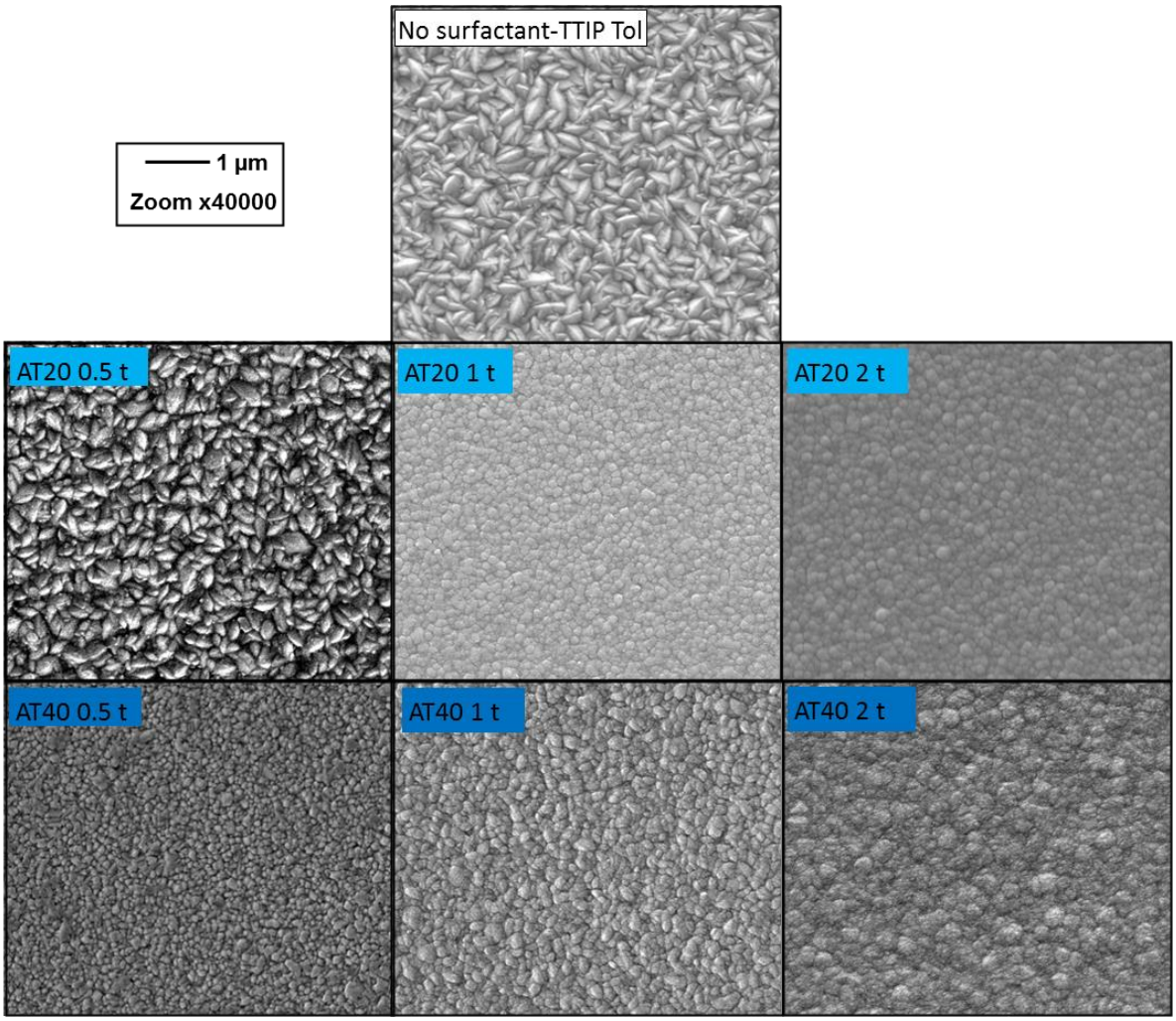

Figure 4.1. SEM images of TiO_2 thin films produced via AACVD with TTIP as precursor, toluene as solvent, with Tween 20 and Tween 40 surfactant addition in concentrations 0.5 M to 2 M. Films were deposited at 400 °C.

The addition of surfactants in the aerosol-assisted chemical vapour deposition of TTIP in toluene was found to alter the morphology of resulting films produced with differences observed depending on the surfactant type and concentration used. The thin films produced without surfactant exhibited a morphology consistent with that observed for films produced in previous AACVD experiments with this particular precursor combination,[30] with rice-like

particles observed in random orientations across the thin film surface. As seen in figure 4.1, the addition of Tween surfactant results in these rice-like particles becoming more circular, whereby it can be seen from the SEM image of the film obtained with the lowest concentration of Tween 20 (0.5 M) that the addition of Tween 20 in this low concentration has resulted in curvature of the edges of the rice-like particles. Increasing the concentration of Tween 20 0.5 M through to 2 M results in a reduction in the particle size, from an average of 75 nm for Tween 20 0.5 M to 50 nm for Tween 20 1 M and 2 M. This is consistent with previous discussions about the surfactants role in stunting and controlling the TiO_2 particle growth. A similar affect is observed for morphological changes induced by the addition of Tween 40; however these films appear to show no similarity to the films produced without surfactant, whereby there is no trace of the rice-like particle shape even with the low concentration of Tween 40 (0.5 M). As Tween 40 is a heavier surfactant, it can be suggested that this has resulted in increased stunting of TiO_2 particles compared to Tween 20. This is observed through much smaller particle sizes in the SEM images in figure 4.1, and confirmed by the reduction in average particle size as calculated from Image J analysis. The average particle size for the Tween 40 0.5 M concentration is just 30 nm, the lowest value observed for all samples produced.

4.2.1.22. Thin film morphology: Brij surfactants

The addition of Brij surfactants in the AACVD of TTIP in toluene was found to produce thin films with several different morphologies, compared to the plain film (TTIP tol) produced without surfactant as seen in figure 4.2. The addition of Brij 58 has resulted in more circular particles being formed, whereby a selection of random sizes are observed for the sample produced with 0.5 M of Brij 58, with an average of 80 nm. This average particle size decreases to 70 nm with the 1 M concentration of Brij 58, whereby much smaller particles are observed which appear to all be of a similar size. The highest Brij 58 concentration of 2 M has produced the most inconsistent morphology with agglomeration and poor definition of particles with the largest average size of 150 nm.

The addition of Brij 98 surfactant has produced thin films with a more unusual morphology, whereby sharp, thin rice-like shapes are observed for the Brij 98 0.5 M sample, with an average size of 40 nm. These rice shapes become more rounded with the increase Brij 98 concentration (1 M) where an average particle size of 70 nm is observed, where some

particles are pointed and some are circular in nature. The Brij 98 2 M sample then shows only rounded particles observed, with a small average particle size of again 70 nm.

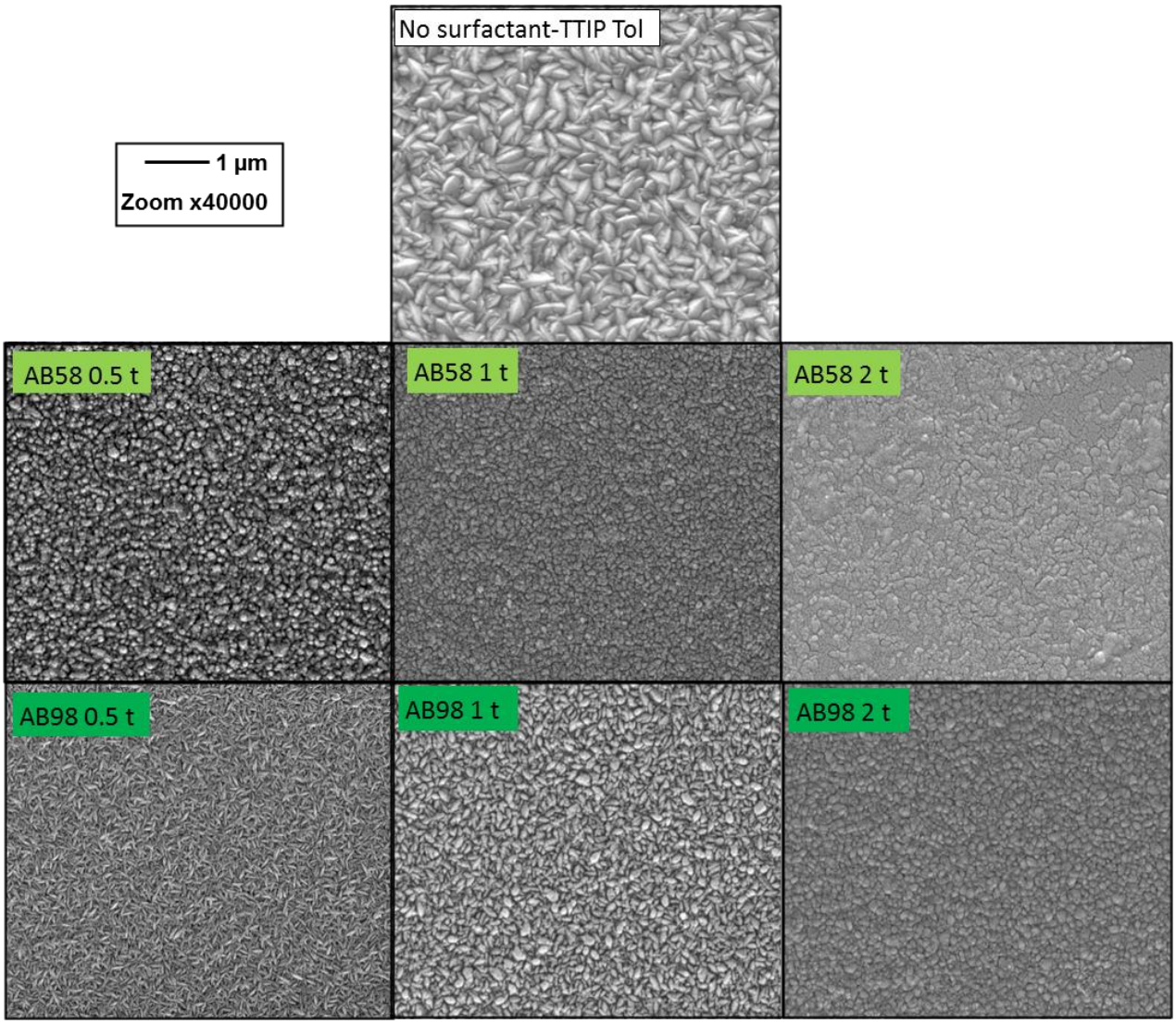

Figure 4.2. SEM images of TiO_2 thin films produced via AACVD with TTIP as precursor, toluene as solvent, with Brij 58 and Brij 98 surfactant addition in concentrations 0.5 M to 2 M. Films were deposited at 400 °C.

4.2.1.3 Surface roughness and wetting properties

The addition of surfactant was found to generally reduce the average surface roughness of the thin films produced by AACVD with toluene solvent, as shown in table 4.2. The roughness is quoted as an average of the root mean square roughness values obtained for three areas across the thin film surface, repeated for at least two thin film samples. The average roughness for the thin produced without surfactant was found to be 134 nm, whereby the lowest surface roughness of all samples was observed for the thin films

produced with Brij 98 surfactant in 2 M concentration. The increased surfactant concentration has been found to increase the particle size and agglomeration between particles, thus creating a smoother overall thin film surface. The highest surface roughness was observed for the Tween 40 sample prepared in lowest concentration (0.5 M) at 155 nm. This sample also has the smallest average particle size of 30 nm, thus demonstrating a correlation between small particle size and high surface roughness due to the variations in the surface caused by the increased surface area to volume ratio.

These reduced roughness values correlate with the larger particle sizes as seen in SEM images in figure 4.1 and 4.2, whereby the rice-like morphology observed for the sample produced without surfactant (TTIP tol) shows a high surface roughness (134 nm) and large particle size (110 nm). The samples with more circular particles, particularly the high surfactant concentration (Brij 58 2 M, Brij 98 2M, Tween 20 2 M and Tween 40 2 M) show reduced average surface roughness values (52 nm, 20 nm, 68 nm and 32 nm respectively) that correlate with the larger particle sizes (150, 70, 50 and 50 nm respectively.) The values for surface roughness and particle sizes are given in table 4.2.

The samples prepared with Brij 58 and Brij 98 appear to show the highest average surface roughness values, whereby those produced with the lower concentrations of 0.5 M and 1 M show average roughness values between 121 nm up to 153 nm. The SEM images for these samples shown in figure 4.2 also show this greater variation in particle size and shape which produces a greater topographical variation across the sample surface and thus a higher surface roughness due to the increased surface area to volume ratio. The surfactant plays a significant role in the growth of TiO_2 particles as found with the sol-gel studies described in chapter 3. The surfactant can either act to reduce particle size and increase surface roughness as for sample T40 0.5 M (particle size 30 nm and RMS 155 nm), or it can work to significantly increase particle size and decrease surface roughness, as observed for the samples prepared with the higher concentration of 2 M, e.g. B58 2 M, particle size 150 nm and RMS 52 nm. The way in which the surfactant behaves can depend on a number of factors including temperature, pH, other reactants present and primarily, the concentration of surfactant used. It is likely that there is an optimum concentration of surfactant addition which can enable films to be produced with the desirable characteristics such as reduced particle size and higher surface roughness. From the studies herein it is likely that this

optimum concentration lies somewhere between 0.5 M and 1 M for the surfactants studied herein.

The wetting properties of the AACVD prepared thin films have been shown to vary considerably depending on the surfactant type used as seen in table 4.1. All AACVD thin film samples exhibit relatively small contact angles with water (less than or equal to 90 °) therefore indicating high wettability, apart from one sample produced with Brij 98 surfactant (0.5 M) which shows a high contact angle of 119 °, which is hydrophobic, verging on the super hydrophobic scale (contact angle greater than 150 °).[232] The samples prepared without surfactant show a small average contact angle of 67 ° which is reduced to just 4 ° after 30 min UV irradiation, thus indicating the surface becomes superhydrophilic (< 5°) with irradiation. The addition of Tween surfactants was found to reduce the hydrophilicity of thin films after UV irradiation, whereby the samples prepared with Tween 20 and Tween 40 showed average contact angles of between 58 ° to 88° before UV irradiation, and 13 to 47 ° after. Only one sample, Tween 20 1M, was found to be very hydrophilic after UV irradiation, with a contact angle reduction from 60° before to 4 ° after.

The samples produced with Brij surfactants shown a variation of contact angles observed that seem to follow no particular trend, apart from the samples produce with the lowest surfactant concentration of 0.5 M which show a significant drop in contact angle after UV irradiation as observed for the plain TTIP Tol sample prepared without surfactant. For example, Brij 58 0.5 has an initial contact angle of 52 ° and becomes hydrophilic after UV irradiation, falling to 4 °. The Brij 98 0.5 M sample is initially hydrophobic (119 °) with the contact angle falling to 10 ° after UV irradiation. These differences in wetting properties are largely related to the particle size and orientation, as well as the average surface roughness of the thin films. With a higher surface area to volume ratio which results from smaller particles in more random orientations, the thin film surface becomes rougher, and thus more hydrophilic whereby the water droplet can penetrate the gaps in between the particles. The opposite is true for samples which have larger particle sizes and low roughness, e.g. sample B98 2M exhibits minimal hydrophilicity (an initial contact angle of 87 ° which becomes 34 ° after UV irradiation. This corresponds with a relatively high particle size of 70 nm with an agglomerated morphology, and a very low surface roughness of just 20 nm RMS.

Table 4.2. Results for samples prepared by AACVD using TTIP in toluene with the addition of surfactant in the precursor solution. Three concentrations of surfactant were used, 0.5 M to 2 M. Sample C represents the control sample prepared without surfactant. Samples were deposited 400°C until all of the precursor solution was depleted.

Sample Name	Contact Angle (°) before UV	Contact angle (°) after UV	Average particle size (nm)	Average film thickness (nm)	Average RMS surface roughness (nm)	XRD predominant phase	Texture Coefficient	Average Crystallite Size (nm)	Photocatalytic half-life for Rz degradation (mins)	Calculated rate of photoactivity (dye molecules degraded s^{-1} cm^{-2})
A B58 0.5 t	52	4	80	1130	134	Anatase	2.70 (004)	11	3	9.50×10^{14}
A B58 1 t	62	<1	70	1170	121	Anatase	2.94 (004)	7	4.5	2.49×10^{13}
A B58 2 t	*57*	*11*	*150*	*740*	*52*	*Rutile*	*4.00 (211)*	*12*	*12*	*3.61×10^{13}*
A B98 0.5 t	119	10	40	3350	97	Anatase	2.75 (004)	5.5	6	1.08×10^{14}
A B98 1 t	32	31	70	520	153	Anatase	2.88 (004)	9.5	4	4.50×10^{13}
A B98 2 t	87	34	70	515	20	Anatase	2.56 (004)	9	10	3.69×10^{13}
TTIP Tol	67	4	110	810	134	Anatase	1.46 (004)	7.5	5	3.88×10^{13}
A T20 0.5 t	76	13	75	1380	92	Anatase	2.96 (004)	10.5	33	8.94×10^{12}
A T20 1 t	60	5	50	910	51	Anatase	3.00 (004)	9	6	7.56×10^{12}
A T20 2 t	46	47	50	250	68	Anatase	3.23 (004)	13	22	1.13×10^{13}
A T40 0.5 t	88	31	30	620	155	Anatase	2.87 (004)	9	9.5	3.27×10^{13}
A T40 1 t	58	41	60	545	75	Anatase	3.05 (004)	8	13	1.82×10^{13}
A T40 2 t	62	39	60	605	32	Anatase	2.97 (004)	12	5	9.75×10^{12}

4.2.1.4 Crystalline phase identification of TiO_2 thin films

The XRD diffraction patterns of the TiO_2 thin films produced by AACVD with TTIP precursor and toluene as solvent are shown in figure 4.3 for the addition of Tween surfactants and 4.4 for the addition of Brij surfactants. The TiO_2 thin films deposited show breakthrough to the underlying cassiterite substrate for all samples, with these peaks identified on the XRD diffraction patterns with an asterisk. The samples analysed produced a range of diffraction peaks associated to the presence of the anatase phase, with a dominant crystal growth typically observed in the [101] plane and [004] planes. The [101] anatase phase is typically the most thermodynamically stable anatase face and is frequently observed in the production of titanium dioxide thin films.[233]

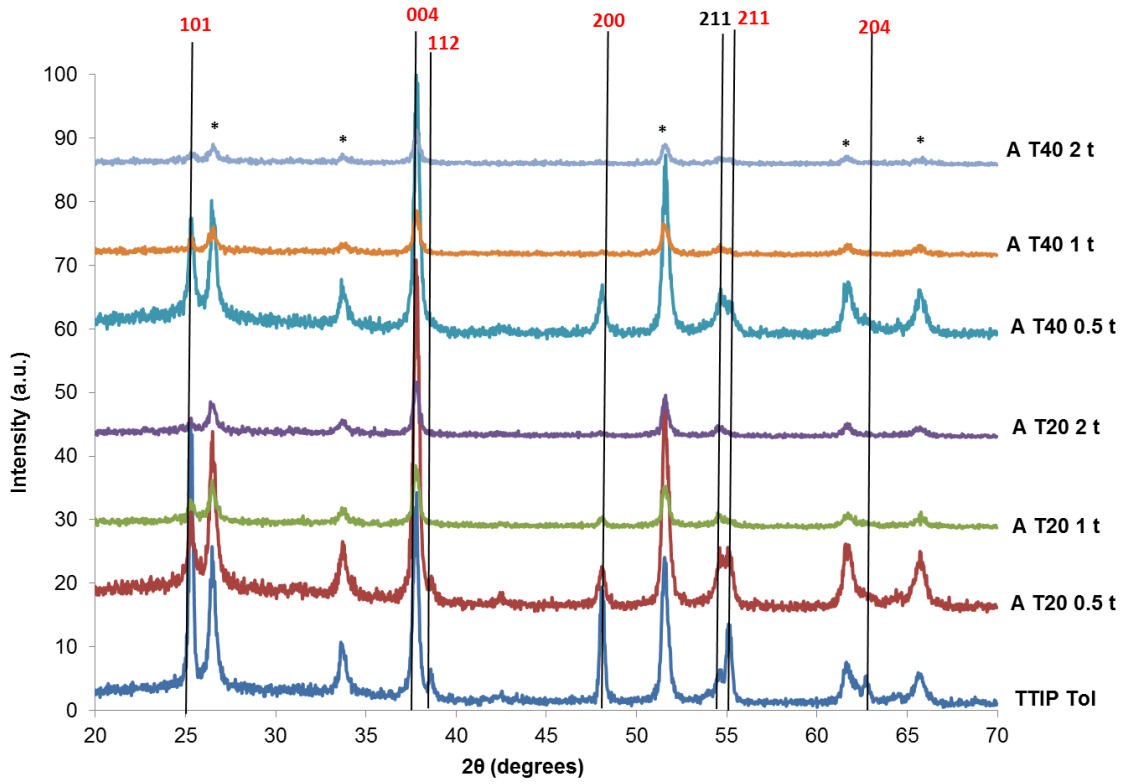

Figure 4.3. XRD for TiO_2 films produced by AACVD using TTIP precursor in toluene solvent, without surfactant (**TTIP Tol**) and with addition of Tween surfactants; **Tween 20** 0.5 M (A T20 0.5 t), 1 M (A T20 1 t), 2 M (A T20 2 t) and **Tween 40**; 0.5 M (A T40 0.5 t), 1M (A T40 1 t), 2 M (A T40 2 t). Peaks identified as anatase phase are marked in red and rutile in black. Peaks denoted with asterisks (*) are assigned to the F:SnO_2 coating of the glass substrate. XRD spectra are normalized for intensity.

The bulk unit cell of anatase and the [101] and [004] planes are shown in figure 4.5, and the truncated tetragonal bipyramid crystal form of anatase TiO_2 is shown in figure 4.6. Some samples also showed the presence of rutile, which is more thermodynamically stable than anatase, and often forms at temperatures in excess of 600 °C.[47] In this instance, rutile was observed at AACVD deposition temperatures of 450 °C, which would appear well below the transition temperature of anatase to rutile. However, due to the nature of the CVD reactor, temperature within reaction chamber is hard to control and monitor, due to ambient temperature fluctuations and the limitations in accuracy of monitoring equipment used. Thus, it is possible that at times fluctuations in temperatures may encourage the formation of rutile as present here. Unusually, rutile is only observed in low intensities in the [211] plane which is an uncommon plane of rutile to be observed. However a mixture of phases is commonly observed in the production of TiO_2 thin films by CVD.[29,211]

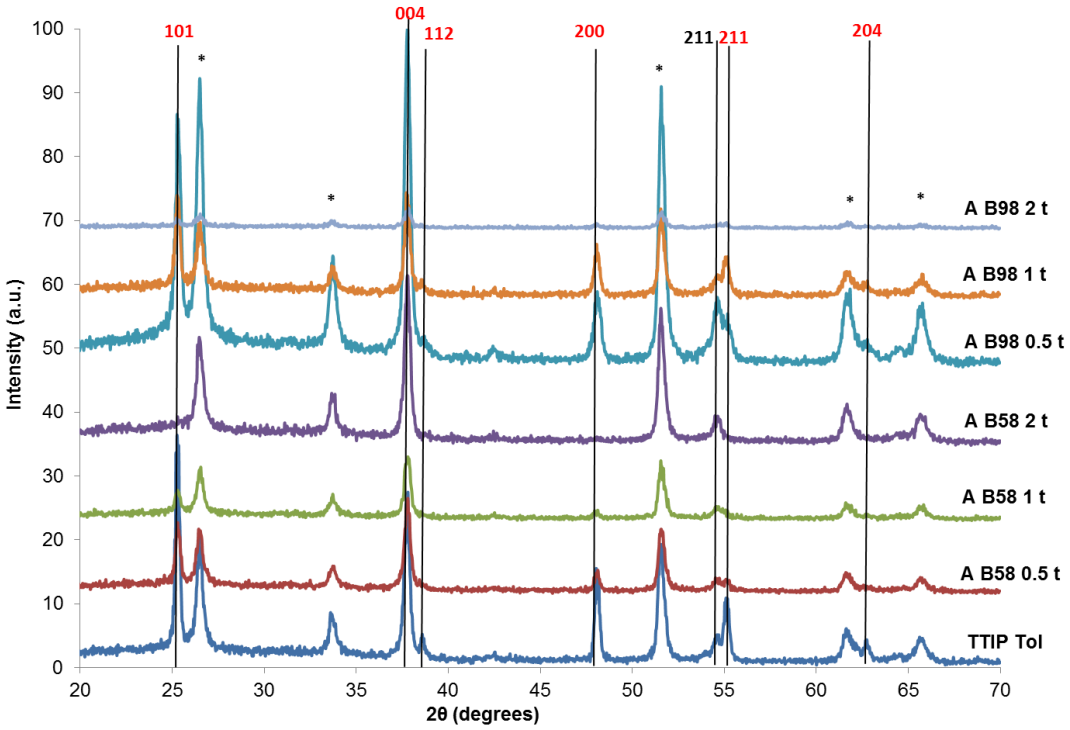

Figure 4.4. XRD for TiO_2 films produced by AACVD using TTIP precursor in toluene solvent, without surfactant (TTIP Tol) and with Brij surfactant addition; **Brij 58** 0.5 M (A B58 0.5 t), 1 M (A B58 1 t), 2 M (A B58 2 t) and **Brij 98**; 0.5 M (A B98 0.5 t), 1M (A B98 1 t), 2 M (A B98 2 t). Peaks identified as anatase are marked in red and rutile marked in black. Peaks denoted with asterisks (*) are assigned to the F:SnO_2 coating of the glass substrate. XRD normalised for intensity.

All films produced were found to exhibit texture, whereby there is a distinct distribution of crystallographic orientations within the sample, with a preferential orientation observed in all. All thin films produced showed anatase as the predominant crystalline phase, with preferential orientation in the [004] plane, with one exception; the thin film produced with Brij 58 surfactant in 2 M concentration, which showed only rutile phase present with preferential orientation in the [211] plane. The texture coefficient and average crystallite size (nm) were determined using the XRD diffraction patterns shown in figures 4.3 and 4.4.

The texture coefficient (TC) describes the orientation of the crystal growth, and how strong the film growth is along that specific crystal facet. When the TC is greater than 1.5 it typically means the crystal structure is oriented, whereas a TC of 3-4 or higher is regarded as strongly oriented.[234] The texture coefficient in the [004] plane for the TiO_2 thin film prepared without surfactant, (TTIP tol) as seen in figure 4.4, was the lowest for all the samples produced; 1.46, however the film can still be regarded as oriented in this plane. The addition of surfactant has been observed to increase the texture coefficient from 1.46 to a range of 2.70 to 3.05, with the highest TC (3.05) observed for the sample prepared with 1 M of Tween 40 (A T40 1 t). This increase in texture coefficient is a result of the surfactant role during thin film growth.

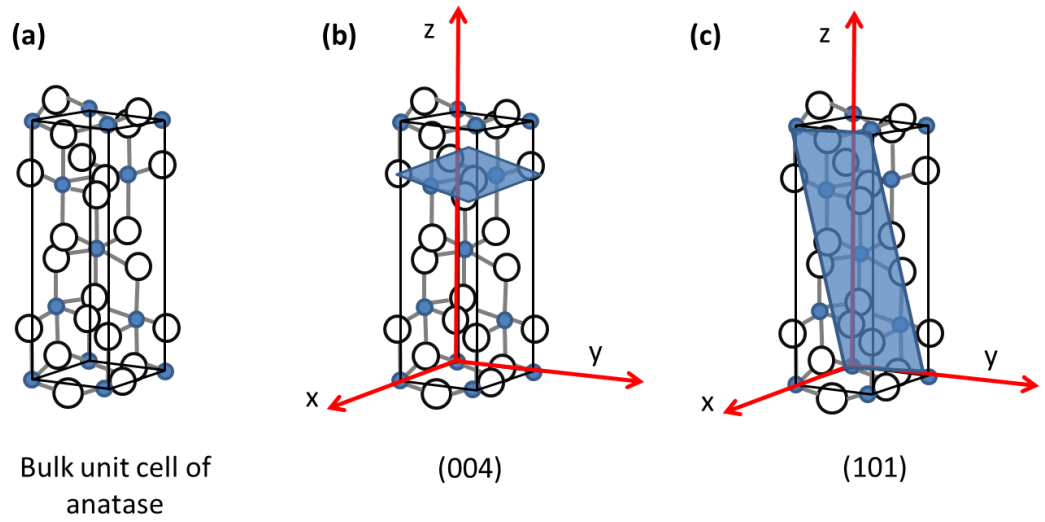

Figure 4.5. (a) Unit cell structure of anatase titanium dioxide, with the lattice planes directed in the (004) plane **(b)** and (101) plane **(c)**.

As the non-ionic surfactants added during this process have a polar, but uncharged head, they are unable to form bonds with the growing titania crystals, but it is possible that due to their polar

nature they have a slight electronegative charge that enables them to bind electrostatically to one particular crystal surface, as shown in figure 4.5. Thus, if one surface of the crystal lattice has more surfactant "bound" to it, less growth in that direction is observed, as and a truncated crystal as shown in figure 4.4 (c) is observed, where the crystal growth is more pronounced in one direction.

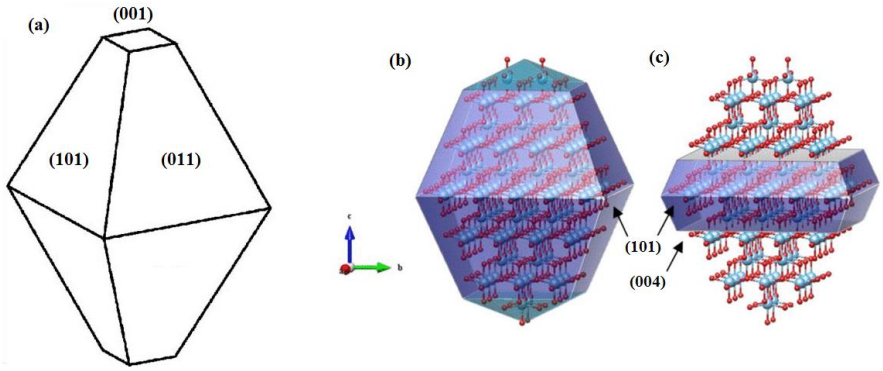

Figure 4.6.(a) The truncated tetragonal bipyramid crystal form of anatase TiO_2, showing the (101), (001) and (011) facets as modified from Diebold et al[233] **(b)** Crystal representation of TiO_2 anatase without the 004 plane and with the (004) plane **(c)**, modified as seen in Ali et al, whom reserve all rights.[235] Blue circles represent titanium atoms, and red represent oxygen.

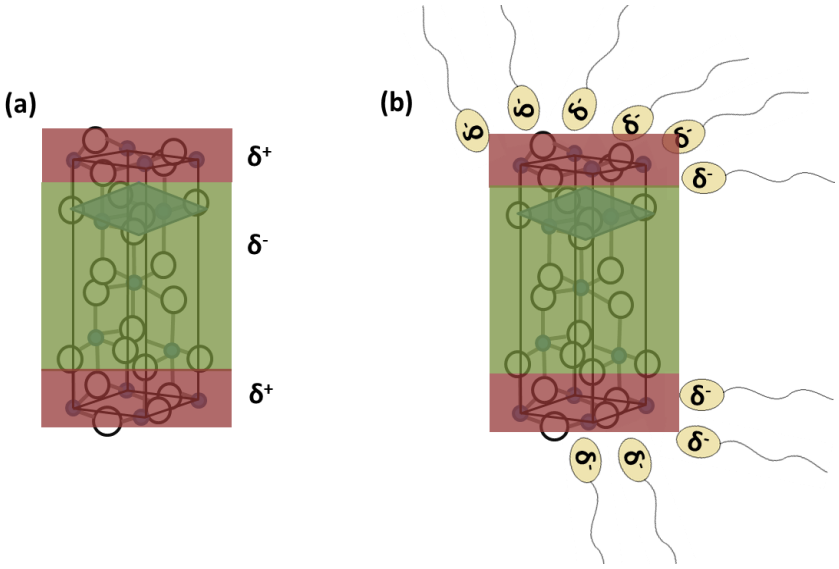

Figure 4.7.(a) Schematic to show potential charges on anatase crystal surfaces as a result of increased oxygen concentration in some planes. **(b)** Schematic of potential binding of polar surfactant molecules to specific surfaces of anatase crystal.

The average crystallite size was found to increase with the addition of Tween surfactant, from 7.5 nm up to a range of 8-13 depending on the type and concentration of Tween surfactant added. The Tween sample prepared with Tween 20 in a 2 M concentration was found to have the highest crystallite size of all samples produced at 13 nm. The Brij prepared samples generally showed lower crystallite sizes, within the range of 5.5-12 nm, with the Brij 98 sample prepared with 0.5 M surfactant exhibiting the smallest crystallite size of just 5.5 nm.

4.2.1.5. Photocatalytic activity of thin films produced from TTIP with toluene and the effects of surfactant addition

All thin films produced by AACVD were photocatalytically active for the degradation of Resazurin 'intelligent ink'. The half-lives determined for the photocatalytic degradation of resazurin dye on the surface of the AACVD prepared films are shown in table 4.1, alongside the calculated rate of photoactivity (dye molecules degraded per s^{-1} cm^{-2}). For the samples prepared without any surfactant addition, an average photocatalytic half-life of 5 minutes was observed, with a calculated rate of photoactivity (dye molecules degraded s^{-1} cm^{-2}) of 3.88×10^{13}. The best photocatalytic performance was observed for the sample prepared with Brij 58 surfactant, in a concentration of 0.5 M, which exhibited an average photocatalytic half-life of 3 minutes and a calculated rate (dye molecules degraded s^{-1} cm^{-2}) of 9.50×10^{14}. This is a considerable enhancement on the sample prepared without surfactant, and is shown as a bar chart in figure 4.9, with the normalised degradation curves used to determine half-life shown in figure 4.8. This is an improvement on the photocatalytic performance of samples prepared by a similar AACVD method, which used the addition of AC electric fields to alter the microstructure of the thin films, whereby an optimum half-life of 4.7 minutes was determined.[30]

In correlation with discussions above, the thin films prepared with the larger concentration of surfactant were found to show the slowest half-lives and lowest rates of photoactivity, which can be attributed to the increased particle sizes, poor definition of particles and increased agglomeration, reduced film thickness, reduced surface roughness and lower hydrophilicity compared to other films produced with lower concentrations of surfactant. For example, A B58 2 t prepared with 2 M of Brij 58, has an observed average particle size of 150 nm, a thin film thickness of 740 nm and an average RMS roughness of just 52 nm, and as a result the photocatalytic half-life is 12 minutes, with a photoactivity rate of 3.61×10^{13} (dye molecules degraded s^{-1} cm^{-2}). All of the factors mentioned work together to produce a lower surface area to

volume ratio, meaning that the adsorption of the resazurin dye to the thin film surface is reduced, there are less active sites available for the photocatalytic reaction to take place, and thus a lower photocatalytic rate is observed. This is in contrast to a thin film such as that prepared with 0.5 M of surfactant (A B58 0.5 t), which has a high surface roughness of 134 nm, a small average particle size and high hydrophilicity with UV light (a contact angle of 4.16 ° after UV irradiation) meaning that there is a higher surface area for photocatalysis, and so a faster degradation of the dye can occur. Furthermore, the Brij 58 2M sample was found to be exclusively rutile in phase, as shown in the XRD patterns in figure 4.4, and as has been well documented, the rutile phase is typically less photocatalytically active than the anatase phase.

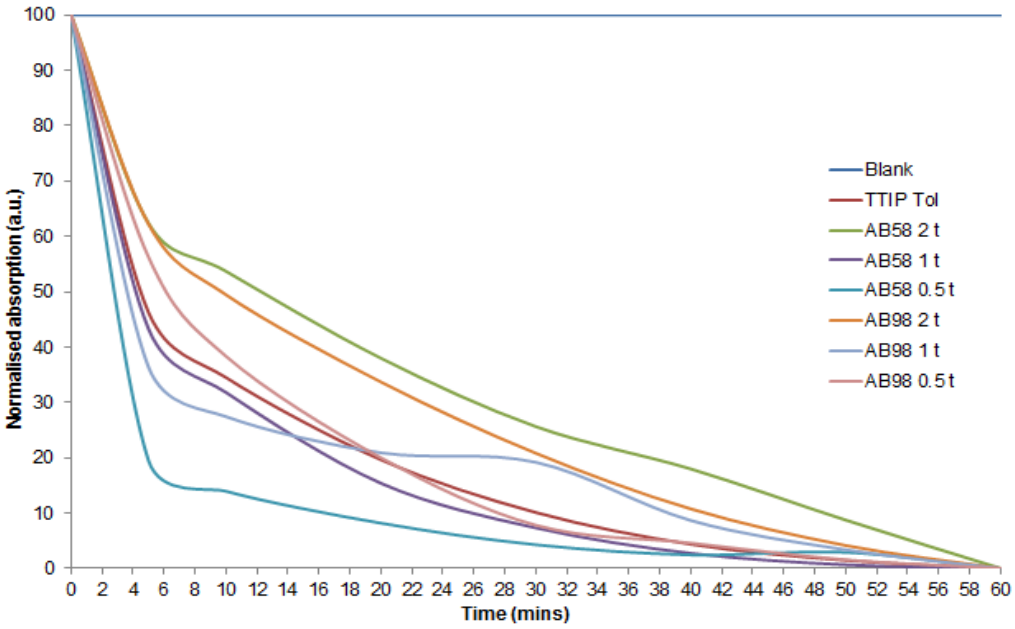

Figure 4.8. Normalised absorption curve used to determine photocatalytic half-life in minutes for samples prepared by AACVD reaction of TTIP in toluene with addition of Brij surfactants. TTIP Tol sample represents the sample prepared without surfactant addition and is used for comparison.

Despite being composed of rutile phase only, the Brij 58 2 M sample does not exhibit the slowest photocatalytic performance. Those thin films produced with Tween surfactant show the slowest half-lives; 33 minutes for sample A T20 0.5 t, 22 minutes for A T20 2 t, and 13 minutes for sample A T40 1 t. The normalised absorption curves used to determine the half-lives are shown in figure 4.10. These degradation curves suffer the same issues as those discussed in detail in section 3.2.1.7, whereby higher values of absorption are obtained due to the degradation

mechanism of the ink. The reasons for these slower photocatalytic performances does not follow previous trends observed when discussing thin film samples as for those prepared by sol-gel and described in chapter 3. These Tween samples show a smaller average particle size in comparison to the film prepared without surfactant (110 nm), whereby they are in the range of 50-76 nm. However, they show poor wetting properties, even after UV light, as seen in table 4.1, which is likely to inhibit formation of hydroxyl radicals on the thin film surface to propagate the photocatalytic reaction, and this will also reduce the adsorption of the dye on the surface.[30] These samples also show a larger average crystallite size compared to other samples, of 10.5 nm (A T20 0.5 t), 13 nm (A T20 2 t) and 12 nm (A T40 2 t) compared to 7.5 nm for the TTIP plain sample prepared without surfactant. Crystallite size and orientation have been directly linked to alterations to photocatalytic performance previously.[30]

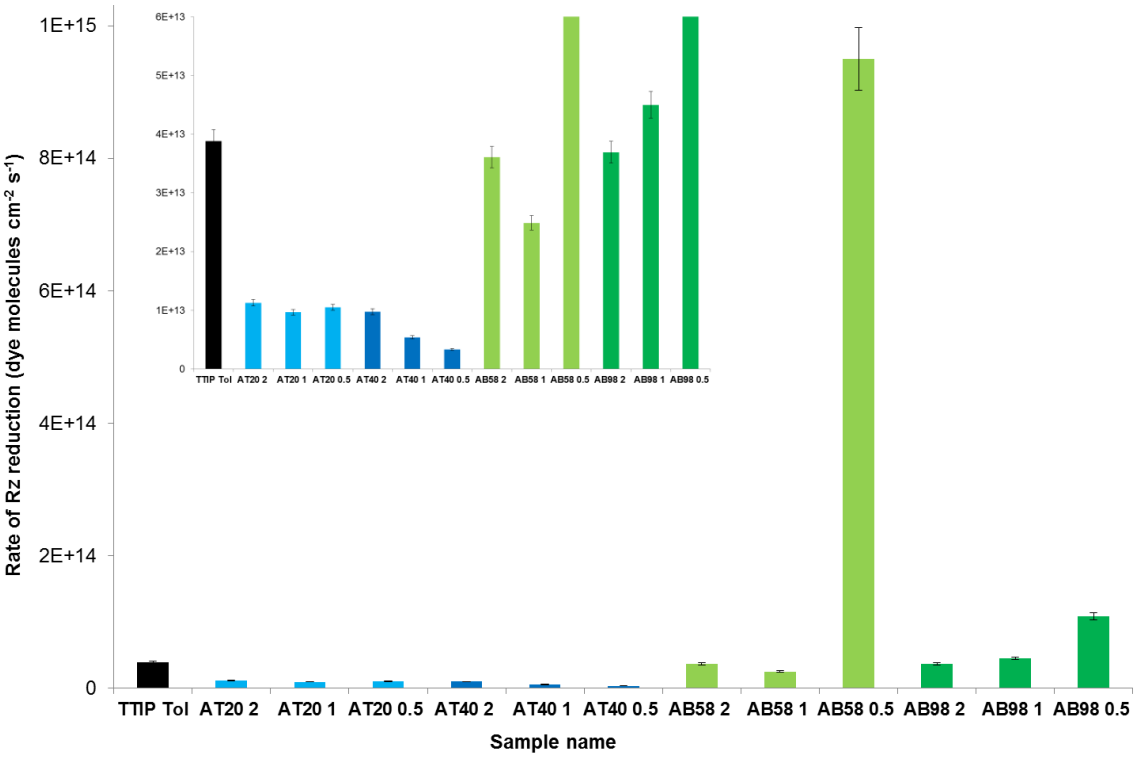

Figure 4.9. Bar chart representing the rate of calculated photoactivity for resazurin dye molecules degraded s^{-1} cm^{-2} for each AACVD sample type prepared with toluene as solvent. "TTIP tol" represents the control sample prepared without any surfactant addition. Surfactant concentrations are 0.5 M, 1 M and 2 M. Errors are shown as experimental percentage error (5%). Inset picture is a magnified version of the bar chart to show differences between the slower rate samples.

In addition, the presence of growth in specific crystallographic planes in TiO_2 can be linked to enhancements to photocatalytic performance.[233,236] The (101) plane is the most commonly observed plane in anatase TiO_2 and has been studied as a factor attributing to enhanced photocatalytic performance.[237,238] Less commonly observed is the (004) plane, which is a plane of anatase which has a low atom-packing density,[239] whereas the (101) plane is the plane with the lowest surface energy.[240] A low atom-packing density means that electron mobility in this plane is enhanced, thus making this surface more favourable for a surface redox reaction, such as photocatalysis.[241]

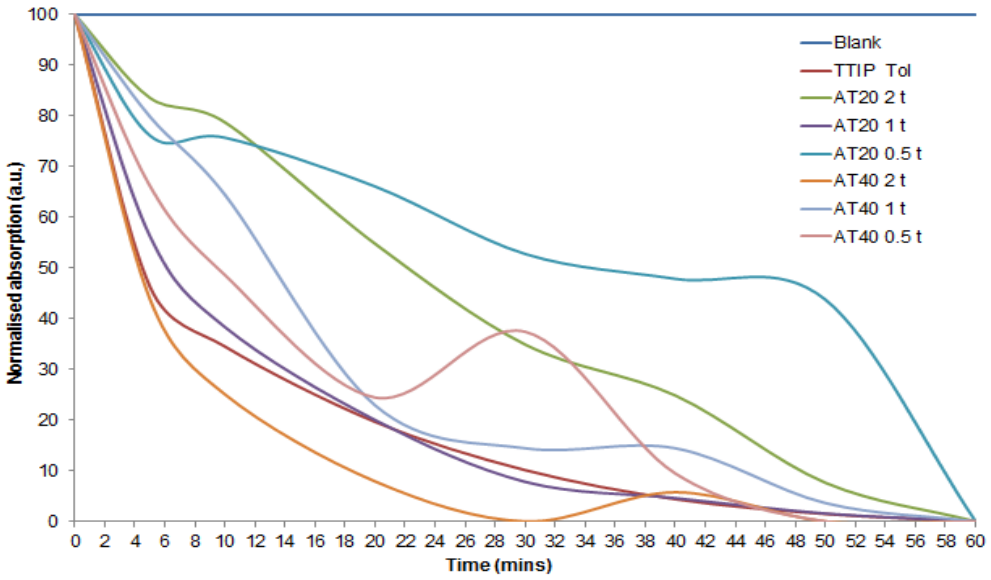

Figure 4.10. Normalised absorption curve used to determine photocatalytic half-life in minutes for samples prepared by AACVD reaction of TTIP in toluene with addition of Tween surfactants. "TTIP Tol" sample represents the sample prepared without surfactant addition and is used for comparison.

4.2.1.6. Conclusions: TTIP precursor with toluene as solvent with surfactant addition

Thin films of photocatalytically active TiO_2 were deposited at 400 °C using TTIP precursor in toluene solvent, with the addition of Tween and Brij surfactants in three concentrations; 0.5 M, 1 M and 2 M. The effects of surfactant addition were explored using several analysis and characterisation methods including SEM, contact angle measurements, AFM surface roughness, XRD, and UV/Vis. The addition of surfactant was found to significantly affect the photocatalytic performance of the deposited thin films, depending on the surfactant type used and the concentration. AACVD films produced without surfactant addition exhibited an average half-life

of 5 minutes for Rz degradation, with a calculated rate of photoactivity of 3.88 x 10^{13} (dye molecules degraded s^{-1} cm^{-2}), compared to the highest photoactivity obtained by the AACVD Tol B58 0.5 M sample which had a half-life of just 3 minutes and a photoactivity rate of 9.40 x 10^{14} (dye molecules degraded s^{-1} cm^{-2}). This enhanced performance was attributed to a number of factors including smaller particle size of 80 nm compared to 110 nm, and increased texture coefficient in the (004) preferential plane of 2.70 vs 1.46 for the control sample.

4.2.2. Results: Titanium Isopropoxide (TTIP) as precursor with dichloromethane (DCM) as solvent with Tween and Brij surfactant addition

Dichloromethane (DCM) was used as an alternative solvent to investigate how the surfactants interact with the precursor and solvent to produce the range of effects observed and described above. As the TTIP precursor is sensitive to all sources of moisture, only organic solvents could be used, and as such these solvents were chosen as they were the only solvents practically available at the time of these experiments. As toluene is a non-polar solvent (2.4 on the polarity index) and DCM is moderately polar (3.1 on the polarity index), it is expected that different thin film properties will be obtained as a result of the differing interactions between TTIP precursor, solvent and surfactants.[242]

From the studies above with toluene as solvent, it was found that the addition of surfactant in concentrations of 2 M did not result in enhanced photocatalytic or functional performance of the thin films produced, and in fact it appeared that this larger concentration of surfactant addition in fact hindered the growth of thin films. As a result, the 2 M concentration has not been included in the following results section with DCM as solvent.

4.2.2.1. Thin film thickness and particle size

The thin films produced from TTIP precursor with DCM as solvent without surfactant addition deposited at 400 °C exhibited an average film thickness of 1100 nm; a higher value than that obtained for the plain TTIP sample prepared with toluene as solvent, which had a an average value of 810 nm. Generally the samples prepared with DCM exhibited higher thickness compared to the same samples prepared with toluene as solvent. For example, toluene samples were within the ranges of 250 nm- 3350 nm, whereas DCM films ranged from 610 nm as the thinnest film up to 3025 nm. A clear trend between thin film thickness, surfactant addition and concentration can be seen in figure 4.20. As DCM is a more polar solvent than toluene, it can be

suggested that solvent-surfactant interactions are increased. This means that the surfactant molecules may favour interactions with the solvent over interactions with the TTIP precursor and the growing titanium dioxide particles. As a result, the blocking interactions mentioned in section 4.2.1.1 may not happen here, rather the opposite. As the surfactant is attracted to the polar solvent, there are more opportunities for the TiO_2 particles to grow and nucleate into thicker films without obstruction.

It can be seen in figure 4.11 that increasing the concentration of surfactant from 0.5 M to 1 M resulted in significantly thicker films forming, specifically for B58 1M d and B98 1M d, which observed thicknesses of 2535 nm and 3025 nm respectively. This was also observed for the films prepared with Tween surfactants to a lesser degree. This observation correlates with the argument that the surfactants coordinate with the solvent to leave more room for TiO_2 particle growth and nucleation into thicker films.

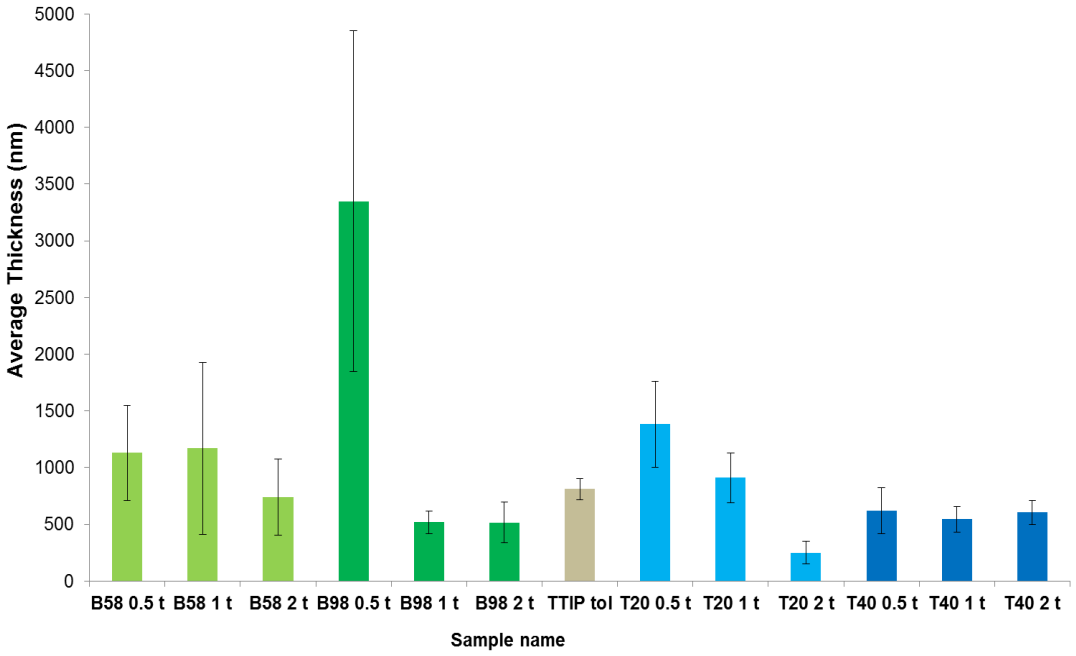

Figure 4.11. Bar chart comparison of the average film thickness. Films were prepared by AACVD with TTIP precursor and DCM, with increasing concentrations (0.5M to 1M) of Brij and Tween surfactants, different types indicated by different colours. Error bars show standard deviation. TTIP DCM column in black represents the control sample prepared without surfactant addition.

4.2.2.21. Thin film morphology: Tween surfactants

The addition of Tween surfactants in the AACVD of TTIP in DCM solvent was found to alter the morphology of resulting films produced. Several differences have been observed depending on the surfactant type and concentration used. The thin films produced without surfactant exhibited a similar morphology to that observed for the films produced in the experiments described above with toluene; however the rice-like particles previously observed are smaller with increased irregularity.

As seen in figure 4.12, the addition of Tween surfactant results in these small pointed particles becoming more circular, which was also observed with Tween surfactant addition with toluene as solvent. Increasing the concentration of Tween 20 0.5 M through to 1M results in a slight increase in particle size, from an average of 50 nm to 65 nm, and increasing the concentration of Tween 40 from 0.5 M to 1 M results in a decreased in particle size from 80 nm to just 40 nm.

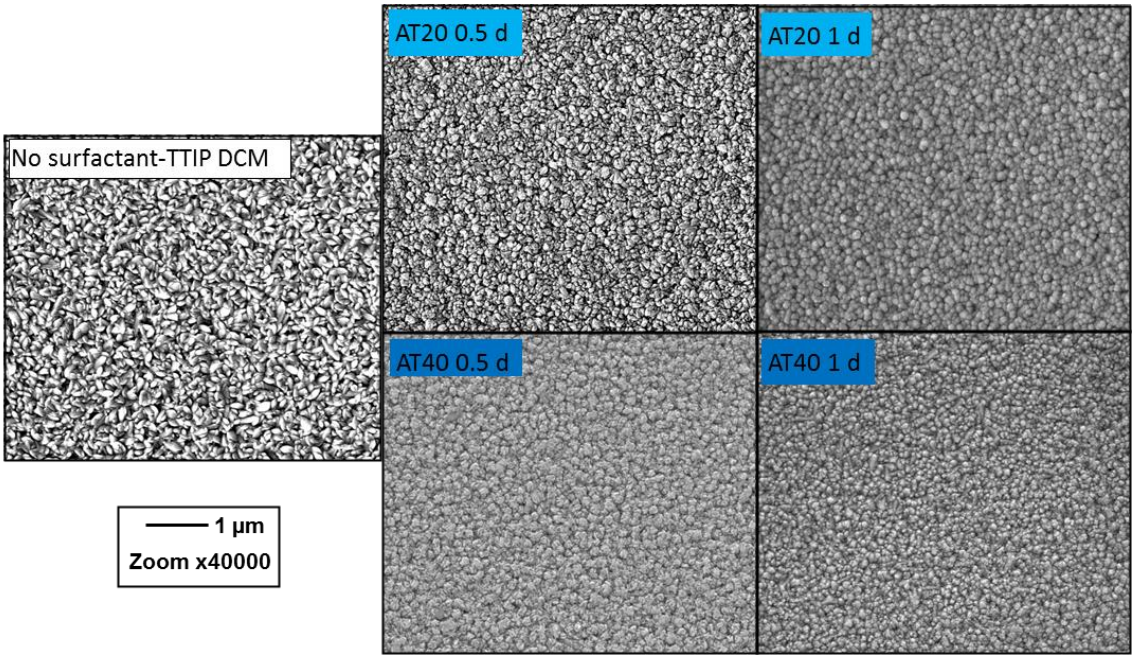

Figure 4.12. SEM images of TiO_2 thin films produced via AACVD with TTIP as precursor, dichloromethane (DCM) as solvent, with Tween 20 and Tween 40 in concentrations 0.5 M to 2 M. Films were deposited at 400 °C.

The average particle size of the film prepared with TTIP and DCM without surfactant was 90 nm. Thus, it can be concluded that the surfactant helps to control particle growth and encourages the formation of spherical particles with increased regularity, as seen in SEM images A T20 1 d

and A T40 1 d, figure 4.21. This is consistent with previous discussions about the surfactants role in controlling TiO_2 particle growth.

4.2.2.22. Thin film morphology: Brij surfactants

The thin films produced with TTIP, DCM as solvent and Brij surfactants show a range of thin film morphologies, from rice-like to spherical and needle/rod- shaped particles, as shown in the SEM images in figure 4.13. The addition of Brij 98 surfactant was found to show similar affects to that observed with the Tween surfactants above in figure 4.21, whereby the rice-like particles became more spherical and regular in size and shape with surfactant addition. Increasing the concentration of Brij 98 from 0.5 M to 1 M resulted in the particle size decreasing from an average of 60 nm to 50 nm as well, in line with the role of surfactant stunting particle growth with increased concentration.

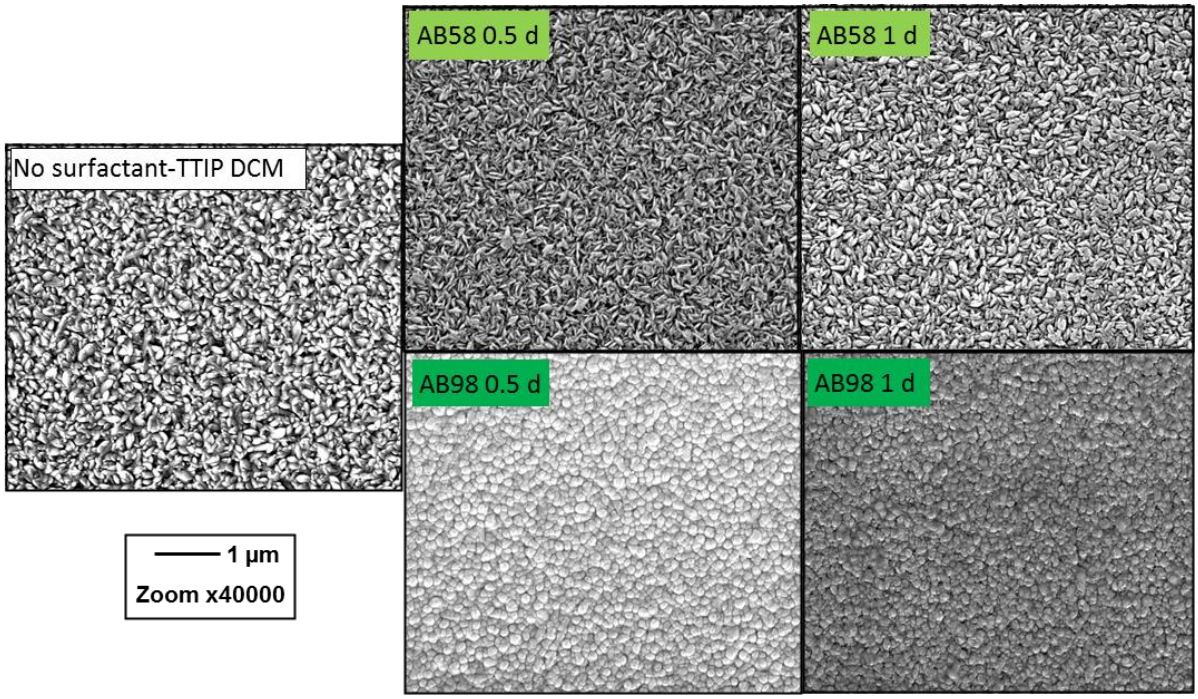

Figure 4.13. SEM images of TiO_2 thin films produced via AACVD with TTIP as precursor, dichloromethane (DCM) as solvent, with Brij 58 and Brij 98 surfactant addition in concentrations 0.5 M to 2 M. Films were deposited at 400 °C.

However, the addition of Brij 58 has resulted in very different particles being produced. Chemically Brij 58 and Brij 98 are very similar, as shown in figure 4.13a, whereby each molecule has the same number of ethylene oxide chain lengths (20 each), with the only

difference being the size of the alkyl chain head group ($C_{16}H_{33}$ for Brij 58 and $C_{18}H_{35}$ for Brij 98). This means that it is the differing size of alkyl chain groups which have resulted in the different morphologies shown above.

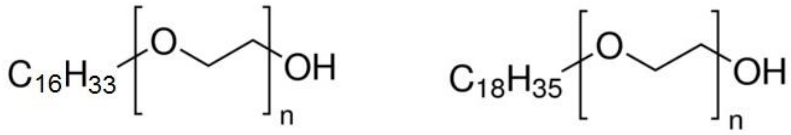

Brij® 58 **Brij® 98**

Figure 4.13a. Chemical structure of Brij 58 and Brij 98 surfactants, where n = 20.

Sample A B58 0.5 d prepared with the lowest concentration of Brij 58 has produced a film which has thin, needle-like particles with an average size of 60 nm, which decrease to 50 nm with increased surfactant addition to a concentration of 1M. Firstly, it is known that the size of surfactant micelles typically decrease as the surfactant concentration is increased.[228] This can account for the reduced average particle sizes observed in both samples (Table 4.3). Secondly, the shape of micelles that form from surfactants depends on the size of the surfactant head, overall ionic strength and the length of the tail. Brij 58 has been identified as a surfactant with a large head group (E_{20-23}) meaning that it exhibits "non-detergent behaviour", whereas those with a small head group (E_{8-10}) behave more like a typical detergent.[228] Thus, Brij 98 must also exhibit non-detergent behaviour. Detergents are characterised as molecules that align at aqueous/non-aqueous interfaces, resulting in reduced surface tension, and increased miscibility and stabilisation of emulsion solutions.[197] As a result, the differing thin film morphology observed with the use of Brij 58 surfactants is likely to be due to the type of micelles that are formed from the Brij 58 surfactant, whereby it has been reported that this size of head group lies in an intermediate region, where typical micellar structures do not form. It is reported that Brij 58 has the ability to form inverted vesicles in solution. This may explain why this different morphology of elliptical or needle-like particles are observed as dominant in the thin film morphology, whereby the packing parameter is different to all other surfactant molecules investigated in this study.[228]

At lower concentrations of surfactant the packing of micelles is decreased, and there is the potential for micelles to revert to cylinder shapes rather than spheres, thereby encouraging the growth of needle-like particles rather than spherical particles. The concept of the 'packing

parameter' as developed by Israelachvili,[243] is used to predict micelle shape and size of self-assembled structures in solution and is shown in explained in figure 4.14.

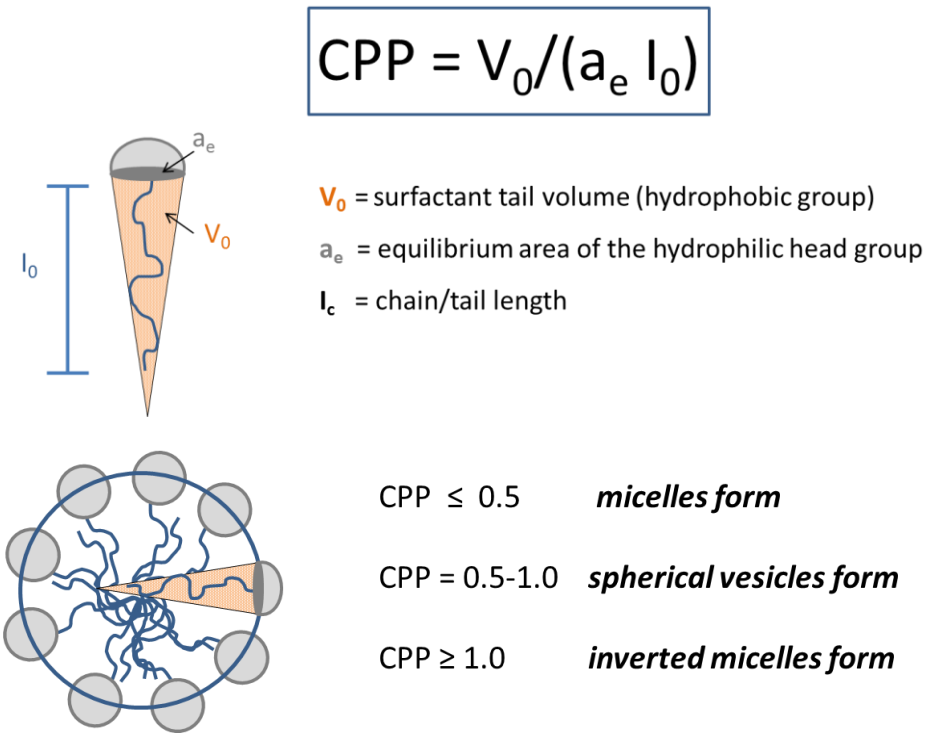

Figure 4.14. Critical packing parameter of an non-ionic surfactant where V_0 is the volume of the hydrophobic tail group, a_e is the equilibrium area of the hydrophilic head group and I_c is the chain/tail length.

4.2.2.3 Surface roughness and wetting properties

The AACVD samples prepared with DCM are much more hydrophobic than the samples prepared with toluene, as seen by comparing the contact angle values in table 4.2 and 4.3. Firstly, for the films prepared without surfactant (A TTIP DCM) the average contact angle was 35 ° and 12 ° after UV irradiation. The films prepared with toluene (A TTIP Tol) showed a contact angle of 67 ° before and just 4 ° after. This shows that although the thin films are inherently hydrophilic, becoming more hydrophilic with UV irradiation, whereby the toluene prepared sample becomes superhydrophilic. Comparing the surface roughness values between the two can offer a reason as to why the toluene prepared sample is more hydrophilic. The average surface roughness of the toluene prepared sample was 134 nm, compared to an average of just 39 nm for the DCM prepared sample. As described before, an increase in surface roughness increases the hydrophilicity of the surface.

Table 4.3. Results for samples prepared by AACVD using TTIP in DCM with the addition of surfactant in the precursor solution. Three concentrations of surfactant were used, 0.5 M to 2 M. Sample C represents the control sample prepared without surfactant. Numbers represent the number of layers. Samples were deposited at annealed at 400°C until all of the precursor solution was depleted.

Sample Name	Contact angle (°) before UV	Contact angle (°) after UV	Average particle size (nm)	Average film thickness (nm)	Average RMS surface roughness (nm)	XRD predominant phase	Texture Coefficient	Average Crystallite Size (nm)	Photocatalytic half-life for Rz degradation (mins)	Calculated rate of photoactivity (dye molecules degraded s^{-1} cm^{-2})
A B58 0.5 d	45	37	60	1085	37	Anatase	3.33 (004)	10	3.5	1.02×10^{13}
A B58 1 d	81	62	50	2530	40	Anatase	2.98 (004)	9	2.5	1.41×10^{13}
A B98 0.5 d	65	29	60	1160	23	Anatase	2.95 (004)	5.5	2.75	1.30×10^{15}
A B98 1 d	86	50	50	3025	62	Anatase	3.19 (004)	9	3	1.40×10^{13}
TTIP DCM	35	12	90	1100	39	Anatase	2.64 (004)	10	12.5	1.86×10^{13}
A T20 0.5 d	90	4	50	610	63	Anatase	3.18 (004)	12	3.5	1.05×10^{13}
A T20 1 d	89	6	65	780	91	Anatase	2.56 (004)	9	5	9.66×10^{12}
A T40 0.5 d	43	19	80	1000	64	Anatase	3.00 (004)	8	2.5	3.31×10^{12}
A T40 1 d	73	39	40	1460	50	Anatase	3.15 (004)	8	2.25	5.39×10^{12}

The addition of surfactant to the DCM prepared thin films samples appears to have reduced the wetting ability of samples, whereby contact angle reductions of only 10-20 ° were most commonly seen. Only two samples exhibited very superhydrophilic behaviour, and this was for the Tween 20 prepared samples where the contact angle is reduced from 90 ° and 89 °to low values of 4 ° and 6 ° for samples A T20 0.5 d and A T20 1 d respectively (Table 4.3). These samples show relatively high surface roughness values of 63 nm and 91 nm, whereby 91 nm as for A T20 1 is the highest roughness value obtained for the DCM prepared samples.

The average surface roughness of the DCM prepared samples was on average much lower than the toluene prepared samples, as seen in the bar chart in figure 4.24. The addition of surfactant for the DCM prepared samples does appear to have increased the average surface roughness value in some instances, compared to the TTIP plain sample which has an average surface roughness of just 39 nm. This was particularly notable for samples A T20 1 d, AT20 0.5 d, A T40 0.5 d and A B98 1 d which exhibited an average surface roughness of 91 nm, 63 nm, 64 nm and 62 nm respectively. Most other samples showed only a marginal increase to surface roughness, whereby only sample B98 0.5 d showed a significantly lower value of 23 nm. Interestingly, sample A B98 0.5 also showed the lowest surface roughness value for the toluene prepared sample, as shown in figure 4.15, therefore indicating that this concentration and type of surfactant results in a smoother overall thin film surface.

These differences in thin film roughness observed through changing the surfactant type/concentration and solvent links back to the discussion in section 4.2.1.4, regarding crystallinity of toluene samples, and also section 4.2.2.22, regarding packing parameter of surfactants. DCM is a much more volatile and polar solvent in comparison to toluene (toluene is 2.4 on polarity index and DCM is 3.1). This means that DCM will evaporate more easily, allowing precursors and growing particles to ‘relax’ more easily onto the substrate surface, thus enabling the growth of a smoother overall film. Toluene however will stay around for longer as it will not evaporate as quickly, this means that it could potentially bind to the positive dipole in the crystal growth, as described in section 4.2.1.4, thereby allowing some kind of crystal structure to be reinforced, producing an overall rougher thin film surface.

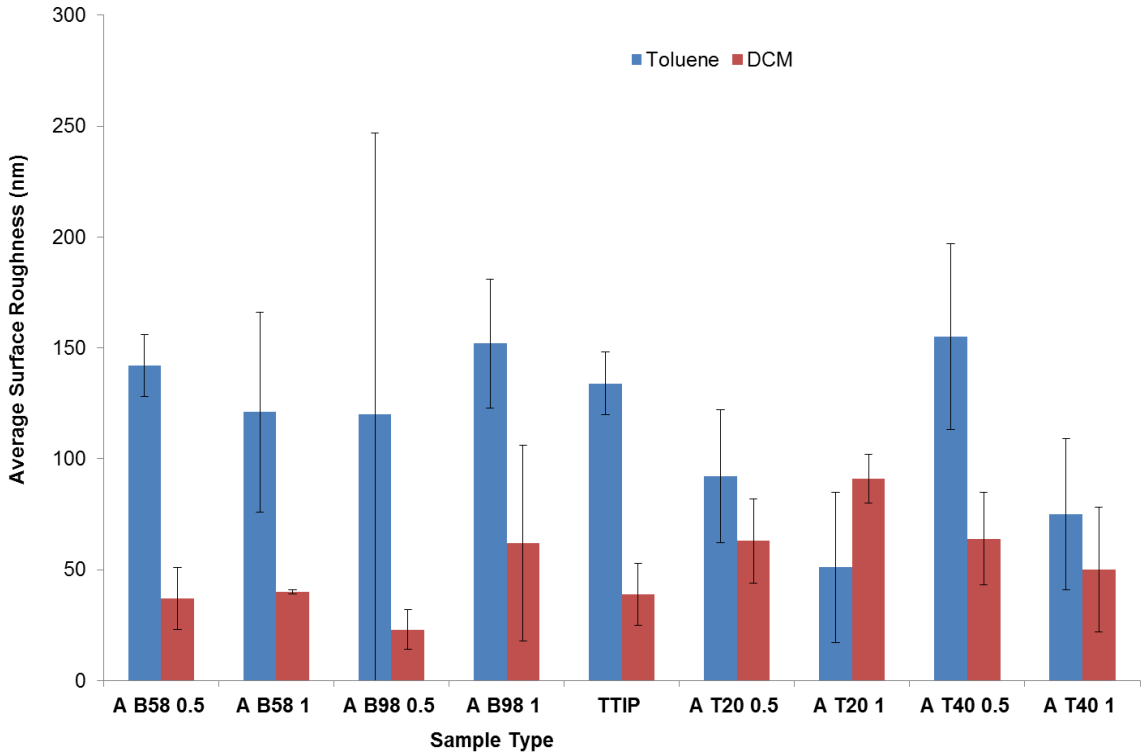

Figure 4.15. Comparison bar chart of average surface roughness of thin films obtained when using a different solvent (Toluene or Dichloromethane) for AACVD with TTIP precursor and surfactant addition, deposited at 400 °C. Surfactants used were Brij 58, Brij 98, Tween 20 and Tween 40 in 0.5 M and 1 M concentrations. 'TTIP' is the control sample prepared without surfactant addition. Errors bars show the standard deviation.

4.2.2.4 Crystalline phase identification of TiO_2 thin films

The thin films prepared by AACVD with TTIP precursor, DCM solvent and surfactant addition were analysed by XRD to determine the diffraction pattern so that the crystalline phase could be identified, and the texture coefficient (TC) and crystallite size obtained. The XRD diffraction patterns of the TiO_2 thin films are shown in figure 4.16 for the films prepared with the addition of Tween surfactants and 4.17 for the addition of Brij surfactants. As for previous samples discussed, all TiO_2 thin films deposited showed breakthrough to the underlying FTO substrate, with these peaks identified on the XRD diffraction patterns with an asterisk. The XRD diffraction patterns obtained for the DCM samples were similar to those obtained by the toluene prepared samples, whereby a mixture of phases was present. Predominantly anatase phase diffraction peaks were observed, with dominant crystal growth typically observed in the [101] plane and [004] planes, as for the toluene prepared samples.. The rutile phase observed was again in low intensities in the uncommonly observed [211] plane.

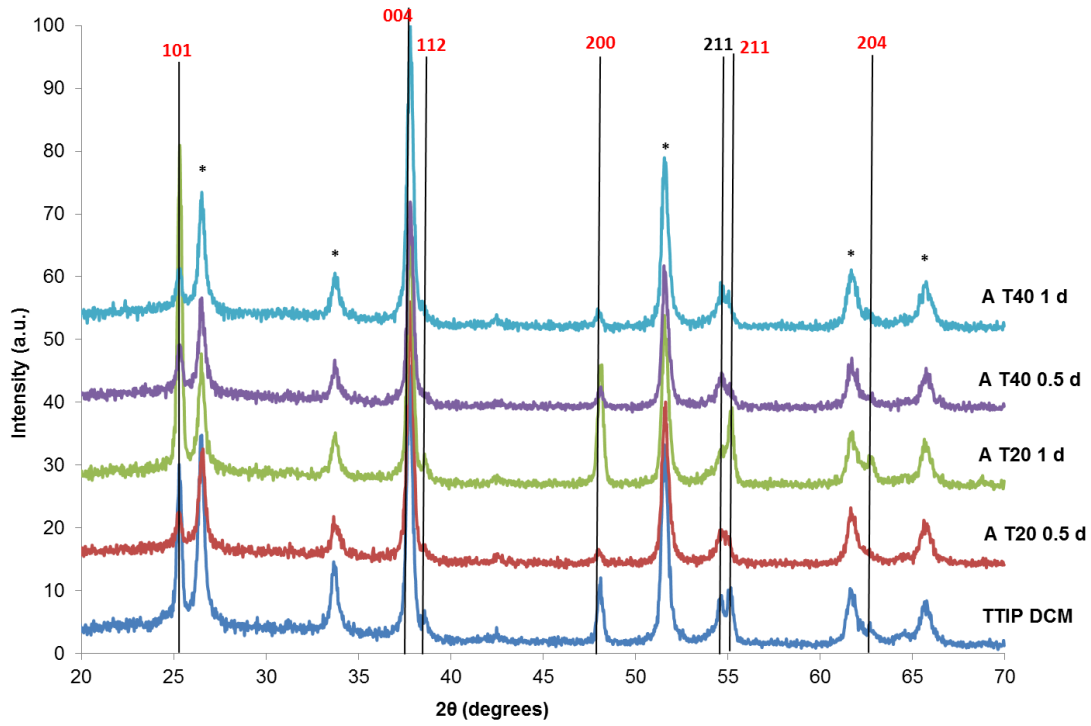

Figure 4.16. XRD of TiO_2 films produced by AACVD using TTIP precursor in DCM solvent, without surfactant (**TTIP DCM**) and with Brij surfactants in 0.5 M, 1M and 2M; **Brij 58** (A B58 0.5 d, A B58 1 d, A B58 2 d) and **Brij 98** (A B98 0.5 d, A B98 1 d, A B98 2 d). Peaks identified as anatase are marked in red and rutile in black. Peaks denoted with asterisks (*) are assigned to the F:SnO_2 coating of the glass substrate. XRD normalised for intensity.

The predominant orientation was observed to be in the (004) plane for all samples, with the highest texture coefficient observed for sample A B58 0.5 d (3.33 TC) and the lowest observed for sample A T20 1 d (2.56 TC). The plain TTIP and DCM sample prepared without surfactant showed a TC of 2.64, thus showing that the addition of surfactant, in particular Brij 58 in 0.5 M concentration results in increased preferential orientation in the (004) plane, and thus a higher texture coefficient. The reasons behind these observations have been described in section 4.2.1.4 and thus will not be repeated here. However, due to the increased polarity of DCM solvent, it is worth analysing the differences between the crystallinity of the toluene samples and the DCM samples by means of comparing the texture coefficient values, as shown in figure 4.26. Overall, the DCM samples exhibit higher texture coefficients for all samples produced in comparison to the toluene samples. This will be due to the increased polarity of the DCM solvent, which would result in an increased version of the surfactant-TiO_2 interactions depicted in figures 4.6 and 4.7 which lead to preferential growth in the (004) plane. The TC of the plain sample prepared

without surfactant shows a large difference between the two solvents used; 1.6 for the toluene sample vs 2.64 for the DCM sample.

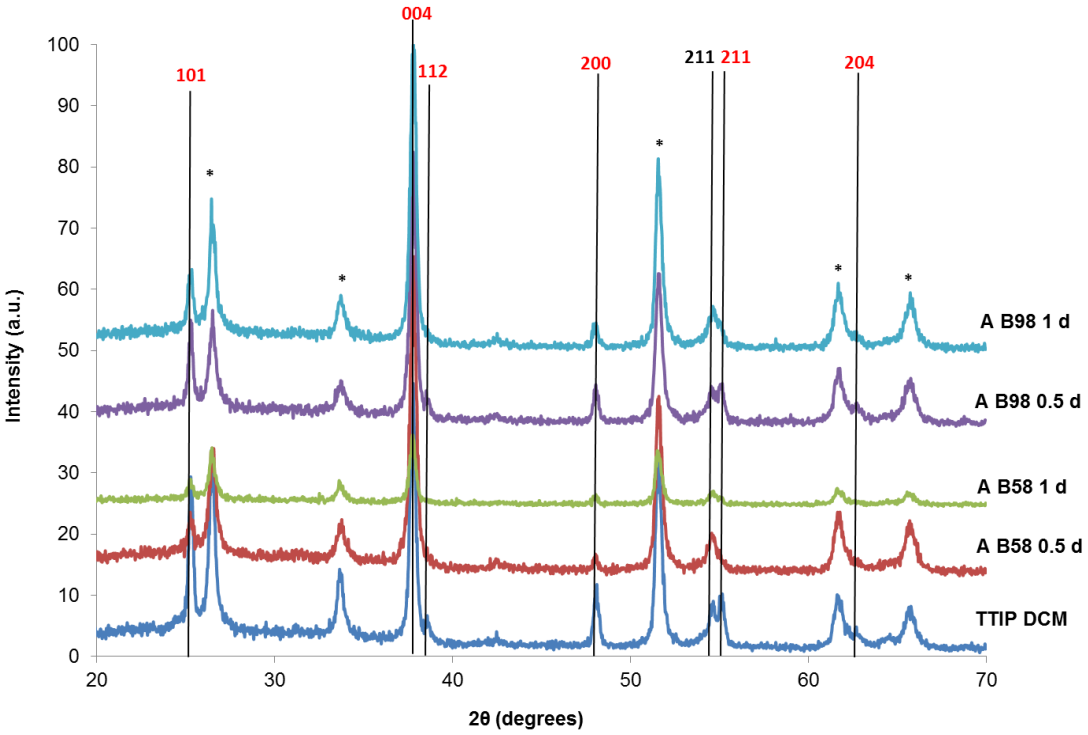

Figure 4.17. XRD of TiO_2 films produced by AACVD using TTIP precursor in DCM solvent, without surfactant (**TTIP DCM**) and with Tween surfactants in 0.5M, 1M and 2M; **Tween 20** (A T20 0.5 d, AT20 1 d, A T20 2 d) and **Tween 40** (A T40 0.5 d, A T40 1 d, A T40 2 d). Peaks identified as anatase are marked in red and rutile in black. Peaks denoted with asterisks (*) are assigned to the F:SnO_2 coating of the glass substrate. XRD normalised for intensity.

Furthermore, the addition of different surfactant types and concentrations does appear to show a general trend irrespective of the solvent used, particularly for Brij 58 0.5 M to 1 M, whereby the texture coefficient increases for both toluene samples and DCM samples with increased addition of surfactant. The same occurs for Brij 98, and Tween 40. The only surfactant not to follow this trend is Tween 20, whereby with increased concentration addition from 0.5 M to 1 M the texture coefficient shows only a marginal increase, and for A T20 1 with DCM, the texture coefficient actually decreases. The distinction between Tween 20 and the other three surfactants investigated is that Tween 20 has a higher hydrophilic-lipophilic balance (HLB) value (table 4.1). This means Tween 20 exhibits more hydrophilic behaviour, and as such exhibits different packing, whereby the surfactant may align with certain parts of the growing crystal to inhibit growth along one facet and encourage growth in another (figures 4.6 and 4.7).

The average crystallite size for the thin films are shown in tables 4.2 and 4.3, whereby the values observed are very similar regardless of which solvent was used, as similar values are obtained for each surfactant type/concentration. e.g. A B58 0.5 t = 11 nm A B58 0.5 d = 10 nm, A B98 1 t = 9.5 nm, A B98 1 d = 9 nm, A T40 1 t = 8, A T40 1d = 8. As expected this indicates that the surfactants provide structuring in crystal growth of the thin film.

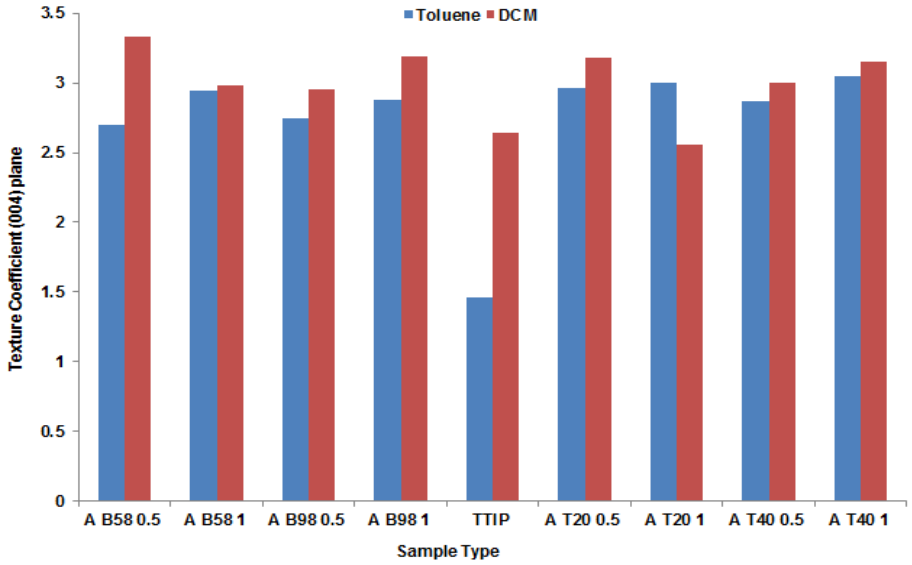

Figure 4.18. Bar chart comparing the texture coefficients of different samples prepared with toluene/DCM solvent, with and without the addition of surfactant. Samples were prepared as stated in Fig 4.23. Surfactants used; Brij 58, Brij 98, Tween 2, Tween 40 in 0.5 M and 1 M concentrations. 'TTIP' is the control sample prepared without surfactant addition.

4.2.2.5. Photocatalytic activity of thin films produced from TTIP with DCM and effects of surfactant addition

All thin films produced by AACVD with TTIP as precursor and DCM as solvent exhibited photocatalytic activity for the degradation of resazurin dye. Photocatalytic half-lives as determined from the normalised absorption curves in figures 4.19 and 4.21 are shown in table 4.3. The addition of surfactant was found to significantly reduce the photocatalytic half-life, whereby the thin films produced with DCM without surfactant addition showed an average half-life of 12.5 minutes, and the thin films produced with surfactant addition showed average half-lives between 2.25 -5 minutes. The fastest half-life of 2.25 minutes was observed for sample A T40 1 d. However, the calculated photocatalytic rate shows the most photocatalytically active sample to be A B98 0.5, which shows an average half-life of 2.75 minutes and a calculated rate

of 1.30 x 10^{15} dye molecules degraded s^{-1} cm^{-2} (table 4.3) which is up to two magnitudes larger than other samples as shown in figure 4.20.

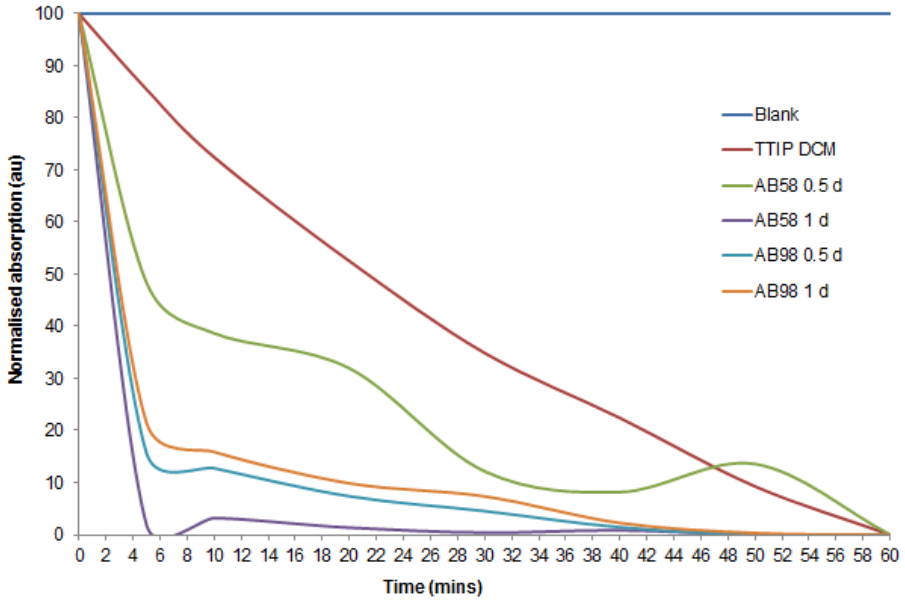

Figure 4.19. Normalised absorption curve used to determine photocatalytic half-life in minutes for samples prepared by AACVD reaction of TTIP in DCM with addition of Brij surfactants in different concentrations from 0.5 M to 1M. TTIP DCM sample represents the sample prepared without surfactant addition.

As discussed previously, there are several limitations in determining the photocatalytic potential of a material using the degradation curve method as in figure 4.19 and 4.21 to obtain a half-life. Significant fluctuation in the absorption curves can be seen in figures 4.19 and particularly 4.21. This is owing to issues such as; movement of the sample during UV-Vis measurement (the same 1 cm x 1 cm is not measured for absorption each time in the spectrometer, thus if a different area is measured it may have higher or lower resazurin concentration there), incomplete degradation of the resazurin dye on the thin film surface, (whereby as an initial layer of resazurin molecules are degraded to resorufin, more resazurin is then exposed to UV light from underneath), incomplete drying of the resazurin dye layer, (whereby the resazurin becomes more concentrated as water is evaporated from the thin film over time).

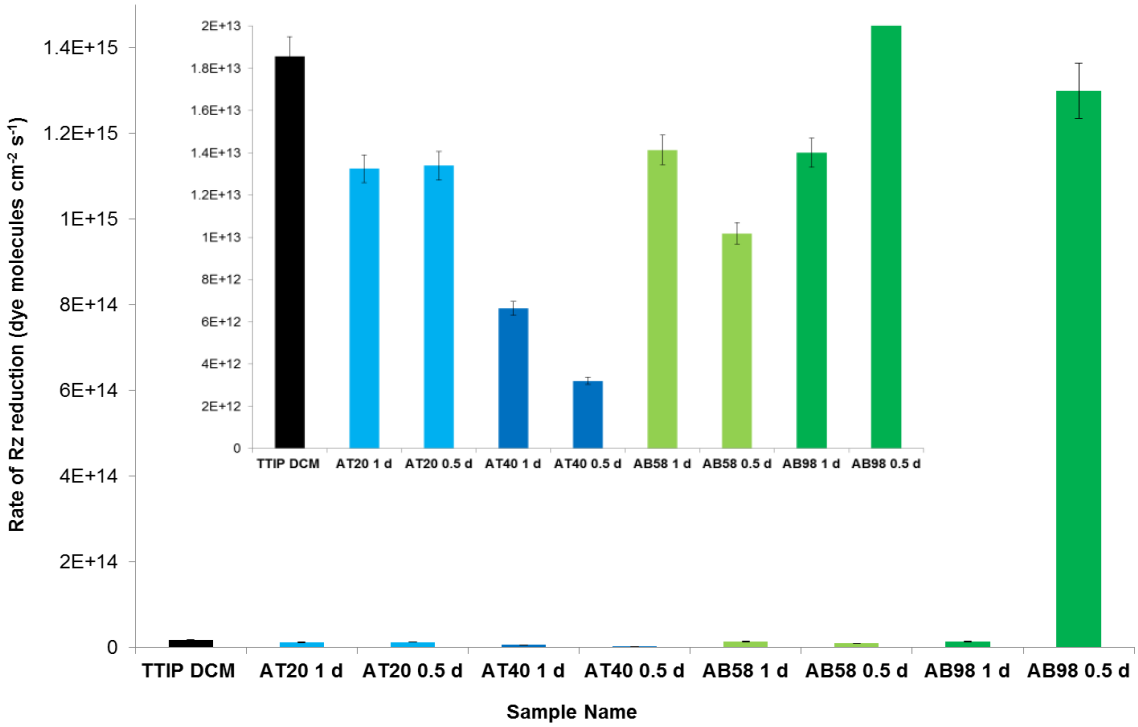

Figure 4.20. Bar chart representing the rate of calculated photoactivity for resazurin dye molecules degraded s^{-1} cm^{-2} for each AACVD sample type prepared with DCM as solvent. TTIP DCM represents the control sample prepared without surfactant addition. **Inset picture** shows magnified version of bar chart to show differences between the slower rate samples.

The calculated rate of reaction (resazurin dye molecules degraded s^{-1} cm^{-2}) as shown as a bar chart in figure 4.20 can be used as an additional measurement of photocatalytic activity, which can be considered more reliable as it does not require normalisation of results, or a first order reaction. Instead this calculated rate uses the maximum measurement of resazurin absorption observed along with the minimum measurement of resazurin absorption to determine the overall rate of degradation. Thus, it does not measure the rate as a first order reaction as above for the absorption curves, meaning that the fluctuations due to incomplete degradation etc. do not affect the overall result.

Using this calculated rate of reaction, depicted in figure 4.20, it can be seen that sample A B98 0.5 d significantly overshadows other samples in terms of photocatalytic performance, with an average rate of degradation of 1.30 x 10^{15} (resazurin molecules degraded s^{-1} cm^{-2}). Table 4.3 shows the relevant data for comparison with other samples, whereby it can be seen that this sample shows the smallest calculated crystallite size of just 5.5 nm which is significantly smaller than that obtained for other samples (all > 8 nm). As mentioned previously, a smaller crystallite

size enables a larger surface area to volume ratio for photocatalysis to take place, and thus a faster photocatalytic performance is to be expected for this sample.

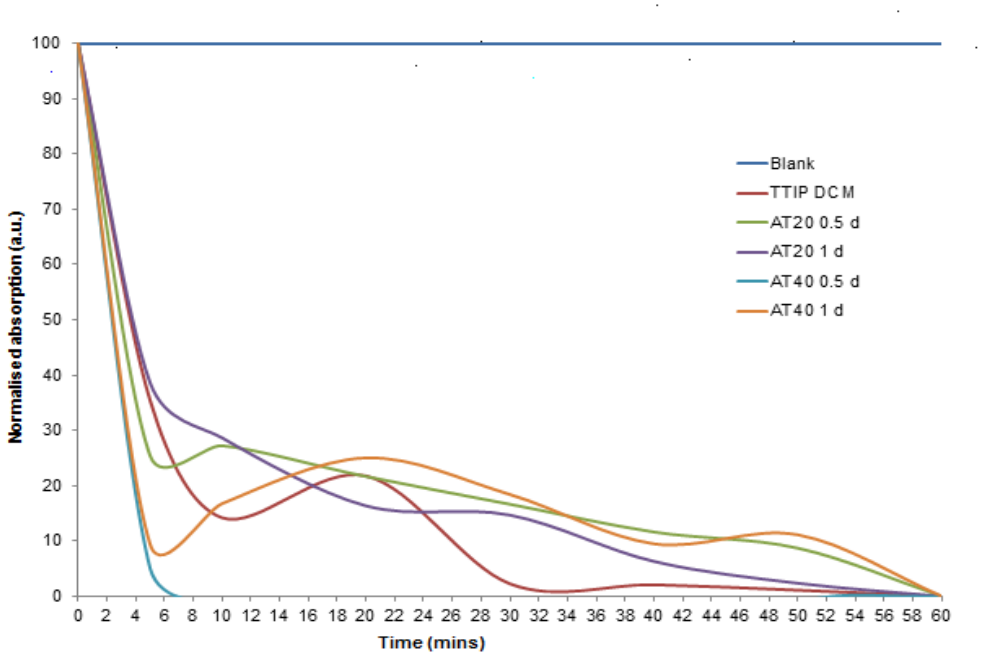

Figure 4.21. Normalised absorption curve used to determine photocatalytic half-life in minutes for samples prepared by AACVD reaction of TTIP in DCM with addition of Tween surfactants. TTIP DCM sample represents the sample prepared without surfactant addition and is used for comparison.

4.2.2.6 Conclusions: TTIP precursor with DCM as solvent with surfactant addition

Thin films of photocatalytically active TiO_2 were deposited at 400 °C using TTIP precursor in DCM solvent, with the addition of Tween and Brij surfactants in two concentrations; 0.5 M and 1 M. The effects of surfactant addition were explored using several analysis and characterisation methods including SEM, contact angle measurements, AFM surface roughness, XRD and UV/Vis. The addition of surfactant was found to significantly affect the photocatalytic performance of the deposited thin films, depending on the surfactant type used and the concentration. AACVD films produced without surfactant addition exhibited an average half-life of 12.5 minutes for Rz degradation, with a calculated rate of photoactivity of 1.86×10^{13} (dye molecules degraded s^{-1} cm^{-2}), compared to the highest photoactivity obtained by sample A B98 0.5 d which had a half-life of just 2.75 minutes and a photoactivity rate of 1.30×10^{15} (dye molecules degraded s^{-1} cm^{-2}). This enhanced performance was attributed to a number of factors

including smaller particle size (60 nm vs 90 nm for control film) and increased texture coefficient (2.95 vs 2.64 for control film) in the (004) preferential plane.

4.2.2.7. Discussion and conclusion: AACVD TiO_2 thin films prepared with toluene as solvent vs DCM as solvent

This chapter has focused on exploring the effects of different solvents on the TiO_2 thin films produced by AACVD. This has been in order to obtain an understanding of which parameters enhance the photocatalytic activity of the samples produced, and thus if the solvent choice affects this. In addition, exploration of the solvent affects enables a better understanding of the role of the surfactant in optimizing the thin film properties.

In figure 4.30(a) and (b) the photocatalytic rates for all the samples produced are shown as a bar chart for comparison. It can be seen from these figures that there is no significant or continual trend across samples that can be used to determine which solvent produces optimum films for photocatalytic applications. However, it does show a clear indication that the use of Brij surfactant has enabled a significant enhancement of photocatalytic activity. In addition, by considering the plain TTIP samples prepared without surfactant addition in isolation from the Brij prepared samples, it can be seen that the use of toluene solvent is clearly favourable as it has produced a thin film with the higher average photocatalytic rate; 3.88×10^{13} (molecules degraded s^{-1} cm^{-2}) vs 1.86×10^{13} (molecules degraded s^{-1} cm^{-2}) for the DCM prepared sample. It can be seen from table 4.4 that the TiO_2 thin film prepared with toluene is more hydrophilic (exhibiting super hydrophilicity after 30 minutes UV irradiation), has increased surface roughness (average of 134 nm RMS vs just 39 nm for the DCM prepared film), and a smaller crystallite size (7.5 nm vs 10 nm for DCM prepared film). It is this combination of factors that enables the sample to exhibit a faster rate of resazurin degradation; owing to better adsorption of the dye on the surface and a greater surface area to volume ratio which the reaction can take place.

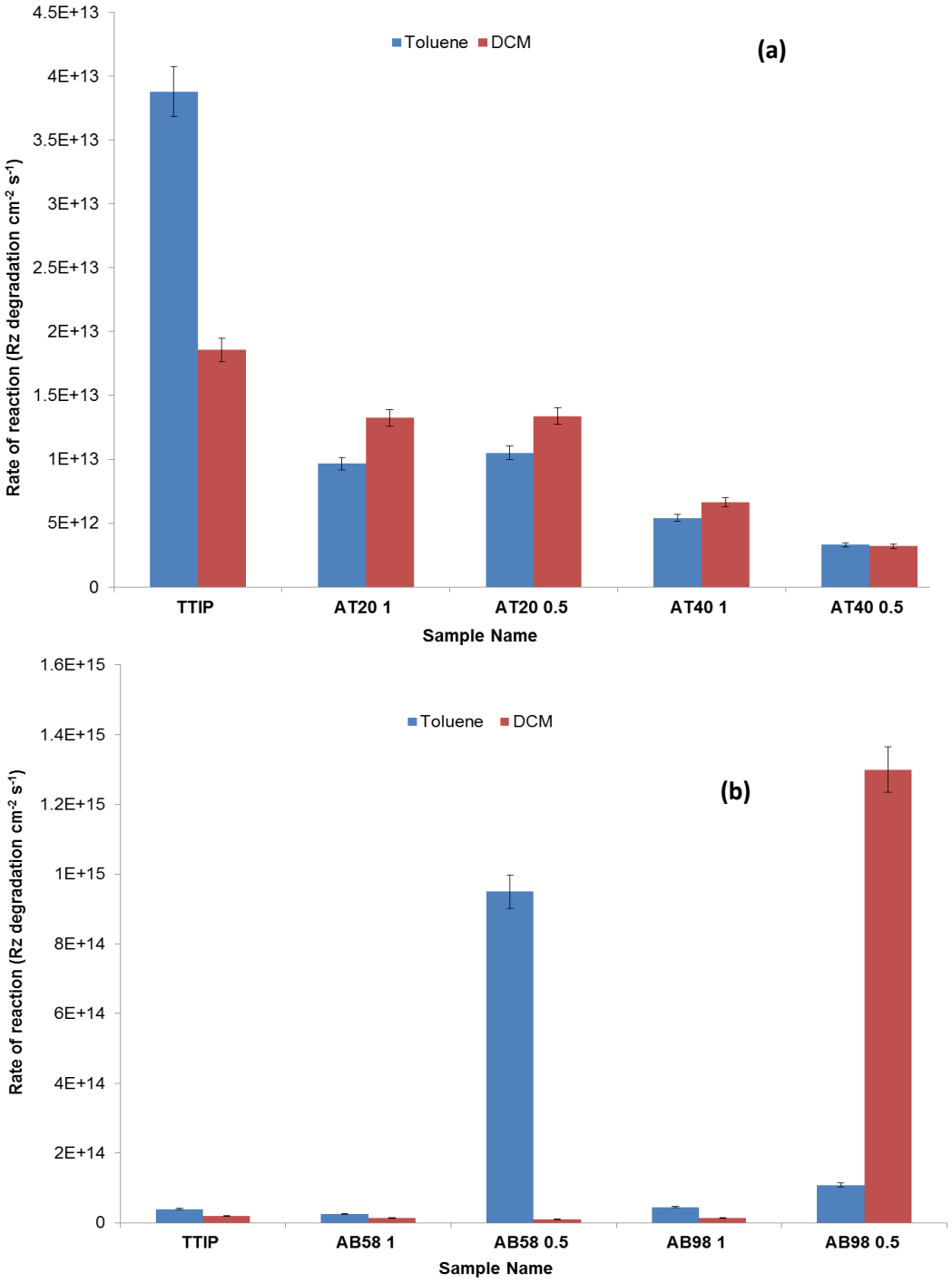

Figure 4.30(a). Bar chart comparison representing the rate of calculated photoactivity for resazurin dye molecules degraded s^{-1} cm^{-2} for each AACVD sample type prepared with toluene (blue) and DCM (red) as solvent. TTIP represents the control sample prepared without any surfactant addition. Surfactant types are represented as T20 and T40 for Tween 20 and Tween 40. Surfactant concentrations are represented by 0.5 (0.5 M) and 1 (1 M). Error bars show 5% experimental error. **(b)** Brij prepared samples.

Table 4.4. Summary table to show the samples exhibiting the fastest photocatalytic degradation rates for resazurin dye and the respective data for each sample that contributes to the enhancement performance observed. Green highlighted values are the highest photocatalytic rates observed. Yellow highlighted areas are an indication of which properties of the material may have contributed to the enhanced photocatalytic performance.

Sample Name	Contact Angle (°) before & after UV irradiation		Average particle size (nm)	Average film thickness (nm)	Average surface roughness RMS (nm)	Texture Coefficient	Average Crystallite Size (nm)	Calculated rate of photoactivity (dye molecules degraded s^{-1} cm^{-2})
A B98 0.5 t	119	10	40	3350	97	2.75 (004)	5.5	1.08×10^{14}
A B58 0.5 t	52	4	80	1130	134	2.70 (004)	11	9.50×10^{14}
TTIP Tol	67	4	110	810	134	1.46 (004)	7.5	3.88×10^{13}
TTIP DCM	35	12	90	1100	39	2.64 (004)	10	1.86×10^{13}
A B98 0.5 d	65	29	60	1160	23	2.95 (004)	5.5	1.30×10^{15}

Of all the samples prepared by AACVD, those produced with the addition of Brij surfactants have exhibited significantly faster photocatalytic degradation rates for resazurin compared to the control films prepared without surfactant, as seen in table 4.4. The fastest activities have been calculated as 9.50×10^{14} (dye molecules degraded s^{-1} cm^{-2}) for sample A B58 0.5 t (prepared with Brij 58 0.5 M in toluene) and 1.30×10^{15} (dye molecules degraded s^{-1} cm^{-2}) for sample AB98 0.5 d (prepared with Brij 98 0.5 M in DCM). As photocatalysis is a complex phenomenon with many interlinking characteristics affecting the performance of a material, it is not possible to attribute this enhanced performance to a single material property. However, in table 4.4 some properties have been highlighted as an indication to the factors that have contributed to improved photocatalytic performance. It can be seen that the two fastest photocatalytic rates have been exhibited for AB58 0.5 t and AB98 0.5 d, samples which have the smallest average crystallite size of 5.5 nm, and the largest texture coefficients in the 004 anatase plane of 2.75 and 2.95 respectively. A small crystallite size is often linked to increased photocatalytic performance owing to the increased surface area upon which the reaction can take place. A large texture coefficient can also lead to increased photocatalytic activity whereby this preferential orientation in the 004 anatase plane has been reported previously by our group.[233,236] The (004) plane is a plane of anatase which has a low atom-packing density,[239] meaning that electron mobility in this plane is enhanced, thus making this surface more favourable for a surface redox reaction, such as photocatalysis.[241]

Chapter 5: Results: Hybrid chemical vapour deposition of titanium dioxide thin films and the effects of surfactant addition

5.1 Introduction

Hybrid chemical vapour deposition (HCVD) incorporates the aerosol-assisted (AACVD) technique with atmospheric pressure (APCVD) in order to combine the distinct advantages of each process. The resulting hybrid method shows great potential for the production of thin films, as hybrid films incorporate the advantages of APCVD (robustness, uniformity and coverage) with the versatility of AACVD, as non-volatile precursors can be used as long as they can be dissolved within a solvent.[244] This hybrid technique has been used only a handful of times in recent literature, primarily for the deposition of thin films where a specific additive is incorporated, such as for the production of nanocomposite vanadium dioxide thin films,[245] and vanadium dioxide films doped with gold nanoparticles.[246] As a result, it is an ideal continuation of the research in this thesis to explore the incorporation of surfactants into the deposition of titanium dioxide thin films via HCVD.

The distinct advantages of APCVD for the production of titanium thin films are that, like AACVD, it is an inexpensive coating technique that is readily applicable to industrial scale up, where APCVD is already used in the mass market production of self-cleaning TiO_2 film coatings on glass.[124] This means that these techniques are particularly appropriate for the application proposed in this thesis; semi-transparent dye solar cells for energy efficient glazing, where large sheets of float glass would be coated with TiO_2 on a continuous manufacturing line before being built up into DSCs. To our knowledge this is the first study of hybrid CVD for the production of TiO_2 thin films with modified morphology from the incorporation of surfactants.

5.2. Results: TiO_2 thin films prepared by HCVD

All films deposited by HCVD at 550 °C covered the entire surface area of the glass, showing evidence of birefringence which indicates a variation in thin film thickness across the film surface. Some carbon incorporation in the films was noticeably visible by the naked eye, particularly for those films produced with higher concentration of surfactant. All films were robust and passed the scotch tape test. The addition of an aerosol of surfactant solvent solution

alongside an APCVD gas stream of TTIP precursor and ethanol solvent was found to modify the thin film thickness, morphology, particle size, surface roughness, wetting properties and photocatalytic performance of the films produced, as will be discussed in the following sections.

In chapter 4, three surfactant concentrations were studied with AACVD; 0.5 M, 1 M and 2 M. It was found that the increase in concentration to 2 M did not produce a significant enhancement to thin film properties; however Brij surfactants were found to show the fastest photocatalytic performance of all samples produced. It is for this reason that the three concentrations 0.5, 1 and 2 M have been studied for Brij surfactants only in this chapter. Tween surfactants have been incorporated in two concentrations; 0.5 M and 1 M only, as increased concentration (2 M) of Tween surfactants was found to not produce any significant enhancements to thin film properties in chapter 4.

Table 5.0. HCVD details: surfactant name, corresponding sample name and concentration of surfactant added (mol/ dm^3) and deposition temperature.

Surfactant used	Sample Name	Concentration of Surfactant (mol/dm^3)	Deposition temperature *(Ramp rate: 15°C min^{-1})*
Nil	HCVD	0	
Brij 58	HB58 0.5	0.5	
	HB58 1	1	
	HB58 2	2	
Brij 98	HB98 0.5	0.5	
	HB98 1	1	**Substrate temperature:** 550 °C **Gas Flow rate:** 1L/min^{-1}
	HB98 2	2	
Tween 20	HT20 0.5	0.5	
	HT20 1	1	
Tween 40	HT40 0.5	0.5	
	HT40 1	1	

5.2.1. Results: HCVD of TiO_2 thin films from TTIP precursor with ethanol as solvent, modified with Tween and Brij surfactant addition via an aerosol stream

5.2.1.10. Thin film morphology: Brij surfactants

In hybrid CVD the surfactant mixture is added separately to the precursor gas stream and so the choice of solvent is less crucial as it does not need to be non-aqueous in order to prevent the precipitation of the water sensitive precursor, TTIP. This means a less polar solvent can be used, such as methanol or ethanol, which has the benefits of increased volatility meaning that a faster reaction time is possible as the solvent atomises much quicker into an aerosol that can be delivered to the reaction chamber by AACVD. Two initial experiments were performed to investigate the suitability of solvents in hybrid CVD, and to see whether the incorporation of a surfactant aerosol stream via hybrid CVD was a viable option. As seen in the SEM images in figure 5.0, two very different thin film morphologies were obtained when different solvents were in a surfactant solution; methanol (HB98 1-m) and toluene (HB98 1-t) with Brij 98 surfactant mixed in a 1 M concentration.

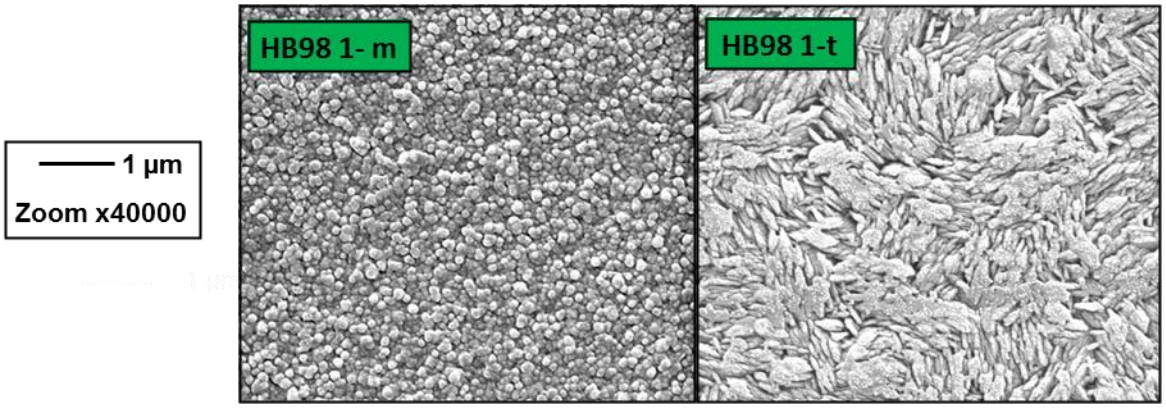

Figure 5.0. SEM images of TiO_2 thin films produced via HCVD with the surfactant mixture added via aerosol in two forms; Brij surfactant in 1M concentration in a solution of methanol (HB98 1-m) and Brij surfactant 1M concentration in toluene (HB98 1-t). Films were deposited at 550 °C.

Toluene is a much heavier solvent with a high miscibility number (23 M^b), reduced polarity (2.4) and low volatility (110.62 °C boiling point) compared to methanol (miscibility number = 12 M^b, polarity 2.4, boiling point = 64.7 °C).[247] The different properties of the solvents affects their behaviour and interaction with the precursors in the gas phase, thereby affecting the subsequent

nucleation and growth of the thin film. It was found that the use of methanol as a solvent produced smaller, more defined spherical particles compared to toluene, due to the increased volatility of methanol. Smaller particle size offers a larger catalyst surface area and greater explosion of active sites to the organic molecules to be degraded. This means that smaller particle sizes/larger surface areas are often reported as the determining factor in photocatalytic performance whereby the large surface area enables increased adsorption of organic molecules and so a faster reaction rate. As a result methanol was used as the solvent for producing the surfactant solution. As mentioned in the introduction to this chapter, the Brij surfactants were found to produce more photocatalytically active thin films from the AACVD experiments discussed in chapter 4, and so three concentrations were studied here, in order to determine whether there is an optimum concentration for thin film enhancement. The SEM images for the thin films produced with Brij 98 and Brij 58 in concentrations of 0.5, 1 and 2 M are shown in figure 5.1.

In order for the experiments to produce a set of films representative of just the effects of surfactant addition in thin film deposition, it is necessary to determine that any changes observed in film morphology, microstructure, photocatalytic performance etc. is not due to the hybrid process used where an additional aerosol stream is passed through the reactor. As a result, the control film used here is not just a plain APCVD film, but rather a thin film produced from APCVD with an additional aerosol stream of just the solvent (methanol, 10ml) passing through the chamber, thus this is still regarded as a hybrid film, and so plain samples without surfactant are named HCVD. This served two purposes; (1) ensured a similar timescale was used for thin film deposition as the APCVD gas flow was turned off after all of the AACVD solution was atomised and passed through the chamber (as with the surfactant solutions ~2-3 minutes) (2) ensured the observed effects when adding surfactants was not just to do with additional solvent vapour passing through the chamber and interacting with the APCVD gas flow.

From the SEM images in figure 5.1 a clear difference in morphology can be observed between the sample prepared without surfactant addition (Named here “no surfactant-TTIP”) and those prepared with Brij surfactants. The plain control sample shows very thin, needle-like particles of random sizes and orientations, with an average particle size of 45 nm determined from ImageJ (table 5.2). The morphology of the Brij prepared samples is different whereby only spherical particles are observed, with a much larger average size, ranging from 70-90 nm depending on the

concentrations used, whereby increased concentrations of surfactant produced larger particle sizes, e.g. 90 nm for HB58 2 and 80 nm for HB98 2 compared to 70 nm for HB58 0.5 and HB98 0.5. This is the opposite effect to that which was observed in chapter 4 for AACVD thin films prepared with Brij surfactants, whereby increased concentration of the surfactant was found to decrease particle size. The difference here is most likely to do with the incorporation of two gas streams, whereby the effects of increased concentration will be combined with increased gas phase interactions, and thus larger agglomerations of growing particles and increased nucleation on the thin film surface, leading to larger particle growth. This also offers an explanation to the increased agglomeration observed in the films as the concentration of surfactant is increased.

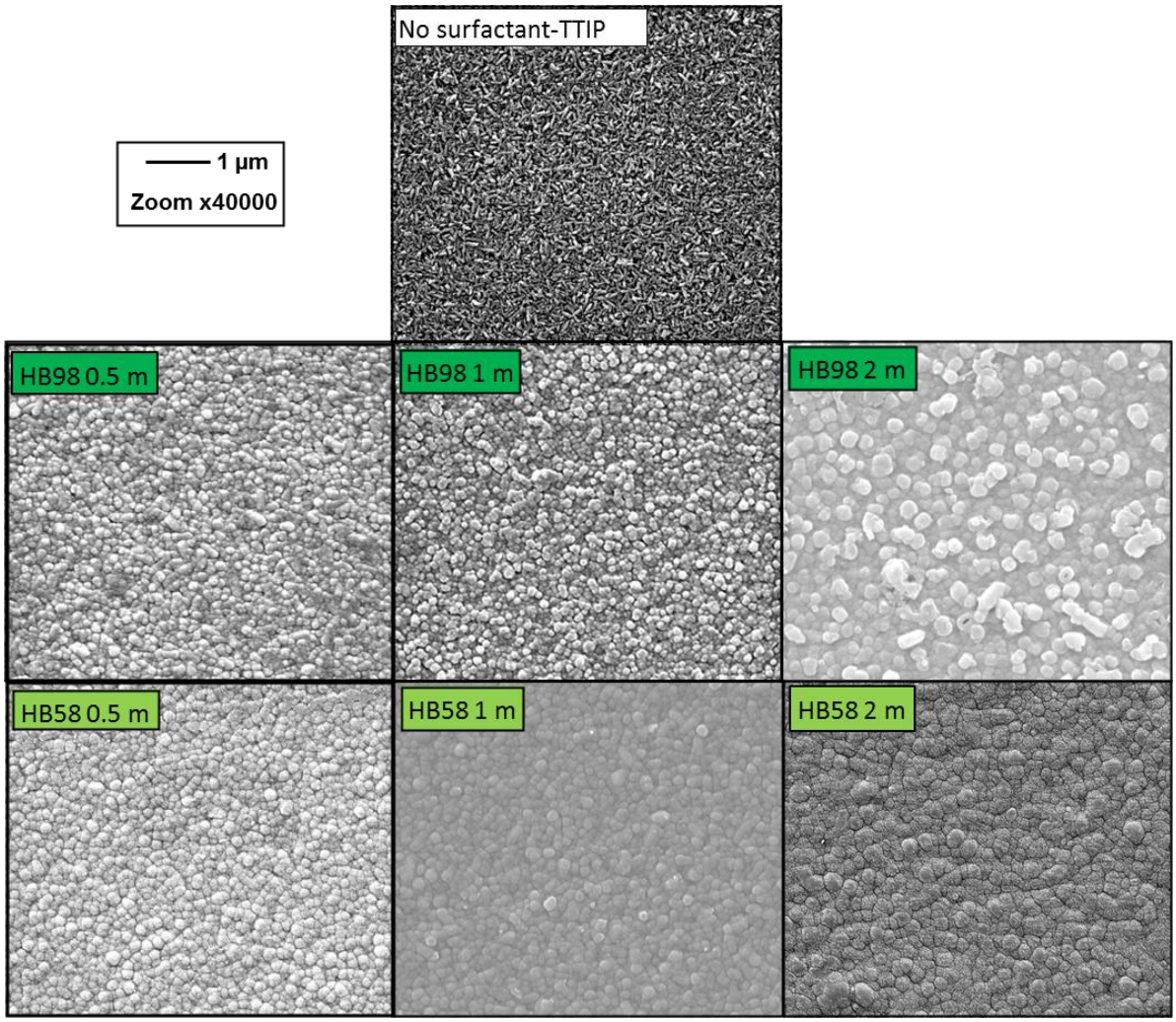

Figure 5.1. SEM images of TiO_2 thin films produced via HCVD with Brij surfactants added via a methanol solution. Surfactants were added in concentrations of 0.5 M – 2 M as indicated by numbers. Films were deposited at 550 °C.

5.2.1.11. Thin film morphology: Tween surfactants

The hybrid thin films produced with Tween surfactants are shown in figure 5.2. As the use of Tween surfactants showed little enhancement to photocatalytic activity in the AACVD experiments described in chapter 4, only the two best concentrations were tested here; 0.5 M and 1 M. Unlike the hybrid Brij films discussed above, the Tween samples produced by hybrid CVD appear to show a combination of both needle like particles (as for the control sample prepared with no surfactant) and spherical particles, as typically observed for thin films produced with surfactants. The average particle sizes observed were the smallest of all HCVD samples produced; just 20 nm and 10 nm for both T 20 and T 40 samples in the 0.5 M and 1 M concentrations respectively (table 5.2). This is most likely to do with the type of micelles that are formed by the surfactant, which can speculatively suggested to be cylindrical or rod-shaped surfactant micelles, whereby the thin film growth occurs around/ in-between or alongside the micelles, thus leading to a combination of particle sizes and shapes.

Furthermore, the addition of Tween surfactant produces similar effects to those observed previously with AACVD samples described in chapter 4, whereby rice-like particles become more circular. It can be seen in the SEM image of the film obtained from HCVD with the lowest concentration of Tween 20 (0.5 M) that the addition of Tween 20 in this low concentration has resulted in some spherical particles forming in among larger rice-like particles. Increasing the concentration of Tween 20 0.5 M through to 1 M results in a reduction in the particle size, as with the AACVD samples, whereby here this is reduced from an average of 20 nm for HCVD T20 0.5 M to just 10 nm for HCVD T20 1 M. This is consistent with previous discussions about the surfactants role in stunting and controlling the TiO_2 particle growth. This is also observed for thin films produced with Tween 40, which show much spherical clusters of small rice-like particles. As Tween 40 is a heavier surfactant, it can be assumed that it has resulted in increased stunting of the TiO_2 particles compared to Tween 20.

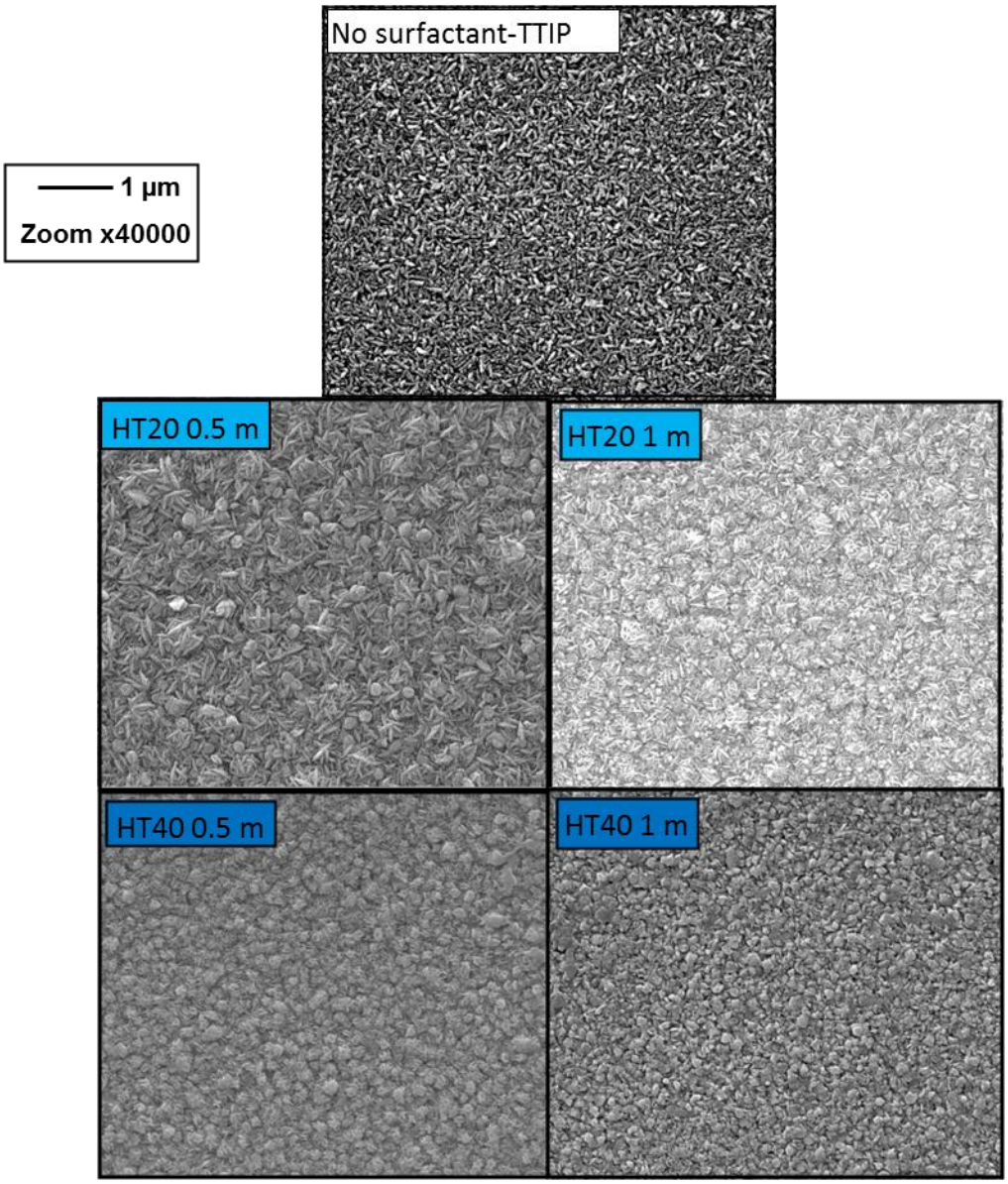

Figure 5.2. SEM images of TiO_2 thin films produced via HCVD with Tween surfactants added via a methanol solution. Surfactants were added in concentrations of 0.5 M – 1 M as indicated by numbers. Films were deposited at 550 °C.

5.2.1.2. Thin film thickness and particle size

The thin films produced by HCVD were overall much thicker than those produced by any other method explored within this thesis; this is owing to the nature of the experimental procedure used. HCVD is a combination between AACVD and APCVD, and it is well known that APCVD thin films are on average much thicker than those deposited by AACVD methods. The APCVD gas flow of precursor and solvent was produced from preheated steel bubblers (heated to 150 ºC for TTIP and 65 ºC for ethanol) after gas was directed to the reaction chamber under high temperature (gas lines at 150 ºC). The reaction was carried out until all 10ml of the

surfactant/solvent mixture was atomised and carried to the reaction chamber via aerosol, where it would then combine with the APCVD gas flow of TTIP precursor and ethanol solvent. The depletion of surfactant/solvent solution would typically take 2-3 minutes, after which the APCVD valves were closed and plain N_2 gas was left to flow through the chamber. As a result of this timescale, 2-3 minutes is a relatively long time for an APCVD reaction, whereby typical reactions are run for 1 minute owing to the thick films produced.

The HCVD films produced were found to be within an average range of 800 nm to 4600 nm. It was found that there was significant variation across the film surface in this thickness, as seen by the large standard deviation observed in the bar chart of average thickness values shown in figure 5.3. This variation in film thickness is due to birefringence across the film surface, which is a result of turbulent gas flow (which is more likely in HCVD reactions due to the meeting of two gas flow streams at the inlet to the reaction chamber) and also due to the temperature gradient across the reactor, where some parts may be hotter or cooler, thus encouraging increased (or decreased) film growth in certain areas. In addition, the incorporation of two gas flow streams is likely to reduce the rate of gas flow into the reactor chamber and subsequent deposition of the thin film whereby the different concentrations and type of surfactants affects the rate of thin film growth in different ways, as evidenced by the thin film thickness shown in figure 5.3.

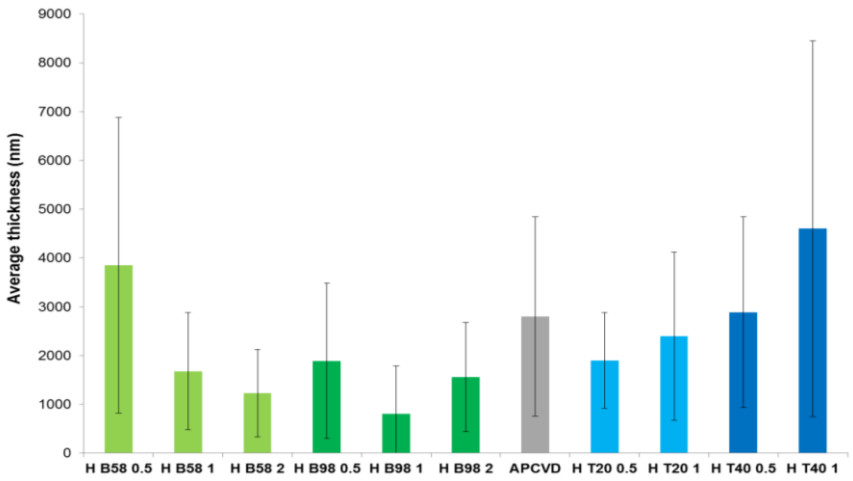

Figure 5.3. Bar chart comparison of the average thin film thickness of thin films prepared by HCVD with TTIP precursor and ethanol as solvent, with increasing concentrations of different surfactant mixtures in methanol added via AACVD, indicated by colours. Error bars show the standard deviation. Numbers represent the molar concentration from 0.5 M – 2 M.

The addition of surfactant was found to modify the average thickness of films depending on the surfactant type and concentration used, whereby the thickest film on average was observed for sample HT40 1 (4500 nm) and the thinnest was observed for HB98 1 (1000 nm). For the Brij surfactants it was found that the increased concentrations resulted in thinner films being produced, whereas the increased concentration of Tween surfactants resulted in an increase to film thickness. As discussed in chapter 4, the theory of the packing model as developed by Israelachvili[230] can be used to understand the behaviour of surfactants in solution relative to their size and shape. Surfactants investigated herein are non-ionic surfactants with ethylene oxide head groups, meaning that they follow a specific behaviour when in solution.

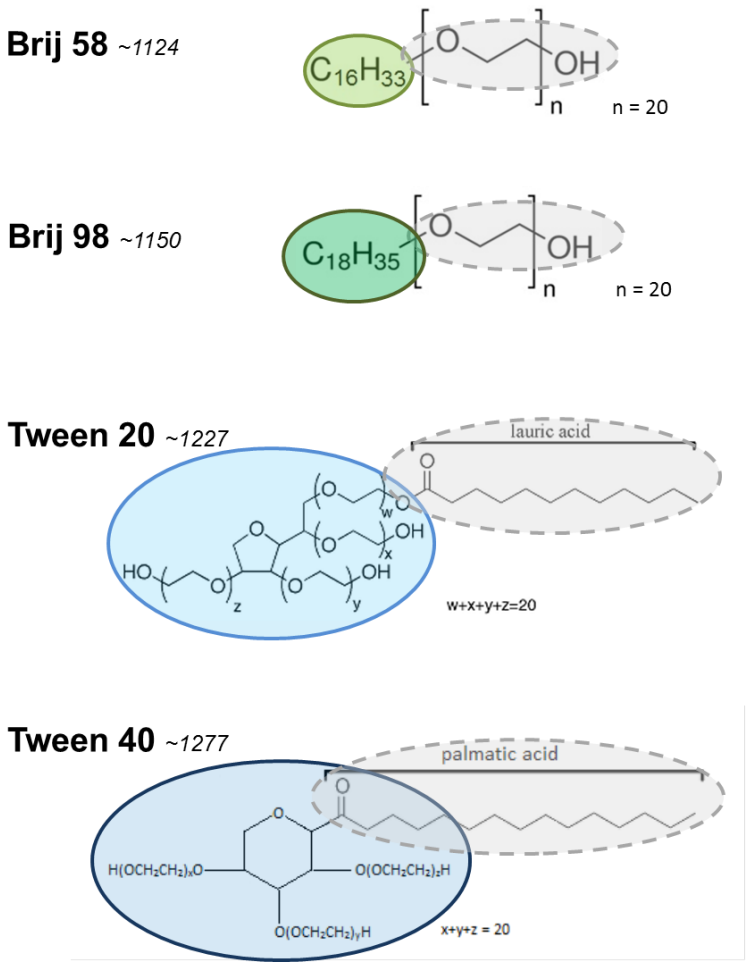

Figure 5.4(a). Schematic representation of surfactant size relative to one another with exaggerated representations of head and tail size.

The differences between the relative sizes of the surfactants used here are shown schematically in figure 5.4(a), as an exaggerated schematic to understand the size and shape of the head groups relevant to the surfactant tail. It has already been discussed in chapter 4 that Brij 58 forms inverted micelles as a result of the large head group which is balanced out by a long alkyl chain tail .[228] As the Brij 58 surfactant concentration is decreased, the micelle size decreases, and this is reflected in the reduction in thin film thickness. As the surfactant concentration is increased, the micelle sizes increase, stunting thin film growth to produce thinner films. Brij 98 films are slightly thinner than Brij 58 films, between a maximum of 800-1890 nm vs 1230-3850 nm for the Brij 58 films. This indicates that the slightly larger head of Brij 98 affects the packing of the surfactant and thus the growth of the film, and as expected, the larger head acts to stunt film growth and produces overall thinner films as seen in the bar chart (figure 5.3).

The Tween surfactants have significantly larger head groups, and much shorter tail lengths (figure 5.4 (a)) and as such they are reported in literature to form large cylindrical or rod shaped micelles.[243] This is a speculative assumption, however it can be used to account for the increased thin film thicknesses observed here when using Tween surfactants, as the Tween film thicknesses are within the range of 1900-4600 nm, much higher than that observed for Brij surfactants (1000-2800 nm) and the control films prepared without surfactant (1500 nm). As a result, if Tween surfactants do in fact form these cylindrical or rod shaped micelles, it can be assumed that there is a larger area for the film to grow and nucleate around the micelles compared to more commonly formed spherical surfactant micelles. This is shown schematically in figure 5.4(b), whereby the film, represented here as orange circles, shows three potential routes for thin film growth, inside the cylindrical micelles (1), alongside (2) or in-between (3). Spherical micelles shown to the right side of figure 5.4(b) however, provide more limited opportunity for thin film growth in pronounced directions; therefore a thinner thin film may be expected when these type of micelles form from surfactants. This relates to previous arguments discussed in chapter 4 sections 4.2.1.1.

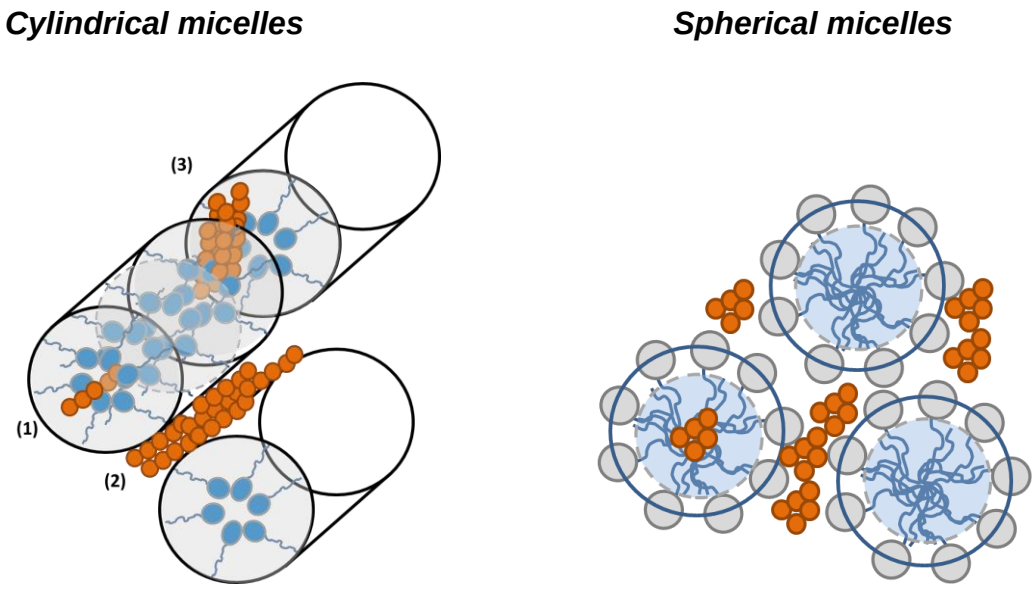

Figure 5.4(b). Schematic of potential micelle formation with non-ionic surfactants and the nucleation/growth of film surrounding them.

5.2.1.3 Surface roughness and wetting properties

The hybrid CVD films produced exhibit a range of surface roughness values, ranging from 17 nm – 68 nm depending on the surfactant and concentration used. These values were on average much lower than the surface roughness values obtained for AACVD samples, as shown in figure 5.5, whereby AACVD samples prepared with toluene solvent have been observed to produce the roughest thin films. This is owing to the reduced volatility of the toluene solvent and its role in binding to the nucleating thin film and directing growth. Overall there was no significant enhancement to surface roughness found through the addition of surfactants in HCVD, whereby the thin film sample produced without surfactant addition (HCVD/ No surfactant-TTIP) showed an average RMS surface roughness of 63 nm, and the highest average RMS value observed for 68 nm as for HB58 0.5 M (table 5.1). The only significant trend observed was that the addition of surfactants was found to in fact reduce the average surface roughness of thin films produced, whereby the lowest value obtained was 17 nm as for HB98 2.

As discussed in chapter 4 with the AACVD samples, increasing the concentration of surfactant can lead to a corresponding increase in particle size and agglomeration between particles, thus leading to an overall smoother thin film surface and reduced surface roughness. This trend has been observed for some of the HCVD results, as seen in figure 5.6, where average particle size has been directly compared with surface roughness, e.g. sample HB98 2 has an average particle size of 80 nm and an average RMS roughness of just 17 nm. In addition, even if an increase in

average particle size has not been observed, those samples prepared with increased concentration of surfactant show lower RMS roughness values regardless, e.g. HB58 2 (55 nm), HB982 (17 nm), HT20 1(42 nm) and HT40 1 (45 nm). This is owing to the "smoothing" effect due to agglomeration between particles that is typically observed when concentration of surfactant is increased, and can be seen in the SEM images in figures 5.1 and 5.2.

Unlike previous studies with the use of surfactants, the samples produced with Brij surfactants did not exhibit higher surface roughness values, whereby the Tween samples showed on average greater surface roughness, as seen in figure 5.5 below. This can be explained by the morphological differences between the samples as seen in the SEM images in figure 5.3 and 5.4. The reduced roughness values observed for the Brij samples correlate with the SEM images in figure 5.3, whereby the samples with less defined spherical particles and increased agglomeration tend to have the reduced roughness values, e.g. HB98 0.5, HB98 1, HB98 2 and HB58 1 (37 nm, 44 nm, 17 nm and 23 nm respectively). Sample HB58 0.5 shows the highest surface roughness value, whereby the SEM image shows a morphology of defined spherical particles, thus indicating a higher surface roughness.

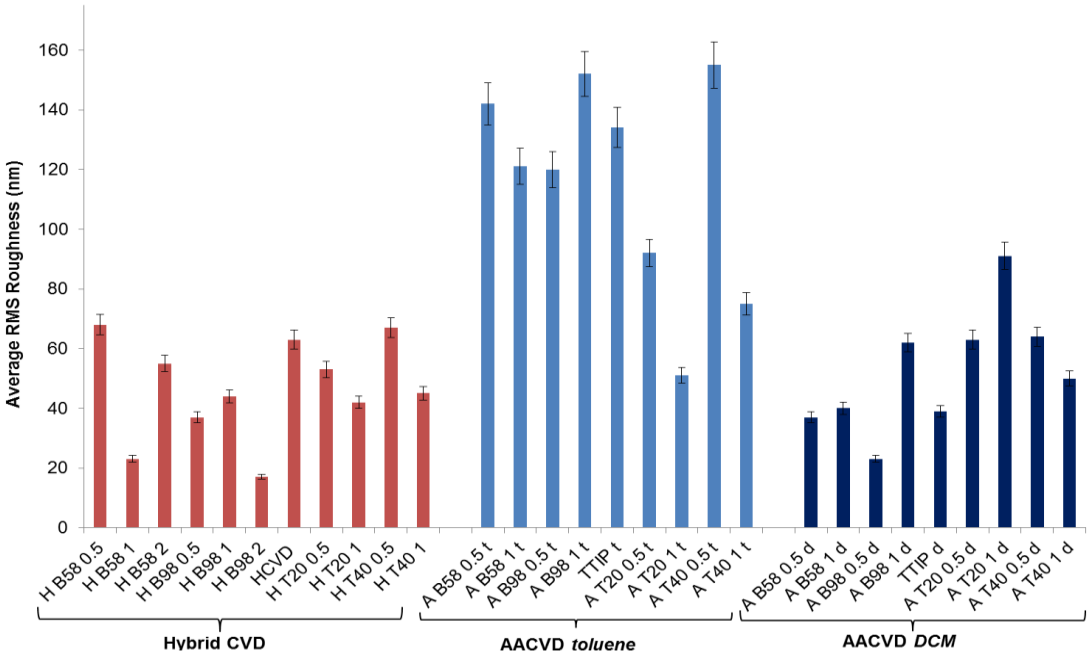

Figure 5.5. Bar chart to show average surface roughness (nm, root mean square) for TiO_2 thin film samples prepared by hybrid CVD (red) , AACVD with toluene as solvent (light blue) and AACVD with DCM as solvent (dark blue). Error bars show 5% experimental error.

The high roughness values observed for Tween samples prepared by hybrid CVD can also be explained by study of the SEM images and film morphology in figure 5.2. The samples prepared with Tween surfactant show the presence of two particle types; both thin needle-like shaped particles (as observed for the plain HCVD control sample without surfactant) in addition to small spherical particles. This unusual combination of two particle shapes and sizes is likely to contribute to a higher overall surface roughness within the thin film.

The SEM images for the Tween samples shown in figure 5.2 also show greater variation in particle size and shape which produces a greater topographical variation across the sample surface and thus a higher surface roughness due to the increased surface area to volume ratio. The surfactant plays a significant role in the growth of TiO_2 particles as found with the sol-gel and AACVD studies described in chapter 3 and 4. The surfactant can either act as an aide to reduce particle size and increase surface roughness or it can work to significantly increase particle size and decrease surface roughness, whereby both trends are observed here with HCVD samples.

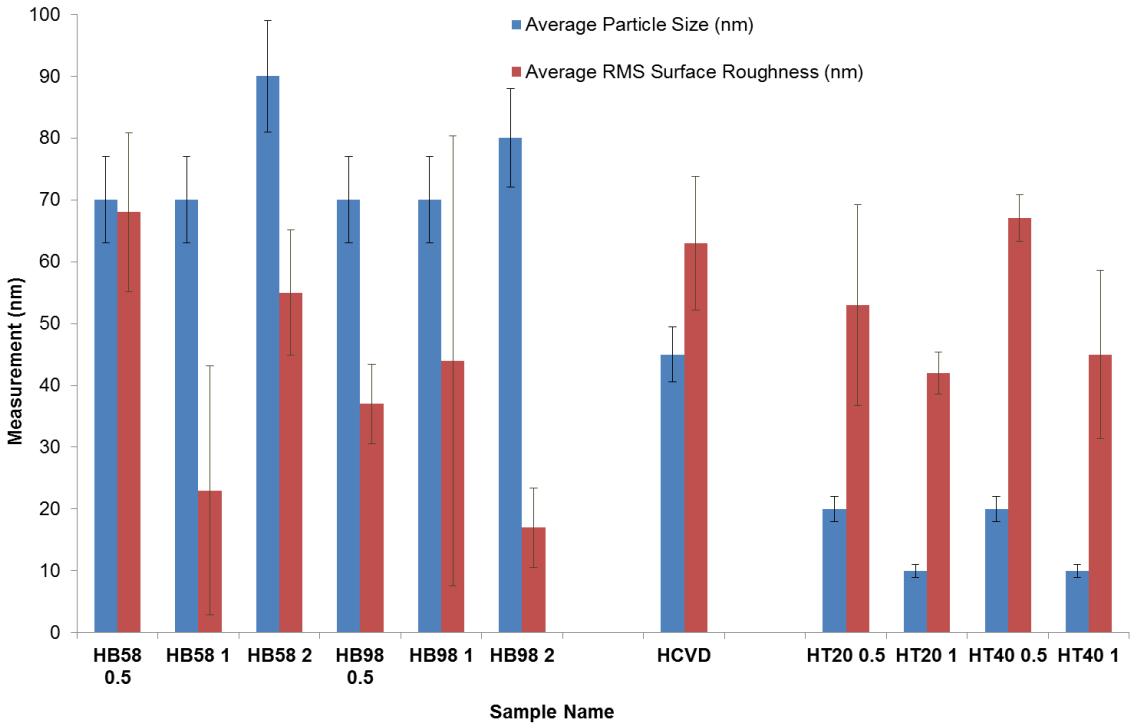

Figure 5.6. Bar chart comparison between average particle size (nm) shown with 10% measurement error, and the average RMS surface roughness (nm) shown with standard deviation error.

All thin films produced by HCVD exhibited a reduction in contact angle after exposure to 30 minutes of UV irradiation, indicating hydrophilic properties, as expected for TiO_2 thin films (table 5.2). However, this hydrophilic behaviour was found to be much less pronounced compared to those produced in chapters 3 and 4 for sol-gel and AACVD derived thin films. This reduced wettability correlates with the reduced surface roughness observed for the HCVD samples and may also be a result of the wetting mechanism of the droplet on the surface when measuring the contact angle. he size and distribution of roughness on a surface affects the contact angle and corresponding wetting properties of a surface whereby the droplet can sit either on top of the roughness features or sink in-between these features. The spacing of these roughness features on the surface are therefore critical in determining whether the droplet sits or sinks and thus whether a sample is more or less hydrophilic. Therefore the surface structure can result in significantly enhanced super hydrophilicity/ hydrophobicity of a sample. These two possible wetting regimes are called Cassie-Baxter and Wenzel, as shown in figure 5.7. For the Wenzel regime to be favoured the droplet that sits on the surface must follow equation 6.0, where P is pillar pitch, D is pillar diameter, R is droplet radius and H is pillar height:

Equation 7.0

$$\frac{(P-D)^2}{8R} \geq H$$

$$\cos\theta_r = \frac{\pi D^2}{4P^2}(\cos\theta + 1) - 1$$

$$\cos\theta_r = \left(1 + \frac{\pi DH}{P^2}\right)\cos\theta$$

Figure 5.7. Schematic to show the two possible wetting regimes of a droplet on a surface; Cassie-Baxter and Wenzel, with corresponding equations for measuring the contact angle on a rough surface (θ_r) when the contact angle on a smooth surface is known, where D = pillar diameter, P is pillar pitch, H is pillar height and r is droplet radius.

The surface features of the HCVD films discussed in this chapter are not 'pillars' as depicted in the Cassie-Baxter and Wenzel wetting regimes described above, as the surface of HCVD features are made up of particles. Thus determination of the exact height of the particles is difficult as they are often small very small and coalesced. As a result, surface roughness values from AFM measurements are used as a proxy of the height of these surface features, whereas the average particle size is used as the diameter. From these values, using equation 7.0 it can be determined whether the HCVD films follow the Cassie-Baxter or Wenzel regime. The SEM images from figure 5.1 and 5.2 are used in figure 5.8.1 below alongside contact angle and average roughness values to show the relationship between morphology, wetting properties and surface roughness. All HCVD thin films produced here follow the Cassie-Baxter regime, (whereby working for a sample is shown as an example in figure 5.8.2 below), meaning that the water droplets sit on top of the thin film surface, thus the films are more hydrophobic, which is a result of the low surface roughness.

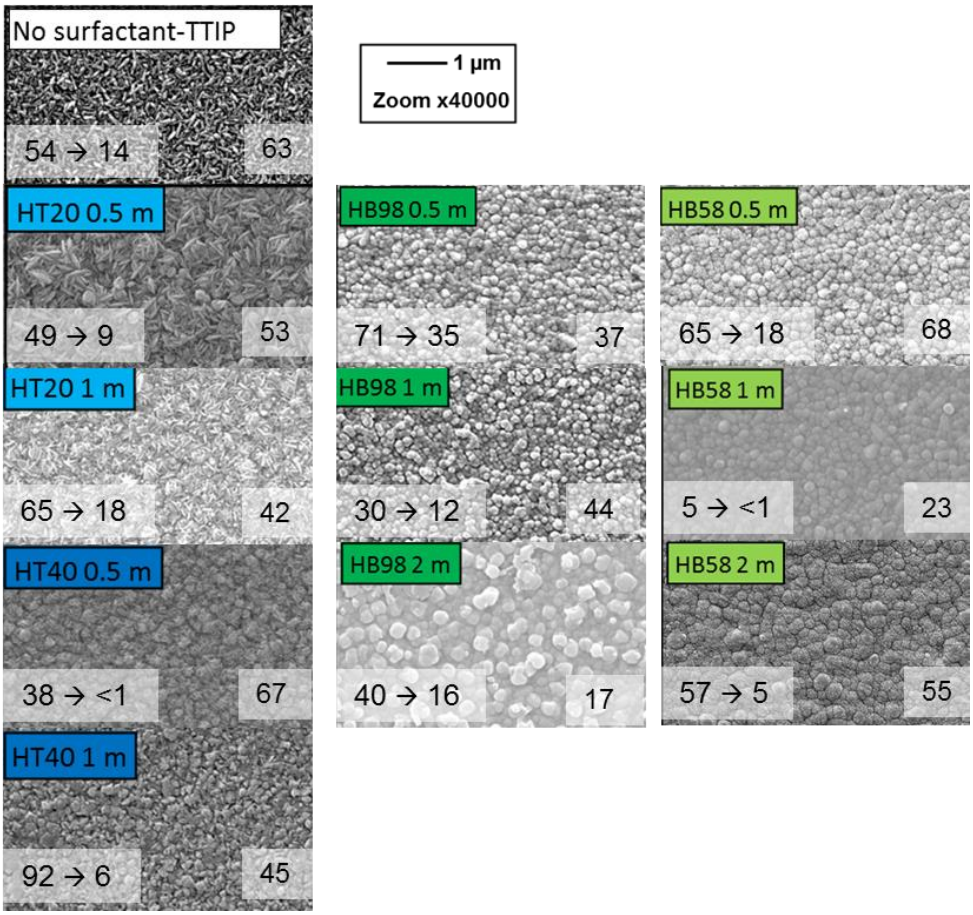

Figure 5.8.1. Cropped SEM images with corresponding contact angles (before° → after °) to the bottom left of each image and surface RMS roughness (nm) to the bottom right of each image.

Some samples, such as the Brij 58 HCVD samples, exhibit superhydrophilic behaviour after UV irradiation, with a reduction of contact angle to <5 °, whereas Brij 98 samples show less hydrophilic behaviour after UV irradiation, as the reduction in contact angle varies between 12-35 °. This links back to the morphology of the thin films, whereby the particle size and the surface roughness affect the hydrophilic properties, as rougher thin films with more defined particles and less agglomeration traditionally exhibit more hydrophilic behaviour. Here the Brij 98 films show reduced surface roughness and more thin film agglomeration, and so exhibit much less hydrophilic behaviour. Those films which behave in a more hydrophilic way tend to have a more varied morphology, such as well-defined, small particles with a higher surface to volume ratio and higher surface roughness. This is evident with the Tween samples (figure 5.8.1 above) which tend towards superhydrophilic behaviour, as contact angles were reduced to <1, 6, 9 and 18 ° for samples HT40 0.5, HT401 and HT20 0.5 and HT20 1 respectively (table 5.1).

$$\frac{(P-D)^2}{8R} \geq H$$

e.g. Sample No surfactant- TTIP HCVD

Pillar pitch (P) ≈ 22.5 nm
Pillar diameter (D) = 45 nm
Droplet radius (R) ≈ 1000 nm

$$\frac{(22.5 - 45)^2}{8 \times 1000} = 0.063 \text{ nm} \quad < 63 \text{ nm}$$

Height ≈ 63 nm

e.g. Sample HB98 0.5 HCVD

Pillar pitch (P) ≈ 35 nm
Pillar diameter (D) = 70 nm
Droplet radius (R) ≈ 1000 nm

$$\frac{(35 - 70)^2}{8 \times 1000} = 0.153 \text{ nm} \quad < 37 \text{ nm}$$

Height ≈ 37 nm

Figure 5.8.2. Worked example for the estimation of wetting regime for HCVD samples. Pillar pitch was estimated at half the pillar (particle) diameter. The height was estimate as an average of RMS surface values, as given in table 5.1. When the left side of the equation is equal to or greater than the height, the sample will follow the Wenzel rather than the Cassie-Baxter regime.

Table 5.1. Results for samples prepared by HCVD using TTIP with ethanol in combination with the addition of surfactant in a methanol solution. Three concentrations of surfactant were used, 0.5 M to 2 M. Sample 'HCVD' represents the control sample prepared by hybrid CVD without surfactant. Samples were deposited at 550°C until all of the surfactant solution was depleted.

Sample Name	Contact Angle (°) before UV	Contact angle (°) after UV	Average particle size (nm)	Average film thickness (nm)	Average RMS surface roughness (nm)	Texture Coefficient Anatase (004) plane	Average Crystallite Size (nm)	Photocatalytic half-life for Rz degradation (mins)	Calculated rate of photoactivity (dye molecules degraded s^{-1} cm^{-2})
H B58 0.5	63	2	70	3850	68	3.47	18	9	2.2×10^{12}
H B58 1	55	<1	70	1680	23	2.84	16	7	8.0×10^{12}
H B58 2	57	5	90	1230	55	2.94	18	5	1.0×10^{13}
H B98 0.5	71	35	70	1890	37	3.44	18	2	5.0×10^{12}
H B98 1	30	12	70	800	44	3.22	12	10	1.5×10^{13}
H B98 2	40	16	80	1560	17	3.01	13	6.5	1.1×10^{13}
HCVD	54	14	45	2800	63	3.38	15	9	9.8×10^{12}
H T20 0.5	49	9	20	1900	53	2.91	13	12	7.5×10^{12}
H T20 1	65	18	10	2400	42	3.19	15	14	6.6×10^{12}
H T40 0.5	38	<1	20	2890	67	3.28	12	11	9.0×10^{12}
H T40 1	92	6	10	4600	45	3.66	27	6	7.5×10^{12}

5.2.1.4 Crystalline phase identification of TiO_2 thin films

The XRD diffraction patterns for the TiO_2 thin films produced by hybrid CVD are shown in figures 5.10 and 5.11. All TiO_2 thin films deposited show breakthrough to the underlying cassiterite (F:SnO_2 coated) glass substrate, with these peaks identified in figures 5.10 and 5.11 with an asterisk. All HCVD samples showed diffraction peaks attributable to anatase phase TiO_2 with dominant crystal growth observed in the [101] plane and [004] planes, and preferential growth in the [004] plane. The presence of rutile in the [211] plane was also observed for most samples, and is expected due to the high deposition temperature used (550 °C), whereby rutile is more thermodynamically stable than anatase and typically forms at temperatures > 600 °C.[47] In addition, some thin films showed the presence of brookite, in the [221] phase in very low intensity (HB58 0.5, H B98 0.5 and HB98 1) and most Tween films.

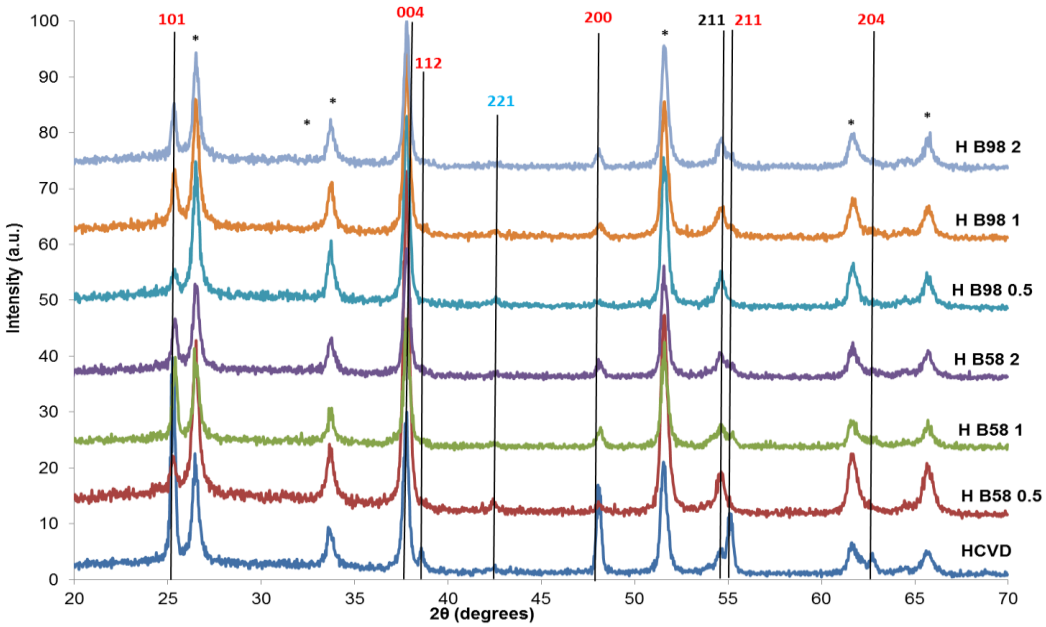

Figure 5.10. XRD of TiO_2 films produced by HCVD without surfactant (HCVD) and with Brij surfactants in methanol via aerosol in several concentrations where numbers represent concentration (M); **Brij 58** (H B58 0.5, H B58 1, H B58 2) and **Brij 98** (H B98 0.5, H B98 1, H B98 2). Peaks identified as anatase are marked in red, brookite in blue and rutile in black. Peaks denoted with asterisks (*) are assigned to the F:SnO_2 coating of the glass substrate. XRD is normalised for intensity.

All hybrid films produced were found to exhibit texture, with the calculated texture coefficients found to be within a narrow range of 2.91-3.66 depending on which surfactant/concentration was used in the film deposition. The texture coefficient (TC) and average crystallite size (nm) were determined using the XRD diffraction patterns shown in figures 5.10 and 5.11, and are listed alongside other thin film properties in table 5.1. The effect of surfactant addition upon texture coefficient is marginal in terms of enhancement, whereby the plain HCVD sample produced without surfactant addition exhibited a texture coefficient of 3.38, and only two samples showed TC values higher than this; 3.47 for HB58 0.5 and 3.44 for HB98 0.5. As the concentration of Brij 58 and Brij 98 surfactant was increased, the TC was observed to decrease, which is in keeping with previous arguments surrounding the role of surfactant in potentially "smoothing" the overall surface of the thin film and reducing roughness, and textural growth within the film. The Tween surfactants showed an opposite effect, whereby the increased concentration from 0.5 M to 1 M resulted in a slight increase to the texture coefficient observed, e.g. HT20 0.5 (2.91) to HT20 1 (3.19) and HT40 0.5 (3.28) to HT40 1 (3.66). The highest texture coefficient was observed for sample HT40 1 with a TC of 3.66, whereby this sample also exhibited the highest crystallite size of 27 nm. However, the XRD pattern for the HT40 1 sample showed very weak peaks of low intensity with a lot of corresponding noise, therefore there is likely to be a large error in the TC and crystallite values calculated. An additional XRD pattern would have to be obtained to determine whether these large values are representative of this sample.

The average crystallite size was found to generally increase with the addition of Brij surfactants; from 15 nm for the HCVD sample prepared without surfactant, to 18, 16 and 18 nm for samples HB58 0.5, 1 and 2 respectively as well as 18,12 and 13 for HB98 0.5, 1 and 2 respectively. On the other hand the Tween surfactants were found to exhibit smaller average crystallite sizes compared to the films prepared without surfactant (15 nm) when added in low concentration (0.5 M; HT20 0.5 = 13 nm and HT40 0.5 = 12 nm). This would be owing to the role of surfactant directing and restricting crystallite growth as discussed in chapter 4, whereby the slight electronegative charge in the surfactants enables them to bind electrostatically to particular crystal surfaces inhibiting and/or directing growth to affect the resulting crystallite size, as observed here.

In comparison to the AACVD samples, the HCVD samples on average were found to exhibit a larger crystallite size as shown in figure 5.12, as well as a slightly higher texture coefficient in

the (004) plane as shown in figure 5.13. This shows that the effects of surfactant addition in HCVD are less pronounced than for AACVD, which is likely to be due to the way in which the surfactant is delivered into the reactor system with the precursor. In AACVD the surfactant is mixed directly with the precursor in a solvent solution and delivered as one into the reaction chamber via atomization. This means the surfactants used in AACVD are much more likely to have an enhanced effect on the thin film growth as they are directly in contact with the precursor from the outset; thus the surfactants stunt the growth of crystallites, making them smaller, and directing the texture of the thin film.

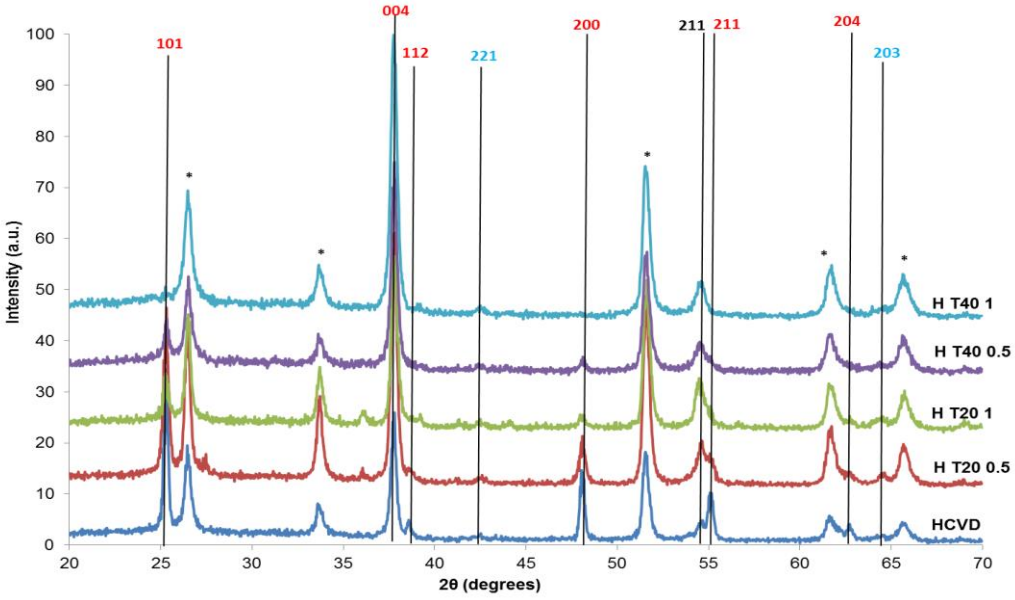

Figure 5.11. XRD of TiO_2 produced by HCVD without surfactant (APCVD) and with Tween surfactants in methanol via aerosol in several concentrations where numbers represent concentration (M); **Tween 20 (**H T20 0.5,H T20 1) and **Tween 40** (H T40 0.5, H T40 1). Peaks identified as anatase are marked in red, brookite in blue and rutile in black. Peaks denoted with asterisks (*) are assigned to the $F:SnO_2$ coating of the glass substrate. XRD are normalized for intensity.

However, in hybrid CVD the surfactant and precursor are delivered to the reaction chamber by two separate routes; by aerosol (surfactant in solvent) and by atmospheric pressure (precursor and solvent). Due to the nature of the APCVD method it is likely that an increased concentration of precursor will be delivered to the reaction chamber and the substrate compared to AACVD. This is because APCVD works by directly heating the TTIP precursor to become a vapour, alongside the solvent which is also heated in a separate chamber to become vapour, and then both

gas streams are carried to the reaction chamber by carrier gas flow where they meet. On the other hand in AACVD the precursor is atomized in a solvent solution before being carried to the reaction chamber by carrier gas flow. As a result the APCVD gas flow will be much more concentrated with TTIP precursor compared to AACVD, and thus the surfactant is likely to have less of an effect when it meets the precursor in the gas phase, as TiO_2 particles are likely to have already begun nucleation.

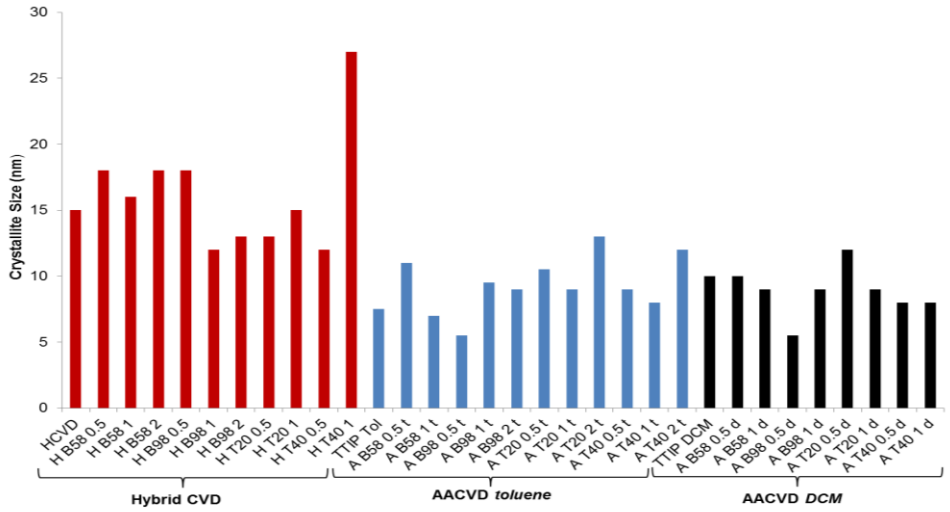

Figure 5.12. Comparison of average crystallite size (nm) for hybrid CVD films (red), AACVD films with toluene (light blue) and AACVD with DCM (black).

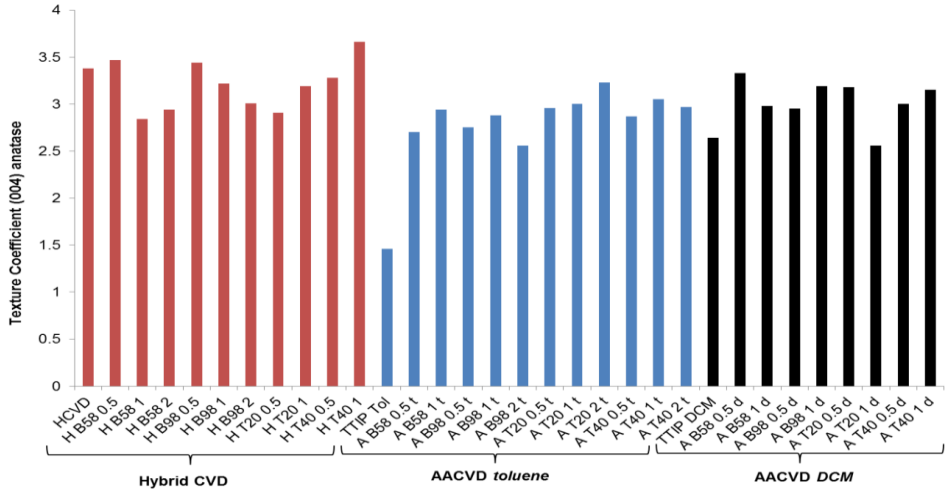

Figure 5.13. Comparison of texture coefficient in the (004) plane of anatase phase thin films produced by hybrid CVD (red), AACVD with toluene (light blue) and AACVD with DCM (black).

5.2.1.5. Photocatalytic activity of thin films produced by HCVD and the effects of surfactant addition

All thin films produced by HCVD were found to be photocatalytically active for the degradation of resazurin dye with UV irradiation. Due to time constraints the average results presented here have been obtained from the average of two repeated experiments rather than three as in other chapters within this thesis. This has resulted in the presentation of results that clearly show the limitations of the analysing the photocatalytic results through normalised absorption curves, as shown by the fluctuations in results shown in figures 5.14 and 5.15 below. Some of the limitations of this method have been discussed in previous chapters, whereby the fluctuations observed in degradation curves is the result of several factors such as; (1) Incomplete drying of the resazurin (Rz) dye on the thin film surface before the start of the experiment resulting in increased fluctuations in absorption as the film dries (2) Number of layers of Rz dye on the film surface whereby increased number of dye layers may mean as one is degraded more Rz dye is exposed underneath causing a jump in the measured absorbance, (3) Analysis of different area of the film- whereby every effort is made to ensure the same 1 cm area is analysed each time, human error may result in another area being tested (4) Quality of Rz ink used, whereby an old batch of Rz has been used which may have already undergone decomposition/ no longer meets standards required for this experiment. Despite the using the normalised degradation curve to assess photocatalytic results, it is used in this chapter as only a comparison with other chapters and will not be discussed in detail. Instead, the calculated rate of photoactivity (dye molecules degraded s^{-1} cm^{-2}) will be used as this was calculated using only the maximum and minimum absorption values and thus is more reliable as it does not take the fluctuating values as seen in the degradation curves into account.

The rate of photoactivity is shown in table 5.1 and is represented as a bar chart in figure 5.16. It can be seen from figure 5.16 that the addition of surfactant to HCVD thin films can lead to an enhanced photocatalytic performance compared to those films prepared without surfactant e.g. APCVD "control" film prepared without surfactant shows an average rate of 9.8 x 10^{12} (dye molecules degraded s^{-1} cm^{-2}) whereas sample HB981 shows a rate of 1.5 x 10^{13} (dye molecules degraded s^{-1} cm^{-2}) and sample Hb98 2 shows a rate of 1.1 10^{13} (dye molecules degraded s^{-1} cm^{-2}). The addition of surfactant has also been found to reduce the photocatalytic performance to as little as 2.2 x 10^{12} (dye molecules degraded s^{-1} cm^{-2}) as for sample HB59 0.5.

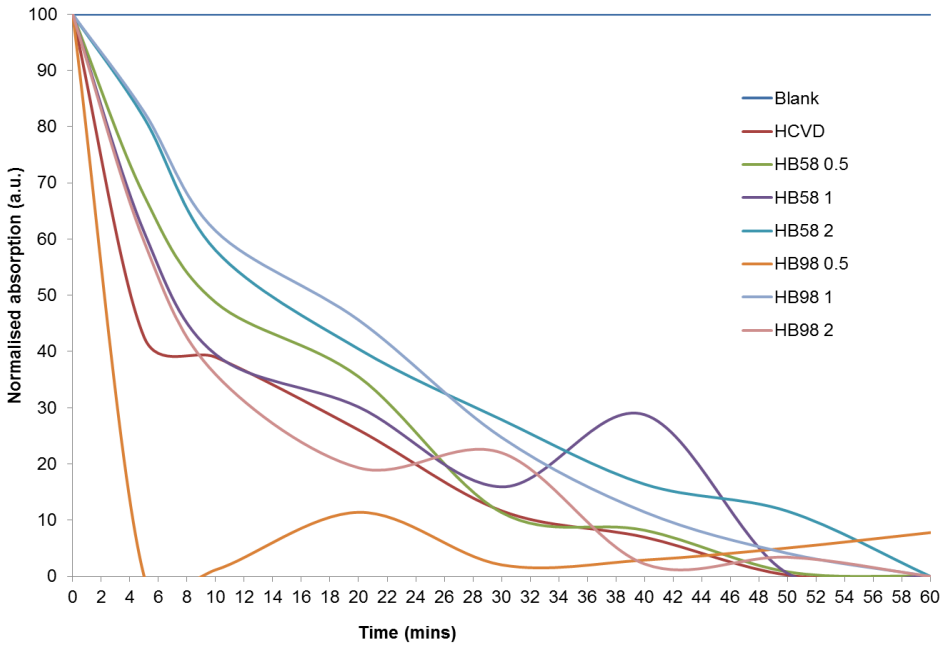

Figure 5.14. Normalised absorption curves for determination of photocatalytic half-life (minutes) for samples prepared by hybrid CVD reactions with and without the addition of Brij surfactants. HCVD represents the films prepared without surfactant and is used for comparison. 0.5, 1 and 2 represent the concentration (M) of surfactant that was used to make the films.

The enhanced performance with the HB98 1 and HB98 2 samples prepared with the highest concentrations of Brij 98 surfactant (1M and 2M respectively) could be due to a number of factors that affect photocatalytic performance such as hydrophilic behaviour, high texture coefficient in the [004] plane (3.22 and 3.44 respectively), and small average particle sizes (12 nm and 13 nm respectively). Unlike samples in previous chapters which have shown increased photocatalytic activity, the samples here do not additionally exhibit enhanced surface roughness. From this we can conclude that crystalline structure is one of the most important properties in assessing the photocatalytic activity of thin films, where a more textured film with small crystallite sizes favour enhanced photocatalytic performance.

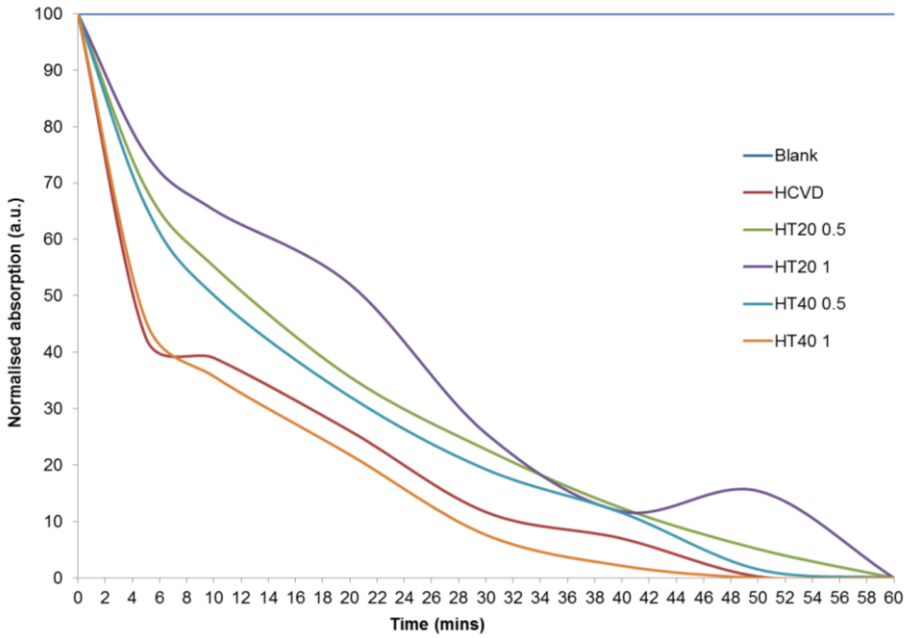

Figure 5.15. Normalised absorption curves for determination of photocatalytic half-life (minutes) for samples prepared by hybrid CVD reactions with and without the addition of Tween surfactants. HCVD represents the films prepared without surfactant and is used for comparison. 0.5 and 1 represent the concentrations (M) of surfactant.

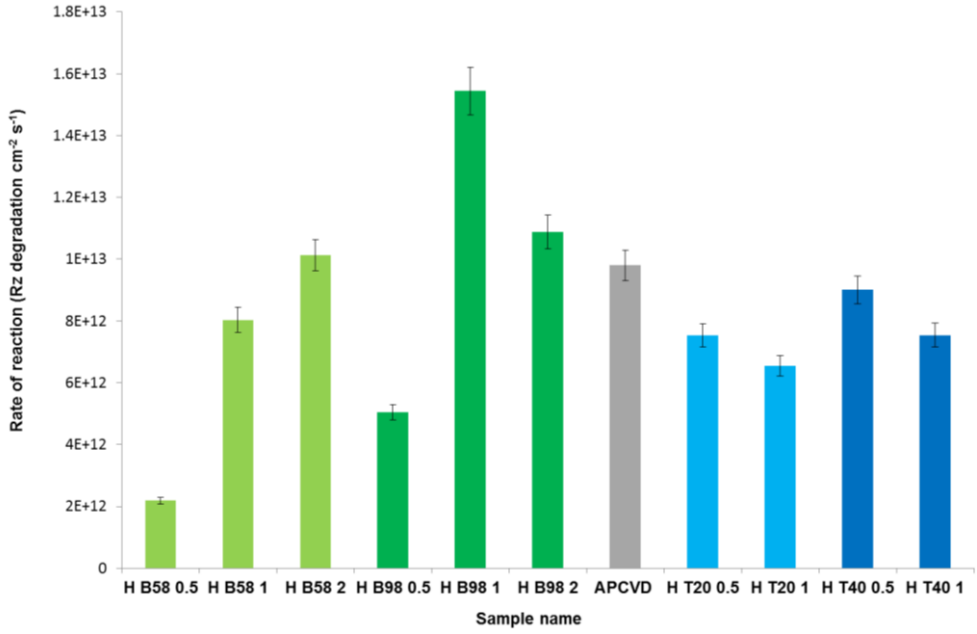

Figure 5.16. Bar chart representing the calculated rate of photoactivity for the degradation of resazurin dye per second per cm^2 for each sample prepared by hybrid CVD with and without surfactant addition. APCVD represents the sample prepared without any surfactant addition. Error bars show standard deviation.

5.3. Discussion on the photocatalytic performance of HCVD thin films in comparison to AACVD and sol-gel prepared films and the effects of surfactant addition

Three methods of thin film deposition have been used to prepare TiO_2 thin films within this thesis; sol-gel, AACVD and HCVD. The addition of Brij and Tween surfactants has been studied to determine the effects of surfactant addition with the aim to find an optimised method for producing photocatalytically active TiO_2 thin films which could also be used in semi-transparent dye solar cells. The photocatalytic performances of all three sets of films are shown below in comparative bar charts in figures 5.18 (a)-(b) as calculated rates of photoactivity (dye molecules degraded s^{-1} cm^{-2}). Only samples which exhibited high performance (> 7.0 x 10^{12} dye molecules degraded s^{-1} cm^{-2}) are shown in these bar charts for simplicity and ease of comparison.

Figure 5.17 (a) shows all samples in one bar chart, where it can be clearly seen that the AACVD samples (shown here in blue) exhibit the best overall photocatalytic performance, with samples prepared with toluene as solvent showing the highest activities, particularly AB58 0.5t and AB98 0.5 t which show rates of 9.50 x 10^{14} and 1.08 x 10^{14} dye molecules degraded s^{-1} cm^{-2}, which is up to two magnitudes higher than the best photoactivities obtained for sol-gel thin films and hybrid films. In addition, comparison of the photoactivities as shown on the magnified bar chart in figure 5.18 (b) it can be seen that the hybrid CVD thin films do perform better on average compared to the sol-gel samples, with the best photoactivities again prepared with Brij 58 and Brij 98; HB58 2 (1.0 x 10^{13} dye molecules degraded s^{-1} cm^{-2}) HB98 1 (1.5 x 10^{13} dye molecules degraded s^{-1} cm^{-2}) and HB98 2 (1.1 x 10^{13} dye molecules degraded s^{-1} cm^{-2}). The sol-gel samples show much lower values, between 1.7 x 10^{12} for the plain TTIP sample prepared without surfactant, up to the highest values obtained with the TiBALD precursor of 9.51 x 10^{12} dye molecules degraded s^{-1} cm^{-2} for the film prepared without surfactant and 8.4 x 10^{12} dye molecules degraded s^{-1} cm^{-2} for the Brij 58 film prepared with a concentration of 0.0004 mol dm^3. The AACVD thin films produced with surfactant are found to exhibit enhanced photocatalytic performance owing to a combination of factors as explained in chapter 4, including small average particles sizes (ranging from 30-80 nm), high surface roughness (ranging from 23-155 nm), small crystallite sizes (5.5- 12 nm), and large texture coefficients in the [004] plane (2.56-3.33).

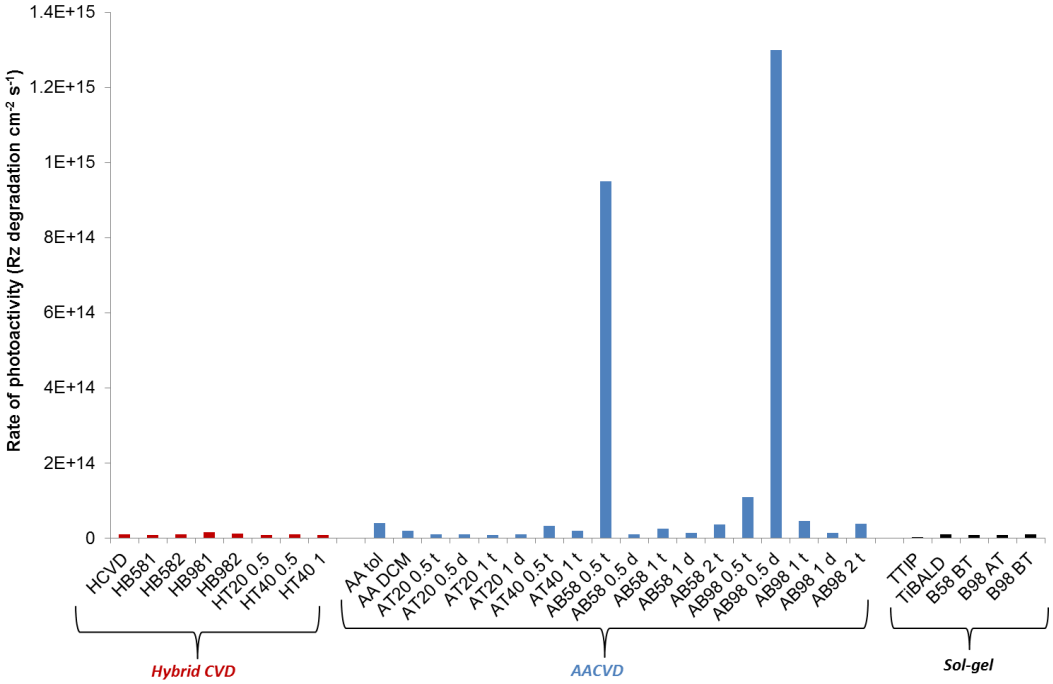

Figure 5.17(a). Bar chart to compare the photoactivity rates of thin films prepared by hybrid CVD (red), AACVD (blue) and sol-gel (black). Rates are shown as rate of photodegradation of resazurin dye s^{-1} cm^2 . APCVD, AA tol, AA DCM and TTIP and TiBALD represent the samples prepared by each method without surfactant addition.

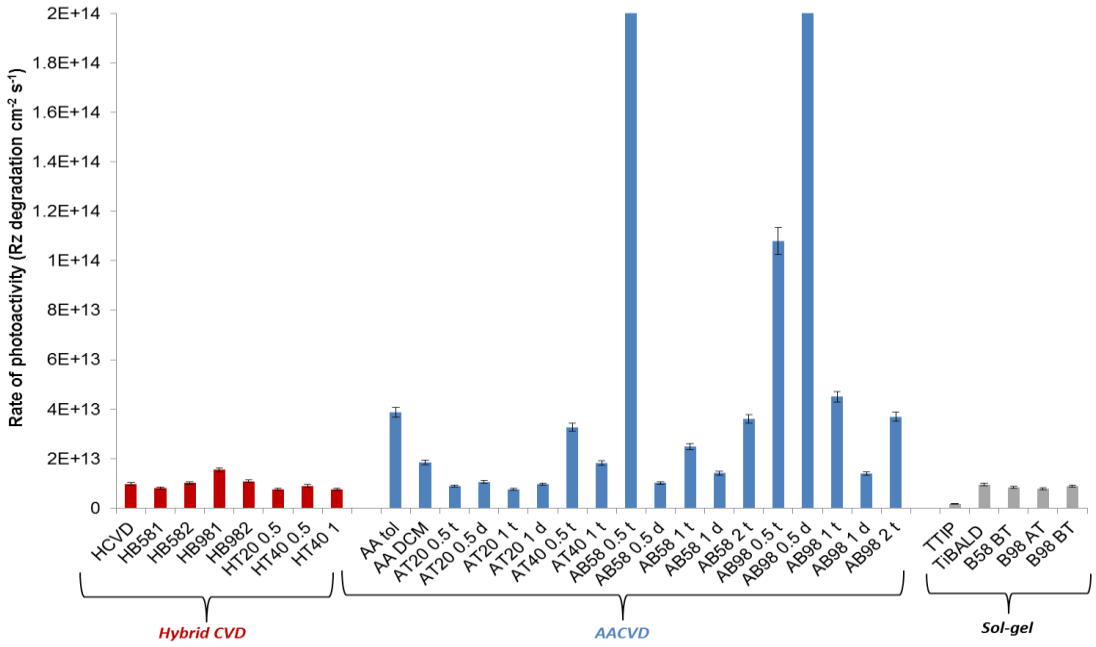

Figure 5.17(b). Enlarged version of fig 5.18(a) for better comparison between sample sets. Bar chart here is as above, comparing the photoactivity rates of thin films prepared by hybrid CVD (red), AACVD (blue) and sol-gel (grey). Errors shown are 5% experimental error.

Chapter 6: Results: Incorporation of surfactant modified TiO_2 thin films into semi-transparent dye-sensitised solar cells

6.1. Introduction

The focus of this thesis has been two fold; to produce TiO_2 thin films by methods which can be easily scaled up in the glazing industry and to then optimise these thin films for use in semi-transparent dye-sensitised solar cells (DSSCs) for use as energy efficient glazing. Since the discovery of dye sensitised solar cells (DSSCs) by Grätzel and O'Regan in 1991,[64] DSSCs have attracted vast academic and industrial interest primarily due to their low cost and ease of fabrication. [248]

The fundamental concept of the DSSC involves the use of a highly porous TiO_2 thin film as a photoanode which is then sensitised by an adsorbed organic dye such as N3 'black' dye, or a similar porphyrin dye. Such highly porous TiO_2 films are typically made from Degussa TiO_2 paste, and are opaque to the eye- thus unsuitable for the preparation of a semi-transparent dye solar cell as is the aim of this thesis. On the contrary, such thin films as those produced in this thesis, from sol-gel, aerosol-assisted CVD and hybrid CVD are all transparent, yet very dense in nature and thus despite exhibiting optimum transparency, they also have significantly reduced porosity as a consequence. This reduction in porosity means that less dye is adsorbed onto the thin film surface, and so less photoexcited electrons are transferred to the conduction band of the TiO_2 as per the mechanism described in detail in the introductory section 1.4.1.

By their very nature of being semi-transparent, the DSSCs produced in this thesis exhibit low efficiency as most incident light passes directly through the device, meaning that there is a very small amount of light which can actually be absorbed. The amount of light absorbed is limited by several factors, of which the primary one is the amount of dye adsorbed onto the thin film surface. The photovoltaic performance of DSSCs depends on the amount of absorbed photons, which is limited by the thickness of the TiO_2 layer and the illumination conditions.[249] In addition, high solar conversion in DSSCs requires a large surface area of porous TiO_2 in order for optimum adsorption of the sensitising dye, as well as optimum construction or a good network between TiO_2 particles for light harvesting and fast electron transportation. Many methods have

been reported for the preparation of TiO_2 photoanodes, including sol-gel, hydrothermal synthesis, electrospinning, anodisation electrodeposition methods and most commonly, screen printing. However, few of these methods produce a semi-transparent TiO_2 thin film with optimum properties as those described above.

Several variations of semi-transparent TiO_2 thin films for DSSC applications have been reported in literature yet there have been no papers to the authors knowledge that directly connect the production of semi-transparent TiO_2 thin films and their direct use in semi-transparent dye solar cell devices.[250,251] Such limited academic reporting of semi-transparent dye-sensitised solar cells and their configurations is likely to be due to their great commercial applicability and interest, whereby there are several patents for transparent dye sensitised solar cell technologies,[252] as well as a specific company called Glass 2 Energy commercialising such devices. Glass 2 Energy[253] is a newly established Swiss company (formed in 2011) that has acquired a DSSC license for a new type of photovoltaic cell developed by Professor Grätzel of the Swiss Federal Institute of Technology in Lausanne (EPFL). This company have developed the production technology and obtained patents for the industrial production of semi-transparent dye solar cell devices for building integrated photovoltaic (BIPV) applications. Their mission is described as "turning glass facades into profitable energy production, and producing facilities without losing transparency."[2] Unfortunately as this technology is patented it is not available for specific discussion in this thesis, however it is reported that the Glass 2 Energy DSSC uses a "perfused hold conductor"[2] in its configuration- something which was not explored at all in this thesis due to time constraints. Figure 6.1 below shows the description of the product from Glass 2 Energy and several pictures of their BIPV window facades, reproduced with permission. Glass 2 Energy have industrially produced DSSC modules of up to 1M x 1M, with four different colour options including green, orange, red and blue (expected 2017), with an optical transmission of 35% and an average energy production of up to 45 kwh/m^2 recorded in 2016.[2]

This commercial application of the semi-transparent DSSC confirms that it is a very attractive variation of PV technology as it effectively enables the solar cell to be embedded within the classic double glazing window unit, meaning that semi-transparent DSSCs could soon become a viable and simple addition to any commercial building or home façade.[254] In order for DSSCs to become viable BIPVs the optical, thermal and photovoltaic efficiency properties need to be

measured and assessed, of which there are several studies already published on this subject by Yoon et al[255,256] and Bouvard et al.[254]

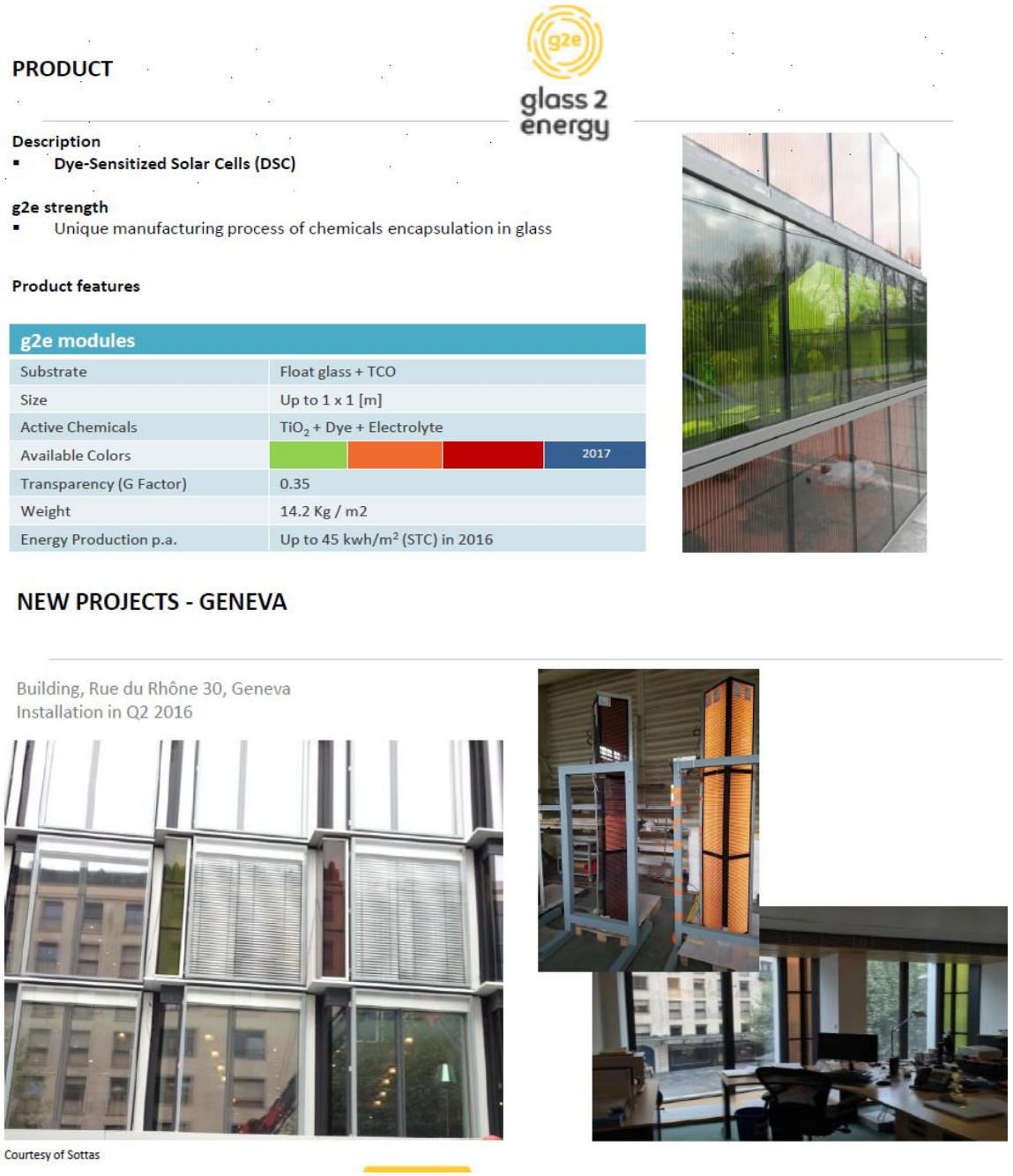

Figure 6.1. Product details of the DSSC technology produced by Glass 2 Energy Ltd for building integrated photovoltaic (BIPV) window facades. Glass 2 Energy reserve all rights to this information and pictures which have been reproduced in this thesis with full permission.[2]

In the paper by Bouvard et al, the optical and thermal properties of the Glass 2 Energy prototype PV modules were studied in order to determine the optimum combination of glazing for enhanced efficiency. This was performed in collaboration with Glass 2 Energy and it was found that although their modules are particularly promising as they can be laminated to the glass pane of a classic double (or triple) glazing unit and be installed as a regular window, the measurements of these modules demonstrated that the visible transmittance of the units were too low to be used as a whole building façade.[254] Thus, the authors concluded that they such modules could be combined with clear glass windows in a building to meet the necessary visibility requirements, and as seen in figure 6.1, Glass 2 Energy have already begun introducing these semi-transparent DSSC units in combination with regular transparent windows into buildings. Bouvard et al,[254] also came to the same conclusion as the main aim of this thesis; that in highly glazed building, such as a high-rise office building, it would be economically attractive to incorporate semi-transparent DSSCs as part of the façade, thus providing a fraction of the energy demand for internal building use, whilst providing a colourful alternative to plain windows thus enhancing the aesthetic of the entire building.

6.2 Experimental Methods: DSSC configuration and variations

The typical dye-sensitised solar cell configuration as described in the introductory section 1.4.1 consists of a sandwich of dye-sensitised TiO_2 thin film on a transparent conducting substrate with a counter electrode between which is a layer of ionic redox electrolyte. This configuration as for a semi-transparent DSSC is shown in figure 6.3 below, whereby the counter electrode is either indium doped tin oxide (ITO) glass or fluorine doped tin oxide (FTO) glass with a layer of finely dispersed platinum deposited on top.

6.2.1. Preparation of the counter electrode (cathode)

6.2.1.1. ITO Counter Electrode

The Indium doped tin oxide (ITO) counter electrodes were obtained as ITO slides (resistivity 70-100 Ω) from Sigma Aldrich and used as supplied. The substrates were cleaned in an ethanol solution placed inside an ultrasonic water bath for 10 minutes and subsequently air dried.

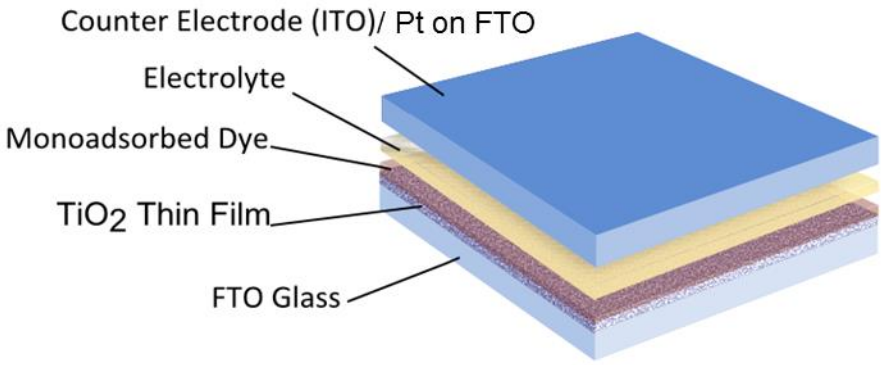

Figure 6.2. Schematic of the semi-transparent dye sensitised solar cell configuration, where the counter electrode is either indium doped tin oxide (ITO) glass or fluorine doped tin oxide (FTO) glass with a layer of finely dispersed platinum is deposited, the electrolyte is a ionic redox electrolyte, the monoadsorbed dye is that which is adsorbed onto the TiO_2 thin film which is deposited onto the FTO glass directly.

6.2.1.2. Pt Counter Electrode

There are several methods reported for fabricating highly active catalytic platinum electrodes,[257] however simple doctor blading method was adopted in this thesis using Platisol T/SP, a platinum precursor supplied by Solaronix. The presence of a catalytic amount of platinum at the cathode greatly enhances the electron transfer rate to the electrolyte, enabling an increased charge density within the solar cell and thus higher photo-currents.[258]

FTO glass slides were cut to size (~3 cm x 3 cm) and cleaned in an ethanol solution placed inside an ultrasonic water bath for 10 minutes and subsequently air dried. The platisol T/SP was applied as a single drop to the FTO conductive surface using a dropping pipette, after which the drop was immediately doctor bladed across the entire FTO surface in one quick continuous motion to ensure complete coverage of the substrate. The platinum precursor was then converted into an activated platinum coating by heat treatment on a hot plate to 450 °C for 10 minutes, after which the electrode was left to cool to room temperature naturally before using within a DSSC device. The Pt activated thin films were stored in the dark until use as extensive light exposure can reduce their activity.[258]

6.2.2. Preparation of dye-sensitised TiO_2 thin film working electrode (anode)

The TiO_2 thin films to be used as DSSC devices were cut to size as required (~ 3 cm x 3 cm) and then washed in an ethanol solution within an ultrasonic water bath for 10 minutes and air dried prior to use.

The dye solution used was N3 dye (Di-tetrabutylammonium cis- *Bis(isothiocyanato) bis(2,2'-bipyridyl-4,4'-dicarboxylato ruthenium(II))* made up into a 0.3mM solution with ethanol. After cleaning the TiO_2 thin film would be left to soak in the dye solution in a wide base container up to a depth of ~2 mm so that the top of the TiO_2 surface was covered by dye. These solutions were covered with parafilm to prevent evaporation of the ethanol solvent and covered in foil/kept in the dark to prevent degradation of the light sensitive dye. As reported in literature, the length of time which the TiO_2 thin film is left in the dye solution can affect the resulting performance of the DSSC device.[137,259–261]After soaking in the dye, the TiO_2 thin film is impregnated with a monoadsorbed layer of dye on its surface, enabling increased light absorption when set up as a DSSC device.

The time length of dye adsorption (and thus the quantity and nature of dye adsorbed on the film surface) is another key factor in DSSC fabrication.[261] The dye adsorption or 'loading' time should be sufficiently long so that the interfacial surface of the TiO_2 film is completely covered with a dye monolayer, however not too long that it results in increased charge recombination and inhibited device performance. Dye loading times of 0.5 hours up to 24 hours are frequently reported in literature, depending on the type of thin film microstructure, whereby more porous films require reduced dye loading times. Several dye loading times were tested for this thesis, starting with 3 - 5 hours, 12 hours and subsequently 24 hours. It was found that the longer dye adsorption time of 24 hours enabled enhanced device performance and so this was chosen as a baseline for testing all DSSC devices herein. A longer soaking time of 42 hours was later tested after several experiments with TiO_2 thin films which had been soaked for 24 hours, whereby it was considered that due to the increased density of the TiO_2 thin films used in this thesis and their reduced porosity, perhaps the monolayer of dye on the film surface was not at an optimum thickness. The longer soaking time of 42 hours was found to produce significantly increased photocurrents and was thus used for the rest of the experiments presented in this thesis. After dye

soaking, the thin films were removed from the solution and washed with ethanol before leaving to air dry in the dark.

6.2.3. Device configuration and addition of electrolyte

After dye loading and air drying, the TiO_2 thin films were built up into a DSSC device using Meltonix 1170-25 Surlyn® thermoplastic sealing film as a spacer, which was 25 πm thick and used as supplied from Solaronix.[262] The electrolyte used for initial testing was an iodide electrolyte solution made with 0.5 M Potassium iodide mixed with 0.05 M iodine in water free ethylene glycol, however this electrolyte is not very stable in direct sunlight and after several experiments as presented in this thesis it is expected that this redox electrolyte may have decomposed and therefore not functioned correctly. Latter experiments use a higher quality electrolyte; Iodolyte HI-30, which is a high performance iodide/tri-iodide electrolyte formulated using a low viscosity solvent with a redox concentration of 30 mM, used as supplied by Solaronix.

For device fabrication, a sealing 'gasket' was cut out of the Meltonix 1170-25 surlyn sheet using a scapel, whereby the outer dimensions were made to be 2-3 mm larger that then TiO_2 anode on all sides to ensure good confinement of the electrolyte within the cell. An inner 1 cm x 1 cm window was cut out of the centre of sealing gasket, which would then correspond to the active area of the cell, as shown in figure 6.3 (a). This sealing gasket would then be placed on top of the conducting side of the anode so that it matched up with the active area of the anode, i.e. at the centre of anode.A clean glass slide was then placed on top of the sealing gasket to form a glass sandwich, after which heat and pressure was applied using a hot plate and a small weight, heating the anode to 110 °C for 1 minute, after which the Meltonix material would be sealed to the anode.

Following this, a drop of the electrolyte would then be dropped into the active area, and the counter electrode would be immediately placed on top of the anode, conducting side down, to complete the DSSC device, leaving a small overlap of counter electrode to make an electrical contact. Small binder clips were then placed on the outside to hold the cell together. A schematic of the overall cell configuration is shown in figure 6.3 (b) with a photograph of a typical cell

under illumination (6.3 (c)). DSSC devices were then connected with crocodile clips to the contact points on either electrode, as shown in figure 6.3 (b).

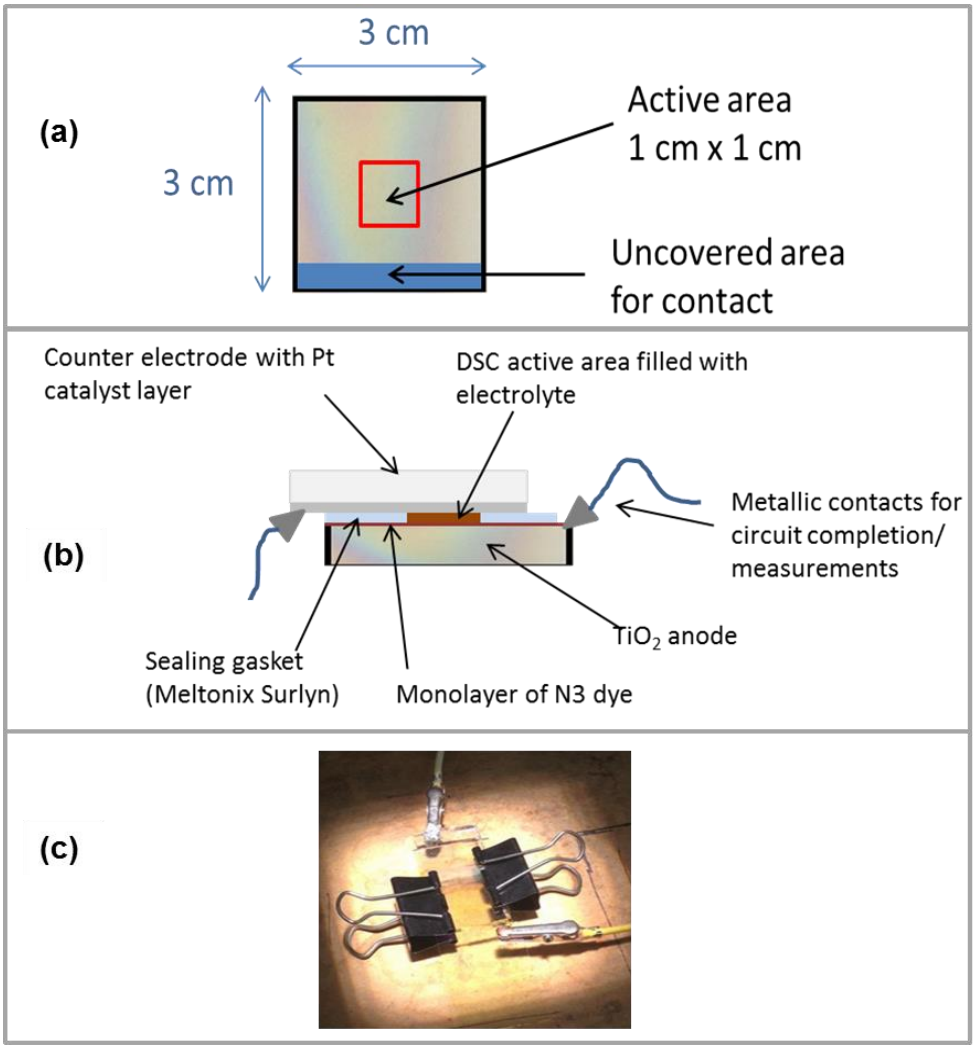

Figure 6.3 (a). Schematic of the dye solar cell active area in red, and the dimensions of the TiO_2 anode. The blue box represents the area of the anode which is left uncovered by the sealing gasket in order to make an electrical contact for connecting the device together and making performance. **6.3 (b)** Schematic of dye sensitised solar cell configuration, and photo of a typical DSSC under illumination.

The current density (J) – voltage (V) relationships were tested using an IVT Solar VS 6820 solar simulator system with a Keithley 2400 source meter under 100 mW/cm^2 , AM 1.5 G simulated sunlight. The incident photon-current conversion efficiency (IPCE) of each device was measured using the IVT Solar VS 6851 system at room temperature with an incident light ranging from

350 to 800 nm and a sampling rate of 5 nm per second. All IV plots are shown with the current axis inverted, as per convention.

6.3. Results: Incorporation ofTiO_2 thin films into DSSC devices

The TiO_2 thin films which demonstrated the best photocatalytic performance as shown in previous chapters 3 (sol-gel) and 4 (AACVD) were incorporated into DSSC devices and assessed for performance under illumination. The intention in this study was to perform analysis on three dye solar cell devices per thin film type, using a different thin film each time, and to assess this in several configurations to obtain the optimum thin film and DSSC configuration for this type of application. However, due to time constraints for some samples it was not possible to repeat DSSC devices when they did not work, and thus there some sample types which show only two repetitions. Due to the delicate nature of connecting DSSC devices through the methodology described above in 6.2, quite often solar cell devices would not produce any photocurrent, owing to several reasons including; leaked electrolyte from the active area resulting in a short circuit of the cell, little or no dye adsorption on the TiO_2 thin film thus poor light absorption, reduced conductivity in the electrolyte (owing to air or direct sunlight exposure) or poor connectivity between the counter electrodes.

Two general configurations were tested, including configuration 1 and 2 as outlined below, whereby the dye soaking time was increased (from 24 hours to 42 hours), a higher performance electrolyte was used (triiodide electrolyte to Iodolyte HI-30) and a different counter electrode was also used (ITO counter electrode to Platinum catalyst electrode).

Configuration 1:

- TiO_2 film soak time in N3 dye: 24 hours.
- Triiodide electrolyte
- ITO counter electrode

Configuration 2:

- TiO_2 film soak time in N3 dye: 42 hours.
- Iodolyte Hi-30 high performance electrolyte
- Platinum on FTO as counter electrode

6.3.1. Performance of DSSC devices prepared using sol-gel thin films derived from TTIP precursor with surfactant addition

The sol-gel thin films used in DSSC devices were those which showed optimum photocatalytic performance in chapter 3, and are shown in table 6.1, with surfactant types and concentrations alongside TiO_2 film sample name. Only two-layer and three-layer thin films were investigated, as it is likely that one layer samples would not provide the optimum thickness for significant light adsorption and electron conduction.

Table 6.1. Surfactant types and concentrations used to prepare TiO_2 thin films by sol-gel, with corresponding TiO_2 sample name and precursor used.

Surfactant used	**Concentration (mol/dm^3)**	**TiO_2 film sample name**	
		TTIP Precursor	**TIBALD precursor**
Nil	Nil	**Control**	**-**
Brij 58	0.0006	**B58 A**	**B58 AT**
Brij 98	0.0004	**B98 B**	**B98 BT**
Tween 20	0.0004	**T20 B**	**-**
Tween 40	0.0004	**T40 B**	**-**

The performance of sol-gel thin films prepared with TTIP precursor used as anodes in DSSC devices can be evaluated by looking at the DSSC performance measurements in tables 6.2-6.7, whereby tables 6.2- 6.3 show the results for those DSSCs made with configuration 1, and table 6.4 shows the results for DSSC made in a 'transitionary' configuration, whereby a longer dye soaking time of 43 hours was used with a a platinum electrode. Tables 6.5-6.7 show the results for those made with configuration 2. The highest PCE (power conversion efficiency) for those DSSCs prepared with configuration 1 was 0.0131 % as for a 2 layer film control film, and 0.0073 % for a three layer thin film prepared with Brij 98 surfactant in 0.0004 mol dm^3 concentration. The best efficiencies are highlighted in the tables in blue for the best within a series of results, and yellow for DSSCs exhibiting efficiencies greater than 0.1 %.

Table 6.2. DSSC device performance for sol-gel TiO_2 thin films prepared with TTIP precursor, without surfactant addition in configuration 1. Power conversion efficiency (PCE, %) values highlighted green are the best PCE values obtained within a group of devices prepared with the same type of TiO_2 thin film in a specific configuration.

Configuration 1:

- TiO_2 film soak time in N3 dye: 24 hours.
- Triiodide electrolyte
- ITO counter electrode

TiO_2 film number of layers	**TiO_2 Sample Name**	**Short-circuit current J_{sc} (mA/cm^2)**	**Open-circuit voltage V_{oc} (V)**	**Fill Factor (FF)**	**Power Conversion Efficiency (PCE) (%)**	**Appendix IV Curve Number**
2- layer	Control -2	0.130	0.47	0.12	**0.0131**	**Figure 6.4**/ A1
	Control- 4	0.048	0.42	0.09	0.0030	A2
	Control- 7	0.048	0.34	0.11	0.0024	A3
3-layer	Control-1	0.013	0.38	0.18	0.0011	A4
	Control- 2	0.051	0.51	0.12	0.0038	A5
	Control-3	0.049	0.40	0.12	0.0042	A6

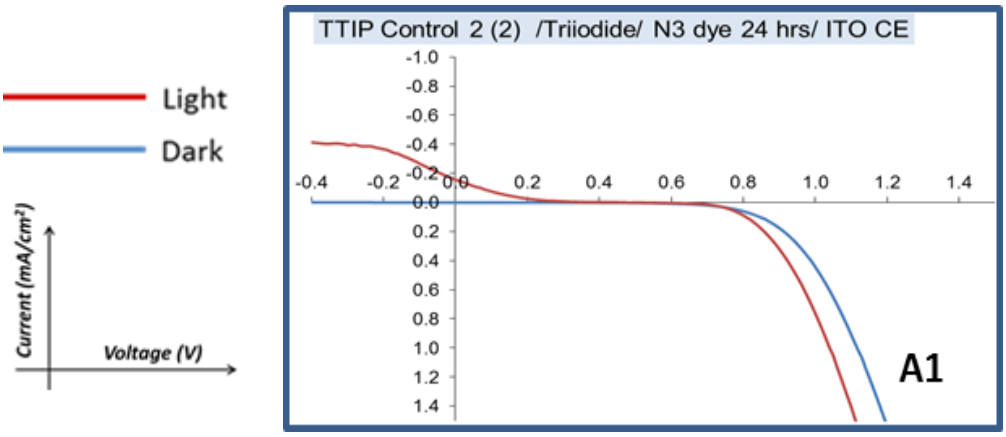

Figure 6.4. Current-Voltage (IV) curve for DSSC device A1 showing 0.0131 % PCE efficiency, highlighted in blue in table 6.2. This was prepared in configuration 1 as detailed above, with a 2 layer control TiO_2 thin film produced by sol-gel with TTIP precursor and no surfactant addition.

Table 6.3. DSSC device performance for sol-gel TiO_2 thin films prepared with TTIP precursor and Brij 98 surfactant in 0.0004 mol dm^3 concentrations. Power conversion efficiency (PCE, %) values highlighted green are the best PCE values obtained within this group of devices.

Configuration 1:

- TiO_2 film soak time in N3 dye: 24 hours.
- Triiodide electrolyte
- ITO counter electrode

TiO_2 film number of layers	TiO_2 Sample Name	Short-circuit current J_{sc} (mA/cm^2)	Open-circuit voltage V_{oc} (V)	Fill Factor (FF)	Power Conversion Efficiency (PCE) (%)	Appendix IV Curve Number
2- layer	B98 B-4	0.039	0.21	0.14	0.0015	A7
	B98 B-8	0.069	0.40	0.08	0.0037	A8
3-layer	B98 B-8	0.084	0.29	0.15	0.0063	A9
	B98 B-0	0.079	0.38	0.11	0.0055	A10
	B98 B-1	0.162	0.41	0.09	**0.0073**	**Figure 6.5/** A11

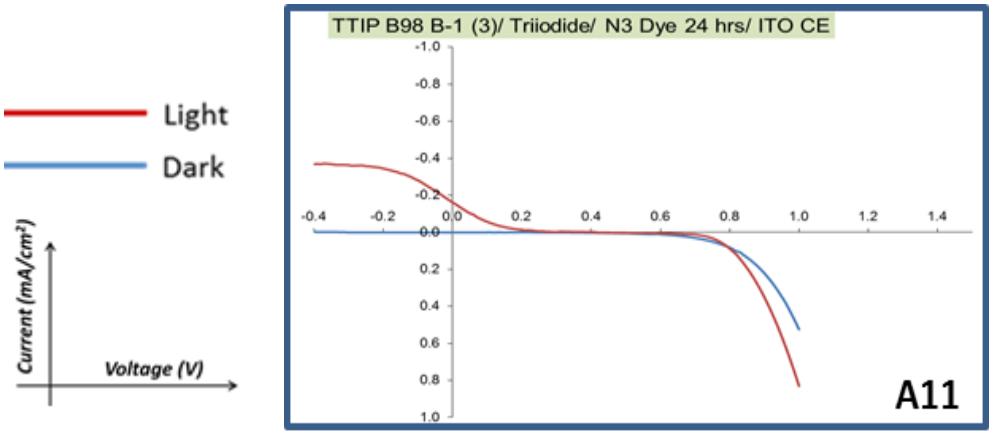

Figure 6.5. Current-Voltage (IV) curve for DSSC device A11, showing 0.0073 % PCE efficiency, highlighted in blue in table 6.3. This was prepared in configuration 1 as detailed above, with a 3 layer TiO_2 thin film produced by sol-gel with TTIP precursor and Brij 98 surfactant addition in 0.0004 mol dm^3 concentration.

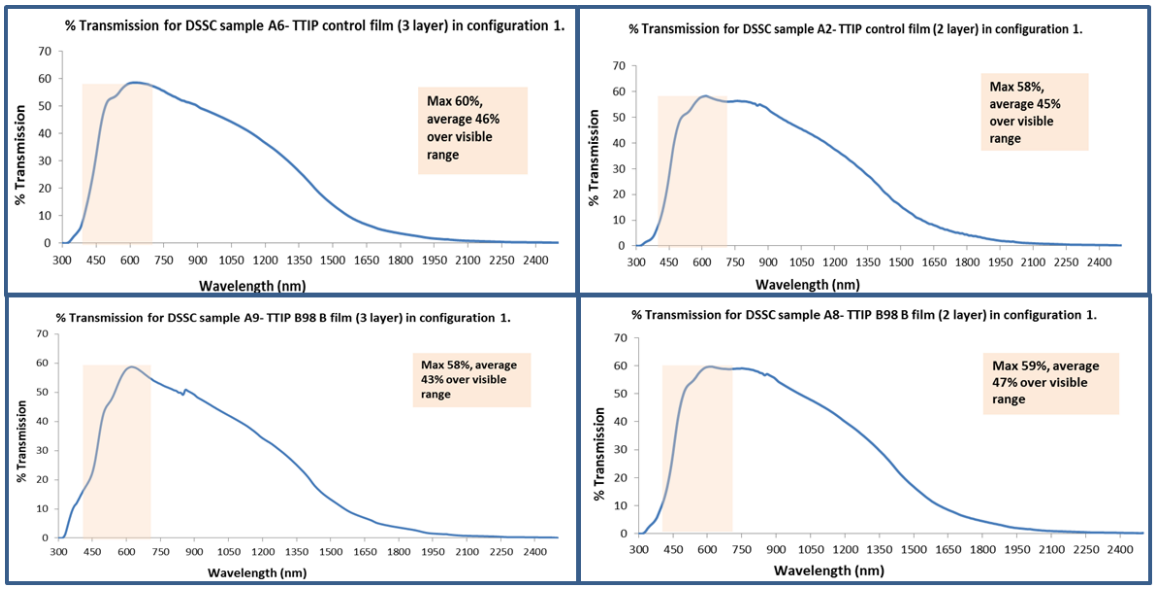

Figure 6.5a. Representative transmission (%) spectra for DSSC devices prepared in configuration 1, with DSSC performance values given in tables 6.2-6.3.

The optical transmission (%) of each DSSC device was measured as a complete cell using UV-Vis spectroscopy after each device had been measured for photovoltaic performance. Representative spectra for thin film devices prepared in configuration 1 are given in figure 6.5a. These spectra can be used to evaluate the transparency of the solar cells to visible light, whereby those produced in configuration 1, as outlined in tables 6.2-6.3 show an average transmission value of between 43-47% in the visible range, with maximum transmission values of up to 60%. As a result this semi-transparent configuration is potentially suitable for window glazing. Furthermore, the measured transparency for these DSSC devices is higher than that of state-of-the-art DSSC modules produced by Glass 2 Energy, which currently exhibit an optical transmission of 35% as recorded in 2016, albeit at a much higher level of power production.[2]

Table 6.4 shows the PCE values for DSSC devices made in the 'transitionary' configuration (1.5) using thin films which had been soaked in dye for a longer time period (42 hours instead of 24 hours). This combined with the addition of the platinum counter electrode has resulted in a significant increase in efficiency, up to 0.2257 % as observed for a Brij 98 3 layer film (B-3) with the IV curve shown in figure 6.6b.

Table 6.4. DSSC device performance for sol-gel TiO_2 thin films prepared with TTIP precursor and Brij 58 in 0.0006 mol dm^3 concentrations (A) and Brij 98 in 0.0004 mol dm^3 concentrations (B). PCE, % values highlighted blue are the best PCE values obtained within this group.

Configuration 1.5:

- TiO_2 film soak time in N3 dye: 42 hours.
- Triiodide electrolyte
- Pt on FTO counter electrode

TiO_2 number of layers	**TiO_2 Sample Name**	**Short-circuit current J_{sc} (mA/cm^2)**	**Open-circuit voltage V_{oc} (V)**	**Fill Factor (FF)**	**Power Conversion Efficiency (PCE) (%)**	**Appendix IV curve number**
2-layer	B58 A-2	0.240	0.40	0.52	0.0503	A12
	B58 A-7	0.186	0.43	0.53	0.0427	A13
3-layer	B58 A-5	0.538	0.47	0.56	0.1429	**Fig 6.6a**/A14
	B58 A-7	0.339	0.46	0.57	0.0891	A15
	B98 B-3	0.541	0.60	0.62	0.2257	**Fig 6.6b**/A16

The reasons for the increased efficiency is likely to be a combination of these changes to the configuration, whereby the longer dye soaking time has enabled more of the dye to be adsorbed onto the TiO_2 thin film, thus increasing light absorption and transfer of electrons into the TiO_2 conduction band. The introduction of the platinum counter electrode is likely to have had more of an impact on the DSSC performance as fluorine-doped tin oxide glass (FTO) and indium-doped tin oxide (ITO) glass are poor counter electrodes due to their very high charge transfer resistances (typically 10 Ω cm^2 and 15- 25 Ω cm^2 respectively).[157] The counter electrode in a DSSC must be catalytically active to ensure rapid reaction and low overpotential, and so a thin layer of platinum applied to FTO or ITO glass, enables the semi-transparency of the counter electrode to be maintained whilst enabling this catalytic regeneration of the iodine electrolyte. At the counter electrode triiodide is reduced to iodide, whereby platinum acts as a suitable catalyst for this as iodine (triiodide) dissociates to iodine atoms and iodide upon adsorption, enabling a rapid one-electron reduction. The charge-transfer reaction at the counter electrode leads to a

series resistance within the DSSC, called the charge-transfer resistance, which ideally should be low within the DSSC to avoid significant losses.[263] A poor counter electrode affects the current-voltage characteristics of the DSSC by lowering the fill factor, which explains why the fill factor has been dramatically increased from configuration 1 to configuration 1.5 by the addition of the platinum layer in the counter electrode; fill factors have increased from 0.08-0.18 (tables 6.2-6.3) to 0.52-0.62 (table 6.4).

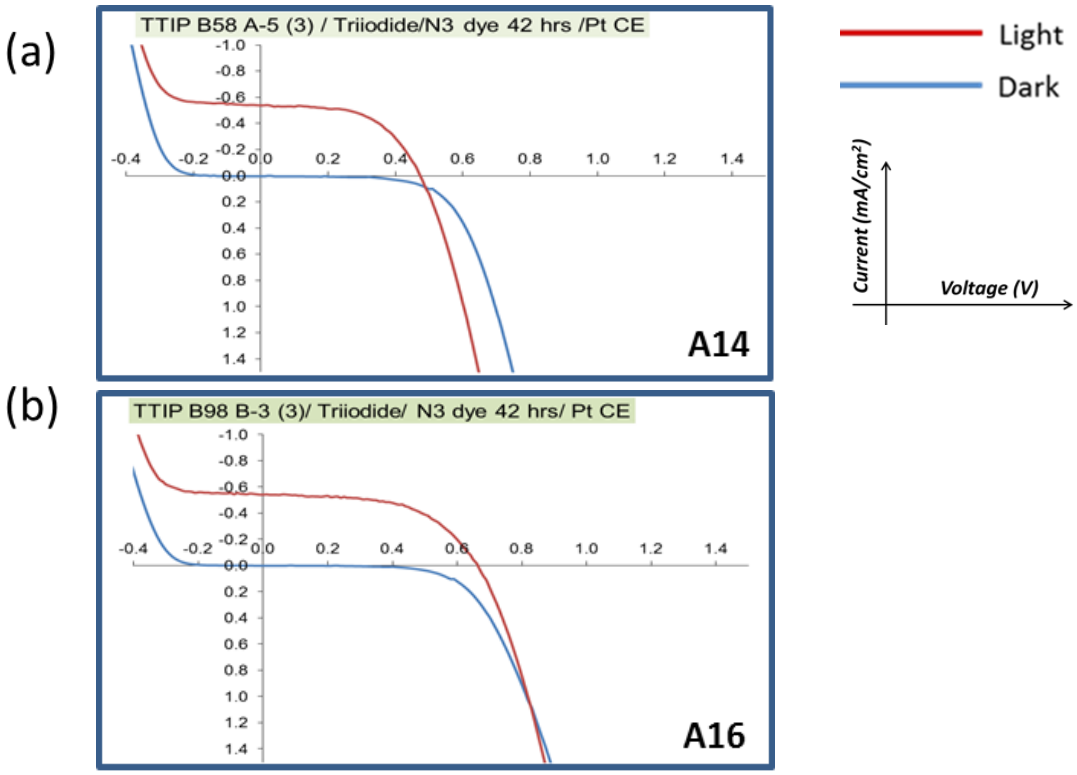

Figure 6.6. Current-Voltage (IV) curves for the DSSC devices prepared in configuration 1.5, with a platinum counter electrode showing enhanced performance compared to the ITO electrode as in figures 6.4 and 6.5. IV curves here are for (a) A14, DSSC with 0.1429 % PCE efficiency, prepared with a sol-gel film made with TTIP precursor and Brij 58 surfactant in a concentration of 0.0006 mol dm^3, and (b) A16 DSSC with 0.2257 % PCE efficiency, prepared with a sol-gel film made from TTIP precursor and Brij 98 surfactant in ca concentration of 0.0004 mol dm^3, as highlighted in blue in table 6.4.

Following on from the enhancements made in configuration 1.5, configuration 2 (with added incorporation of HI-30 Iodolyte- high performance electrolyte) in place of standard triiodide was found to produce DSSC efficiency values that were much higher than those obtained for

configuration 1 and 1.5. This improvement is expected due to the several modifications made to enhance the device; such as increased dye soaking time (24 hrs vs 48 hrs), use of a higher performance electrolyte (HI-30 iodolyte in place of triiodide) and the platinum catalyst on FTO rather than plain ITO as the counter electrode. The most efficient DSSCs produced with configuration 2 showed power conversion efficiencies (PCE) within the range of 0.11-0.38 %, with greatly improved fill factors in the range of 0.45-0.63 for the best devices, indicating that the modifications described above greatly improved the DSSCs performance. The best efficiencies are highlighted in yellow in tables 6.5- 6.7, with the highest for each type of thin film used highlighted in blue. The representative % transmission for these devices is shown in figure 6.7a, whereby the average % transmission is 49-53% over the visible range.

Table 6.5. DSSC device performance for sol-gel TiO_2 thin films prepared with TTIP precursor without surfactant addition. Power conversion efficiency (PCE, %) values highlighted yellow are for those showing optimum performance (> 0.1 %)and blue for the best PCE values obtained within a group of devices prepared with the similar TiO_2 thin film types.

Configuration 2:

- TiO_2 film soak time in N3 dye: 42 hours.
- Iodolyte Hi-30 high performance electrolyte
- Platinum on FTO as counter electrode

TiO_2 film number of layers	TiO_2 Sample Name	Short-circuit current J_{sc} (mA/cm^2)	Open-circuit voltage V_{oc} (V)	Fill Factor (FF)	Power Conversion Efficiency (PCE) (%)	Appendix IV curve number
2- layer	Control -4	0.369	0.65	0.45	0.1792	**Fig 6.7a**/A17
	Control -7	0.358	0.65	0.47	0.1134	**Fig 6.7b** /A18
3-layer	Control -9	0.369	0.69	0.45	0.1193	**Fig 6.7c**/ A19

From these tables it can be concluded that the DSSCs produced with surfactant derived TiO_2 thin films demonstrated higher efficiencies than for those produced with plain control TiO_2 thin films (highest for plain control film = 0.1792 % vs 0.3814 % for Brij A film, and 0.3749 for T40 B film). The highest efficiency for a control TiO_2 thin film via configuration 2 was 0.1792 % as for

a 2 layer thin film (Control-4) device (A17, IV curve shown in figure 6.7a), which also exhibited a much higher short-circuit current (J_{sc}) of 0.369 mA/cm^2 and a higher open-circuit voltage (V_{oc}) of 0.65 V compared to a similar film made into a DSSC device (A1) via configuration 1 (2 layer-Control 2; 0.0131 % PCE, 0.130 mA/cm^2 (J_{sc}), 0.47 V (V_{oc})). The device produced via configuration 2 also exhibited a much higher fill factor of 0.45 vs just 0.12 for the configuration 1 device. The representative % transmission for these devices is shown in figure 6.7a, whereby the average % transmission is 49-53% over the visible range.

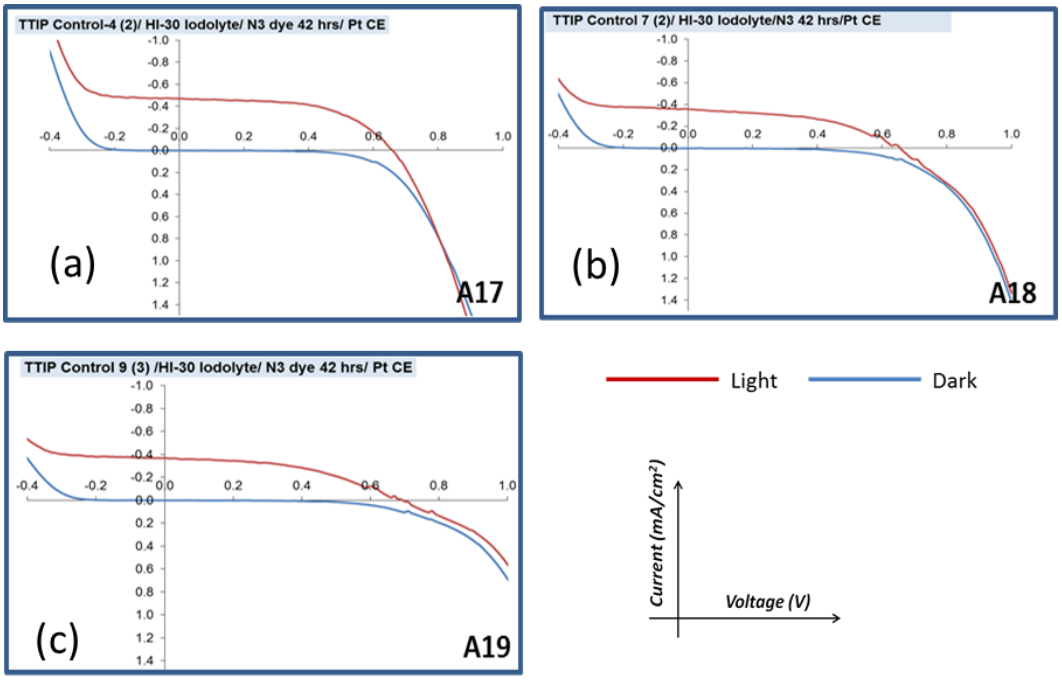

Figure 6.7. Current-Voltage (IV) curves for the DSSC devices prepared in configuration 2, with 42 hours dye soaking time, HI-30 Iodolyte (high performance electrolyte) and a platinum counter electrode. IV curves here are for (a) A17 -DSSC with 0.1792 % PCE efficiency (b) A18- DSSC with 0.1134 % PCE efficiency and (c) A19- DSSC with 0.1193 % PCE efficiency, as shown in table 6.5.

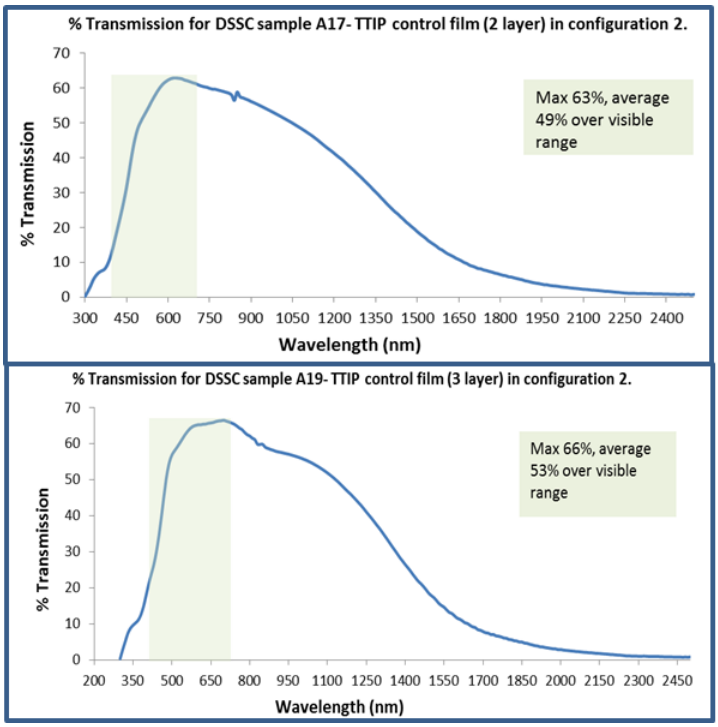

Figure 6.7a. Representative transmission (%) spectra for DSSC devices prepared in configuration 2. Devices shown here are A17 and A19, control thin film devices as described in figure 6.7 above.

The sol-gel thin films prepared with surfactant addition showed higher device efficiencies when used in DSSCs compared to the control films, whereby the results for Brij surfactants are shown in table 6.6, and Tween surfactants are shown in table 6.7. On average those DSSC devices made with Brij films showed consistently higher efficiencies, with the best PCE values ranging between 0.1833-0.2484 % for two layer films and 0.1922-0.3814 % for 3 layer thin films. The 3 layer thin films showed consistently higher efficiencies, as shown in table 6.6, which is as expected because these TiO_2 thin films are thicker and rougher, thus enabling better adsorption of the N3 dye onto the film surface to trap incident light and enable promotion of electrons into the TiO_2 conduction band.[264]

Table 6.6. DSSC device performance for sol-gel TiO_2 thin films prepared with TTIP precursor and Brij 58 and Brij 98 surfactants in concentrations A (0.0006 mol dm^3) and B (0.0004 mol dm^3). Power conversion efficiency (PCE, %) values highlighted yellow are for those showing optimum performance (> 0.1 %) and blue for the best PCE values obtained within this group of devices.

Configuration 2:

- TiO_2 film soak time in N3 dye: 42 hours.
- Iodolyte Hi-30 high performance electrolyte
- Platinum on FTO as counter electrode

TiO_2 film number of layers	TiO_2 Sample Name	Short-circuit current J_{sc} (mA/cm^2)	Open-circuit voltage V_{oc} (V)	Fill Factor (FF)	Power Conversion Efficiency (PCE) (%)	Appendix IV curve number
2- layer	B58 A-8	0.318	0.16	0.34	0.0178	A20
	B58 A-2	0.467	0.67	0.52	0.1833	A21
	B58 A-4	0.501	0.69	0.56	0.2171	A22
	B98 B-1	0.600	0.68	0.54	0.2484	Fig 6.8d/A23
	B98 B-4	0.622	0.68	0.16	0.0759	A24
	B98 B-3	0.463	0.60	0.63	0.1980	A25
3-layer	B58 A-8	0.857	0.71	0.60	0.3814	Fig 6.8a/A26
	B58 A-2	0.601	0.60	0.64	0.2580	A27
	B58 A-4	0.852	0.71	0.59	0.3721	Fig 6.8b/A28
	B98 B-3	0.541	0.66	0.56	0.2257	A29
	B98 B-8	0.723	0.68	0.60	0.3303	Fig 6.8 c/A30
	B98 B-5	0.430	0.67	0.59	0.1922	A31

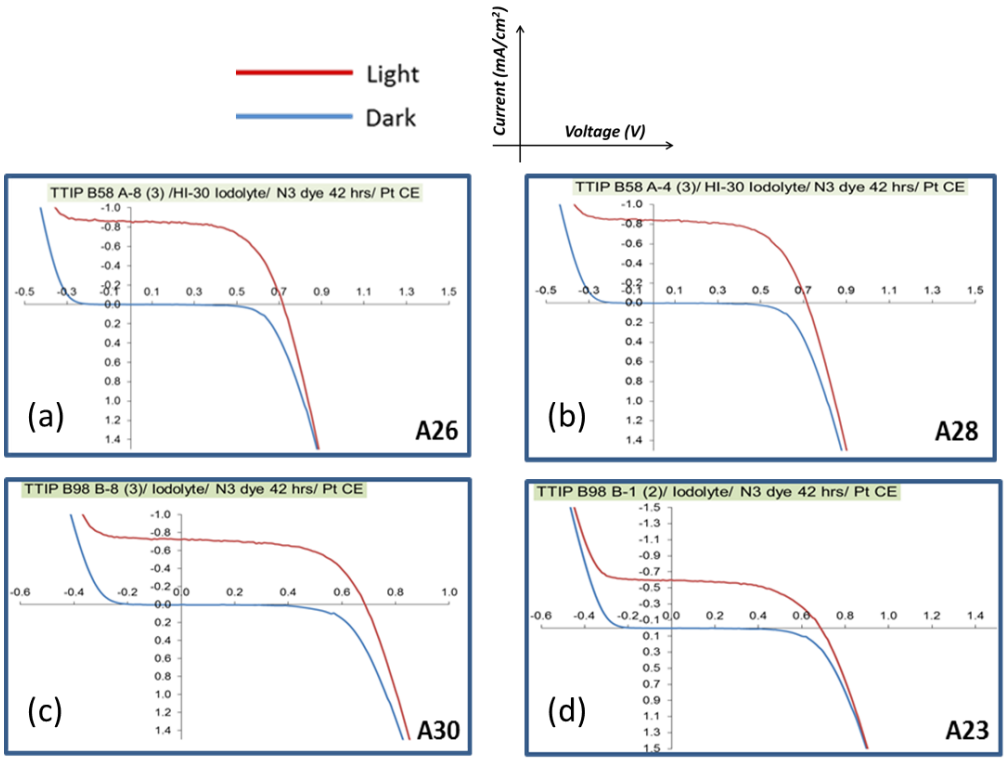

Figure 6.8. Current-Voltage (IV) curves for the DSSC devices prepared in configuration 2, with 42 hours dye soaking time, HI-30 Iodolyte (high performance electrolyte) and a platinum counter electrode. IV curves here are for (a) A26-DSSC with 0.3814 % PCE efficiency (b) A28-DSSC with 0.3721 % PCE efficiency (c) A30- DSSC with 0.3303 % PCE efficiency and (d)A23- DSSC with 0.2484 % efficiency as shown in table 6.6.

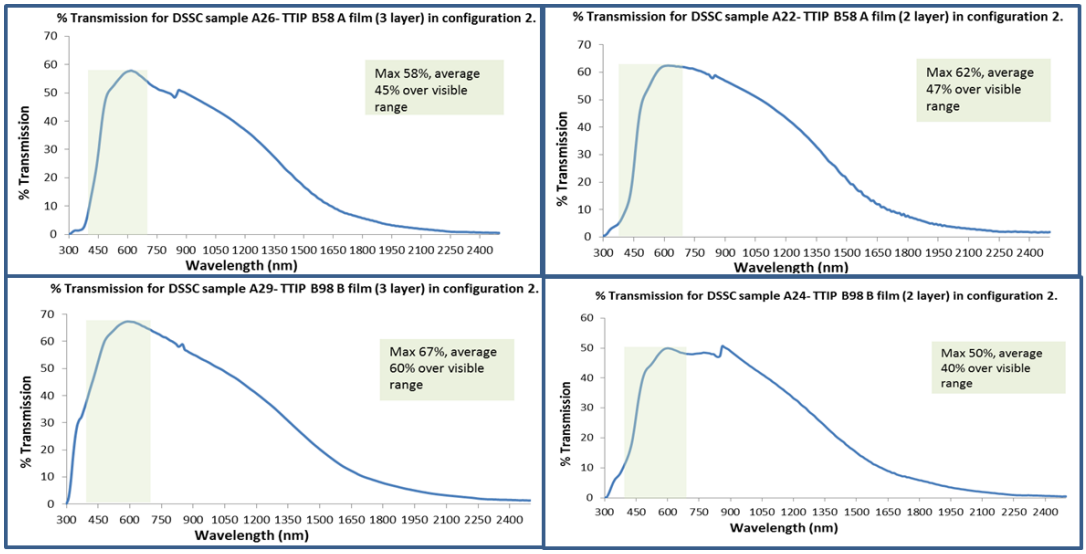

Figure 6.8a. Representative transmission (%) spectra for DSSC devices prepared in configuration 2. Devices shown here are A26, A22, A29 and A24, Brij 58/Brij 98 thin film devices as described in figure 6.8 and table 6.6.

Representative spectra for optical transmission of these configuration 2 devices from table 6.6 are given in figure 6.8a, whereby the average transmission is 40-60% over the visible range, with maximum transmission values of 50-62 %.There is little correlation between the performance of these DSSC devices and % transmission, whereby the highest performing device, A26, exhibits a PCE efficiency of 0.3874 %, with an average optical transmission of 45 % over the visible range and a maximum % transmission of 58%. The lowest performing device does not show an increased transparency, with a PCE of 0.0759% and an average transmission of 40% over the visible range.

The sol-gel thin films produced with Tween 20 and Tween 40 surfactants in concentrations of 0.0004 mol dm^3 are shown in table 6.7, whereby it can be seen that these films did not perform as well as the Brij films in DSSC devices. Only the devices prepared with Tween 40 derived thin films enabled higher device efficiencies (> 0.1 %), as highlighted in table 6.7, with the IV curves for the best four devices shown in figure 6.9. The highest efficiency observed was 0.3749 % PCE for 3 layer film T40 B, with the IV curve shown in figure 6.9 (b) above. The Tween 20 prepared films all exhibited much lower efficiencies between 0.0008- 0.0016 % PCE. The reasons as to why the Tween 20 thin films did not perform as well as the Tween 40 thin films is hard to determine. The characterisation data for these thin films is shown in table 3.3, chapter 3, section 3.2.1, whereby little difference can be observed between the two thin film types- both exhibit small average particle sizes (~35 nm), larger average film thicknesses and high average surface roughness. Tween 20 samples in fact exhibit larger film thicknesses (183 nm vs 111 nm for Tween 40 films) and higher roughness values (210 nm for T20 B/ 2 layer vs 110 nm for T40 B/ 2 layer). Therefore it can be considered whether there is an optimum roughness and thickness for TiO_2 thin films when used in DSSC devices, whereby it has been reported in literature that increased thickness of TiO_2 thin films can result in lower incident light intensity due to the lower transmittance of the thin film.[264] It is likely that there is a combination of effects at play here, whereby the DSSC device performance can be affected by a wide number of factors, not just limited to the thin film characteristics, but also by the quality of the other components used.

Table 6.7. DSSC device performance for sol-gel TiO_2 thin films prepared with TTIP precursor and Tween 20 and Tween 40 surfactants in concentration B (0.0004 mol dm^3). Power conversion efficiency (PCE, %) values highlighted yellow are for those showing optimum performance (> 0.1 %)and blue for the best PCE values obtained within this group of devices.

Configuration 2:

- TiO_2 film soak time in N3 dye: 42 hours
- Iodolyte HI-30 high performance electrolyte
- Platinum on FTO counter electrode

TiO_2 film number of layers	**TiO_2 Sample Name**	**Short-circuit current J_{sc} (mA/cm^2)**	**Open-circuit voltage V_{oc} (V)**	**Fill Factor (FF)**	**Power Conversion Efficiency (PCE) (%)**	**Appendix IV curve number**
2- layer	T20 B-1	0.012	0.40	0.19	0.0012	A32
	T20 B-4	0.010	0.39	0.19	0.0010	A33
	T20 B-0	0.010	0.39	0.25	0.0016	A34
	T40 B-4	0.181	0.47	0.51	0.0430	A35
	T40 B-7	0.172	0.47	0.54	0.0441	A36
	T40 B-3	0.353	0.71	0.60	0.1689	A37
	T40 B-6	0.395	0.71	0.60	0.1899	Fig 6.9a/A38
	T40 B-5	0.145	0.47	0.55	0.0378	A39
3-layer	T20 B-6	0.009	0.35	0.20	0.0008	A40
	T20 B-7	0.012	0.40	0.22	0.0013	A41
	T40 B-5	0.240	0.41	0.54	0.0529	A42
	T40 B-7	0.782	0.71	0.60	0.3749	Fig 6.9b/A43
	T40 B-3	0.519	0.70	0.59	0.2396	Fig 6.9c/A44
	T40 B-9	0.686	0.72	0.61	0.3392	Fig 6.9d/A45
	T40 B-8	0.380	0.47	0.62	0.1109	A46

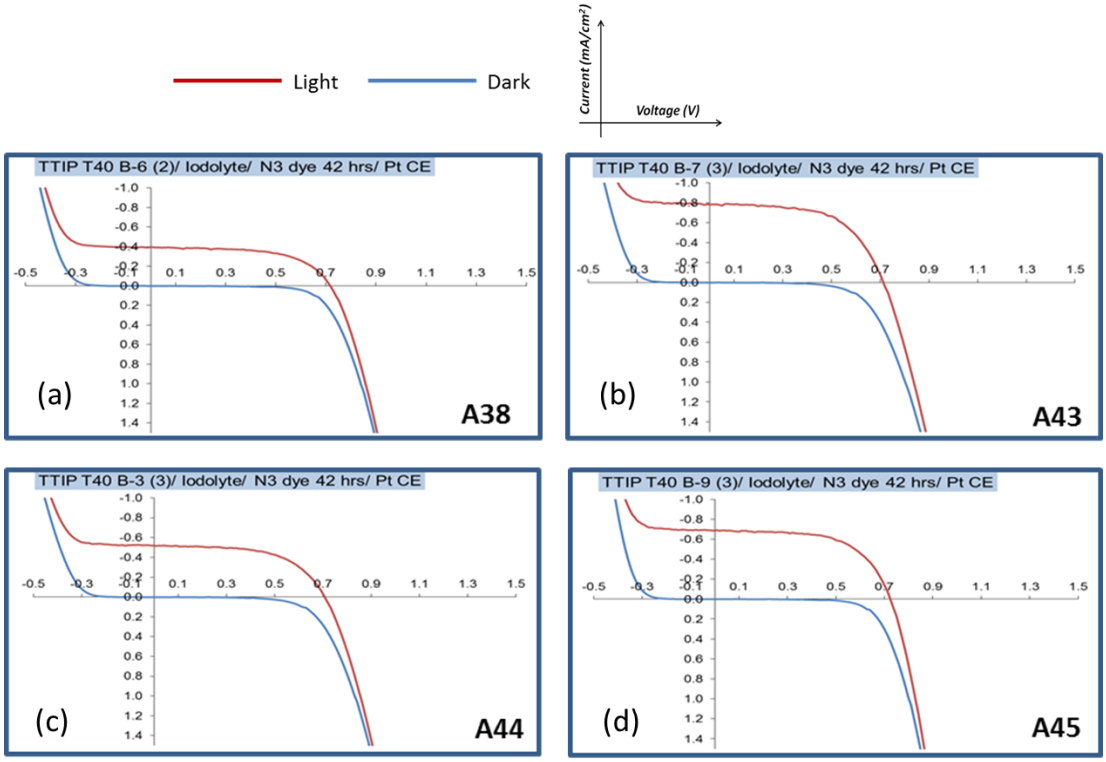

Figure 6.9. Current-Voltage (IV) curves for the DSSC devices prepared in configuration 2, with 42 hours dye soaking time, HI-30 Iodolyte (high performance electrolyte) and a platinum counter electrode. IV curves here are for (a) DSSC with 0.1899 % PCE efficiency (b) DSSC with 0.3749 % PCE efficiency (c) DSSC with 0.2396 % PCE efficiency and (d) DSSC with 0.3392 % efficiency as shown in table 6.7.

6.3.1.1. Conclusions: DSSC devices using TiO_2 thin films prepared with TTIP precursor and the effects of surfactant addition

Titanium dioxide thin films prepared by TTIP precursor with and without surfactant addition were tested within two dye-sensitised solar cell configurations; configuration 1 and configuration 2. In configuration 1 the thin films were left to soak in N3 dye for 24 hours, and were combined with standard triiodide electrolyte and an ITO counter electrode. In configuration 2 the thin films were left to soak for a longer time period in N3 dye (42 hours), a high performance electrolyte (Iodolyte HI-30) was used in combination with an FTO counter electrode that had a layer of platinum catalyst on its conductive surface. It was found that DSSCs with configuration 2 produced consistently higher power conversion efficiencies, with the best DSSCs exhibiting 0.1109-0.3814%. The optimum DSSC was found to show efficiency of 0.3814 %, which was produced with a 3-layer Brij 58 thin film (concentration A (0.0006 mol dm^3)) which also exhibited an short-circuit current of 0.857 mA/cm^2, an open-circuit voltage of 0.71 V and a fill factor of 0.60.

6.3.2. Performance of DSSC devices prepared using sol-gel thin films derived from TiBALD precursor with surfactant addition

The TiBALD derived thin film samples were only tested in DSSC configuration 2 owing to the results observed with the TTIP derived thin films whereby configuration 2 enabled significantly higher efficiencies. As before, only two/three-layer films were tested, and only those thin films which have shown optimum photocatalytic performance in chapter 3 were used for DSSC testing, of which the concentrations and sample names are in table 6.1. As the Tween thin films did not perform as well as the Brij films, only Brij TiBALD thin films were tested in DSSC devices, and the results are shown in tables 6.8-6.9. In addition, the control TIBALD thin film was not tested due to time constraints, whereby maximum attention was given to the Brij 58 and Brij 98 thin films that had shown better efficiencies for the TTIP derived DSSC devices.

Table 6.8. DSSC performance of sol-gel TiO_2 thin films prepared with TIBALD precursor and Brij 58 surfactant in concentrations A (0.0006 mol dm^3) and B (0.0004 mol dm^3). The highest power conversion efficiency (PCE, %) value obtained within this group is highlighted blue.

Configuration 2:

- TiO_2 film soak time in N3 dye: 42 hours
- Iodolyte HI-30 high performance electrolyte
- Platinum on FTO counter electrode

TiO_2 film number of layers	TiO_2 Sample Name	Short-circuit current J_{sc} (mA/cm^2)	Open-circuit voltage V_{oc} (V)	Fill Factor (FF)	Power Conversion Efficiency (PCE) (%)	Appendix IV curve number
2- layer	B58 AT -8	0.181	0.66	0.50	0.0598	A47
	B58 AT -6	0.099	0.63	0.49	0.0305	A48
3- layer	B58 AT -5	0.104	0.58	0.49	0.0292	A49
	B58 BT -1	0.146	0.71	0.51	0.0525	A50
	B58 BT -7	0.161	0.65	0.53	0.0558	A51

Table 6.9. DSSC performance of sol-gel TiO_2 thin films prepared with TIBALD precursor and Brij 98 surfactant in concentrations A (0.0006 mol dm^3) and B (0.0004 mol dm^3). The highest power conversion efficiency (PCE, %) values obtained within this group are highlighted blue.

Configuration 2

- TiO_2 film soak time in N3 dye: 42 hours
- Iodolyte HI-30 high performance electrolyte
- Platinum on FTO counter electrode

TiO_2 film number of layers	TiO_2 Sample Name	Short-circuit current J_{sc} (mA/cm^2)	Open-circuit voltage V_{oc} (V)	Fill Factor (FF)	Power Conversion Efficiency (PCE) (%)	Appendix IV curve number
2 layer	B98 BT -7	0.164	0.73	0.52	0.0619	A52
	B98 AT -5	0.101	0.60	0.24	0.0146	A53
3- layer	B98 AT -7	0.154	0.67	0.52	0.0536	A54
	B98 AT -1	0.144	0.66	0.53	0.0504	A55
	B98 BT -1	0.101	0.59	0.24	0.0144	A56
	B98 BT -2	0.071	0.46	0.49	0.0160	A57

In comparison with the TTIP thin films used in DSSCs, the TIBALD thin films showed overall reduced efficiency values. Comparison of the Brij 58 and Brij 98 thin film can be made through looking at tables 6.7 above (TTIP) and table 6.8 and 6.9 (TiBALD) below. The Brij 58 and Brij 98 TIBALD thin films all showed efficiencies below 0.1 %, ranging between 0.0144% -0.0619 %. Generally these TiBALD DSSC devices showed reduced fill factors compared to the TTIP DSSC devices (~ 0.2-0.5 for TiBALD vs 0.5-0.6 for the best TTIP devices). The IV curves for these devices are shown in appendix C, figures E-F. These low efficiencies observed indicate that the TiBALD thin films do not have improved properties over TTIP derived thin films for use in DSSC devices, despite showing higher photocatalytic activities as discussed in chapter 3. TiBALD thin films were reported in chapter 3 as exhibiting increased density, through studies of

SEM thickness and AFM surface roughness measurements. As the TiBALD films have smaller average particle sizes the particles pack better together, producing a lower roughness and exposed surface; thus these films are less suited to dye adsorption in DSSCs.

A selection of optical transmission plots which are representative of those obtained for DSSCs produced via configuration 2 are given in Figure 6.10. Devices shown here are those prepared with Brij 58 and Brij 98 thin films as shown in tables 6.8 and 6.9. These % transmission plots show the effect of the increase number of layers within the TiO_2 thin film on optical transmission, whereby those with 3 layer films (A50 and A54) show reduced optical transmission, an average of 26% and 33% over the visible range, compared to an average of 53% and 53% for the two layer devices. This is to be expected whereby the increased number of layers reduces optical transmission through the film due absorption and scattering.

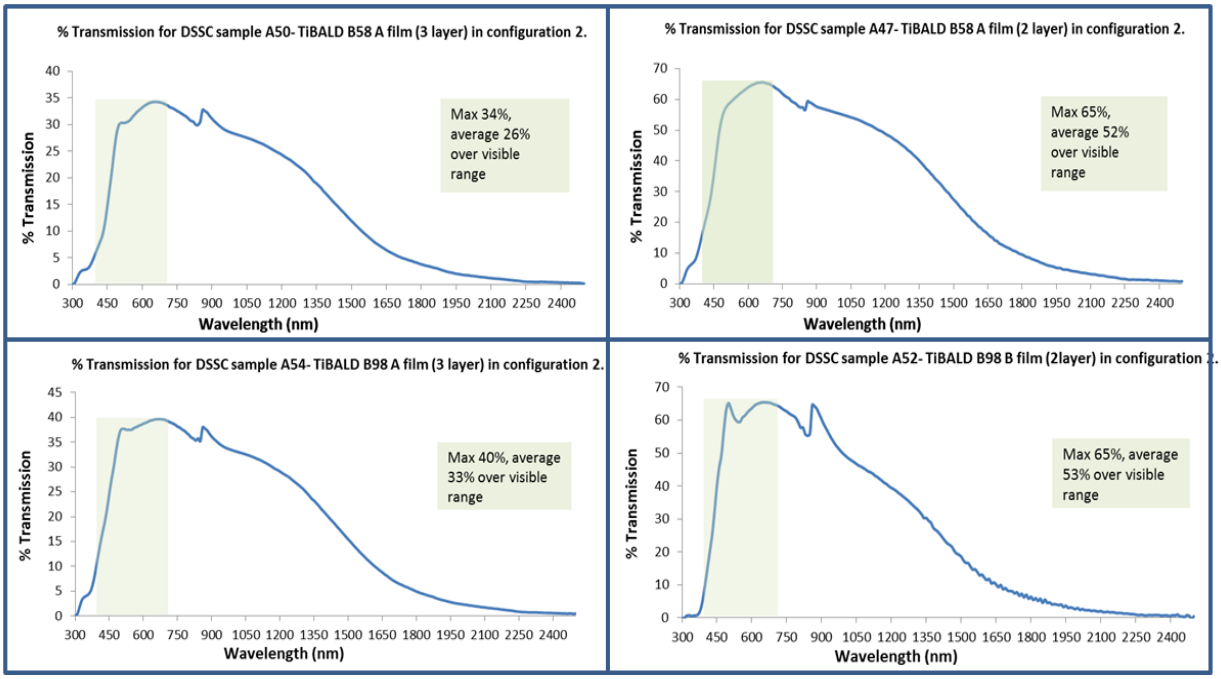

Figure 6.10. Representative transmission (%) spectra for DSSC devices prepared in configuration 2. Devices shown here are A50, A47, A54 and A52, Brij 58/Brij 98 thin film devices as described in figure 6.8 and table 6.9.

6.3.2.1 Conclusions: DSSC devices using TiO_2thin films prepared with TiBALD precursor and the effects of surfactant addition

Titanium dioxide thin films prepared by TIBALD precursor with Brij 58 and Brij 98 surfactant addition were tested with one dye-sensitised solar cell configuration; configuration 2 where the thin films were left to soak for a longer time period in N3 dye (42 hours) and a high performance electrolyte (Iodolyte HI-30) was used in combination with an FTO counter electrode that had a layer of platinum catalyst on its conductive surface. It was found that the DSSCs produced did not rival the efficiencies of those DSSCs produced with TTIP derived sol-gel films described in section 6.3.1.All devices exhibited efficiencies below 0.1 %, ranging between 0.0144 % -0.0619 %. This was attributed to a reduced density and porosity of the thin films and therefore reduced dye adsorption as described above.

6.3.2. Performance of DSSC devices prepared using AACVD thin films derived from TTIP precursor in solvents of toluene DCM with surfactant addition

Titanium dioxide thin films produced using AACVD with TTIP precursor and toluene solvent were tested in DSSC devices, owing to the results in chapter 4 whereby toluene prepared samples showed significantly higher photocatalytic rates. As these experiments were run concurrently with the sol-gel experiments, results shown in tables 6.10-6.12 show the use of configuration 1, whereas table 6.13 and 6.14 show the use of configuration 1.5, with the incorporation of the platinum catalyst counter electrode in place of the plain ITO electrode. Configuration 2 was only used with samples prepared with Brij 98 and Brij 58 surfactant, as shown in table 6.15. All current-voltage (IV) curves are shown in Appendix C; figures F, G and H.

All AACVD samples exhibited reduced power conversion efficiencies as DSSC devices compared to the sol-gel thin films described in sections 6.3.1-6.3.2. Despite the enhanced properties of the AACVD thin films such as small crystallite size (average 5.5 nm- 12 nm), increased presence of anatase TiO_2 and increased thin film thicknesses (250-3350 nm) and higher surface roughness than the sol-gel thin films (typically 32-153 nm vs just 14 -110 nm for sol-gel Brij films) as shown in table 4.2 (chapter 4).

Despite these advantages, the AACVD TiO_2 thin films are much denser than the sol-gel derived thin films, owing to the packing of the TiO_2 particles during nucleation and growth of the thin film, as discussed in chapter 4. Thus it is believed that there is significantly reduced porosity in these thin films, thereby making the structure of the thin film less suitable for adsorbing dye sensitiser for trapping light and enabling the DSSC process of converting incident light into electrons for photocurrent.

For DSSC devices in configuration 1, PCE efficiencies as low as 0.0008 % were obtained, up to a maximum of 0.0074%. The fill factors observed were also low, within the range of 0.05-0.39, indicating that as expected, the dense AACVD thin films do not adsorb a sufficient layer of sensitiser to enable light trapping in the device.

Table 6.10. DSSC performance of AACVD TiO_2 thin films prepared with TTIP precursor and toluene as solvent with no surfactant addition.

Configuration 1:

- TiO_2 film soak time in N3 dye: 24 hours.
- Triiodide electrolyte
- ITO counter electrode

Surfactant concentration	TiO_2 Sample Name	Short-circuit current J_{sc} (mA/cm^2)	Open-circuit voltage V_{oc} (V)	Fill Factor (FF)	Power Conversion Efficiency (PCE) (%)	Appendix IV curve number
Nil	AACVD Tol (1)	0.018	0.44	0.21	0.0026	A58
	AACVD Tol (2)	0.067	0.25	0.16	0.0040	A59

The highest observed power conversion efficiencies for DSSC devices prepared with AACVD TiO_2 thin films were observed for those in configuration 2, which was only tested for Brij 98 and Brij 58 samples as shown in table 6.15. The PCE values observed for configuration 2 were in the range of 0.00063%- 0.0337%, with the highest efficiency of 0.0337% obtained for an AACVD sample prepared with 0.5 M of Brij 98 surfactant. This sample did exhibit one of the higher photocatalytic rates and smallest average crystallite size (5.5 nm) as described in chapter 4,

which again may be an indication that this thin film had a slight advantage for adsorbing dye onto its surface for light absorption.

Table 6.11. DSSC performance of AACVD TiO_2 thin films prepared with TTIP precursor, toluene as solvent and Brij 98 surfactant in concentrations of 0.5 M and 1M. The highest power conversion efficiency (PCE, %) value obtained within this group is highlighted blue.

Configuration 1:

- TiO_2 film soak time in N3 dye: 24 hours.
- Triiodide electrolyte
- ITO counter electrode

Surfactant concentration	TiO_2 Sample Name	Short-circuit current J_{sc} (mA/cm^2)	Open-circuit voltage V_{oc} (V)	Fill Factor (FF)	Power Conversion Efficiency (PCE) (%)	Appendix IV curve number
0.5 M	B98 0.5 t (1)	0.051	0.39	0.08	0.0024	A60
	B98 0.5 t (2)	0.017	0.45	0.17	0.0020	A61
	B98 0.5 t (3)	0.030	0.39	0.27	0.0031	A62
1 M	B98 1 t (1)	0.006	0.27	0.30	0.0007	A63
	B98 1 t (2)	0.020	0.22	0.05	0.0014	A64
	B98 1 t (3)	0.046	0.47	0.28	0.0063	A65

Some representative IV plots and corresponding %transmission plots are given in figure 6.11 for comparison between performance as a photovoltaic and potential to be used as a semi-transparent window. All devices are semi-transparent, with up to 67% maximum transmission and an average of 40-47% over the visible range, with little difference in transparency between devices.

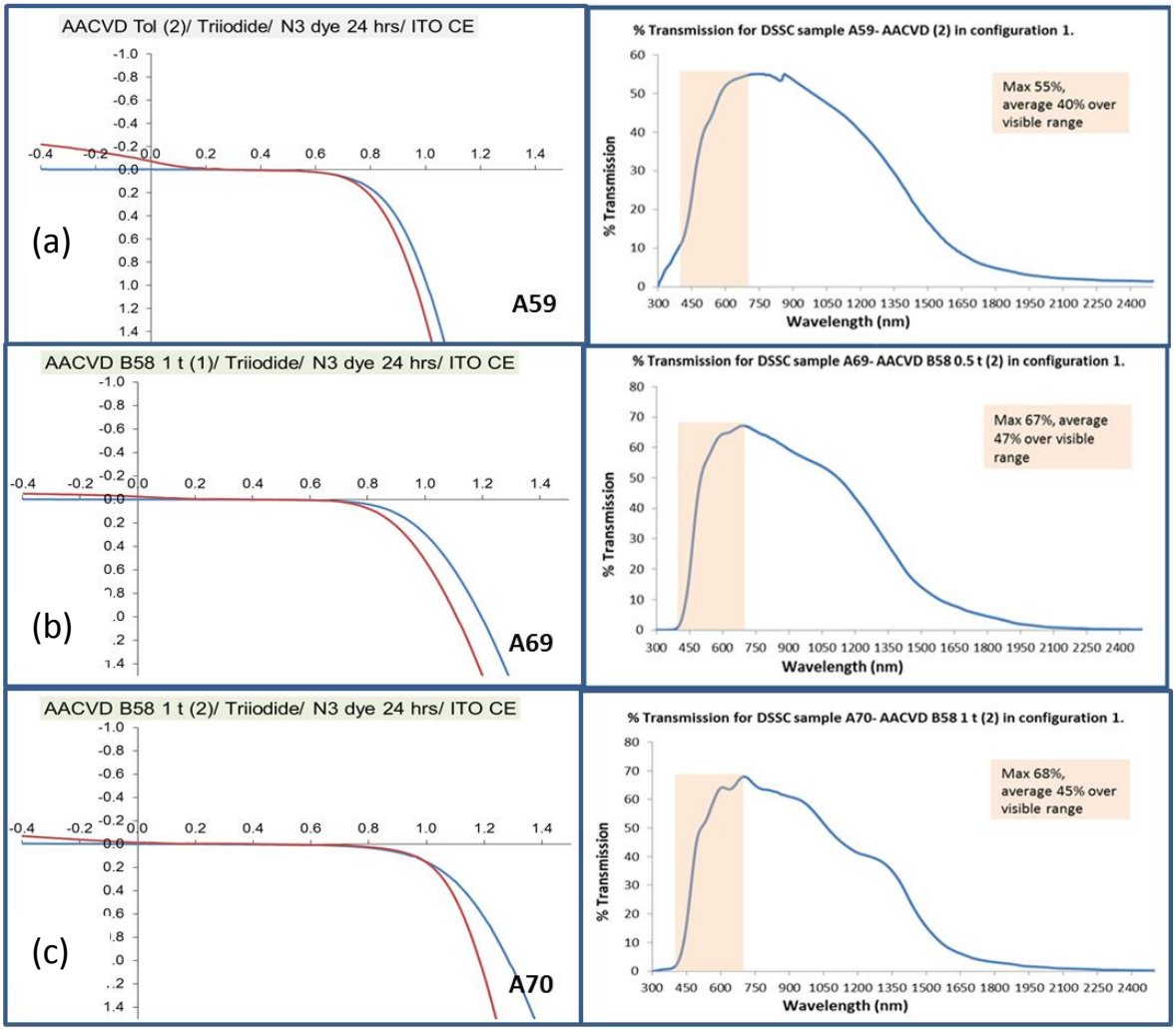

Figure 6.11. Current-Voltage (IV) curves for the DSSC devices prepared from AACVD films in configuration 1, with corresponding optical % transmission plots. Configuration 1= 24 hours dye soaking time, triiodide electrolyte and an ITO counter electrode. IV curves here are for (a) DSSC with 0.004 % PCE efficiency (b) DSSC with 0.0021 % PCE efficiency (c) DSSC with 0.011 % PCE efficiency as shown in tables 6.10-6.12.

Table 6.12. DSSC performance of AACVD TiO_2 thin films prepared with TTIP precursor, toluene as solvent and Brij 58 surfactant in concentrations of 0.5 M and 1 M. The highest power conversion efficiency (PCE, %) value obtained within this group is highlighted blue.

Configuration 1:

- TiO_2 film soak time in N3 dye: 24 hours.
- Triiodide electrolyte
- ITO counter electrode

Surfactant concentration	TiO_2 Sample Name	Short-circuit current J_{sc} (mA/cm^2)	Open-circuit voltage V_{oc} (V)	Fill Factor (FF)	Power Conversion Efficiency (PCE) (%)	Appendix IV curve number
0.5 M	B58 0.5 t (1)	0.010	0.25	0.19	0.0008	A66
	B58 0.5 t (2)	0.014	0.51	0.27	0.0031	A67
	B58 0.5 t (3)	0.030	0.42	0.39	0.0074	A68
1 M	B58 1 t (1)	0.024	0.35	0.16	0.0021	A69
	B58 1 t (2)	0.012	0.39	0.16	0.0011	A70
	B58 1 t (3)	0.005	0.38	0.28	0.0008	A71

The performance of some devices prepared in configuration 1.5, with the addition of a platinum counter electrode in place of the indium-doped tin oxide electrode are given in table 6.13and table 6.14, for the Tween prepared thin films. These devices showed low efficiencies similar to those obtained in configuration 1, within the range of 0.0008-0.0096%. A representation of the % transmission spectra for these devices is shown in figure 6.12, whereby the lowest transmission rating for all devices has been observed (device A75, which shows a maximum transmission of 10% and 9% over the entire visible range). This device exhibited the highest PCE of these devices- 0.0096%, thereby indicating that the transparency of this device has been sacrificed for the performance; it is likely that this thin film adsorbed a thicker layer of dye, resulting in a reduced transmission of light through the device upon UV-Vis measurement, but leading to an increased performance as a photovoltaic.

Table 6.13. DSSC device performance for AACVD TiO_2 thin film prepared with TTIP precursor, toluene as solvent and Tween 20 surfactant in concentrations of 0.5 M and 1 M. The highest power conversion efficiency (PCE, %) value obtained within this group is highlighted blue.

Configuration 1.5:

- TiO_2 film soak time in N3 dye: 24 hours.
- Triiodide electrolyte
- **Pt on FTO used as counter electrode**

Surfactant concentration	TiO_2 Sample Name	Short-circuit current J_{sc} (mA/cm^2)	Open-circuit voltage V_{oc} (V)	Fill Factor (FF)	Power Conversion Efficiency (PCE) (%)	Appendix IV curve number
0.5 M	T20 0.5 t (1)	0.013	0.23	0.27	0.0008	A72
	T20 0.5 t (2)	0.013	0.24	0.42	0.0013	A73
	T20 1 t (1)	0.013	0.35	0.20	0.0009	A74
	T20 1 t (2)	0.108	0.28	0.32	0.0096	A75

Table 6.14. DSSC performance of AACVD TiO_2 thin films prepared with TTIP precursor, toluene as solvent and Tween 40 surfactant in concentrations of 0.5 M and 1 M. The highest power conversion efficiency (PCE, %) value obtained within this group is highlighted blue.

Configuration 1.5:

- TiO_2 film soak time in N3 dye: 24 hours.
- Triiodide electrolyte
- **Pt on FTO used as counter electrode**

Surfactant concentration	TiO_2 Sample Name	Short-circuit current J_{sc} (mA/cm^2)	Open-circuit voltage V_{oc} (V)	Fill Factor (FF)	Power Conversion Efficiency (PCE) (%)	Appendix IV curve number
0.5 M	T40 0.5 t (1)	0.039	0.18	0.23	0.0017	A76
	T40 0.5 t (2)	0.027	0.34	0.42	0.0038	A77
	T40 0.5 t (3)	0.141	0.31	0.23	0.0100	A78

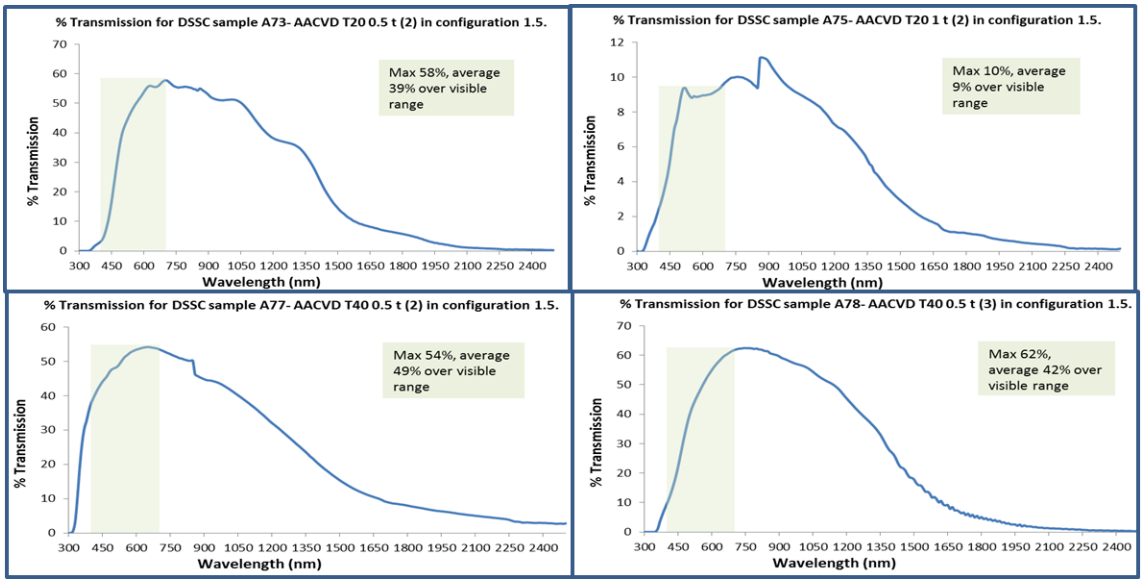

Figure 6.12. Representative transmission (%) spectra for DSSC devices prepared in configuration 1.5, with 24 hours dye soaking time, triiodide electrolyte and platinum counter electrode. Devices shown here are A73, A75, A77 and A78, Tween 20/ Tween 40 thin film devices as described in figure 6.13 and table 6.14.

Table 6.15. DSSC performance of AACVD TiO_2 thin films prepared with TTIP precursor, toluene as solvent and Brij 58 or Brij 98 surfactants in concentrations of 0.5 M and 1. The highest power conversion efficiency (PCE, %) values within this group are highlighted blue.

Configuration 2:

- TiO_2 film soak time in N3 dye: 42 hours
- Iodolyte HI-30 high performance electrolyte
- Platinum on FTO counter electrode

Surfactant concentration	TiO_2 Sample Name	Short-circuit current J_{sc} (mA/cm^2)	Open-circuit voltage V_{oc} (V)	Fill Factor (FF)	Power Conversion Efficiency (PCE) (%)	Appendix IV curve number
0.5 M	B98 0.5 t (1)	0.121	0.70	0.38	0.0337	A79
	B98 0.5 t (2)	0.047	0.63	0.28	0.0087	A80
	B98 0.5 t (3)	0.031	0.63	0.31	0.0064	A81
1 M	B98 1 t (1)	0.111	0.44	0.29	0.0149	A82
	B58 1 t (1)	0.124	0.62	0.37	0.0295	A83
	B58 1 t (2)	0.061	0.54	0.51	0.0175	A84

The IV plots for the AACVD Brij devices with best efficiency (A79, 0.0337% and A83, 0.0295%) are shown in figure 6.13(ab), alongside the corresponding % transmission plots for each device in (c) and (d). Device A79 shows a maximum transmission of 60% and 43% over the visible range, whereas device A83 shows limited transmission over the visible range of 37% with a maximum of 49%. The average transmission over the visible range is in line with that obtained for other AACVD devices.

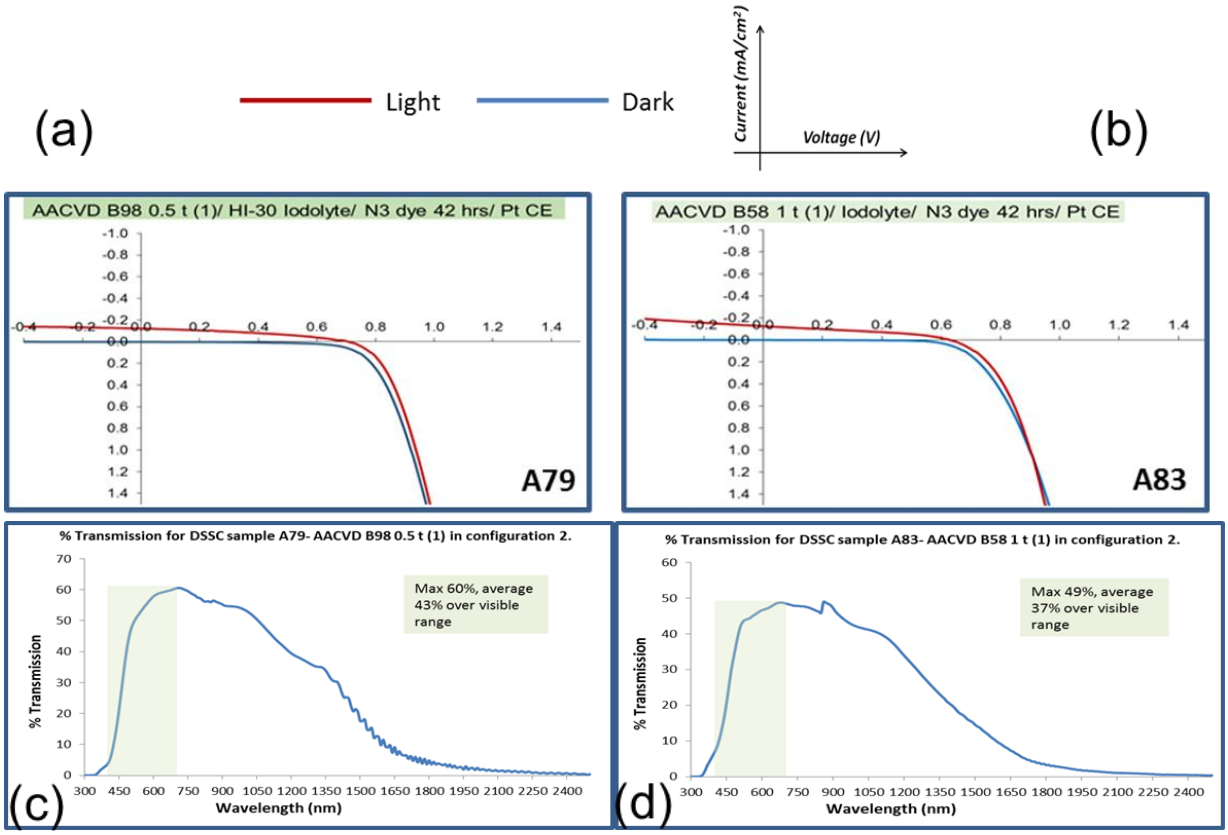

Figure 6.13(ab). Current-Voltage (IV) curves for the optimum DSSC devices prepared with AACVD thin films, in configuration 2, with 42 hours dye soaking time, HI-30 Iodolyte (high performance electrolyte) and a platinum counter electrode. IV curves here are for (a) DSSC with 0.0337 % PCE efficiency (b) DSSC with 0.0295 % PCE efficiency as shown in table 6.15. **(c)** % transmission plot for sample A79 **(d)** % transmission plot for sample A83.

6.3.2.1. Conclusions: DSSC devices using TiO_2thin films prepared by AACVD with TTIP precursor and the effects of surfactant addition

Titanium dioxide thin films prepared by AACVD with and without surfactant addition were tested within three dye-sensitised solar cell configurations; configuration 1, 1.5 and configuration 2. In configuration 1 the thin films were left to soak in N3 dye for 24 hours, and were combined with standard triiodide electrolyte and an ITO counter electrode. In configuration 1.5, the same configuration as 1 was used except with a platinum catalyst counter electrode used instead of ITO. In configuration 2 the thin films were left to soak for a longer time period in N3 dye (42 hours), a high performance electrolyte (Iodolyte HI-30) was used in combination with an FTO counter electrode that had a layer of platinum catalyst on its conductive surface. It was found that DSSCs with configuration 2 produced slightly better power conversion efficiencies than those

observed for 1 and 1.5, with the best DSSC prepared with Brij 98 0.5 M film showing an efficiency of 0.0337 %. This is still much lower than that observed for the best DSSC device measured in this study, 0.3814 % as observed for the TiO_2 sol-gel TTIP film prepared with Brij 58 A-8 (3 layer film prepared with 0.0006 mol/dm^3 Brij 58).

6.3.3. Additional investigations into DSSC configurations: natural vegetable dyes

Perhaps one of the most important components of the dye-sensitised solar cell is the sensitising dye itself, whereby the production of photocurrent within the cell relies on the dye-sensitisation of the semiconductor band gap, which has allowed efficiencies as high as 13% to be achieved from DSSCs (this efficiency value was obtained with a combination of porphyrin sensitiser and graphene nanoplatelets at the counter electrode).[265] Most sensitisers used are metal-organic dyes, typically Ruthenium or Osmium polypyridil complexes, which despite being highly efficient sensitisers, require long, multi-step preparation and purification using expensive equipment; thus these compounds are typically difficult and expensive to prepare, and even more expensive to buy ready-made.[3]

A much cheaper, non-toxic and more readily available alternative to metal-organic dyes are vegetable-based natural dyes, which have been recently reviewed in detail by Calogero et al.[3] Natural dyes have been extracted from plant leaves, red Sicilian oranges, purple egg plants, grapes, Sicilian prickly pears, blackberries, pea flowers, black rice, and many more natural sources and derivatives from all types of plants, vegetables and fruits. [266–273] The study of natural dyes for use in dye solar cells was first reported in 1993 when the photo-electrochemical properties of chlorophyll pigment were exploited by Gratzel's research group to obtain a DSSC a device efficiency (η) of 2.6 %.[266] Since then there has been extensive research into the use of natural dyes in DSSCs, with anthocyanins, betalains, caretenoids, and co-pigments used alongside chlorophyll, as shown in figure 6.11, of which the latter has still been found to produce the highest DSSC efficiency, now at 4.6 %.[3]

As mentioned, anthocyanins are another class of natural dye that have been used within DSSC devices and currently demonstrate the second highest efficiency at 2.9% (figure 6.14). Anthocyanins are a water-soluble vegetable dye traditionally extracted from flowers and berries,

exhibiting a dark red/purple colour.[271] Other sources of anthocyanin aside from flowers, berries, grapes and purple eggplant as mentioned were researched in order to find an novel source for use in this thesis. It was found that the purple potato is a source of anthocyanin dye which to the authors' knowledge has not yet been used as a dye pigment in dye-sensitised solar cells, and thus its extraction and use was explored for novelty as described below.

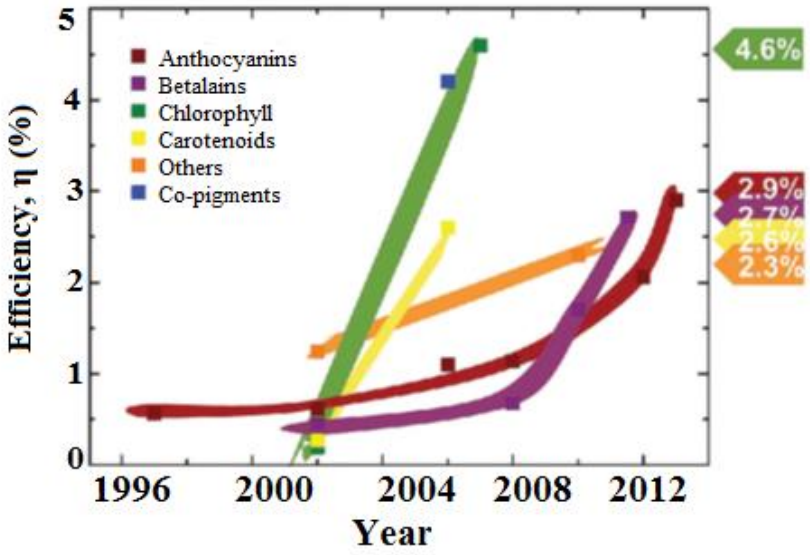

Figure 6.14. As seen and modified from the review by Calogero et al,[3] of whom reserve all rights. Chart to show progression of DSSC performance using different vegetable based natural dyes. Data on the right shows state-of-the-art vegetable dye-based DSSC efficiency (2015), all data references found within this reference.[3]

6.3.3.1. Organic anthocyanin dye derived from purple potatoes used as sensitising dye for semi-transparent DSSC

Since the early 2000s the purple potato has been often highlighted as a rich, natural source of anthocyanins; phytochemicals which offer high free-radical scavenging activity thus ability to act as antioxidants. This has resulted in the purple potato being extensively advertised as a food source with specific health benefits such as reduced risk of chronic diseases and age-related degeneration.[274] This combined with the fact that purple potatoes are a low-cost and high yielding crop has led to a wide variation of studies dedicated to the enhancement of pigment extraction from purple potatoes to enable application as a natural colourant or antioxidant in food, pharmaceutical and textile industries.[275–277]The method of purple pigment (anthocyanin)

extraction used here was modified from a procedure reported in literature by Lachman et al,[274] involving freeze drying and acid hydrolysis as described below.

As the aim of this PhD thesis is to investigate a low-cost method for producing semi-transparent DSSC devices for window glazing, the use of an organic dye derived from purple potato has been explored as an alternative to the expensive N3 ruthenium dye which costs £343.50 per gram (Sigma Aldrich costing January 2017).

6.3.3.2. Purple pigment extraction method

The purple potatoes were washed and cut into thin slices to increase the surface area for freeze drying. Only the purple areas (indicating that they contained pigment) were used, and any white areas were cut out. The potato slices were batch freeze dried for 72 hours in shallow glass petri dishes as shown in figure 6.13. The dried potatoes were then ground down into a fine powder using a pestle and mortar, after which 5g of purple potato powder was mixed with ethanol (40 ml) and hydrochloric acid (5ml, 37%) was added dropwise to the mixture. This mixture was placed in an ultra-sonic water bath for 10 minutes, after which the solution was filtered, as shown in figure 6.15 to produce a purple liquid.

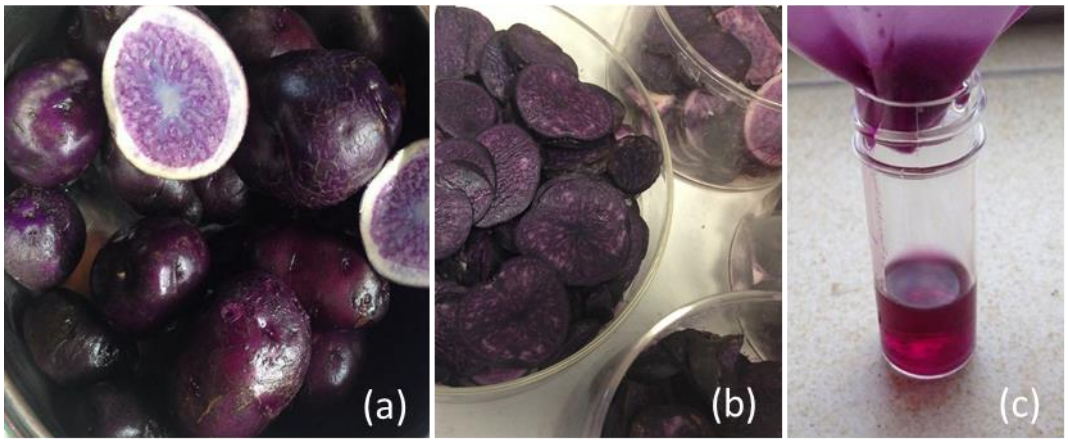

Figure 6.15. Photographs of washed purple potatoes (a), sliced for freeze drying (b), and undergoing filtering after hydrolysis steps to produce purple dye.

This purple liquid was then used directly as a dye for DSSC devices. One caveat with this process is that due to equipment and time constraints the additional purification steps reported in literature were not performed, thus it is likely that this solution may have lacked purity and may not result in the best performance in DSSCs than if the full purification steps had been used.[278] In

addition, no analysis of the purple solution was performed in order to obtain an exact quantification of anthocyanin content within the solution.

6.3.3.3. Results: DSSC device performance with natural anthocyanin dye derived from purple potato.

The results of the DSSC produced with a sol-gel TiO_2 thin film prepared with TTIP precursor, no surfactant addition and 3 layers of film (as produced in chapter 3), sensitised with dye derived from purple potato are shown in table 6.16, with the IV curve shown in figure 6.13, in comparison with DSSC devices of the same configuration and thin film type, synthesised with synthetic N3 ruthenium dye. These results show that the use of purple potato dye as a sensitiser does produce a working DSSC device, however with very low efficiency of just 0.0027 %. The fill factor, open-circuit voltage and short-circuit current are also very low, with values of just 0.15 (FF), 0.35 V (V_{oc}) and 0.031 mA/cm^2 (J_{sc}). The low fill factor is effectively an indication of the quality of the solar cell, and this low value of 0.15 shows that this device may have flaws in its configuration, such as poor connectivity between electrodes, poor dye adsorption or electrolyte leakage resulting in short circuiting of the cell.

Table 6.16. DSSC performance of sol-gel TiO_2thin film prepared with TTIP precursor and no surfactant addition, tested with an organic anthocyanin dye derived from purple potatoes.

Configuration 1:

- TiO_2 film soak time: 24 hours in organic dye extracted from potatoes
- Triiodide electrolyte
- ITO counter electrode

TiO_2 Sample Name	**Short-circuit current J_{sc} (mA/cm^2)**	**Open-circuit voltage V_{oc} (V)**	**Fill Factor (FF)**	**Power Conversion Efficiency (PCE) (%)**	**Appendix IV curve**
Control 3 (3 layer)	0.031	0.35	0.15	0.0027	A85

However, this result still remains promising whereby it is actually higher than some DSSC performances presented in the tables above where the typical N3 porphyrin dye sensitiser was used. For example, for the same type of TiO_2 film prepared by sol-gel without surfactant, 'control' films, as shown in table 6.2, produced DSSC device efficiencies of 0.0024 % (Control-

7, 2 layer) and 0.0011 % (Control-1, 3 layer, shown below in figure 6.14), with fill factors of 0.11 and 0.18 respectively. This shows that even with a low fill factor of just 0.15, the DSSC cell produced here with purple potato dye as the sensitiser was able to produce efficiency comparable to that of a DSSC produced with synthetic dye. This suggests that the natural anthocyanin pigment derived from purple potatoes can be used as a potential alternative to traditional metal-organic ruthenium based sensitisers for dye-solar cells. This would enable a significant cost reduction to the production of DSSCs, whereby the synthetic ruthenium dyes are often the most expensive component within the device. Further investigation into this work as well as sufficient repetitions of this experiment would have to be conducted in order to demonstrate the purple potatoes validity as a natural dye sensitiser source for DSSC devices, however results here remain encouraging for an alternative to the costly ruthenium dye used in this study.

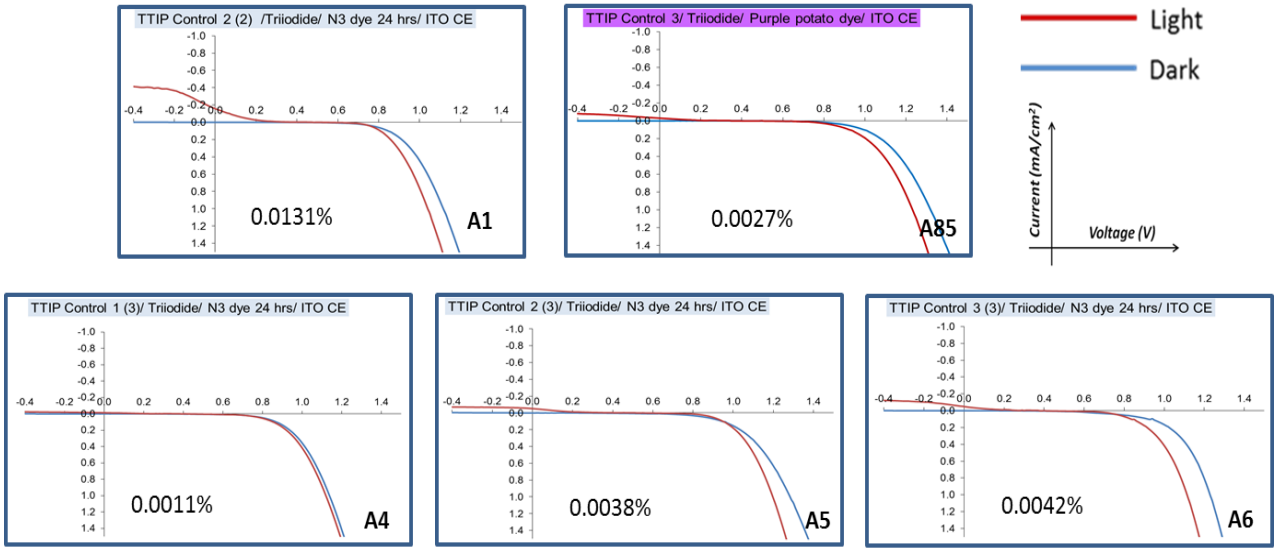

Figure 6.16. Current-Voltage (IV) curves for TiO_2 thin film devices prepared with 3 layer "control" thin films (prepared without surfactant) and ruthenium dye sensitiser (A1, A4, A5 and A6) compared to that prepared with anthocyanin dye derived from purple potatoes (A85). DSSC devices were prepared in configuration 1, with 24 hours dye soaking time, triiodide electrolyte and an indium-doped tin oxide counter electrode. %PCE efficiency are given in each IV curve for comparison.

6.3.4. Additional DSSC configuration investigation: Ionic liquids as electrolytes

One of the main problems with DSSCs for long-term operation lies in the difficulty of encapsulating the volatile solvents such as the triiodide redox couple electrolyte which is made from acetonitrile solvent. The use of ionic liquids as electrolytes for dye-sensitised solar cells offers a viable alternative, whereby room temperature ionic liquids offer good chemical and thermal stability combined with negligible vapour pressure, non-flammability and high ionic conductivity, making them ideal for use in DSSCs where they have already been widely studied for this purpose. [179,279,280]

6.3.4.1. Ionic liquids including copper oxide nanofluids used as ionic electrolyte for semi-transparent DSSCs

Several varieties of copper oxide nanofluids were synthesised by Claire Boudie (Queen's University Ionic Liquid Laboratories (QUILL), Queens University Belfast) and used for testing as ionic electrolytes in dye-sensitised solar cells as part of this thesis. The composition and colours of the ionic liquids are shown in table 6.17, along with abbreviations for the relevant precursors used listed underneath.

Some samples were very viscous and required stirring using a pre-heated (30-50 °C) ultrasonic bath for 5 minutes prior to use. Some samples were also identified as air-sensitive (samples 7 and 8), thus were handled in a glovebox where the device was prepared, using epoxy resin to seal the DSSC device before removal from the glovebox. All ionic liquids were added as a drop in place of the traditional triiodide redox electrolytes described above in section 6.2.3.

Table 6.17. Table of compositions for the 7 ionic liquids tested as ionic electrolytes in dye-sensitised solar cells. Abbreviations for precursors and details of categories are listed below.

Type	Ionic liquid name	Ionic liquid precursor used	Metal precursor used	Reaction preparation conditions	Colour of ionic liquid
(a)	**CB-1-a**	[Emim][OAc]	$Cu(OAc)_2.H_2O$	50-70 °C	Green
	CB-3-a	[Emim][Oct]	$Cu(Oct)_2.H_2O$	50-70 °C	Green
(b)	**CB-4**	[Emim][OAc]	None	80 °C	Yellow-transparent
	CB-5	[Emim][But]	None	80 °C	Yellow-transparent
	CB-6	[Emim][Oct]	None	80 °C	Yellow-transparent
(c)	**CB-7**	[Bmim][SCN]	$[Bmim]_2[Co(SCN)]_4$	50-70 °C	Deep blue-green
	CB-8	$[P_{66614}][SCN]$	$[P_{66614}]_2[Co(SCN)_4]$	50-70 °C	Deep blue

Types:

(a) Pure ionic liquids dissolved with respective Cu carboxylates at 70°C
(b) Pure ionic liquids
(c) Cobalt and Thiocyanate linked to ionic liquids

Abbreviations:

[Emim] = 1-ethyl, 3-methylimidazolium
[Bmim] = 1-buthyl, 3-methylimidazolium
[OAc] = Acetate
[Oct] = Octanoate
[But] = Butanoate
$[P_{66614}]$ = trihexyl(tetradecyl)phosphonium
[SCN] = thiocyanate

$Cu(OAc)_2.H_2O$ = Copper (II) Acetate hydrate
$Cu(Oct)_2.H_2O$ = Copper (II) Octanoate hydrate

6.3.4.2. Results: DSSC device performance with various ionic liquids used as redox electrolyte

DSSC devices were prepared in configuration 1 using sol-gel derived TiO_2 thin films that were made with TTIP precursor and Brij 98 surfactant in just one concentration: 0.0004 mol dm^3. Mostly 3 layer films were used, but some 2 layer films were also tested. Results are shown in table 6.18, and photographs of the resulting colours of DSSC devices are shown in figure 6.17. IV curves are shown in appendix C, figures H-I.

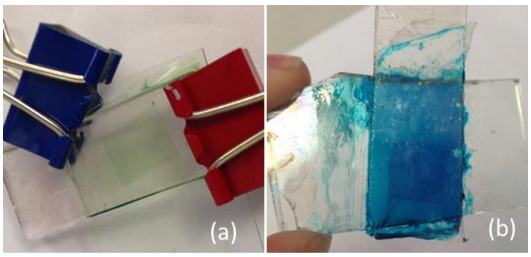

Figure 6.17. Photographs of DSSC devices prepared with ionic liquids; (a) shows a non-sealed DSSC prepared with CB-1a ionic liquid showing a light green colour, (b) shows a sealed DSSC prepared with CB-8 with a dark blue hue owing to the presence of cobalt in the ionic liquid.

All ionic liquids tested proved to be effective in working as an ionic electrolyte whereby all devices tested exhibited power conversion efficiency, in a range from 0.0002-0.0030 %. The best PCE values were obtained for CB-1a (efficiency of 0.0030 %) and CB-5 (efficiency of 0.0015 %). Of particular note are those devices tested with CB-7 and CB-8 electrolytes which showed very high fill factors, 0.97 and 0.74 respectively. This indicates that despite the low efficiencies obtained for these devices; these ionic electrolytes are likely to be very efficient redox charge carriers. A particular advantage of CB-7 and CB-8 are that they contain a cobalt, whereby cobalt poly-pyridine complexes have already been identified as a potential replacement for the triiodide redox shuttle,[156,281,282] owing to their less competitive visible light absorption compared to triiodide resulting in higher photocurrent densities being possible within DSSCS employing cobalt redox electrolytes.[282]

Table 6.18. DSSC performance of sol-gel TiO_2 thin films prepared with Brij 58 and Brij 98 surfactants in concentrations A (0.0006 mol dm^3) and B (0.0004 mol dm^3. Numbers in TiO_2 sample name (2 or 3) represent number of thin film layers. Power conversion efficiency (PCE, %) values and fill factor (FF) values highlighted yellow are the best PCE/ FF values obtained for these devices.

Configuration 1:

Ionic liquid used	TiO_2 sample	Short-circuit current J_{sc} (mA/cm^2)	Open-circuit voltage V_{oc} (V)	Fill Factor (FF)	Power Conversion Efficiency (PCE) (%)
CB-1a	Brij 58 A-**3**	0.0420	0.40	0.18	0.0030
	Brij 58 A-**3**	0.0062	0.40	0.24	0.0006
CB-3a	Brij 58 B-**2**	0.0072	0.30	0.19	0.0004
	Brij 98 B-**2**	0.0125	0.32	0.18	0.0007
	Brij 98 A-**3**	0.0120	0.31	0.23	0.0009
	Brij 98 A-**3**	0.0067	0.24	0.22	0.0003
CB-4	Brij 98 B-**2**	0.0062	0.23	0.25	0.0004
CB-5	Brij 98 B-**3**	0.0141	0.50	0.21	0.0015
CB-6	Brij 98 A-**2**	0.0041	0.18	0.30	0.0002
CB-7	Brij 98 A-**2**	0.0013	0.44	0.97	0.0006
CB-8	Brij 98 A-**2**	0.0016	0.21	0.74	0.0003

6.3.5. Conclusions: use of purple potatoes as a source for natural dye sensitiser and ionic liquids as a replacement for the triiodide redox electrolyte in semi-transparent DSSCs

Purple potatoes were used as a source of dye pigment for dye sensitising DSSC devices, whereby the pigment was extracted from the potato and tested to demonstrate a power conversion efficiency of 0.0027 %. This result is promising when comparing this value to that of some DSSC performances of those prepared with N3 synthetic porphyrin dye sensitiser, for example for the same type of TiO_2 film prepared by sol-gel without surfactant, 'control' films, as shown in table 6.2, DSSC device efficiencies of 0.0022 % (Control-2, 2 layer) and 0.0011 (Control-1, 3 layer), with fill factors of 0.39 and 0.01 respectively were obtained for those prepared with N3 dye. This shows that even with a low fill factor of just 0.15, the DSSC cell produced with purple potato dye as the sensitiser is able to produce a higher efficiency (0.0027) than that of the traditional N3 dye DSSC (0.0022%) which had a fill factor of 0.39. This suggests that natural pigments from purple potatoes can be investigated as a potential alternative to synthetic N3 dyes in DSSC devices, however a much greater study including several repetitions would have to be conducted in order to validate this finding.

Ionic liquids were used in replacement of the triiodide redox electrolyte to determine their potential application in DSSCs. It was found that all ionic liquids tested produced working DSSC devices, however very low efficiencies between 0.0002-0.0030 % were observed in a configuration with N3 dye and ITO counter electrode. Of particular interest is the performance of the cobalt containing ionic liquids which exhibited low efficiencies but high fill factors of 0.74-0.97indicating that they may show high performance when used in a better configuration device, e.g. with a platinum counter electrode.

6.4. Discussion and conclusion: Semi-transparent dye-sensitised solar cells

A small selection of TiO_2 thin films were tested as working electrodes in semi-transparent dye-sensitised solar cell devices, with up to 70% transparency. A total of 96 devices were configured and tested. Repetitions were performed by way of making duplicate devices, prepared from the same type of thin film, with the same configuration. Three variations to the semi-transparent DSSC configuration were tested, whereby efficiencies as high as 0.3 % were obtained for configuration 2 devices, prepared with increased dye soaking time of 42 hours, high performance electrolyte (HI-30 Iodolyte) and a platinum counter electrode.

The optimum devices were those which used sol-gel derived TiO_2 thin films which had been made with TTIP precursor, both with and without surfactant addition. It was found that the DSSCs made with configuration 2 produced consistently higher power conversion efficiencies, with the best DSSCs exhibiting 0.1109-0.3814%. The optimum DSSC (0.3814 % PCE) was made with a three layer sol-gel TiO_2 thin film from TTIP precursor with surfactant addition (Brij 58, concentration A (0.0006 mol dm^3)). This DSSC device also exhibited a relatively high short-circuit current of 0.857 mA/cm^2, an open-circuit voltage of 0.71 V and a fill factor of 0.60.

Those devices prepared with films that had been produced from TIBALD precursor via sol-gel were found to show reduced performance despite the increased photocatalytic efficiencies observed in chapter 3. These DSSCs did not rival the efficiencies of the TTIP thin film DSSCs, whereby all devices exhibited efficiencies below 0.1 %, ranging between 0.0144 % -0.0619 %. This was attributed to a reduced density and porosity of the thin films and therefore reduced dye adsorption.

AACVD thin films were also used in DSSC devices and tested in a number of configurations, whereby configuration 1.5 and 2 were found to exhibit enhanced efficiencies compared to 1, a result which was observed for all thin films tested, whereby configuration 2 was identified as the optimum configuration tested in this study. In comparison with the TTIP sol-gel devices, AACVD DSSCs exhibited poor performance, likely to be due to the high density and low porosity of these films. The optimum DSSC prepared with an AACVD film was for the Brij 98 0.5 M film, exhibiting a PCE efficiency of 0.0337 %. This is much lower than that observed for the best DSSC device, 0.3814 % as observed for the TiO_2 sol-gel TTIP film described above.

In addition to the incorporation of different thin film types into DSSC devices, several smaller studies were conducted to understand the influence of other DSSC components on device performance. Purple potatoes were used as a source of pigment for an organic dye sensitiser, whereby the pigment was extracted from potatoes and made into an ethanol solution for dye loading of the film. This dye was tested in only one DSSC configuration with an ITO electrode and triiodide electrolyte and a power conversion efficiency of 0.0027 % was observed. This result is promising when compared to some of the DSSC performances observed for devices prepared with N3 synthetic porphyrin dye sensitiser , as shown in table 6.2, where DSSC device efficiencies of 0.0024 % (Control-7, 2 layer) and 0.0011 (Control-1, 3 layer) were obtained with fill factors of 0.11 and 0.18 respectively. This shows that even with a low fill factor of just 0.15, the DSSC cell produced with purple potato dye as sensitiser was still able to produce a comparable efficiency (0.0027) to that produced with a synthetic dye (0.0022%). This suggests that natural pigments from purple potatoes could be investigated as a potential alternative to synthetic dye sensitisers, offering wider availability and significant cost reductions, especially for the employment of a low-cost semi-transparent solar cell for window glazing. However, a much larger study would have to be conducted to determine the optimum dye extraction and purification process, as well as the anthocyanin content in the pigment. Furthermore, a significant number of repetitions of the use of this organic dye in DSSC devices would have to be performed to understand its performance and reliability as a dye sensitiser for a solar cell device. In addition, ionic liquids were used as a replacement for triiodide redox electrolytes in DSSC devices. It was found that all ionic liquids tested produced working DSSC devices but with very low efficiencies ranging between 0.0002-0.0030 %.

The transparency of each DSSC was evaluated by measuring the %optical transmission of each device after each photovoltaic assessment had been made. DSSC devices generally showed an average optical transmission within the range of 45-50%, with maximum % transmission values within the range of 55-70%. Only one device measured showed an exception to this transparency, with a low optical transmission of 10%. This indicates that the thin film and configurations used within this study are suitable for the production of semi-transparent DSSCs that have potential to be used in window glazing.

Overall, through the preparation of 96 semi-transparent DSSCs, it can be concluded that TTIP derived sol-gel thin films have the optimum characteristics for use in this type of DSSC. Several

devices have shown optimum power conversion efficiencies of between 0.1 %- 0.3 %, with relatively high open circuit voltages of 0.5 – 0.7 V, and fill factors between 0.5- 0.7. The use of surfactant has been found to enhance the thin film microstructure in such a way that DSSC device performance is improved, whereby the highest device performances (0.3814 % and 0.3749 %) were observed for surfactant derived thin films (Brij 58 (0.0004 mol dm^3, 3 layers) and Tween 40 (0.0004 mol dm^3), 3 layers) respectively.

In conclusion, this study has shown that the semi-transparency of the DSSC devices produced in this thesis has been at the cost of the solar cell performance, whereby an optimum balance between transparency and performance has not been achieved beyond 0.3 % PCE. Efficient light harvesting has been sacrificed for transparency in these devices, whereby light passes through the device rather than being trapped by the sensitiser and absorbed by the TiO_2 layer. The semi-transparent thin films produced in this thesis have tended to be much thinner, with increased density and reduced porosity compared to standard mesoporous TiO_2 thin films used in DSSCs, thus although potentially offering lower series resistance and greater transparency, a much smaller fraction of incoming light is absorbed within the films, resulting in a lower power conversion efficiency. Although non-transparent, the thicker, nanoporous TiO_2 layers made famous by Grätzel in 1991,[142] still offer the benefits of optimum power conversion efficiency when used as the working electrode in a DSSC device, owing to enhanced dye (and thus light) absorption. It is unsurprising that Grätzel has since commercialised his research into DSSC devices as described in the introduction to this chapter, whereby the company Glass 2 Energy Ltd has been founded with the sole purpose of producing semi-transparent DSSCs for building integrated photovoltaics, showing that an optimum balance between transparency and performance has potentially been found.

7. Conclusions and future work

7.1. Overall conclusions

This thesis has focused on the production and characterisation of TiO_2 thin films for photocatalytic applications and for use within semi-transparent dye-sensitised solar cell (DSSC) devices. The production methods used have included sol-gel synthesis with two TiO_2 precursors (titanium tetra-isopropoxide (TTIP) and titanium bis-ammonium lactato dihydroxide (TiBALD)) as well as chemical vapour deposition (CVD) methods of aerosol-assisted CVD and hybrid CVD. The use of non-ionic surfactants in the synthesis of TiO_2 thin films has been extensively explored through the use of five surfactants; Tween 60, Tween 40, Tween 20, Brij 58 and Brij 98 in concentrations of 0.0008 mol dm^3, 0.0006 mol dm^3 and 0.0004 mol dm^3.

An initial investigation into surfactant use in the preparation of TiO_2 thin films was conducted in chapter 3 through sol-gel synthesis. As the heaviest and bulkiest surfactant studied, Tween 60 was found to not produce any enhanced characteristics in the resulting thin films produced, and was not studied further in this thesis. Sol-gel synthesis with Brij 58/98 surfactants and Tween 20/40 surfactants in differing concentrations were found to exhibit some enhanced effects such as increased particle definition, increased film thickness, increased surface roughness, reduces particle sizes and increased superhydrophilicity. This change in thin properties are due to the role of the surfactant during particle growth and nucleation to form the film on the substrate surface, whereby Tween 60 surfactant is likely to have increased particle agglomeration due to its increased mass. These enhanced thin film properties are likely reasons for the enhanced photocatalytic performance observed for these samples. It was found that the photocatalytic half-life of resazurin dye degradation could be reduced from 12 minutes to 3 minutes with the addition of some surfactants, whereby the photoactivity has been improved, from a rate of 1.76 x 10^{12} (dye molecules degraded s^{-1} cm^{-2}) for a plain TTIP derived thin film to a maximum of 2.96 x 10^{12} (dye molecules degraded s^{-1} cm^{-2}) as observed for sample B98 B2 prepared with Brij 98 surfactant in a concentration of 0.004 mol dm^3. This increased photoactivity was attributed to a higher surface roughness (110 nm RMS) indicating a greater surface area for the dye to be absorbed and for photocatalysis to occur.

Chapter 3 also saw the use of a novel TiO_2 thin film precursor; TiBALD, used as an alternative precursor to TTIP. The effects of surfactant addition were explored using the same surfactant types and concentrations as for TTIP, in order to determine whether TiBALD should be used as a preferential precursor for the preparation of photocatalytically active TiO_2 thin films. Indeed, the TiBALD prepared films were found to exhibit higher photocatalytic activities compared to the TTIP prepared films, whereby the addition of surfactant was found to in fact hinder the photocatalytic performance of the thin films. The highest photoactivity observed for a TiBALD prepared film was for that produced without surfactant addition, exhibiting a rate of 9.52×10^{12} (dye molecules degraded s^{-1} cm^{-2}), which is a great enhancement on the same non-surfactant thin film produced with TTIP, which exhibited a rate of just 1.76×10^{12} (dye molecules degraded s^{-1} cm^{-2}). This enhanced photoactivity was attributed to several factors including the increased thin film thickness, surface roughness and superhydrophilicity observed in TiBALD prepared films.

The use of aerosol-assisted CVD for the production of TiO_2 thin films was explored in chapter 4 with surfactant addition and two solvents; toluene and dichloromethane (DCM). Two solvents were used to determine whether the changes to thin film microstructure and photocatalytic performance were a result of surfactant addition or the solvent choice. With toluene as solvent, thin films were prepared, with the addition of Tween and Brij surfactants in three concentrations; 0.5 M, 1 M and 2 M. The effects of surfactant addition were explored and the addition of surfactant was found to significantly affect the photocatalytic performance of the deposited thin films, depending on the surfactant type used and the concentration. The AACVD films produced without surfactant addition exhibited an average half-life of 5 minutes for resazurin degradation, with a calculated rate of photoactivity of 3.88×10^{13} (dye molecules degraded s^{-1} cm^{-2}), compared to the highest photoactivity obtained by the AACVD Brij 58 0.5 M sample which had a half-life of just 3 minutes and a photoactivity rate of 9.40×10^{14} (dye molecules degraded s^{-1} cm^{-2}). This enhanced photocatalytic performance for the Brij 58 surfactant prepared film was attributed to several factors, including a smaller particle size of 80 nm within the film compared to 110 nm for the non-surfactant sample as well as an increased texture coefficient in the (004) preferential plane of 2.70 vs 1.46 for the control sample.

The use of DCM as solvent was also explored in order to determine whether the enhancements seemingly made by surfactant addition were limited by the solvent used. The addition of Tween and Brij surfactants in two concentrations; 0.5 M and 1 M were explored as the higher

concentration of 2 M was not found to produce any enhanced thin film characteristics. Surfactant addition with DCM as solvent through AACVD was found to significantly affect the photocatalytic performance of the deposited TiO_2 thin films, whereby films produced without surfactant addition exhibited an average half-life of 12.5 minutes for resazurin (much lower than films of the same type prepared without surfactant addition but toluene solvent which showed an average half-life of 5 minutes), with a calculated rate of photoactivity of 1.86 x 10^{13} (dye molecules degraded s^{-1} cm^{-2}). The addition of surfactant was found to enhance this activity, with the highest performance exhibited sample AACVD B98 0.5 DCM which had a half-life of just 2.75 minutes and a photoactivity rate of 1.30 x 10^{15} (dye molecules degraded s^{-1} cm^{-2}). This enhanced performance was comparable to those produced with toluene thin films, and was attributed to a number of factors including smaller particle size (60 nm vs 90 nm for control DCM film) and increased texture coefficient (2.95 vs 2.64 for control film) in the (004) preferential plane.

This exploration into the use of surfactants and two different solvents in the AACVD of TiO_2 thin films was made in chapter 4 in order to obtain an understanding of the processing parameters which can result in enhanced characteristics and properties for the films produced. The exploration of the solvent affects has enabled a better understanding of the role of the surfactant in optimizing the thin film properties. Through comparison of the photocatalytic performance across the AACVD samples produced with both toluene and DCM as solvent it was found that no significant trend across all samples was present due to the different use of solvent with surfactant. However, the results gave a clear indication that the use of Brij surfactant enables a significant enhancement of photocatalytic activity in AACVD derived thin films compared to plain films prepared without surfactant, regardless of solvent choice. Furthermore toluene was observed to be a preferential solvent for the production of photocatalytically active thin films, whereby comparison of the plain TTIP samples prepared without surfactant addition showed that those films produced with toluene exhibited higher average photocatalytic rates; 3.88 x 10^{13} (molecules degraded s^{-1} cm^{-2}) vs 1.86 x 10^{13} (molecules degraded s^{-1} cm^{-2}) for the DCM prepared films. This was attributed to the toluene prepared TiO_2 thin film exhibiting higher hydrophilicity (showing super hydrophilicity after 30 minutes UV irradiation), an increased average surface roughness (average of 134 nm RMS vs just 39 nm for the DCM prepared films), and a smaller crystallite size (7.5 nm vs 10 nm for DCM prepared film). This combination of

properties is suggested to have enabled the film to exhibit a faster rate of resazurin degradation; owing to better adsorption of the dye on the surface and a greater surface area to volume ratio upon which the photocatalytic reaction could take place.

In correlation with the sol-gel thin film samples, the AACVD samples produced with the addition of Brij surfactants were again found to show significantly faster photocatalytic degradation rates for resazurin dye compared to the plain films prepared without surfactant, whereby the fastest activities were calculated as 9.50×10^{14} (dye molecules degraded s^{-1} cm^{-2}) for sample AACVD B58 0.5 t (prepared with Brij 58 0.5 M in toluene) and 1.30×10^{15} (dye molecules degraded s^{-1} cm^{-2}) for sample AACVD B98 0.5 d (prepared with Brij 98 0.5 M in DCM). As photocatalysis is a complex phenomenon with many interlinking characteristics affecting the performance of a material, this enhanced performance was not attributed to a single material property. Some thin film properties were highlighted as potential factors resulting in the improved photocatalytic performance, such as smaller average crystallite sizes (~5.5 nm), and larger texture coefficients in the 004 anatase plane.

In chapter 5, hybrid chemical vapour deposition (HCVD) was explored as an alternative to AACVD derived thin films, aiming to combine the advantages of AACVD with the advantages of atmospheric pressure CVD, including faster reaction times and more robust thin films. The effect of surfactant addition was again studied to determine its effects on the properties and performance of the thin films produced, whereby surfactants were found to greatly alter the morphology, particle sizes and thickness of HCVD films. Typically HCVD films were found to show much greater variation in thin film thickness, with the addition of surfactant found to produce much thicker films compared to those made by AACVD, with average thicknesses as high as 4.5 μm (as for HT40 1- thin film prepared with Tween 40 surfactant in 1M concentration). HCVD films prepared without surfactant were much thinner, ranging from 1-1.5 μm. This variation in thin film thickness was attributed to the different sizes of surfactants used, whereby those with higher masses and larger structures (Tweens) tended to form different shapes of micelles that enabled increased thin film nucleation and growth, thus leading to thicker films produced. In terms of photocatalytic performance, the addition of surfactant was not found to produce any enhanced effects, with only two instances showing improvements to thin film performance. Again it was the Brij samples that enabled higher photocatalytic activities to be obtained, through samples HB98 1 and HB982 with photoactivities of 1.5×10^{13} and 1.1×10^{13}

(dye molecules degraded s^{-1} cm^{-2}) respectively compared to 9.8 x 10^{12} (dye molecules degraded s^{-1} cm^{-2}) for the plain HCVD sample prepared without surfactant. This enhanced photocatalytic performance was again attributed to higher texture coefficients observed in the [004] plane and smaller average crystallite sizes between 12- 13 nm.

Overall, three methods of thin film deposition were used to prepare TiO_2 thin films within this thesis; sol-gel, AACVD and HCVD. The addition of Brij and Tween surfactants were studied in order to determine the effects of surfactant addition with the overarching aim to establish an optimised method for producing photocatalytically active TiO_2 thin films which was cheap and could be easily scaled up for industrial use. The photocatalytic performances of all three sets of films were compared whereby it was concluded that the AACVD samples demonstrated the best overall photocatalytic performances, with samples prepared with toluene as solvent and Brij surfactant showing the highest activities (rates of 9.50 x 10^{14} and 1.08 x 10^{14} dye molecules degraded s^{-1} cm^{-2} for AB58 0.5t and AB98 0.5 t respectively). This was found to be up to two magnitudes higher than the best photoactivities obtained for sol-gel thin films and hybrid films. In addition, hybrid CVD thin films were found to perform better on average compared to the sol-gel samples, with the best photoactivities again prepared with Brij 58 and Brij 98; HB58 2 (1.0 x 10^{13} dye molecules degraded s^{-1} cm^{-2}) HB98 1 (1.5 x 10^{13} dye molecules degraded s^{-1} cm^{-2}) and HB98 2 (1.1 x 10^{13} dye molecules degraded s^{-1} cm^{-2}). The sol-gel samples demonstrated inferior photocatalytic activities by comparison, with much lower activities of between 1.7 x 10^{12} dye molecules degraded s^{-1} cm^{-2} (plain TTIP sample prepared without surfactant) up to the highest values which were obtained using TiBALD precursor, of 9.51 x 10^{12} dye molecules degraded s^{-1} cm^{-2} for the film prepared without surfactant and 8.4 x 10^{12} dye molecules degraded s^{-1} cm^{-2} for the Brij 58 film prepared with a concentration of 0.0004 mol dm^3. Overall, the thin film production methods can be tentatively ranked in the following order for producing photocatalytically active thin films; AACVD films, Hybrid CVD films, sol-gel films prepared with TiBALD and lastly sol-gel with TTIP precursor. The use of Brij surfactants was found across the board to generally produce more photocatalytically active thin films.

In chapter 6, a small selection of TiO_2 thin films were used within semi-transparent dye-sensitised solar cell devices, with up to 70% maximum transparency. A total of 96 devices were configured and tested, with repetitions performed by way of making duplicate devices, prepared from the same type of thin film, with the same configuration. Three configurations were tested,

including increasing the thin film soaking time in N3 dye from 24 hours to 42 hours, using a high-performance electrolyte (HI-30 Iodolyte) and a platinum counter electrode in place of a plain indium doped tin oxide (ITO) electrode. The latter configuration (2) using increased dye soaking time (42 hours) combined with the high-performance electrolyte (HI-30 Iodolyte) and a platinum counter electrode was found to enable enhanced device performances across the range of films tested, with PCE values as high as 0.3 % observed.

In contrast to the assessments and conclusions made through evaluating the photocatalytic performance of the thin films in chapters 3-5, the optimum DSSC devices were those prepared with TiO_2 thin films derived from sol-gel where TTIP precursor had been used. It was found that these DSSCs made with configuration 2 produced consistently higher power conversion efficiencies, with the best DSSCs exhibiting 0.1109-0.3814%. The optimum DSSC (0.3814 % PCE) was made with a TiO_2 thin film that had been produced with surfactant addition; a 3-layer Brij 58 thin film (concentration A (0.0006 mol dm^3)) which also exhibited an short-circuit current of 0.857 mA/cm^2, an open-circuit voltage of 0.71 V and a fill factor of 0.60. In contrast, the TIBALD derived thin films which showed promising photocatalytic performances were found to demonstrate reduced performance in DSSC devices, whereby all devices exhibited efficiencies below 0.1 %, ranging between 0.0144 % -0.0619 %. This was attributed to reduced density and thin film porosity in the TiBALD prepared films, resulting in reduced dye adsorption and thus limited light absorption to catalyse the DSSC reaction. In addition, the use of AACVD thin films in DSSC devices were also found to inhibit the overall PCE performance, with only a few toluene thin films that were prepared with Brij surfactant tested in DSSCs. This poor performance was again attributed to the high density and low porosity of these films. The optimum DSSC prepared with an AACVD derived thin film had an efficiency of 0.0337 % (thin film prepared with Brij 98 0.5 M), which is much lower than that observed for the best DSSC device, 0.3814 % (for the TiO_2 sol-gel TTIP film described above).

As well as the incorporation of different thin film types into DSSC devices, several smaller studies were conducted to explore the influence of other components on DSSC device performance. An alternative natural dye sensitiser was studied by using dye extracted from purple potatoes, demonstrating a power conversion efficiency of 0.0027 % for a configuration using reduced dye loading time (24 hours), the less efficient electrolyte (Triiodide) and a plain ITO electrode. This was discussed as a promising result through performance comparison to the

DSSC performances of some devices prepared with N3 synthetic porphyrin dye sensitiser whereby efficiencies as low as 0.0024 % (Control-7, 2 layer) and 0.0011 (Control-1, 3 layer), with fill factors of just 0.118and 0.01 were obtained. Conclusions were drawn that natural pigments from purple potatoes could be investigated as potential alternatives to synthetic dye sensitisers, as even with a low fill factor of just 0.15, the DSSC cell produced with purple potato dye as sensitiser was able to produce a comparable efficiency (0.0027) to that obtained with the synthetic N3 dye DSSC (0.0022%) at a fraction of the cost. N3 synthetic dye costs £343.50 per gram (Sigma Aldrich costing January 2017) whereas the purple potatoes were grown effectively for free, with the only associated costs derived from the minimal use of acid and solvent, in addition to access to freeze drying equipment. However, a much larger study including repetitions would have to be conducted to determine the true potential of sensitising dye derived from purple potatoes. its true potential. In addition to exploring alternative sensitisers, ionic liquids were investigated as a replacement for triiodide redox electrolytes in DSSC devices, whereby those studied were found to function within the DSSC configurations but at very low efficiencies between 0.0002-0.0030 % PCE.

In summary, the use of photocatalytic performance as an indicator for DSSC device performance has been shown to be an inadequate, whereby those thin films which produced the highest photocatalytic performances (AACVD and TiBALD sol-gel films) were found to exhibit the lowest efficiencies in DSSC devices, a result which was attributed to the increased density and reduced porosity of the thin films.

7.2. Future Work

The chapters focusing on the production of semi-transparent TiO_2 thin films via sol-gel (chapter 3), aerosol-assisted CVD (chapter 4) and hybrid CVD (chapter 5) produced a range of conclusions focused around photocatalytic degradation of resazurin dye as an indicator for general photocatalytic performance, and potential performance within DSSC devices. Further work could focus on broadening this photocatalytic study to incorporate testing using other organic materials, such as stearic acid, which would offer more insights into the photocatalytic mechanisms and properties of the thin films which enable improved performance. Furthermore, this study focused only on the use of two brand named non-ionic surfactants; Tween and Brij, whereby these procedures could now be tested across a much wider range of commonly used

surfactants, such as CTAB and Pluronic surfactants, to add further insights into how surfactants interact with TiO_2 thin film growth to alter the resulting thin film properties. In addition, now that specific concentrations of Tween and Brij surfactants have been found to enable enhanced photocatalytically active TiO_2 thin films to be produced by sol-gel, AACVD and hybrid CVD, these surfactants could also be explored for the modification of zinc oxide or other similar semiconducting thin films.

The final chapter focusing on the incorporation of TiO_2 thin films into DSSC devices gave a good indication of thin film performance for this application; however a much larger study including increased repetitions would need to be carried out in able to add validity to the results. In addition, only a few configurations were tested, whereby a much larger array of variations could be investigated to improve device performance whilst maintaining transparency, including incorporation of solid state electrolytes, extra TiO_2 light scattering layers and device sealing.

The original intention of this work was to incorporate the results of DSSC devices into energy modelling in order to determine whether DSSCs could be viable candidates for energy efficient glazing, whereby those produced in this thesis showed maximum transparency of 70%, with most DSSC devices showing an average transmission of 45-50% in the visible range. Future work would look at not only finding the optimum configuration for a semi-transparent DSSC using thin films produced by sol-gel and AACVD, but also input these results into a range of energy modelling scenarios to determine the energy and subsequent cost savings if these DSSC devices were incorporated into window glazing. These models could then be used to quickly evaluate whether new glazing systems utilising DSSC technology produced in this manner could enable potential energy savings for new buildings, work which would be of great interest to those companies already attempting to commercialise DSSC technology, such as Glass 2 Energy.

8. References

1. Ohsaka, T., Izumi, F. & Fujiki, Y. Raman spectrum of anatase, TiO2. *J. Raman Spectrosc.* **7,** 321–324 (1978).
2. Islami, F. Energy Glass- Where Aesthetics and Transaprency Matter. *Glas. 2 Energy Ltd*
3. Calogero, G. *et al.* Vegetable-based dye-sensitized solar cells. *Chem. Soc. Rev.* **44,** 3244–3294 (2015).
4. Clarke, J. ., Janak, M. & Ruyssevelt, P. Assessing the overall performance of advanced glazing systems. *Sol. Energy* **63,** 231–241 (1998).
5. Gustavsen, A., Grynning, S., Arasteh, D., Jelle, B. P. & Goudey, H. Key elements of and material performance targets for highly insulating window frames. *Energy Build.* **43,** 2583–2594 (2011).
6. Kanu, S. S. & Binions, R. Thin films for solar control applications. (2010). doi:10.1098/rspa.2009.0259
7. Peng, C., Huang, Y. & Wu, Z. Building-integrated photovoltaics (BIPV) in architectural design in China. *Energy Build.* **43,** 3592–3598 (2011).
8. Petter Jelle, B., Breivik, C. & Drolsum Røkenes, H. Building integrated photovoltaic products: A state-of-the-art review and future research opportunities. *Sol. Energy Mater. Sol. Cells* **100,** 69–96 (2012).
9. Jelle, B. P. *et al.* Fenestration of today and tomorrow: A state-of-the-art review and future research opportunities. *Sol. Energy Mater. Sol. Cells* **96,** 1–28 (2012).
10. Eperon, G. E., Burlakov, V. M., Goriely, A. & Snaith, H. J. Neutral color semitransparent microstructured perovskite solar cells. *ACS Nano* **8,** 591–8 (2014).
11. Gevorgyan, S. A. *et al.* Lifetime of Organic Photovoltaics: Status and Predictions. *Adv. Energy Mater.* **6,** 1501208 (2016).
12. Kang, M. G., Park, N.-G., Park, Y. J., Ryu, K. S. & Chang, S. H. Manufacturing method for transparent electric windows using dye-sensitized TiO2 solar cells. *Sol. Energy Mater. Sol. Cells* **75,** 475–479 (2003).
13. Chiang, Y.-F. *et al.* Non-color distortion for visible light transmitted tandem solid state dye-sensitized solar cells. *Renew. Energy* **59,** 136–140 (2013).

14. Chen, K.-S. *et al.* Semi-transparent polymer solar cells with 6% PCE, 25% average visible transmittance and a color rendering index close to 100 for power generating window applications. *Energy Environ. Sci.* **5,** 9551 (2012).
15. Chen, C.-C., Dou, L. & Zhu, R. Visibly Transparent Polymer Solar Cells Produced by Solution Processing. **6,** 7185–7190 (2012).
16. Chen, C.-C. *et al.* High-performance semi-transparent polymer solar cells possessing tandem structures. *Energy Environ. Sci.* **6,** 2714 (2013).
17. Snaith, H. J. Perovskites: The Emergence of a New Era for Low-Cost, High-Efficiency Solar Cells. *J. Phys. Chem. Lett.* **4,** 3623–3630 (2013).
18. Niu, G., Guo, X. & Wang, L. Review of Recent Progress in Chemical Stability of Perovskite Solar Cells. *J. Mater. Chem. A* **3,** 8970–8980 (2014).
19. Fujishima, A. & Honda, K. Electrochemical Photolysis of Water at a Semiconductor Electrode. *Nature* **238,** 37–38 (1972).
20. Hashimoto, K., Irie, H. & Fujishima, A. A Historical Overview and Future Prospects. **17,** (2007).
21. Page, K., Wilson, M. & Parkin, I. P. Antimicrobial surfaces and their potential in reducing the role of the inanimate environment in the incidence of hospital-acquired infections. *J. Mater. Chem.* **19,** 3819 (2009).
22. Panjawi, N., Naik, A., Warwick, M. E. a., Hyett, G. & Binions, R. The Preparation of Titanium Dioxide Gas Sensors by the Electric Field Assisted Aerosol CVD Reaction of Titanium Isopropoxide in Toluene. *Chem. Vap. Depos.* **18,** 102–106 (2012).
23. Park, H., Park, Y., Kim, W. & Choi, W. Surface modification of TiO2 photocatalyst for environmental applications. *J. Photochem. Photobiol. C Photochem. Rev.* **15,** 1–20 (2013).
24. Park, N. Comparison of dye-sensitized rutile-and anatase-based TiO2 solar cells. *J. Phys. …* **104,** 8989–8994 (2000).
25. Macwan, D. P., Dave, P. N. & Chaturvedi, S. A review on nano-TiO2 sol–gel type syntheses and its applications. *J. Mater. Sci.* **46,** 3669–3686 (2011).
26. Kim, D. S. & Kwak, S.-Y. The hydrothermal synthesis of mesoporous TiO2 with high crystallinity, thermal stability, large surface area, and enhanced photocatalytic activity. *Appl. Catal. A Gen.* **323,** 110–118 (2007).
27. Shinde, P. S. & Bhosale, C. H. Properties of chemical vapour deposited

nanocrystalline TiO2 thin films and their use in dye-sensitized solar cells. *J. Anal. Appl. Pyrolysis* **82,** 83–88 (2008).

28. Choy, K. L. Chemical vapour deposition of coatings. *Prog. Mater. Sci.* **48,** 57–170 (2003).
29. Edusi, C., Hyett, G., Sankar, G. & Parkin, I. P. Aerosol-Assisted CVD of Titanium Dioxide Thin Films from Methanolic Solutions of Titanium Tetraisopropoxide; Substrate and Aerosol-Selective Deposition of Rutile or Anatase. *Chem. Vap. Depos.* **17,** 30–36 (2011).
30. Romero, L. & Binions, R. Effect of AC electric fields on the aerosol assisted chemical vapour deposition growth of titanium dioxide thin films. *Surf. Coatings Technol.* **230,** 196–201 (2013).
31. Pelizzetti, E. & Minero, C. Mechanism of the photo-oxidative degradation of organic pollutants over TiO2 particles. *Electrochim. Acta* **38,** 47–55 (1993).
32. Ochiai, T. & Fujishima, A. Photoelectrochemical properties of TiO2 photocatalyst and its applications for environmental purification. *J. Photochem. Photobiol. C Photochem. Rev.* **13,** 247–262 (2012).
33. Ni, M., Leung, M. K. H., Leung, D. Y. C. & Sumathy, K. A review and recent developments in photocatalytic water-splitting using TiO2 for hydrogen production. *Renew. Sustain. Energy Rev.* **11,** 401–425 (2007).
34. *Sol-Gel Processing for Conventional and Alternative Energy*. **65,** (Springer Science & Business Media, 2012).
35. Dvoranová, D., Brezová, V., Mazúr, M. & Malati, M. A. Investigations of metal-doped titanium dioxide photocatalysts. *Appl. Catal. B Environ.* **37,** 91–105 (2002).
36. Malati, M. A. & Wong, W. K. Doping TiO2 for solar energy applications. *Surf. Technol.* **22,** 305–322 (1984).
37. Yates, H. M., Nolan, M. G., Sheel, D. W. & Pemble, M. E. The role of nitrogen doping on the development of visible light-induced photocatalytic activity in thin TiO2 films grown on glass by chemical vapour deposition. *J. Photochem. Photobiol. A Chem.* **179,** 213–223 (2006).
38. Kumar, S. G. & Devi, L. G. Review on modified TiO2 photocatalysis under UV/visible light: selected results and related mechanisms on interfacial charge carrier transfer dynamics. *J. Phys. Chem. A* **115,** 13211–41 (2011).

39. Dunnill, C. W., Kafizas, A. & Parkin, I. P. CVD Production of Doped Titanium Dioxide Thin Films. *Chem. Vap. Depos.* **18,** 89–101 (2012).
40. Dunnill, C. *et al.* Visible light photocatalysts-N-doped TiO2 by sol-gel, enhanced with surface bound silver nanoparticle islands. *J. Mater. Chem.* **21,** 11854–11861 (2011).
41. Serpone, N., Salinaro, A., Horikoshi, S. & Hidaka, H. Beneficial effects of photo-inactive titanium dioxide specimens on plasmid DNA, human cells and yeast cells exposed to UVA/UVB simulated sunlight. *J. Photochem. Photobiol. A Chem.* **179,** 200–212 (2006).
42. Wold, A. Photocatalytic properties of titanium dioxide (TiO2). *Chem. Mater.* **5,** 280–283 (1993).
43. *Application of Titanium Dioxide Photocatalysis to Construction Materials: State-of-the-Art Report of the RILEM Technical Committee 194-TDP*. (Springer Science & Business Media, 2011). at <https://books.google.com/books?id=LwYgLW0nwu0C&pgis=1>
44. Testino, A. *et al.* Optimizing the photocatalytic properties of hydrothermal TiO2 by the control of phase composition and particle morphology. a systematic approach. *J. Am. Chem. Soc.* **129,** 3564–75 (2007).
45. Linsebigler, A. L., Lu, G. & Yates, J. T. Photocatalysis on TiO2 Surfaces: Principles, Mechanisms, and Selected Results. *Chem. Rev.* **95,** 735–758 (1995).
46. Carp, O. Photoinduced reactivity of titanium dioxide. *Prog. Solid State Chem.* **32,** 33–177 (2004).
47. Dambournet, D., Belharouak, I. & Amine, K. Tailored Preparation Methods of TiO 2 Anatase, Rutile, Brookite: Mechanism of Formation and Electrochemical Properties †. *Chem. Mater.* **22,** 1173–1179 (2010).
48. Kafizas, A., Carmalt, C. J. & Parkin, I. P. Does a Photocatalytic Synergy in an Anatase-Rutile TiO(2) Composite Thin-Film Exist? *Chemistry* **18,** 13048–58 (2012).
49. Shi, D. *Nanomaterials and Devices*. (Elsevier Science, 2014). at <https://books.google.com/books?id=OER0AwAAQBAJ&pgis=1>
50. Reyes-Coronado, D. *et al.* Phase-pure TiO(2) nanoparticles: anatase, brookite and rutile. *Nanotechnology* **19,** 145605 (2008).
51. Arconada, N. *et al.* Synthesis and photocatalytic properties of dense and porous TiO2-anatase thin films prepared by sol–gel. *Appl. Catal. B Environ.* **86,** 1–7 (2009).

52. Cross, A. J., Dunnill, C. W. & Parkin, I. P. Production of Predominantly Anatase Thin Films on Various Grades of Steel and Other Metallic Substrates From TiCl4 and Ethyl Acetate by Atmospheric Pressure CVD. *Chem. Vap. Depos.* **18,** 133–139 (2012).
53. Nakamura, T. *et al.* Preferential formation of anatase in laser-ablated titanium dioxide films. *Acta Mater.* **53,** 323–329 (2005).
54. Lee, S. C., Yu, H., Yu, J. & Ao, C. H. Fabrication, characterization and photocatalytic activity of preferentially oriented TiO2 films. *J. Cryst. Growth* **295,** 60–68 (2006).
55. Ibhadon, A. & Fitzpatrick, P. Heterogeneous Photocatalysis: Recent Advances and Applications. *Catalysts* **3,** 189–218 (2013).
56. Zhang, H. & Banfield, J. F. Understanding Polymorphic Phase Transformation Behavior during Growth of Nanocrystalline Aggregates: Insights from TiO 2. *J. Phys. Chem. B* **104,** 3481–3487 (2000).
57. Zhang, H. & Banfield, J. F. Thermodynamic analysis of phase stability of nanocrystalline titania. *J. Mater. Chem.* **8,** 2073–2076 (1998).
58. Chen, Y., Stathatos, E. & Dionysiou, D. D. Microstructure characterization and photocatalytic activity of mesoporous TiO2 films with ultrafine anatase nanocrystallites. *Surf. Coatings Technol.* **202,** 1944–1950 (2008).
59. Ohtani, B., Ogawa, Y. & Nishimoto, S. Photocatalytic Activity of Amorphous−Anatase Mixture of Titanium(IV) Oxide Particles Suspended in Aqueous Solutions. *J. Phys. Chem. B* **101,** 3746–3752 (1997).
60. Sathasivam, S. *et al.* Highly Photocatalytically Active Iron(III) Titanium Oxide Thin films via Aerosol-Assisted CVD. *Chem. Vap. Depos.* **21,** 21–25 (2015).
61. Mills, A. & McGrady, M. A study of new photocatalyst indicator inks. *J. Photochem. Photobiol. A Chem.* **193,** 228–236 (2008).
62. Dunnill, C. W. *et al.* Nanoparticulate silver coated-titania thin films—Photo-oxidative destruction of stearic acid under different light sources and antimicrobial effects under hospital lighting conditions. *J. Photochem. Photobiol. A Chem.* **220,** 113–123 (2011).
63. Foster, H. A. *et al.* Antimicrobial activity of titania/silver and titania/copper films prepared by CVD. *J. Photochem. Photobiol. A Chem.* **216,** 283–289 (2010).
64. O'Regan, B. & Grätzel, M. A low-cost, high-efficiency solar cell based on dye-sensitized colloidal TiO2 films. *Nature* **353,** 737–740 (1991).
65. Pagliaro, M., Palmisano, G., Ciriminna, R. & Loddo, V. Nanochemistry aspects of

titania in dye-sensitized solar cells. *Energy Environ. Sci.* **2,** 838 (2009).

66. Kabra, K., Chaudhary, R. & Sawhney, R. L. Treatment of Hazardous Organic and Inorganic Compounds through Aqueous-Phase Photocatalysis: A Review. *Ind. Eng. Chem. Res.* **43,** 7683–7696 (2004).
67. Serpone, N. Is the band gap of pristine TiO(2) narrowed by anion- and cation-doping of titanium dioxide in second-generation photocatalysts? *J. Phys. Chem. B* **110,** 24287–93 (2006).
68. Hagfeldt, A. & Gratzel, M. Light-induced redox reactions in nanocrystalline systems. *Chem. Rev.* 49–68 (1995).
69. Choi, H., Stathatos, E. & Dionysiou, D. D. Synthesis of nanocrystalline photocatalytic TiO2 thin films and particles using sol–gel method modified with nonionic surfactants. *Thin Solid Films* **510,** 107–114 (2006).
70. Černigoj, U., Štangar, U. L., Trebše, P., Krašovec, U. O. & Gross, S. Photocatalytically active TiO2 thin films produced by surfactant-assisted sol–gel processing. *Thin Solid Films* **495,** 327–332 (2006).
71. Legrand-Buscema, C., Malibert, C. & Bach, S. Elaboration and characterization of thin films of TiO2 prepared by sol–gel process. *Thin Solid Films* **418,** 79–84 (2002).
72. Kontos, A. I. *et al.* Nanostructured TiO2 films for DSSCS prepared by combining doctor-blade and sol–gel techniques. *J. Mater. Process. Technol.* **196,** 243–248 (2008).
73. Yang, J., Peterlik, H., Lomoschitz, M. & Schubert, U. Preparation of mesoporous titania by surfactant-assisted sol–gel processing of acetaldoxime-modified titanium alkoxides. *J. Non. Cryst. Solids* **356,** 1217–1227 (2010).
74. Malengreaux, C. M. *et al.* Optimized deposition of TiO2 thin films produced by a non-aqueous sol–gel method and quantification of their photocatalytic activity. *Chem. Eng. J.* **195–196,** 347–358 (2012).
75. Saito, Y., Kambe, S., Kitamura, T., Wada, Y. & Yanagida, S. Morphology control of mesoporous TiO2 nanocrystalline films for performance of dye-sensitized solar cells. *Sol. Energy Mater. Sol. Cells* **83,** 1–13 (2004).
76. Yu, J., Zhao, X. & Zhao, Q. Effect of surface structure on photocatalytic activity of TiO2 thin films prepared by sol-gel method. *Thin Solid Films* **379,** 7–14 (2000).
77. Wang, C. & Ying, J. Y. Sol-Gel Synthesis and Hydrothermal Processing of Anatase and Rutile Titania Nanocrystals. *Chem. Mater.* 3113–3120 (1999).

78. Sommeling, P. M. *et al.* Influence of a TiCl4 post-treatment on nanocrystalline TiO2 films in dye-sensitized solar cells. *J. Phys. Chem. B* **110,** 19191–7 (2006).
79. Addamo, M. *et al.* Photocatalytic thin films of TiO2 formed by a sol–gel process using titanium tetraisopropoxide as the precursor. *Thin Solid Films* **516,** 3802–3807 (2008).
80. Garzella, C., Comini, E., Tempesti, E., Frigeri, C. & Sberveglieri, G. TiO2 thin films by a novel sol – gel processing for gas sensor applications. 189–196 (2000).
81. Nagpal, V. J., Davis, R. M. & Desu, S. B. Novel thin films of titanium dioxide particles synthesized by a sol-gel process. *J. Mater. Res.* **10,** 3068–3078 (2011).
82. Chen, Y. & Dionysiou, D. D. TiO 2 photocatalytic films on stainless steel : The role of Degussa P-25 in modified sol – gel methods. **62,** 255–264 (2006).
83. Uchida, H. *et al.* Highly-ordered mesoporous titania thin films prepared via surfactant assembly on conductive indium–tin-oxide/glass substrate and its optical properties. *Thin Solid Films* **518,** 3169–3176 (2010).
84. Gratzel, M. Sol-gel processed TiO2 films for photovoltaic applications. *J. SOL-GEL Sci. Technol.* **22,** 7–13 (2001).
85. Khan, M. A., Shaheer Akhtar, M. & Yang, O.-B. Synthesis, characterization and application of sol–gel derived mesoporous TiO2 nanoparticles for dye-sensitized solar cells. *Sol. Energy* **84,** 2195–2201 (2010).
86. Kim, D. J., Hahn, S. H., Oh, S. H. & Kim, E. J. Influence of calcination temperature on structural and optical properties of TiO2 thin films prepared by sol–gel dip coating. *Mater. Lett.* **57,** 355–360 (2002).
87. Yang, J. *et al.* Effect of particle size of starting material TiO2 on morphology and properties of layered titanates. *Mater. Lett.* **50,** 230–234 (2001).
88. Huber, B. *et al.* Nanocrystalline anatase TiO2 thin films: preparation and crystallite size-dependent properties. *Thin Solid Films* **472,** 114–124 (2005).
89. Mechiakh, R., Sedrine, N. Ben, Chtourou, R. & Bensaha, R. Correlation between microstructure and optical properties of nano-crystalline TiO2 thin films prepared by sol–gel dip coating. *Appl. Surf. Sci.* **257,** 670–676 (2010).
90. Dislich, H. New Routes to Multicomponent Oxide Glasses. *Angew. Chemie Int. Ed. English* **10,** 363–370 (1971).
91. Klein, L. C. *Sol-Gel Technology for Thin Films, Fibers, Preforms, Electronics and Speciality Shapes*. (Noyes Publications, 1988).

92. Pierre, A. . *Introduction to Sol-Gel Processing*. (Kluwer Academic Publishers, 1998).
93. Livage, J., Henry, M. & Sanchez, C. Sol-gel chemistry of transition metal oxides. *Prog. Solid State Chem.* **18,** 259–341 (1988).
94. Hench, L. L. & West, J. K. The sol-gel process. *Chem. Rev.* **90,** 33–72 (1990).
95. Brinker, C.J.; Scherrer, G. *Sol-Gel Science: The Physics and Chemistry of Sol-Gel Processing*. (Academic Press, 1990).
96. Hench, Larry L.;Orefice, R. Sol-Gel Technology. *Kirk-Othmer Encycl. Chem. Technol.* (2000). doi:10.1002/0471238961.19151208051403.a01
97. Chen, X. & Mao, S. S. Titanium dioxide nanomaterials: synthesis, properties, modifications, and applications. *Chem. Rev.* **107,** 2891–959 (2007).
98. Uhlmann, D.R.; Kreidl, N. J. . *Glass: Science and Technology Volume 2: Processing I*. (Academic Press Inc, 1984).
99. Aegerter, M. A. & Mennig, M. *Sol-Gel Technologies for Glass Producers and Users*. (Springer Science & Business Media, 2004).
100. Schubert, U. Chemical modification of titanium alkoxides for sol–gel processing. *J. Mater. Chem.* **15,** 3701 (2005).
101. Babonneau, F. *et al.* XANES and EXAFS study of titanium alkoxides. *Inorg. Chem.* **27,** 3166–3172 (1988).
102. Malengreaux, C. M. *et al.* Optimized deposition of TiO2 thin films produced by a non-aqueous sol–gel method and quantification of their photocatalytic activity. *Chem. Eng. J.* **195–196,** 347–358 (2012).
103. Pelentridou, K., Stathatos, E., Lianos, P. & Drakopoulos, V. A New Precursor for the Preparation of Nanocrystalline TiO2 Films and Their Photocatalytic Properties. *J. Nanosci. Nanotechnol.* **10,** 6093–6098 (2010).
104. Yu, H. K. *et al.* Surfactant-Assisted Synthesis of Uniform Titania Microspheres and Their Clusters. *Chem. Mater.* **20,** 2704–2710 (2008).
105. Schattka, J. H., Wong, E. H.-M., Antonietti, M. & Caruso, R. A. Sol-gel templating of membranes to form thick, porous titania, titania/zirconia and titania/silica films. *J. Mater. Chem.* **16,** 1414 (2006).
106. Stathatos, E., Lianos, P., Monte, F. Del & Levy, D. Formation of TiO 2 Nanoparticles in Reverse Micelles and Their Deposition as Thin Films on Glass Substrates. **7463,** 4295–4300 (1997).

107. Rosen, M. J. & Dahanayake, M. *Industrial Utilization of Surfactants: Principles and Practice*. (Amer Oil Chemists Society, 2000).
108. Wang, C.-T. & Yen, C.-F. Titania nanocomposite thin films with enhanced photovoltaic efficiency: Effects of Ti-alkoxide sol and compact layer. *Surf. Coatings Technol.* **206,** 2622–2627 (2012).
109. Li, X. S., Fryxell, G. E., Engelhard, M. H. & Wang, C. The synthesis of cadmium doped mesoporous TiO2. *Inorg. Chem. Commun.* **10,** 639–641 (2007).
110. Li, X. S., Fryxell, G. E., Wang, C. & Engelhard, M. H. The synthesis of Ag-doped mesoporous TiO2. *Microporous Mesoporous Mater.* **111,** 639–642 (2008).
111. Morozova, M. *et al.* Role of the template molecular structure on the photo-electrochemical functionality of the sol–gel titania thin films. *J. Sol-Gel Sci. Technol.* **52,** 398–407 (2009).
112. Hidalgo, D. *et al.* Thick mesoporous TiO2 films through a sol–gel method involving a non-ionic surfactant: Characterization and enhanced performance for water photo-electrolysis. *Int. J. Hydrogen Energy* **39,** 21512–21522 (2014).
113. Herregods, S. J. F. *et al.* Controlling pore size and uniformity of mesoporous titania by early stage low temperature stabilization. *J. Colloid Interface Sci.* **391,** 36–44 (2013).
114. Chen, L.-H. *et al.* Hydrothermal and surfactant treatment to enhance the photocatalytic activity of hierarchically meso–macroporous titanias. *Catal. Today* **212,** 89–97 (2013).
115. Grosso, D. *et al.* Highly Organized Mesoporous Titania Thin Films Showing Mono-Oriented 2D Hexagonal Channels. *Adv. Mater.* **13,** 1085–1090 (2001).
116. Solis, D. *et al.* Textural, structural and electrical properties of TiO2 nanoparticles using Brij 35 and P123 as surfactants. *Sci. Technol. Adv. Mater.* **9,** (2008).
117. Zhang, X., Zhou, G., Xu, J., Bai, G. & Wang, L. Synthesis and photocatalytic activity of co-doped mesoporous TiO2 on Brij98/CTAB composite surfactant template. *J. Solid State Chem.* **183,** 1394–1399 (2010).
118. Jones, A. C., Hitchman, M. L. & Krumdieck, S. P. Chemical Vapour Deposition: Precursors, Processes and Applications Edited by Anthony C. Jones and Michael L. Hitchman. (2009).
119. Pierson, H. O. *Handbook of Chemical Vapor Deposition (CVD) Principles, Technology, and Applications*. (Noyes Publications, 1999).
120. Choy, K. Chemical vapour deposition of coatings. *Prog. Mater. Sci.* **48,** 57–170

(2003).

121. Hou, X. & Choy, K.-L. Processing and Applications of Aerosol-Assisted Chemical Vapor Deposition. *Chem. Vap. Depos.* **12,** 583–596 (2006).
122. Marchand, P., Hassan, I. A., Parkin, I. P., Carmalt, C. J. & Marchand, P. Aerosol-assisted delivery of precursors for chemical vapour deposition: expanding the scope of CVD for materials fabrication. *Dalt. Trans.* **42,** 9406–9422 (2013).
123. Hou, X. & Choy, K.-L. Processing and Applications of Aerosol-Assisted Chemical Vapor Deposition. *Chem. Vap. Depos.* **12,** 583–596 (2006).
124. Hyett, G., Darr, J. A., Mills, A. & Parkin, I. P. An investigation into the optimum thickness of titanium dioxide thin films synthesized by using atmospheric pressure chemical vapour deposition for use in photocatalytic water oxidation. *Chemistry* **16,** 10546–52 (2010).
125. Dunnill, C. W. *et al.* White light induced photocatalytic activity of sulfur-doped TiO2 thin films and their potential for antibacterial application. *J. Mater. Chem.* **19,** 8747 (2009).
126. Evans, P., Pemble, M. E. & Sheel, D. W. Precursor-Directed Control of Crystalline Type in Atmospheric Pressure CVD Growth of TiO 2 on Stainless Steel. *Chem. Mater.* **18,** 5750–5755 (2006).
127. Binions, R., Piccirillo, C., Palgrave, R. G. & Parkin, I. P. Hybrid Aerosol Assisted and Atmospheric Pressure CVD of Gold-Doped Vanadium Dioxide. *Chem. Vap. Depos.* **14,** 33–39 (2008).
128. Warwick, M. E. A., Dunnill, C. W., Goodall, J., Darr, J. A. & Binions, R. Hybrid chemical vapour and nanoceramic aerosol assisted deposition for multifunctional nanocomposite thin films. *Thin Solid Films* **519,** 5942–5948 (2011).
129. Green, M. A. Third generation photovoltaics: Ultra-high conversion efficiency at low cost. *Prog. Photovoltaics Res. Appl.* **9,** 123–135 (2001).
130. Gonçalves, L. M., de Zea Bermudez, V., Ribeiro, H. A. & Mendes, A. M. Dye-sensitized solar cells: A safe bet for the future. *Energy Environ. Sci.* **1,** 655 (2008).
131. Grätzel, M. Dye-sensitized solar cells. *J. Photochem. Photobiol. C Photochem. Rev.* **4,** 145–153 (2003).
132. Ito, S. *et al.* High-Efficiency Organic-Dye- Sensitized Solar Cells Controlled by Nanocrystalline-TiO2 Electrode Thickness. *Adv. Mater.* **18,** 1202–1205 (2006).

133. Gratzel, M. Photoelectrochemical cells. *Nature* **414,** 338–344 (2001).
134. *Handbook of Photovoltaic Science and Engineering*. (John Wiley & Sons, Ltd, 2011). doi:10.1002/9780470974704
135. Tennakone, K. & Kumara, G. An efficient dye-sensitized photoelectrochemical solar cell made from oxides of tin and zinc. *Chem. …* 15–16 (1999).
136. Sayama, K., Sugihara, H. & Arakawa, H. Photoelectrochemical properties of a porous Nb2O5 electrode sensitized by a ruthenium dye. *Chem. Mater.* **100,** 3825–3832 (1998).
137. Hagfeldt, A., Boschloo, G., Sun, L., Kloo, L. & Pettersson, H. Dye-sensitized solar cells. *Chem. Rev.* **110,** 6595–663 (2010).
138. Otaka, H. *et al.* Multi-colored dye-sensitized solar cells. *J. Photochem. Photobiol. A Chem.* **164,** 67–73 (2004).
139. Grätzel, M. Solar energy conversion by dye-sensitized photovoltaic cells. *Inorg. Chem.* **44,** 6841–51 (2005).
140. Robertson, N. Optimizing dyes for dye-sensitized solar cells. *Angew. Chem. Int. Ed. Engl.* **45,** 2338–45 (2006).
141. K. Kalyanasundaram (Editor). *Dye-sensitized solar cells*. (EPFL Press, 2010).
142. Grätzel, M. & O'Regan, B. A low-cost, high-efficiency solar cell based on dye-sensitized colloidal TiO2 films. *Nature* **353,** 737–740 (1991).
143. Matsumura, M., Nomura, Y. & Tsubomura, H. Dye-sensitization on the Photocurrent at Zinc Oxide Electrode in Aqueous Electrolyte Solution. *Bull. Chem. Soc. Jpn.* **50,** 2533–2537 (1977).
144. Alonso V., N., Beley, M., Chartier, P. & Ern, V. Dye sensitization of ceramic semiconducting electrodes for photoelectrochemical conversion. *Rev. Phys. Appliquée* **16,** 5–10 (1981).
145. Nazeeruddin, M. K., Liska, P., Moser, J., Vlachopoulos, N. & Gratzel, M. Conversion of Light into Electricity with Trinuclear Ruthenium Complexes Adsorbed on Textured TiO2 Films. *Helv. Chim. Acta* **73,** 1788–1803 (1990).
146. Amadelli, R., Argazzi, R., Bignozzi, C. A. & Scandola, F. Design of antenna-sensitizer polynuclear complexes. Sensitization of titanium dioxide with [Ru(bpy)2(CN)2]2Ru(bpy(COO)2)22-. *J. Am. Chem. Soc.* **112,** 7099–7103 (1990).
147. Nazeeruddin, M. K. *et al.* Conversion of light to electricity by cis-X2bis(2,2'-

bipyridyl-4,4’-dicarboxylate)ruthenium(II) charge-transfer sensitizers (X = Cl-, Br-, I-, CN-, and SCN-) on nanocrystalline titanium dioxide electrodes. *J. Am. Chem. Soc.* **115,** 6382–6390 (1993).

148. Nazeeruddin, M. K. *et al.* Combined experimental and DFT-TDDFT computational study of photoelectrochemical cell ruthenium sensitizers. *J. Am. Chem. Soc.* **127,** 16835–47 (2005).
149. Reynal, A. & Palomares, E. Dye structure – charge transfer process relationship in efficient ruthenium-dye based dye sensitized solar cells. 805–812 (2010). doi:10.1039/b925488a
150. Kuang, D. *et al.* High-Efficiency and Stable Mesoscopic Dye-Sensitized Solar Cells Based on a High Molar Extinction Coefficient Ruthenium Sensitizer and Nonvolatile Electrolyte. *Adv. Mater.* **19,** 1133–1137 (2007).
151. Wang, M. *et al.* An organic redox electrolyte to rival triiodide/iodide in dye-sensitized solar cells. *Nat. Chem.* **2,** 385–9 (2010).
152. Nei de Freitas, J., Nogueira, A. F. & De Paoli, M.-A. New insights into dye-sensitized solar cells with polymer electrolytes. *J. Mater. Chem.* **19,** 5279 (2009).
153. Tian, H., Jiang, X. & Yu, Z. Efficient Organic-Dye-Sensitized Solar Cells Based on an Iodine-Free Electrolyte. *Angew. Chem. Int. Ed. Engl.* 7328–7331 (2010). doi:10.1002/anie.201003740
154. Ye, M. *et al.* Recent advances in dye-sensitized solar cells: from photoanodes, sensitizers and electrolytes to counter electrodes. *Mater. Today* **18,** 155–162 (2015).
155. Green, M. A., Emery, K., Hishikawa, Y., Warta, W. & Dunlop, E. D. Solar cell efficiency tables (Version 38). *Prog. Photovoltaics Res. Appl.* **19,** 565–572 (2011).
156. Yella, A. *et al.* Porphyrin-sensitized solar cells with cobalt (II/III)-based redox electrolyte exceed 12 percent efficiency. *Science* **334,** 629–34 (2011).
157. Hagfeldt, A., Boschloo, G., Sun, L., Kloo, L. & Pettersson, H. Dye-Sensitized Solar Cells. *Chem. Rev.* **110,** 6595–6663 (2010).
158. Upadhyaya, H. M., Senthilarasu, S., Hsu, M.-H. & Kumar, D. K. Recent progress and the status of dye-sensitised solar cell (DSSC) technology with state-of-the-art conversion efficiencies. *Sol. Energy Mater. Sol. Cells* **119,** 291–295 (2013).
159. Campbell, W. M., Burrell, A. K., Officer, D. L. & Jolley, K. W. Porphyrins as light harvesters in the dye-sensitised TiO2 solar cell. *Coord. Chem. Rev.* **248,** 1363–1379

(2004).

160. Narayan, M. R. Review: Dye sensitized solar cells based on natural photosensitizers. *Renew. Sustain. Energy Rev.* **16,** 208–215 (2011).

161. Ileperuma, O. A. Gel polymer electrolytes for dye sensitised solar cells: a review. *Mater. Technol. Adv. Perform. Mater.* **28,** 65–70 (2013).

162. Parisi, M. L., Maranghi, S. & Basosi, R. The evolution of the dye sensitized solar cells from Grätzel prototype to up-scaled solar applications: A life cycle assessment approach. *Renew. Sustain. Energy Rev.* **39,** 124–138 (2014).

163. Nazeeruddin, M. K. *et al.* Conversion of light to electricity by cis-X2bis(2,2'-bipyridyl-4,4'-dicarboxylate)ruthenium(II) charge-transfer sensitizers (X = Cl-, Br-, I-, CN-, and SCN-) on nanocrystalline titanium dioxide electrodes. *J. Am. Chem. Soc.* **115,** 6382–6390 (1993).

164. Islam, A. *et al.* Sensitization of nanocrystalline TiO2 film by ruthenium(II) diimine dithiolate complexes. *J. Photochem. Photobiol. A Chem.* **145,** 135–141 (2001).

165. Nazeeruddin, M. K., Péchy, P. & Grätzel, M. Efficient panchromatic sensitization of nanocrystalline TiO2 films by a black dye based on a trithiocyanato–ruthenium complex. *Chem. Commun.* 1705–1706 (1997). doi:10.1039/a703277c

166. Grätzel, M. Dye-sensitized solar cells. *J. Photochem. Photobiol. C Photochem. Rev.* **4,** 145–153 (2003).

167. Kuciauskas, D., Freund, M. S., Gray, H. B., Winkler, J. R. & Lewis, N. S. Electron Transfer Dynamics in Nanocrystalline Titanium Dioxide Solar Cells Sensitized with Ruthenium or Osmium Polypyridyl Complexes. *J. Phys. Chem. B* **105,** 392–403 (2001).

168. Argazzi, R., Larramona, G., Contado, C. & Bignozzi, C. A. Preparation and photoelectrochemical characterization of a red sensitive osmium complex containing 4,4′,4″-tricarboxy-2,2′:6′,2″-terpyridine and cyanide ligands. *J. Photochem. Photobiol. A Chem.* **164,** 15–21 (2004).

169. Islam, A. *et al.* Dye Sensitization of Nanocrystalline Titanium Dioxide with Square Planar Platinum(II) Diimine Dithiolate Complexes. *Inorg. Chem.* **40,** 5371–5380 (2001).

170. Geary, E. A. M. *et al.* Synthesis, structure, and properties of [Pt(II)(diimine)(dithiolate)] dyes with 3,3'-, 4,4'-, and 5,5'-disubstituted bipyridyl:

applications in dye-sensitized solar cells. *Inorg. Chem.* **44,** 242–50 (2005).

171. Hasselmann, GM, Meyer & GJ. Sensitization of nanocrystalline TiO2 by Re(I) polypyridyl compounds. **212,** 39–44 (1999).
172. Alonso-Vante, N., Nierengarten, J.-F. & Sauvage, J.-P. Spectral sensitization of large-band-gap semiconductors (thin films and ceramics) by a carboxylated bis(1,10-phenanthroline)copper(I) complex. *J. Chem. Soc. Dalt. Trans.* 1649 (1994). doi:10.1039/dt9940001649
173. Jayaweera, P. M., Palayangoda, S. S. & Tennakone, K. Nanoporous TiO2 solar cells sensitized with iron(II) complexes of bromopyrogallol red ligand. *J. Photochem. Photobiol. A Chem.* **140,** 173–177 (2001).
174. Mann, J. R., Gannon, M. K., Fitzgibbons, T. C., Detty, M. R. & Watson, D. F. Optimizing the Photocurrent Efficiency of Dye-Sensitized Solar Cells through the Controlled Aggregation of Chalcogenoxanthylium Dyes on Nanocrystalline Titania Films. *J. Phys. Chem. C* **112,** 13057–13061 (2008).
175. Kalyanasundaram, K. Applications of functionalized transition metal complexes in photonic and optoelectronic devices. *Coord. Chem. Rev.* **177,** 347–414 (1998).
176. Wang, Q. *et al.* Efficient light harvesting by using green Zn-porphyrin-sensitized nanocrystalline TiO2 films. *J. Phys. Chem. B* **109,** 15397–409 (2005).
177. Ragoussi, M.-E., Ince, M. & Torres, T. Recent Advances in Phthalocyanine-Based Sensitizers for Dye-Sensitized Solar Cells. *European J. Org. Chem.* **2013,** 6475–6489 (2013).
178. Velusamy, M., Justin Thomas, K. R., Lin, J. T., Hsu, Y.-C. & Ho, K.-C. Organic dyes incorporating low-band-gap chromophores for dye-sensitized solar cells. *Org. Lett.* **7,** 1899–902 (2005).
179. Cao, Y. *et al.* Dye-Sensitized Solar Cells with Solvent-Free Ionic Liquid Electrolytes. *J. Phys. Chem. C* **112,** 13775–13781 (2008).
180. Nakade, S., Kanzaki, T., Kambe, S., Wada, Y. & Yanagida, S. Investigation of cation-induced degradation of dye-sensitized solar cells for a new strategy to long-term stability. *Langmuir* **21,** 11414–7 (2005).
181. Tributsch, H. Dye sensitization solar cells: a critical assessment of the learning curve. *Coord. Chem. Rev.* **248,** 1511–1530 (2004).
182. Nei de Freitas, J., Nogueira, A. F. & De Paoli, M.-A. New insights into dye-sensitized

solar cells with polymer electrolytes. *J. Mater. Chem.* **19,** 5279 (2009).

183. Tennakone, K., Perera, V. P. S., Kottegoda, I. R. M. & Kumara, G. R. R. A. Dye-sensitized solid state photovoltaic cell based on composite zinc oxide/tin (IV) oxide films. *J. Phys. D. Appl. Phys.* **32,** 374–379 (1999).
184. Bella, F. & Bongiovanni, R. Photoinduced polymerization: An innovative, powerful and environmentally friendly technique for the preparation of polymer electrolytes for dye-sensitized solar cells. *J. Photochem. Photobiol. C Photochem. Rev.* **16,** 1–21 (2013).
185. Cai, N., Moon, S.-J. & Cevey-Ha, L. An Organic D-pi-A Dye for Record Efficiency Solid-State Sensitized Heterojunction Solar Cells. **11,** 1452–1456 (2011).
186. Liu, X., Zhang, W. & Uchida, S. An Efficient Organic-Dye-Sensitized Solar Cell with in situ Polymerized Poly(3,4-ethylenedioxythiophene) as a Hole-Transporting Material. **22,** (2010).
187. Hardin, B. E., Snaith, H. J. & McGehee, M. D. The renaissance of dye-sensitized solar cells. **6,** 162–169 (2012).
188. Hamann, T. W., Jensen, R. a., Martinson, A. B. F., Van Ryswyk, H. & Hupp, J. T. Advancing beyond current generation dye-sensitized solar cells. *Energy Environ. Sci.* **1,** 66 (2008).
189. Jose, R., Thavasi, V. & Ramakrishna, S. Metal Oxides for Dye-Sensitized Solar Cells. *J. Am. Ceram. Soc.* **92,** 289–301 (2009).
190. Zhang, Q., Dandeneau, C. S., Zhou, X. & Cao, G. ZnO Nanostructures for Dye-Sensitized Solar Cells. *Adv. Mater.* **21,** 4087–4108 (2009).
191. Park, N.-G., van de Lagemaat, J. & Frank, A. J. Comparison of Dye-Sensitized Rutile- and Anatase-Based TiO 2 Solar Cells. *J. Phys. Chem. B* **104,** 8989–8994 (2000).
192. Kopidakis, N., Benkstein, K. D., Lagemaat, J. Van De & Frank, A. J. Transport-Limited Recombination of Photocarriers in Dye-Sensitized Nanocrystalline TiO 2 Solar Cells. 11307–11315 (2003).
193. Miyazaki, T., Akisawa, A. & Kashiwagi, T. Energy savings of office buildings by the use of semi-transparent solar cells for windows. *Renew. Energy* **30,** 281–304 (2005).
194. Poirazis, H., Blomsterberg, Å. & Wall, M. Energy simulations for glazed office buildings in Sweden. *Energy Build.* **40,** 1161–1170 (2008).
195. Li, D. H. W., Lam, T. N. T. & Cheung, K. L. Energy and cost studies of semi-

transparent photovoltaic skylight. *Energy Convers. Manag.* **50,** 1981–1990 (2009).

196. Hinsch, A. *et al.* Dye solar modules for facade applications: Recent results from project ColorSol. *Sol. Energy Mater. Sol. Cells* **93,** 820–824 (2009).
197. Vicki Caligur. Detergent Properties and Applications. *BioFiles, 3.3, 14* (2008).
198. Schneider, C. A., Rasband, W. S. & Eliceiri, K. W. NIH Image to ImageJ: 25 years of image analysis. *Nat. Methods* **9,** 671–675 (2012).
199. Tauc, J. Optical properties and electronic structure of amorphous Ge and Si. *Mater. Res. Bull.* **3,** 37–46 (1968).
200. Evans, P., Mantke, S., Mills, A., Robinson, A. & Sheel, D. W. A comparative study of three techniques for determining photocatalytic activity. *J. Photochem. Photobiol. A Chem.* **188,** 387–391 (2007).
201. Kafizas, A., Mills, A. & Parkin, I. P. A comprehensive aerosol spray method for the rapid photocatalytic grid area analysis of semiconductor photocatalyst thin films. *Anal. Chim. Acta* **663,** 69–76 (2010).
202. Ponja, S. *et al.* Aerosol assisted chemical vapour deposition of hydrophobic TiO2–SnO2 composite film with novel microstructure and enhanced photocatalytic activity. *J. Mater. Chem. A* **1,** 6271 (2013).
203. Stathatos, E., Lianos, P. & Tsakiroglou, C. Highly efficient nanocrystalline titania films made from organic/inorganic nanocomposite gels. *Microporous Mesoporous Mater.* **75,** 255–260 (2004).
204. Schwenzer, B. *et al.* Tuning the Optical Properties of Mesoporous TiO 2 Films by Nanoscale Engineering. *Langmuir* **28,** 10072–10081 (2012).
205. Möckel, H., Giersig, M. & Willig, F. Formation of uniform size anatase nanocrystals from bis(ammonium lactato)titanium dihydroxide by thermohydrolysis. *J. Mater. Chem.* **9,** 3051–3056 (1999).
206. Kessler, V. G. Aqueous route to TiO2-based nanomaterials using pH-neutral carboxylate precursors. *J. Sol-Gel Sci. Technol.* **68,** 464–470 (2013).
207. Pelentridou, K., Stathatos, E., Lianos, P. & Drakopoulos, V. A New Precursor for the Preparation of Nanocrystalline TiO2 Films and Their Photocatalytic Properties. *J. Nanosci. Nanotechnol.* **10,** 6093–6098 (2010).
208. Kafizas, A., Kellici, S., Darr, J. A. & Parkin, I. P. Titanium dioxide and composite metal/metal oxide titania thin films on glass: A comparative study of photocatalytic

activity. *J. Photochem. Photobiol. A Chem.* **204,** 183–190 (2009).

209. Schuler, T., Krajewski, T., Grobelsek, I. & Aegerter, M. A. A Microstructural Zone Model for the Morphology of Sol-Gel Coatings. *J. Sol-Gel Sci. Technol.* **31,** 235–239 (2004).
210. Wang, C., Meinhardt, J. & Löbmann, P. Growth mechanism of Nb-doped TiO2 sol–gel multilayer films characterized by SEM and focus/defocus TEM. *J. Sol-Gel Sci. Technol.* **53,** 148–153 (2009).
211. Page, K. *et al.* Titania and silver?titania composite films on glass?potent antimicrobial coatings. *J. Mater. Chem.* **17,** 95 (2007).
212. Sönmezoğlu, S., Çankaya, G. & Serin, N. Phase transformation of nanostructured titanium dioxide thin films grown by sol–gel method. *Appl. Phys. A* **107,** 233–241 (2012).
213. Kluson, P. *et al.* Ultrathin functional films of titanium(IV) oxide. *Chem. Pap.* **66,** 446–460 (2012).
214. Chigane, M. & Shinagawa, T. Titanium dioxide thin films prepared by electrolysis from aqueous solution of titanium–lactic acid complex for dye-sensitized solar cells. *Thin Solid Films* **520,** 3510–3514 (2012).
215. Groenke, N. *et al.* Structural characterization, solution stability, and potential health and environmental effects of the Nano-TiO2 bioencapsulation matrix and the model product of its biodegradation TiBALDH. *RSC Adv.* **2,** 4228 (2012).
216. Kinsinger, N. M., Wong, A., Li, D., Villalobos, F. & Kisailus, D. Nucleation and Crystal Growth of Nanocrystalline Anatase and Rutile Phase TiO 2 from a Water-Soluble Precursor. *Cryst. Growth Des.* **10,** 5254–5261 (2010).
217. Tan, Z. *et al.* Particle size for photocatalytic activity of anatase TiO2 nanosheets with highly exposed {001} facets. *RSC Adv.* **3,** 19268 (2013).
218. Bhachu, D. S., Sathasivam, S., Carmalt, C. J. & Parkin, I. P. PbO-modified TiO2 thin films: a route to visible light photocatalysts. *Langmuir* **30,** 624–30 (2014).
219. Alotaibi, A. M., Sathasivam, S. & Parkin, I. P. Aerosol assisted chemical vapour deposition of a ZrO_2 –TiO_2 composite thin film with enhanced photocatalytic activity. *RSC Adv.* **5,** 67944–67950 (2015).
220. Palgrave, R. G. & Parkin, I. P. Aerosol assisted chemical vapor deposition using nanoparticle precursors: a route to nanocomposite thin films. *J. Am. Chem. Soc.* **128,**

1587–97 (2006).

221. Kaye, K., Turner, D., McKenna, D., Cackett, A. & Hyett, G. The Use of Additives to Control the Morphology of Thin Films Synthesized Using Aerosol Assisted Chemical Vapour Deposition. *Phys. Procedia* **46,** 21–26 (2013).
222. Penfold, J., Staples, E., Tucker, I. & Cummins, P. The Structure of Nonionic Micelles in Less Polar Solvents. *J. Colloid Interface Sci.* **185,** 424–431 (1997).
223. in *IUPAC Compendium of Chemical Terminology* (IUPAC). doi:10.1351/goldbook.C01395
224. *Phase Behaviour of Surface-Active Solutes*. *Particle Science, Drug Development Services* (2012).
225. Sheet, S. D. SIGMA-ALDRICH. 1–7 (2013).
226. Avantil Lipids Data sheet. *Avantil Lipids* (2016).
227. Kim, C. & Hsieh, Y.-L. Wetting and absorbency of nonionic surfactant solutions on cotton fabrics. *Colloids Surfaces A Physicochem. Eng. Asp.* **187–188,** 385–397 (2001).
228. Kumar, G. P. & Rajeshwarrao, P. Nonionic surfactant vesicular systems for effective drug delivery—an overview. *Acta Pharm. Sin. B* **1,** 208–219 (2011).
229. Lee, D.-H., Kim, E.-S. & Chang, H.-W. Effect of Tween surfactant components for remediation of toluene-contaminated groundwater. *Geosci. J.* **9,** 261–267 (2005).
230. Israelachvili, J. *Intermolecular and Surface Forces*. (Academic Press, 1985).
231. Griffin, W. C. Classification of Surface-Active Agents by 'HLB'. *J. Soc. Cosmet. Chem.* **1,** 311–26 (1949).
232. Yuan, Y. & T. Randall, L. in *Surface Science Techniques* 3–34 (2013).
233. Diebold, U. The surface science of titanium dioxide. *Surf. Sci. Rep.* **48,** 53–229 (2003).
234. Lyandres, O., Finkelstein-Shapiro, D., Chakthranont, P., Graham, M. & Gray, K. A. Preferred Orientation in Sputtered TiO_2 Thin Films and Its Effect on the Photo-Oxidation of Acetaldehyde. *Chem. Mater.* **24,** 3355–3362 (2012).
235. Ali, A., Yassitepe, E., Ruzybayev, I., Ismat Shah, S. & Bhatti, A. S. Improvement of (004) texturing by slow growth of Nd doped TiO2 films. *J. Appl. Phys.* **112,** 113505 (2012).
236. Selloni, A. Crystal growth: Anatase shows its reactive side. *Nat. Mater.* **7,** 613–615 (2008).
237. Amano, F. *et al.* Photocatalytic activity of octahedral single-crystalline mesoparticles

of anatase titanium(iv) oxide. *Chem. Commun.* **105,** 2311 (2009).

238. Li, W. *et al.* Enhanced Photocatalytic Activity in Anatase/TiO $_2$ (B) Core−Shell Nanofiber. *J. Phys. Chem. C* **112,** 20539–20545 (2008).
239. Huang, P. J., Chang, H., Yeh, C. T. & Tsai, C. W. Phase transformation of TiO2 monitored by Thermo-Raman spectroscopy with TGA/DTA. *Thermochim. Acta* **297,** 85–92 (1997).
240. Tu, R. & Goto, T. High Temperature Stability of Anatase Films Prepared by MOCVD. *Mater. Trans.* **49,** 2040–2046 (2008).
241. Romero, L. & Binions, R. Effect of AC electric fields on the aerosol assisted chemical vapour deposition growth of titanium dioxide thin films. *Surf. Coatings Technol.* **230,** 196–201 (2013).
242. Harris, D. *Solvent Polarity Index*. *Quantitative Chemical Analysis* (2015).
243. Israelachvili, J. N., Mitchell, D. J. & Ninham, B. W. Theory of self-assembly of hydrocarbon amphiphiles into micelles and bilayers. *J. Chem. Soc. Faraday Trans. 2* **72,** 1525 (1976).
244. Saeli, M., Binions, R., Piccirillo, C. & Parkin, I. P. Templated growth of smart coatings: Hybrid chemical vapour deposition of vanadyl acetylacetonate with tetraoctyl ammonium bromide. *Appl. Surf. Sci.* **255,** 7291–7295 (2009).
245. Warwick, M. E. A., Dunnill, C. W., Goodall, J., Darr, J. A. & Binions, R. Hybrid chemical vapour and nanoceramic aerosol assisted deposition for multifunctional nanocomposite thin films. *Thin Solid Films* **519,** 5942–5948 (2011).
246. Binions, B. R., Piccirillo, C., Palgrave, R. G. & Parkin, I. P. Hybrid Aerosol Assisted and Atmospheric Pressure CVD of Gold-Doped Vanadium Dioxide **. 33–39 (2008). doi:10.1002/cvde.200706641
247. Snyder, L. R., Kirkland, J. J. & Glajch, J. L. in *Practical HPLC Method Development* 721–728 (John Wiley & Sons, Inc., 2012). doi:10.1002/9781118592014.app2
248. Lim, S. P., Huang, N. M., Lim, H. N. & Mazhar, M. Aerosol assisted chemical vapour deposited (AACVD) of TiO2 thin film as compact layer for dye-sensitised solar cell. *Ceram. Int.* **40,** 8045–8052 (2014).
249. Xie, K., Guo, M., Liu, X. & Huang, H. Enhanced efficiencies in thin and semi-transparent dye-sensitized solar cells under low photon flux conditions using TiO2 nanotube photonic crystal. *J. Power Sources* **293,** 170–177 (2015).

250. Vesce, L. & Riccitelli, R. Processing and characterization of a TiO_2 paste based on small particle size powders for dye-sensitized solar cell semi-transparent photo-electrodes. *Prog. Photovoltaics Res. Appl.* **20,** 960–966 (2012).
251. Guo, M. *et al.* Design and coupling of multifunctional TiO2 nanotube photonic crystal to nanocrystalline titania layer as semi-transparent photoanode for dye-sensitized solar cell. *Energy Environ. Sci.* **5,** 9881 (2012).
252. Henrik LINDSTRÖM, G. F. A transparent dye-sensitized solar cell and a method for manufacturing the solar cell. (2015).
253. Glass 2 Energy. GLASS 2 ENERGY LTD. (2016). at <http://www.g2e.ch/references/bipv>
254. Bouvard, O., Vanzo, S. & Schüler, A. Experimental Determination of Optical and Thermal Properties of Semi-transparent Photovoltaic Modules Based on Dye-sensitized Solar Cells. *Energy Procedia* **78,** 453–458 (2015).
255. Yoon, S. *et al.* Application of transparent dye-sensitized solar cells to building integrated photovoltaic systems. *Build. Environ.* **46,** 1899–1904 (2011).
256. Seok, J. Y. *et al.* A Review of Three-Dimensional Resistive Switching Cross-Bar Array Memories from the Integration and Materials Property Points of View. *Adv. Funct. Mater.* **24,** 5316–5339 (2014).
257. Iefanova, A. *et al.* Transparent platinum counter electrode for efficient semi-transparent dye-sensitized solar cells. *Thin Solid Films* **562,** 578–584 (2014).
258. Solaronix. Solaronix- Platisol T/SP Application Notes. (2016). at <http://shop.solaronix.com/platisol-t-sp.html>
259. Nazeeruddin, M. K., Humphry-Baker, R., Liska, P. & Grätzel, M. Investigation of Sensitizer Adsorption and the Influence of Protons on Current and Voltage of a Dye-Sensitized Nanocrystalline TiO 2 Solar Cell. *J. Phys. Chem. B* **107,** 8981–8987 (2003).
260. Kim, B. *et al.* Rapid Dye Adsorption via Surface Modification of TiO_2 Photoanodes for Dye-Sensitized Solar Cells. *ACS Appl. Mater. Interfaces* **5,** 5201–5207 (2013).
261. Chang, W.-C., Lee, C.-H., Yu, W.-C. & Lin, C.-M. Optimization of dye adsorption time and film thickness for efficient ZnO dye-sensitized solar cells with high at-rest stability. *Nanoscale Res. Lett.* **7,** 688 (2012).
262. Solaronix- Meltonix 1170-25. at <http://shop.solaronix.com/sealing-materials.html>
263. Cells, P., Hagfeldt, A., Cappel, U. B., Boschloo, G. & Sun, L. *Dye-Sensitized and*

Organic Solar Cells.

264. Kao, M. C., Chen, H. Z., Young, S. L., Kung, C. Y. & Lin, C. C. The effects of the thickness of TiO2 films on the performance of dye-sensitized solar cells. *Thin Solid Films* **517,** 5096–5099 (2009).
265. Mathew, S. *et al.* Dye-sensitized solar cells with 13% efficiency achieved through the molecular engineering of porphyrin sensitizers. *Nat. Chem.* **6,** 242–247 (2014).
266. Kay, A. & Graetzel, M. Artificial photosynthesis. 1. Photosensitization of titania solar cells with chlorophyll derivatives and related natural porphyrins. *J. Phys. Chem.* **97,** 6272–6277 (1993).
267. Gokilamani, N., Muthukumarasamy, N., Thambidurai, M., Ranjitha, A. & Velauthapillai, D. Utilization of natural anthocyanin pigments as photosensitizers for dye-sensitized solar cells. *J. Sol-Gel Sci. Technol.* **66,** 212–219 (2013).
268. Hao, W., Hsun, Y., Gaik, L. & Hsiung, M. Commercial and natural dyes as photosensitizers for a water-based dye-sensitized solar cell loaded with gold nanoparticles. **195,** 307–313 (2008).
269. Zhou, H., Wu, L., Gao, Y. & Ma, T. Dye-sensitized solar cells using 20 natural dyes as sensitizers. *J. Photochem. Photobiol. A Chem.* **219,** 188–194 (2011).
270. Calogero, G. & Marco, G. Di. Red Sicilian orange and purple eggplant fruits as natural sensitizers for dye-sensitized solar cells. *Sol. Energy Mater. Sol. Cells* **92,** 1341–1346 (2008).
271. Calogero, G. *et al.* Anthocyanins and betalains as light-harvesting pigments for dye-sensitized solar cells. *Sol. Energy* **86,** 1563–1575 (2012).
272. Wongcharee, K., Meeyoo, V. & Chavadej, S. Dye-sensitized solar cell using natural dyes extracted from rosella and blue pea flowers. **91,** 566–571 (2007).
273. Hao, S., Wu, J., Huang, Y. & Lin, J. Natural dyes as photosensitizers for dye-sensitized solar cell. **80,** 209–214 (2006).
274. Lachman, J. *et al.* Cultivar differences of total anthocyanins and anthocyanidins in red and purple-fleshed potatoes and their relation to antioxidant activity. *Food Chem.* **114,** 836–843 (2009).
275. Liu, X., Mu, T., Sun, H., Zhang, M. & Chen, J. Optimisation of aqueous two-phase extraction of anthocyanins from purple sweet potatoes by response surface methodology. *Food Chem.* **141,** 3034–3041 (2013).

276. de Aguiar Cipriano, P., Ekici, L., Barnes, R. C., Gomes, C. & Talcott, S. T. Pre-heating and polyphenol oxidase inhibition impact on extraction of purple sweet potato anthocyanins. *Food Chem.* **180,** 227–234 (2015).
277. Mane, S., Bremner, D. H., Tziboula-Clarke, A. & Lemos, M. A. Effect of ultrasound on the extraction of total anthocyanins from Purple Majesty potato. *Ultrason. Sonochem.* **27,** 509–514 (2015).
278. Lachman, J. *et al.* Cultivar differences of total anthocyanins and anthocyanidins in red and purple-fleshed potatoes and their relation to antioxidant activity. *Food Chem.* **114,** 836–843 (2009).
279. Kawano, R. *et al.* High performance dye-sensitized solar cells using ionic liquids as their electrolytes. *J. Photochem. Photobiol. A Chem.* **164,** 87–92 (2004).
280. Wang, P., Zakeeruddin, S. M., Moser, J.-E. & Grätzel, M. A New Ionic Liquid Electrolyte Enhances the Conversion Efficiency of Dye-Sensitized Solar Cells. *J. Phys. Chem. B* **107,** 13280–13285 (2003).
281. Mosconi, E. *et al.* Cobalt Electrolyte/Dye Interactions in Dye-Sensitized Solar Cells: A Combined Computational and Experimental Study. *J. Am. Chem. Soc.* **134,** 19438–19453 (2012).
282. Hamann, T. W. *et al.* The end of iodide? Cobalt complex redox shuttles in DSSCs. *Dalt. Trans.* **41,** 3111 (2012).

Appendix A.

A1. Selection of representative Tauc Plots (used to determine band gap of TiO_2 thin films)

- Sol-gel prepared samples (TTIP or TiBALD precursor with and without surfactant addition).

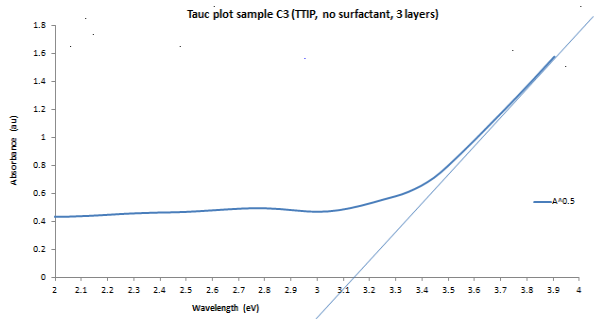

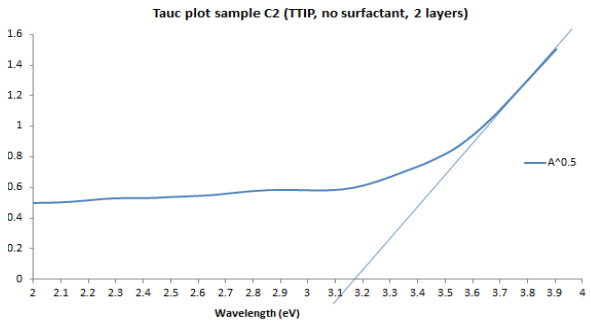

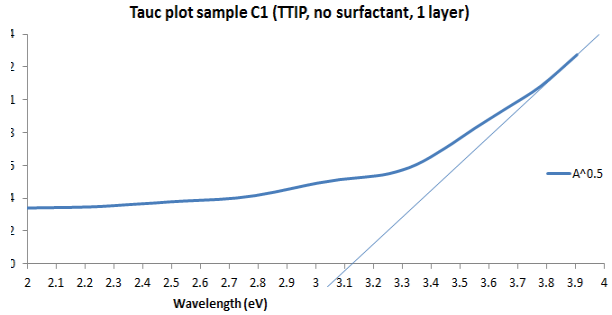

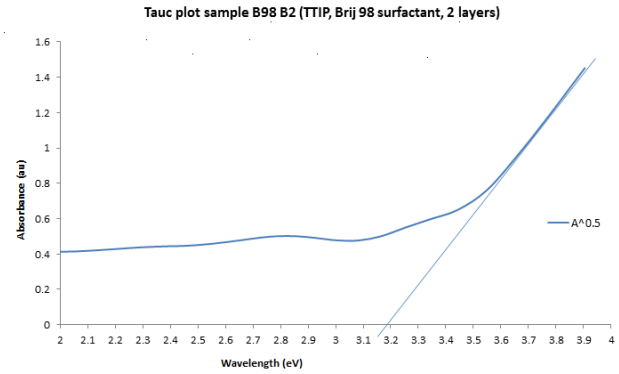

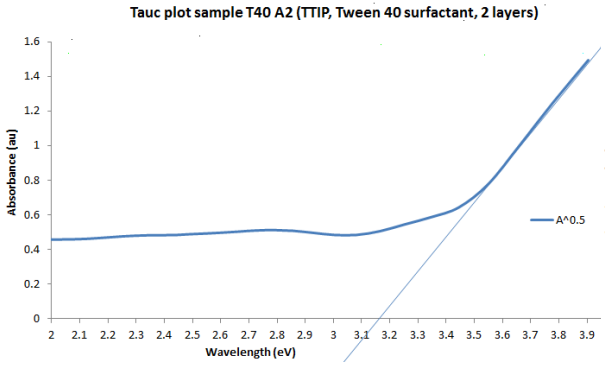

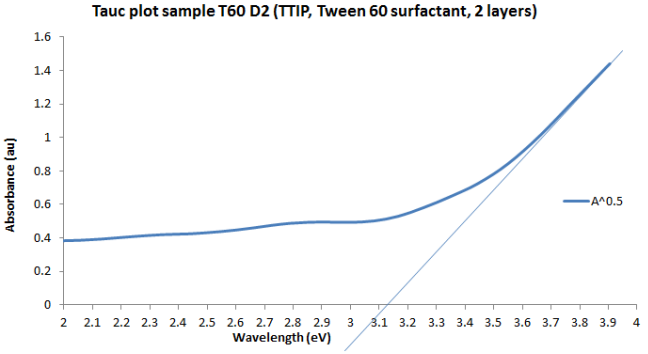

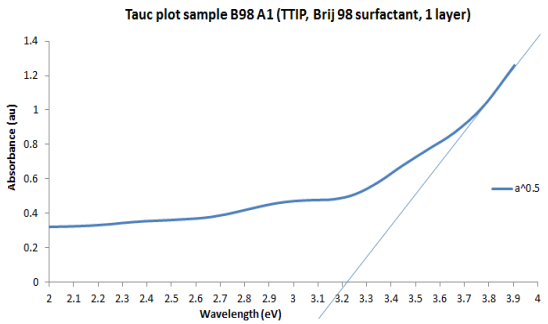
Tauc plot sample B98 A1 (TTIP, Brij 98 surfactant, 1 layer)
Absorbance (au)
Wavelength (eV)
a^0.5

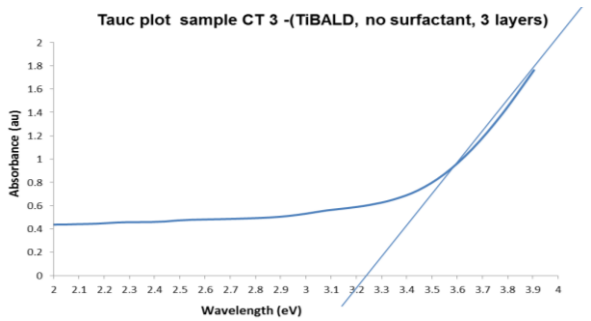
Tauc plot sample CT 3 -(TiBALD, no surfactant, 3 layers)
Absorbance (au)
Wavelength (eV)

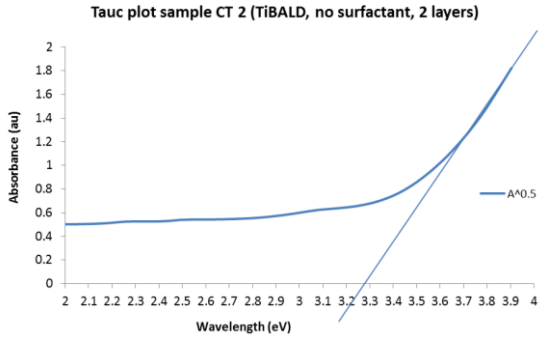
Tauc plot sample CT 2 (TiBALD, no surfactant, 2 layers)
Absorbance (au)
Wavelength (eV)
A^0.5

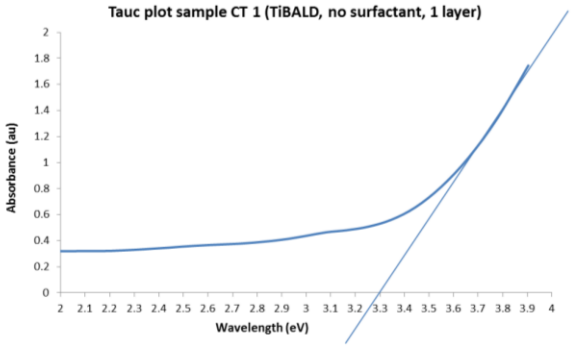
Tauc plot sample CT 1 (TiBALD, no surfactant, 1 layer)
Absorbance (au)
Wavelength (eV)

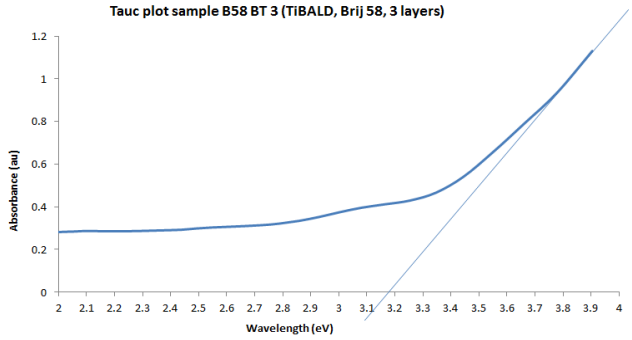
Tauc plot sample B58 BT 3 (TiBALD, Brij 58, 3 layers)
Absorbance (au)
Wavelength (eV)

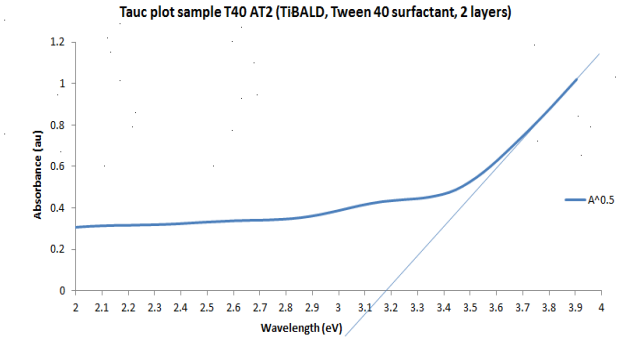
Tauc plot sample T40 AT2 (TiBALD, Tween 40 surfactant, 2 layers)
Absorbance (au)
Wavelength (eV)
A^0.5

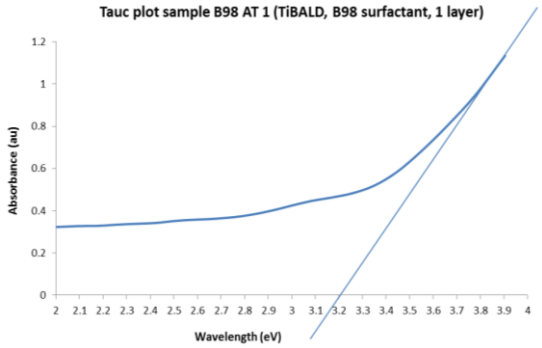
Tauc plot sample B98 AT 1 (TiBALD, B98 surfactant, 1 layer)
Absorbance (au)
Wavelength (eV)

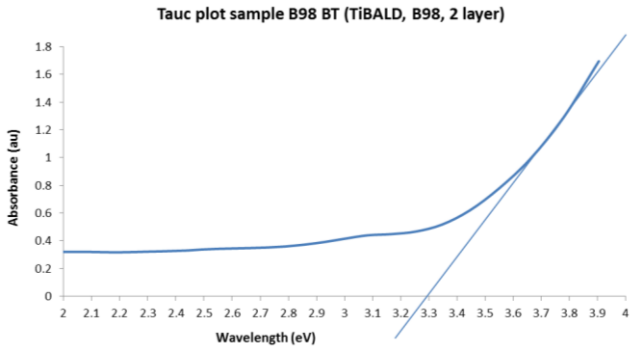
Tauc plot sample B98 BT (TiBALD, B98, 2 layer)
Absorbance (au)
Wavelength (eV)

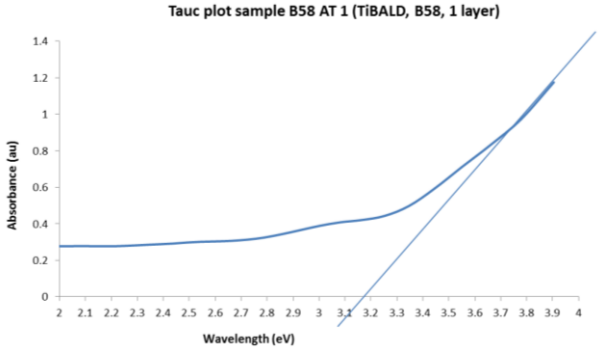
Tauc plot sample B58 AT 1 (TiBALD, B58, 1 layer)
Absorbance (au)
Wavelength (eV)

- AACVD prepared samples: with toluene and DCM solvent and Hybrid samples.

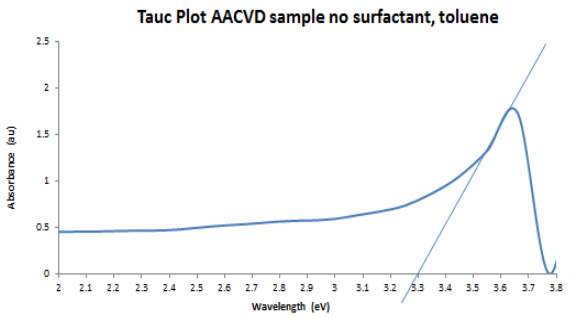

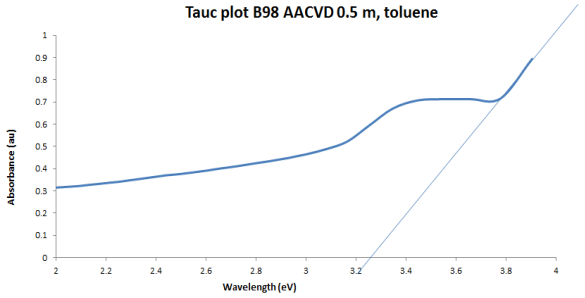

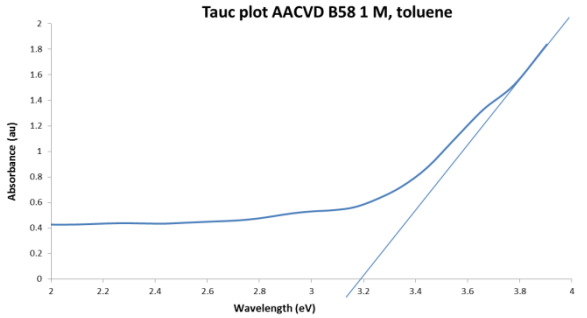

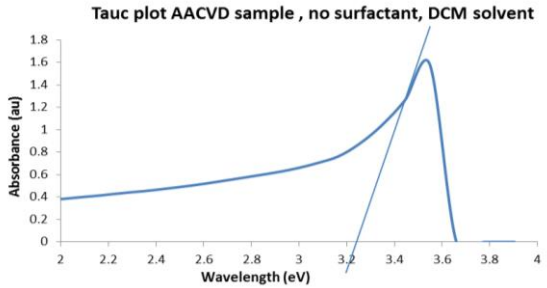

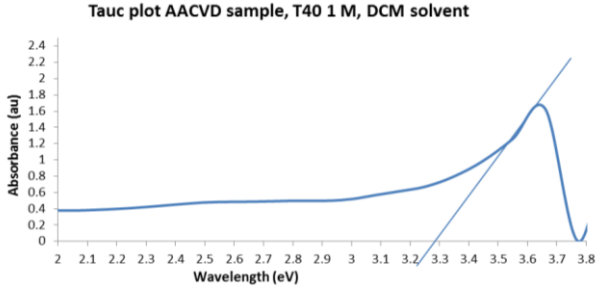

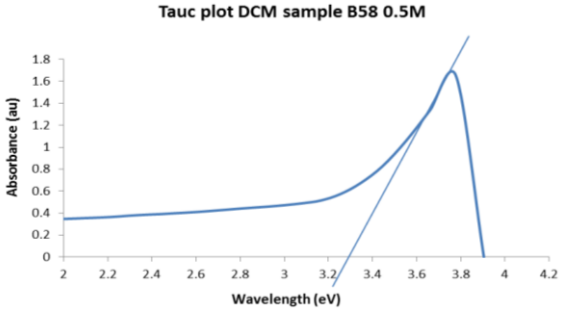

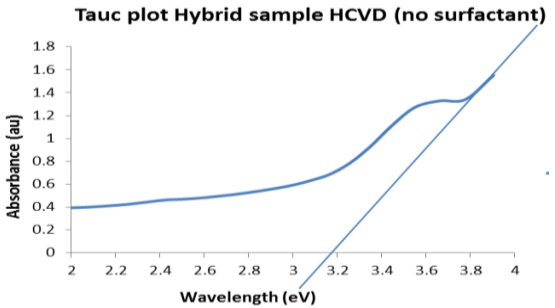

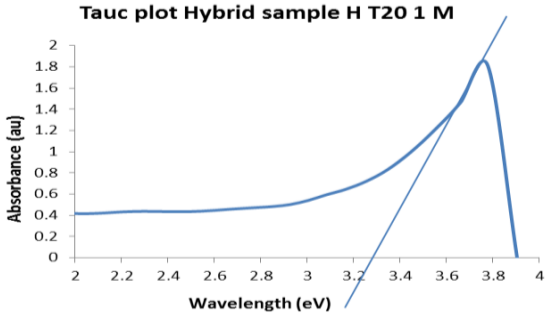

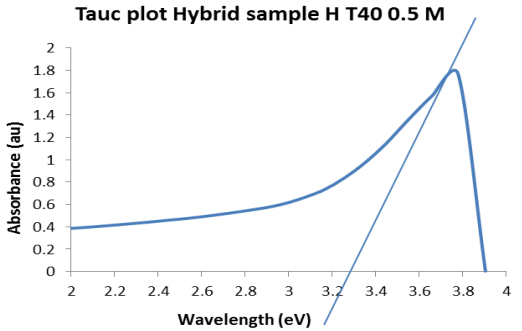

A2. Example photographs of wetting behaviour of TiO_2thin films

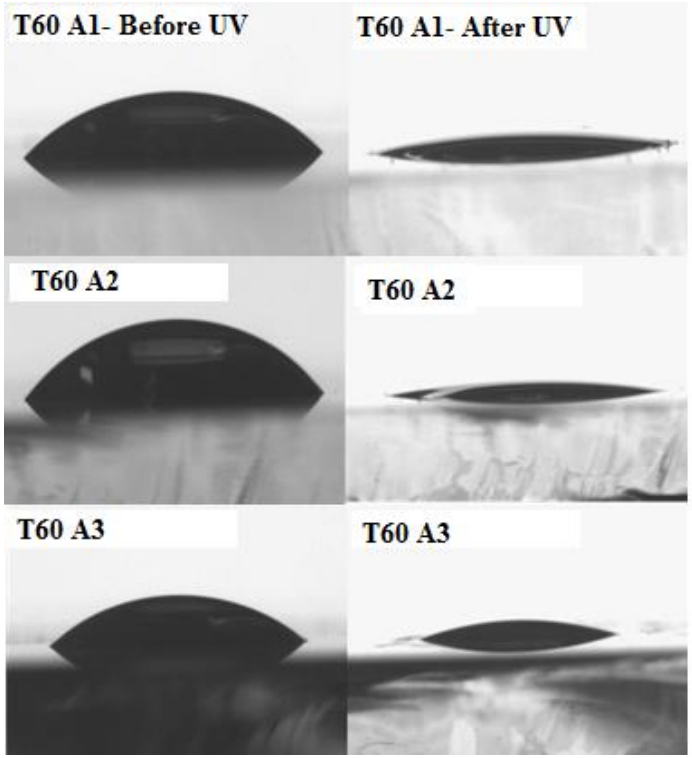

Figure A2. Typical photographic example of wetting behaviour of TiO_2 thin films before and after UV irradiation. Film sample shown here was prepared with Tween 60 surfactant ($6x10^{-4}$ mol dm^3)

Appendix B.

B1- SEM images for sol-gel samples prepared with TTIP and TiBALD

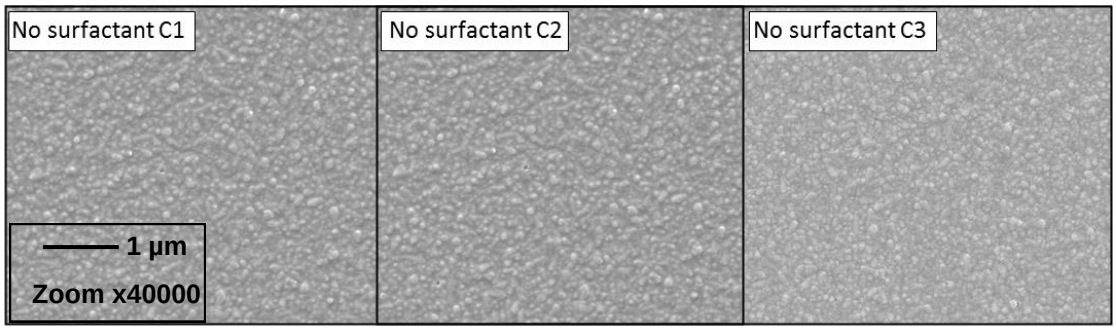

Figure B1. SEM images of samples prepared by sol-gel with TTIP as precursor, with no surfactant addition. Numbers represent the number of layers. Samples were annealed at 500°C for 15 minutes.

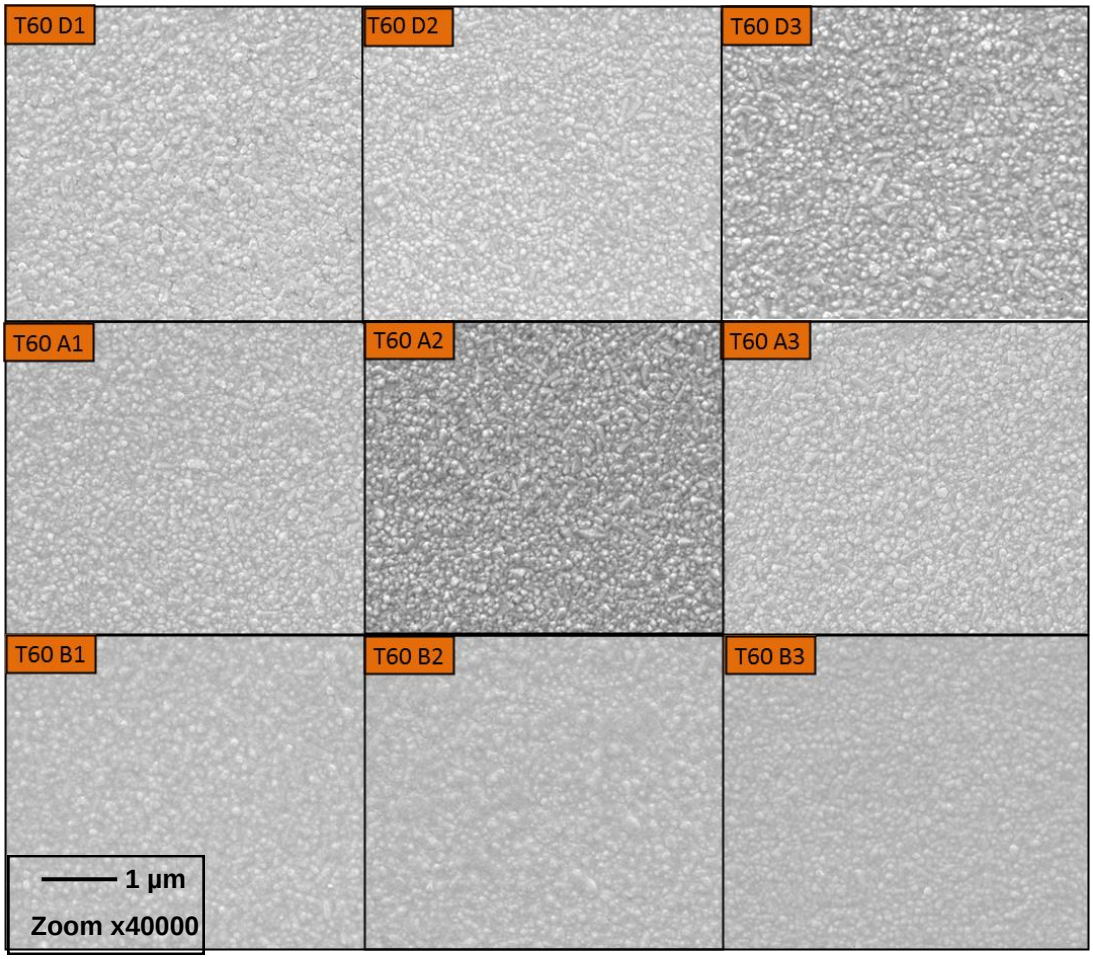

Figure B2. SEM Images of samples prepared by sol-gel with TTIP as precursor and decreasing concentrations of Tween® 60 surfactant. T60 D= $8x10^{-4}$ mol dm^3, T60 A= $6x10^{-4}$ mol dm^3, T60 B=$4x10^{-4}$ mol dm^3. Numbers represent the number of layers. Samples were annealed at 500°C for 15 minutes.

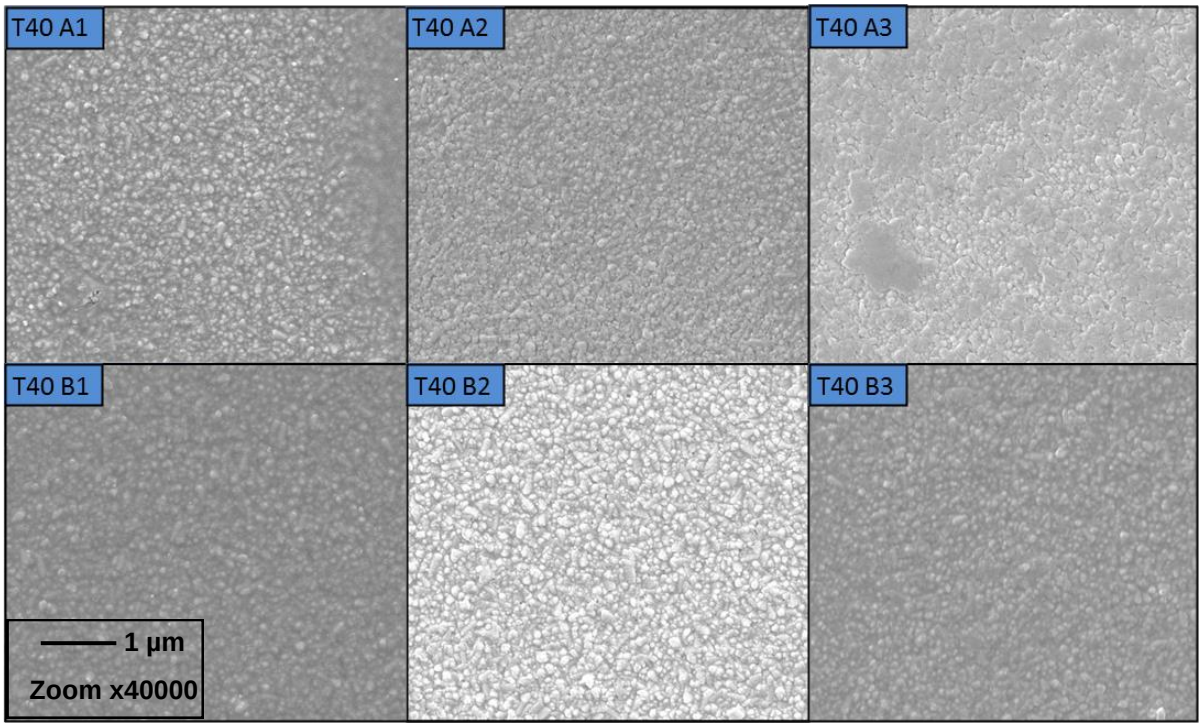

Figure B3. SEM Images of samples prepared by sol-gel with TTIP as precursor and decreasing concentration of Tween® 40 surfactant. T40 A= $6x10^{-4}$ mol dm^3, T40 B=$4x10^{-4}$ mol dm^3. Numbers represent the number of layers. Samples were annealed at 500 °C for 15 minutes.

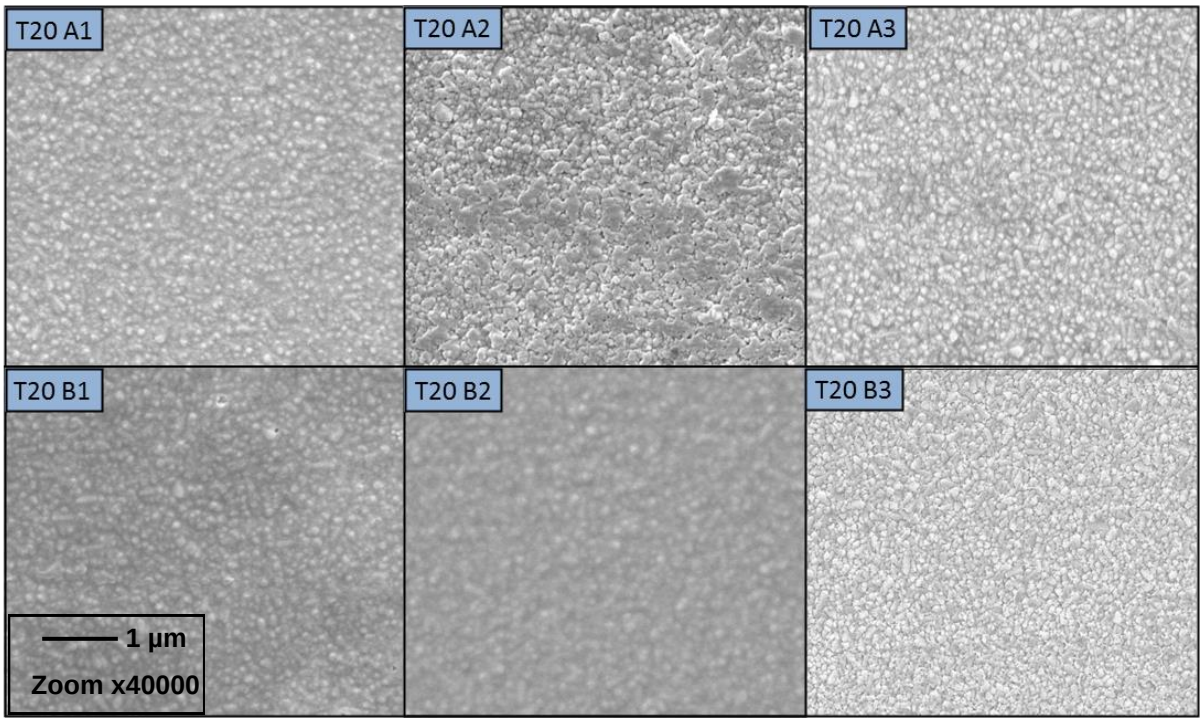

Figure B4. SEM Images of samples prepared by sol-gel with TTIP as precursor and decreasing concentration of Tween® 20 surfactant. T20 A= $6x10^{-4}$ mol dm^3, T20 B=$4x10^{-4}$ mol dm^3. Numbers represent the number of layers. Samples were annealed at 500 °C for 15 minutes.

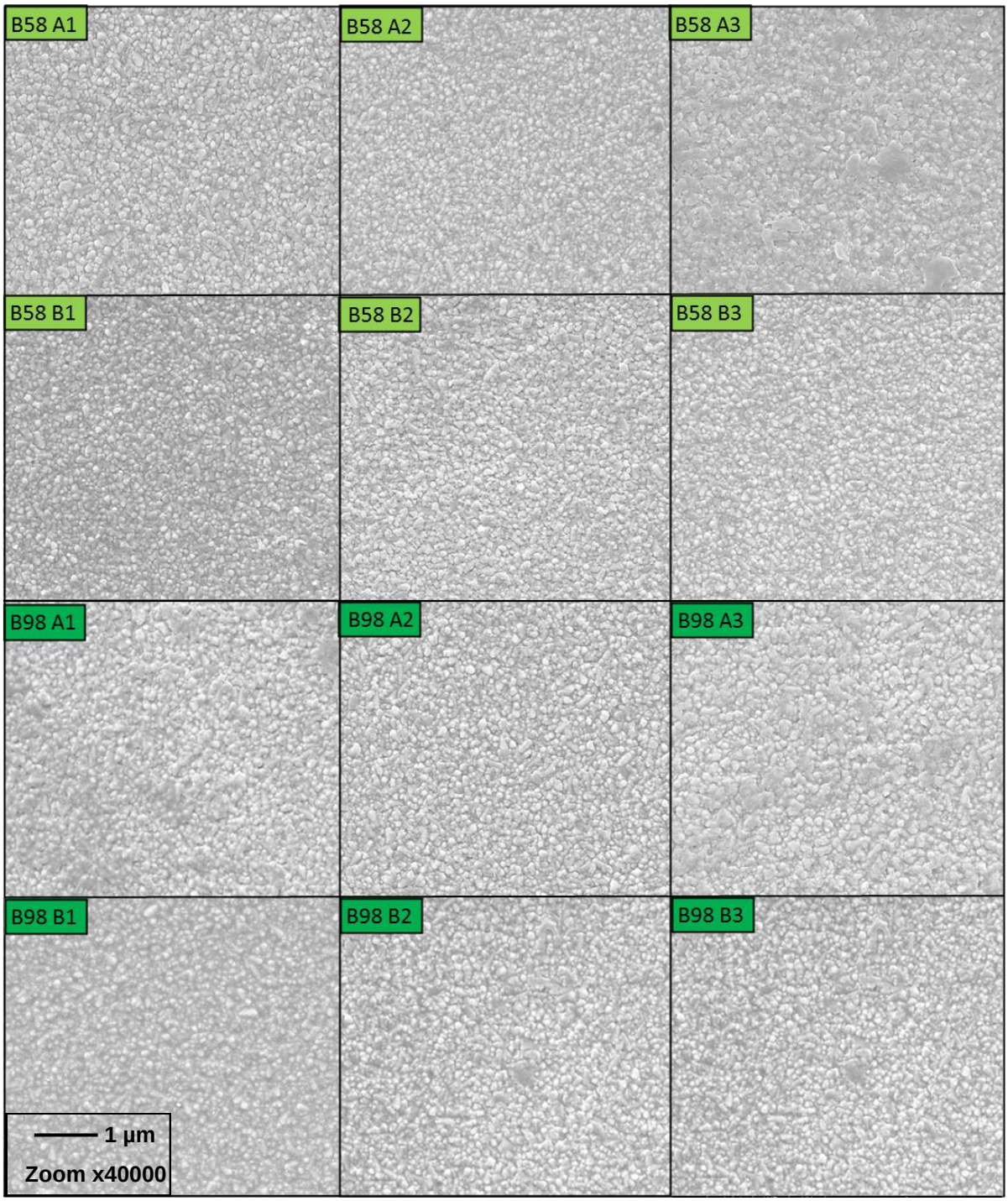

Figure B5. SEM Images of samples prepared by sol-gel with TTIP as precursor and decreasing concentration of Brij® 98 surfactant. B98 A= $6x10^{-4}$ mol dm^3, B98 B=$4x10^{-4}$ mol dm^3. Numbers represent the number of layers. Samples were annealed at 500 °C for 15 minutes.

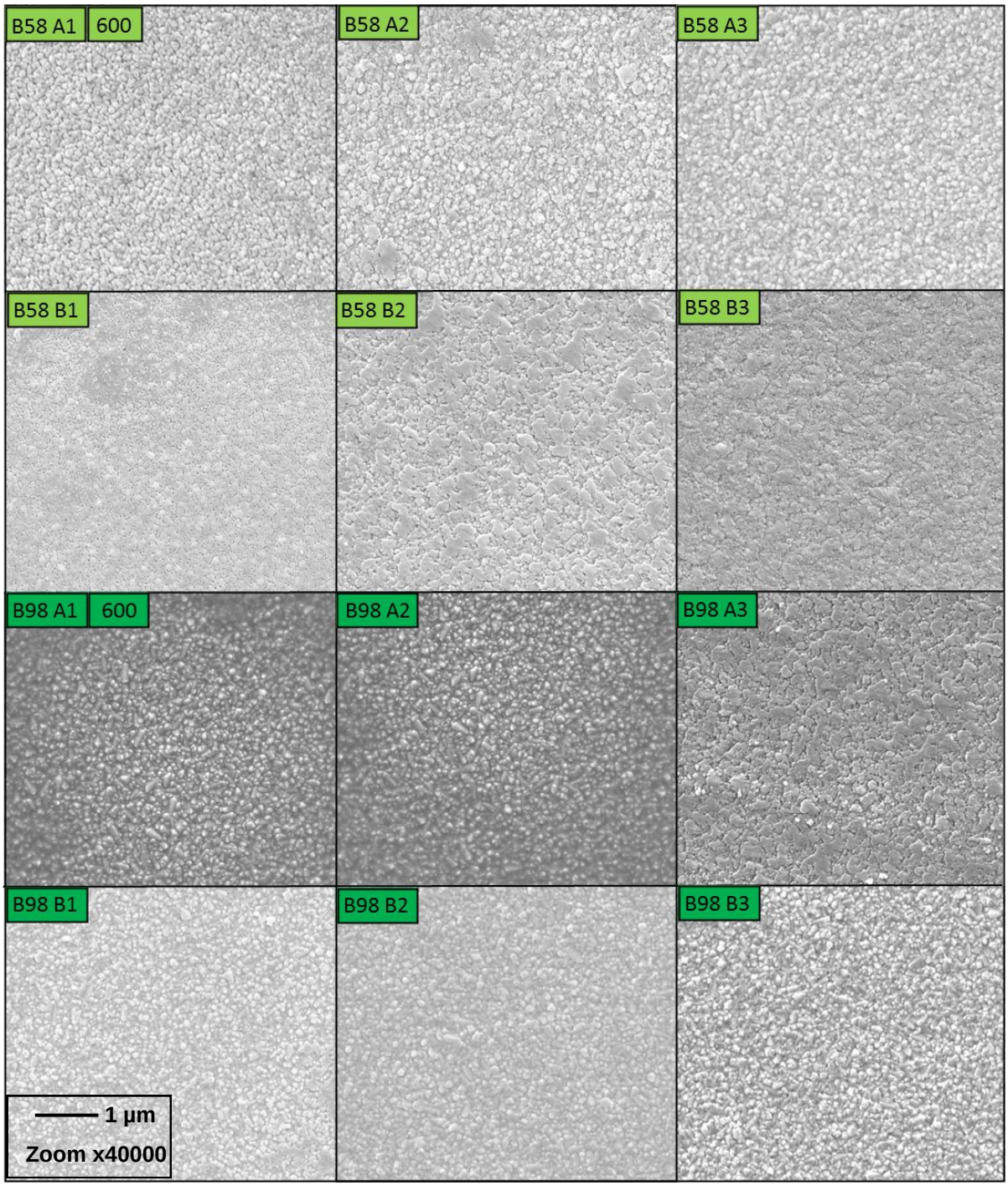

Figure B6. SEM Images of samples prepared by sol-gel with TTIP as precursor and decreasing concentration of Brij® 98 surfactant. B98 A= $6x10^{-4}$ mol dm^3, B98 B=$4x10^{-4}$ mol $dm^{3.}$ Numbers represent the number of layers. Samples were annealed at 600 °C for 1 hour.

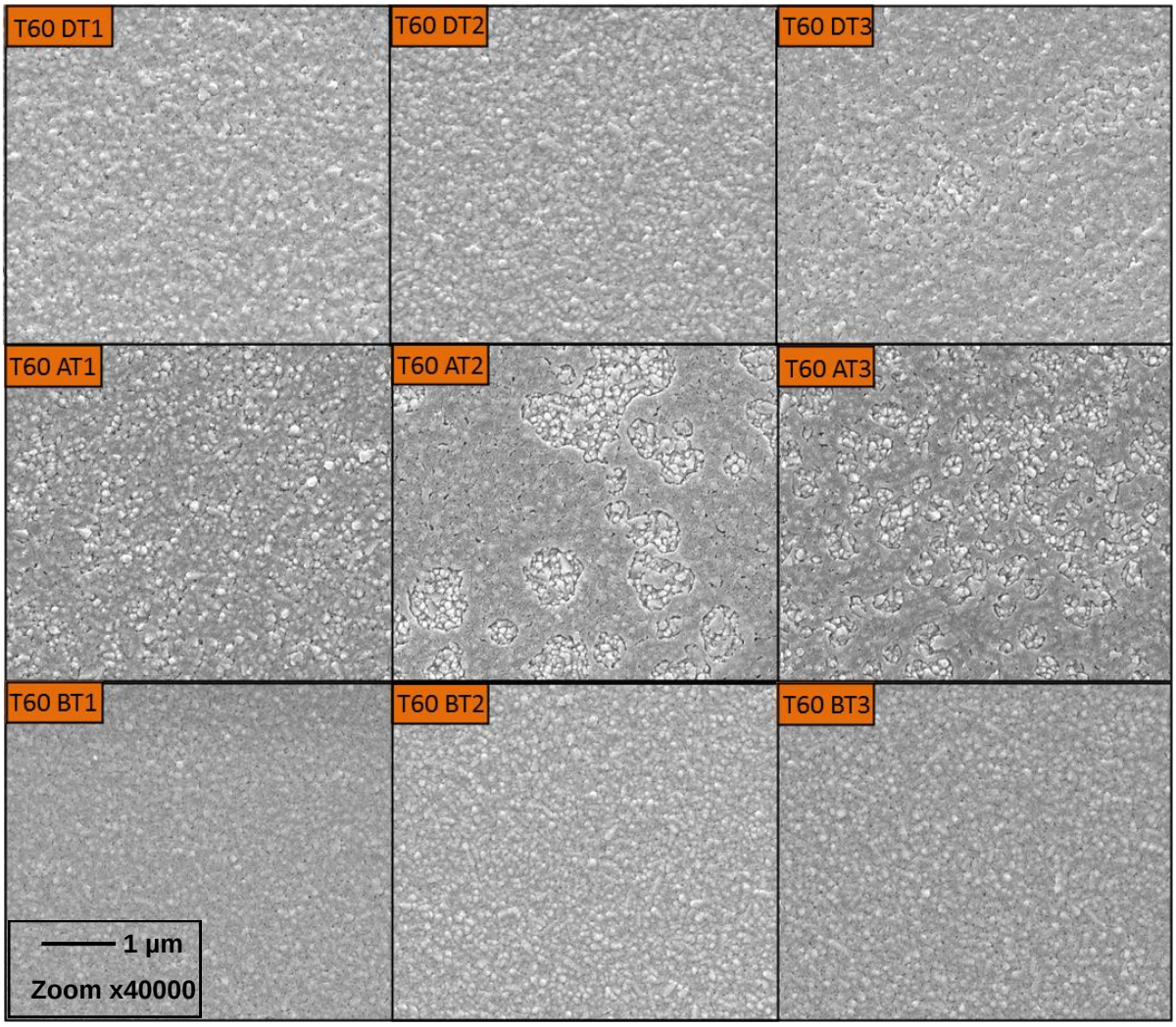

Figure B7. SEM Images of samples prepared by sol-gel with TiBALD as precursor and decreasing concentration of Tween® 60 surfactant. T60 DT = $8x10^{-4}$ mol dm^3, T60 AT = $6x10^{-4}$ mol dm^3, T60 BT = $4x10^{-4}$ mol dm^3. Numbers represent the number of layers. Samples were annealed at 600 °C for 1 hour.

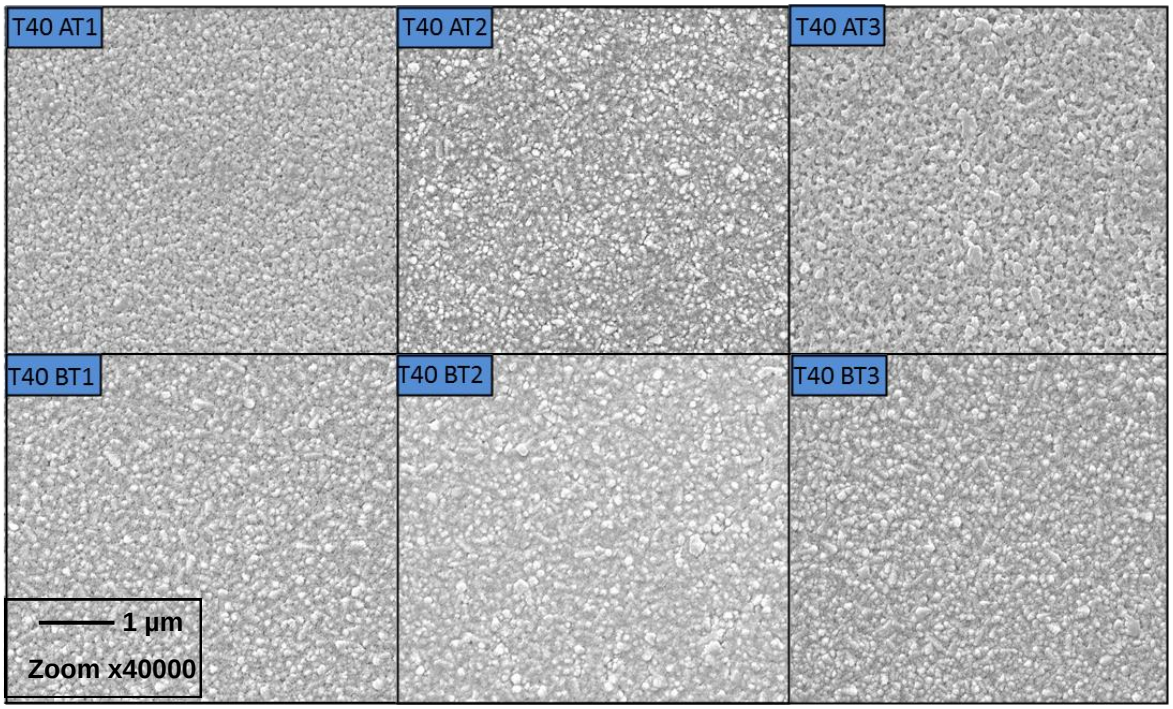

Figure B8. SEM Images of samples prepared by sol-gel with TiBALD as precursor and decreasing concentration of Tween® 40 surfactant. T40 AT = $6x10^{-4}$ mol dm^3, T40 BT = $4x10^{-4}$ mol dm^3. Numbers represent the number of layers. Samples were annealed at 600 °C for 1 hour.

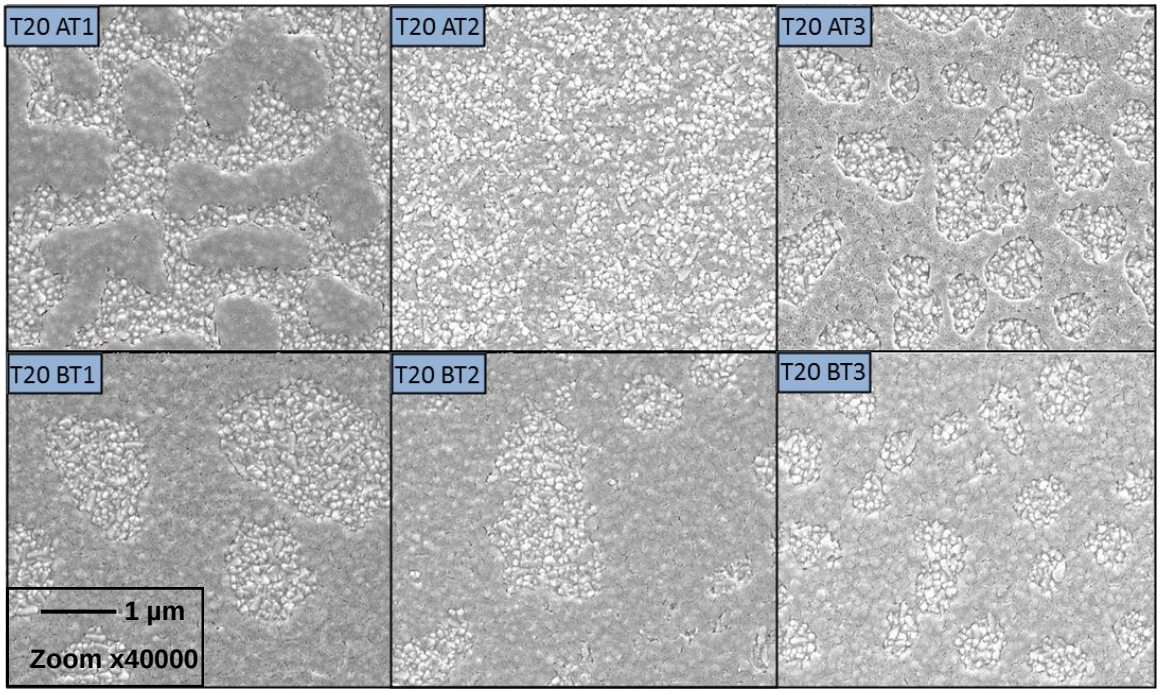

Figure B9. SEM Images of samples prepared by sol-gel with TiBALD as precursor and decreasing concentration of Tween® 20 surfactant. T20 AT = $6x10^{-4}$ mol dm^3, T20 BT = $4x10^{-4}$ mol dm^3. Numbers represent the number of layers. Samples were annealed at 600 °C for 1 hour.

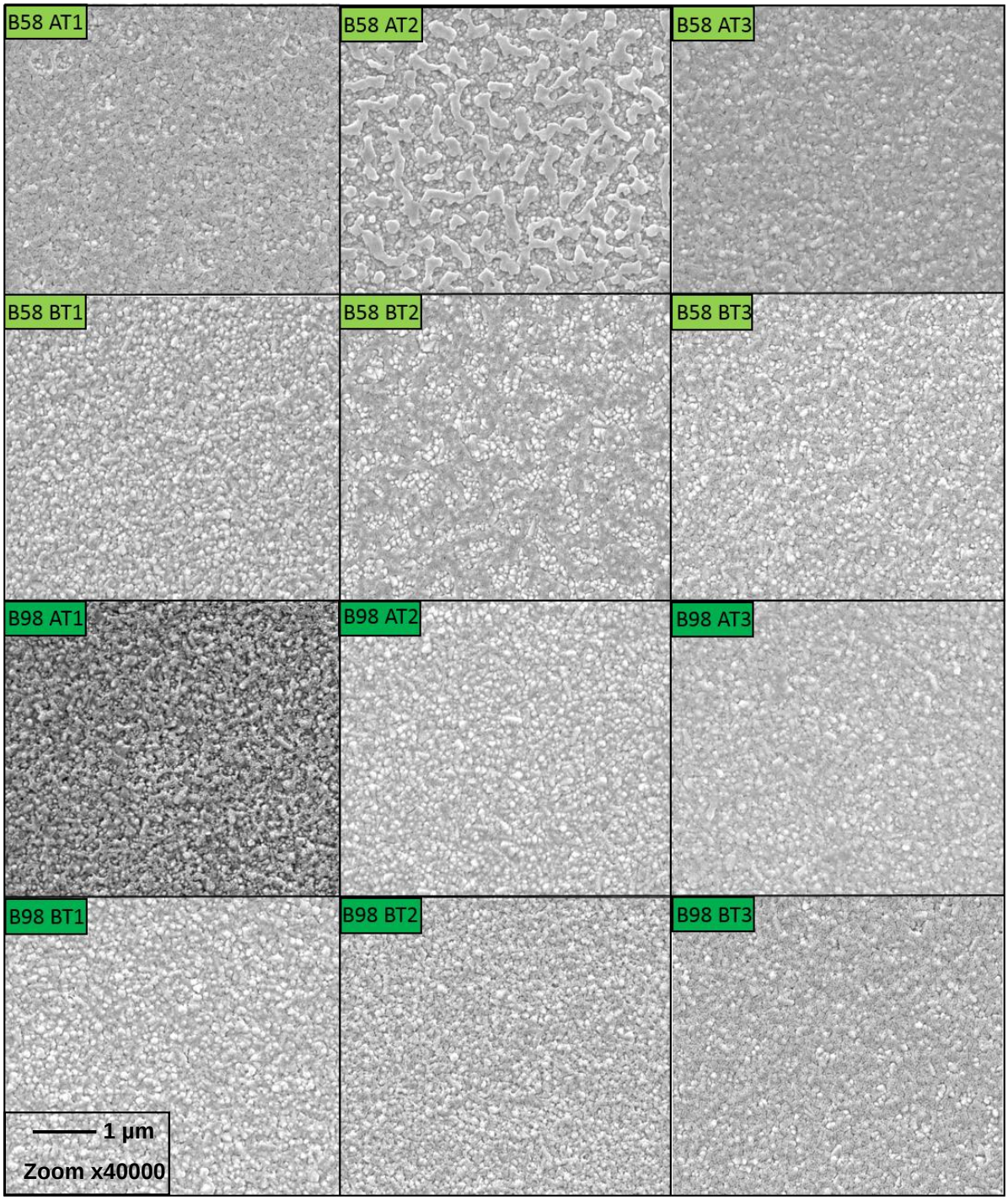

Figure B10. SEM Images of samples prepared by sol-gel with TiBALD as precursor and decreasing concentration of Brij 58 and Brij 98 surfactant. AT = $6x10^{-4}$ mol dm^3, BT = $4x10^{-4}$ mol dm^3. Numbers represent the number of layers. Samples were annealed at 600 °C for 1 hour.

Appendix C.

Figure A-H: Current (I) –voltage (V) curves showing performance of DSSC devices produced in chapter 6.

Abbreviations:

Device configuration is given by title of each IV curve, corresponding to the following:

Thin film on FTO/ electrolyte/ Dye and film soaking time/ counter electrode (CE)

- **Sol-gel films:** TTIP (titanium tetraisopropoxide) or TiBALD (titanium bis-ammonium lactato dihydroxide) used as precursor, without surfactant (Control) or with surfactant addition in preparation (B58, B98, T20, T40) in concentrations described in chapter 3.
- **Aerosol-assisted chemical vapour deposition films-** (AACVD) films prepared with toluene (tol/ t) were tested in DSSC devices. %.
- **Triiodide-** Triiodide electrolyte
- **Iodolyte-** HI 30 Iodolyte (High performance electrolyte)
- **ITO CE-** Indium doped tin oxide counter electrode
- **Pt CE-** Platinum layer on fluorine doped tin oxide glass counter electrode

Figure A.

A1- TTIP Control 2 (2)/ Triiodide/ N3 dye 24 hrs/ ITO CE

A2- TTIP Control 4 (2)/ Triiodide/ N3 dye 24 hrs/ ITO CE

A3- TTIP Control 7 (2)/ Triiodide/ N3 dye 24 hrs/ ITO CE

A4- TTIP Control 1 (3)/ Triiodide/ N3 dye 24 hrs/ ITO CE

A5- TTIP Control 2 (3)/ Triiodide/ N3 dye 24 hrs/ ITO CE

A6- TTIP Control 3 (3)/ Triiodide/ N3 dye 24 hrs/ ITO CE

A7- TTIP B98 B-4 (2)/ Triiodide/ N3 dye 24 hrs/ ITO CE

A8- TTIP B98 B-8 (2)/ Triiodide/ N3 dye 24 hrs/ ITO CE

A9- TTIP B98 B-8 (3)/ Triiodide/ N3 dye 24 hrs/ ITO CE

A10- TTIP B98 B-0 (3)/ Triiodide/ N3 dye 24 hrs/ ITO CE

A11- TTIP B98 B-1 (3)/ Triiodide/ N3 dye 24 hrs/ ITO CE

Figure B.

A12- TTIP B58 A-2 (2)/ Triiodide/ N3 dye 42 hrs/ Pt CE

A13- TTIP B58 A-7 (2)/ Triiodide/ N3 dye 42 hrs/ Pt CE

A14- TTIP B58 A-5 (3)/ Triiodide/ N3 dye 42 hrs/ Pt CE

A15 - TTIP B58 A-7 (3)/ Triiodide/ N3 dye 42 hrs/ Pt CE

A16- TTIP B98 B-3 (3)/ Triiodide/ N3 dye 42 hrs/ Pt CE

A17- TTIP Control 4 (2)/ Iodolyte/ N3 dye 42 hrs/ Pt CE

A18- TTIP Control 7 (2)/ Iodolyte/ N3 dye 42 hrs/ Pt CE

A19- TTIP Control 9 (3)/ Iodolyte/ N3 dye 42 hrs/ Pt CE

A20- TTIP B58 A-8 (2)/ Iodolyte/ N3 dye 42 hrs/ Pt CE

A21- TTIP B58 A-2 (2) / Iodolyte/ N3 dye 42 hrs/ Pt CE

A22- TTIP B58 A-4 (2)/ Iodolyte/ N3 dye 42 hrs/ Pt CE

Figure C.

A23- TTIP B98 B-1 (2)/ Triiodide/ N3 dye 42 hrs/ Pt CE

A24- TTIP B98 B-4 (2)/ Triiodide/ N3 dye 42 hrs/ Pt CE

A25- TTIP B98 B-3 (2)/ Triiodide/ N3 dye 42 hrs/ Pt CE

A26 - TTIP B58 A-8 (3)/ Triiodide/ N3 dye 42 hrs/ Pt CE

A27- TTIP B58 A-2 (3)/ Triiodide/ N3 dye 42 hrs/ Pt CE

A28- TTIP B58 A-4 (3)/ Iodolyte/ N3 dye 42 hrs/ Pt CE

A29- TTIP B98 B-3 (3)/ Iodolyte/ N3 dye 42 hrs/ Pt CE

A30- TTIP B98 B-8 (3)/ Iodolyte/ N3 dye 42 hrs/ Pt CE

A31- TTIP B98 B-5 (3)/ Iodolyte/ N3 dye 42 hrs/ Pt CE

A32- TTIP T20 B-1 (2)/ Iodolyte/ N3 dye 42 hrs/ Pt CE

A33- TTIP T20 B-4 (2)/ Iodolyte/ N3 dye 42 hrs/ Pt CE

Figure D.

A34- TTIP T20 B-0 (2)/ Iodolyte/ N3 dye 42 hrs/ Pt CE

A35- TTIP T40 B-4 (2)/ Iodolyte/ N3 dye 42 hrs/ Pt CE

A36- TTIP T40 B-7 (2)/ Iodolyte/ N3 dye 42 hrs/ Pt CE

A37 - TTIP T40 B-3 (2)/ Iodolyte/ N3 dye 42 hrs/ Pt CE

A38- TTIP T40 B-6 (2)/ Iodolyte/ N3 dye 42 hrs/ Pt CE

A39- TTIP T40 B-5 (2)/ Iodolyte/ N3 dye 42 hrs/ Pt CE

A40- TTIP T20 B-6 (3)/ Iodolyte/ N3 dye 42 hrs/ Pt CE

A41- TTIP T20 B-7 (3)/ Iodolyte/ N3 dye 42 hrs/ Pt CE

A42- TTIP T40 B-5 (3)/ Iodolyte/ N3 dye 42 hrs/ Pt CE

A43- TTIP T40 B-7 (3)/ Iodolyte/ N3 dye 42 hrs/ Pt CE

A44- TTIP T40 B-3 (3)/ Iodolyte/ N3 dye 42 hrs/ Pt CE

Figure E.

A45- TTIP T40 B-9 (3)/ Iodolyte/ N3 dye 42 hrs/ Pt CE

A46- TTIP T40 B-8 (3)/ Iodolyte/ N3 dye 42 hrs/ Pt CE

A47- TiBALD B58 AT-8 (2)/ Iodolyte/ N3 dye 42 hrs/ Pt CE

A48 - TiBALD B58 AT-6 (2)/ Iodolyte/ N3 dye 42 hrs/ Pt CE

A49- TiBALD B58 AT-5 (3)/ Iodolyte/ N3 dye 42 hrs/ Pt CE

A50- TiBALD B58 BT-1 (3)/ Iodolyte/ N3 dye 42 hrs/ Pt CE

A51- TiBALD B58 BT-7 (3) / Iodolyte/ N3 dye 42 hrs/ Pt CE

A52- TiBALD B98 BT-7 (2)/ Iodolyte/ N3 dye 42 hrs/ Pt CE

A53- TiBALD B58 BT-5 (2)/ Iodolyte/ N3 dye 42 hrs/ Pt CE

A54- TiBALD B58 AT-7 (3)/ Iodolyte/ N3 dye 42 hrs/ Pt CE

A55- TiBALD B58 AT-1 (3)/ Iodolyte/ N3 dye 42 hrs/ Pt CE

Figure F.

A56- TiBALD B98 BT-1 (1)/ Iodolyte/ N3 dye 42 hrs/ Pt CE

A57- TiBALD B98 BT-2 (3)/ Iodolyte/ N3 dye 42 hrs/ Pt CE

A58- AACVD Tol (1)/ Triiodide/ N3 dye 24 hrs/ ITO CE

A59 - AACVD Tol (2)/ Triiodide/ N3 dye 24 hrs/ ITO CE

A60- AACVD B98 0.5 t (1)/ Triiodide/ N3 dye 24 hrs/ ITO CE

A61- AACVD B98 0.5 t (2)/ Triiodide/ N3 dye 24 hrs/ ITO CE

A62- AACVD B98 0.5 t (3)/ Triiodide/ N3 dye 24 hrs/ ITO CE

A63- AACVD B98 1 t (1)/ Triiodide/ N3 dye 24 hrs/ ITO CE

A64- AACVD B98 1 t (2)/ Triiodide/ N3 dye 24 hrs/ ITO CE

A65- AACVD B98 1 t (3)/ Triiodide/ N3 dye 24 hrs/ ITO CE

A66- AACVD B58 0.5 t (1) Triiodide/ N3 dye 24 hrs/ ITO CE

Figure G.

A67- AACVD B58 0.5 t (2) Triiodide/ N3 dye 24 hrs/ ITO CE

A68- AACVD B58 0.5 t (3) Triiodide/ N3 dye 24 hrs/ ITO CE

A69- AACVD B58 1 t (1) Triiodide/ N3 dye 24 hrs/ ITO CE

A70 - AACVD B58 1 t (2) Triiodide/ N3 dye 24 hrs/ ITO CE

A71- AACVD B58 1 t (3) Triiodide/ N3 dye 24 hrs/ ITO CE

A72- AACVD T20 0.5 t (1)/ Triiodide/ N3 dye 24 hrs/ Pt CE

A73- AACVD T20 0.5 t (2)/ Triiodide/ N3 dye 24 hrs/ Pt CE

A74- AACVD T20 1 t (1)/ Triiodide/ N3 dye 24 hrs/ Pt CE

A75- AACVD T20 1 t (1)/ Triiodide/ N3 dye 24 hrs/ Pt CE

A76- AACVD T40 0.5 t (1)/ Triiodide/ N3 dye 24 hrs/ Pt CE

A77- AACVD T40 0.5 t (2)/ Triiodide/ N3 dye 24 hrs/ Pt CE

Figure H.

A78- AACVD T40 0.5 t (3)/ Triiodide/ N3 dye 24 hrs/ Pt CE

A79- AACVD B98 0.5 t (1)/ Iodolyte/ N3 dye 42 hrs/ Pt CE

A80- AACVD B98 0.5 t (2) Iodolyte/ N3 dye 42 hrs/ Pt CE

A81- AACVD B98 0.5 t (3) Iodolyte/ N3 dye 42 hrs/ Pt CE

A82- AACVD B98 1 t (1) Iodolyte/ N3 dye 42 hrs/ Pt CE

A83- AACVD B58 1 t (1) /Iodolyte/ N3 dye 42 hrs/ Pt CE

A84- AACVD B58 1 t (2) /Iodolyte/ N3 dye 42 hrs/ Pt CE

A85- TTIP Control 3/ Triiodide/ Purple potato dye/ ITO CE

A86- TTIP B58 A-3/ CB-1a/ N3 dye 24 hrs/ ITO CE

A87- TTIP B58 A-3/ CB-1a/ N3 dye 24 hrs/ ITO CE

A88- TTIP B58 B-2/ CB-3a/ N3 dye 24 hrs/ ITO CE

Figure I.

A89- TTIP B98 B-2/ CB-3a/ N3 dye 24 hrs/ ITO CE

A90- TTIP B98 A-3/ CB-3a/N3 dye 24 hrs/ ITO CE

A91- TTIP B98 A-3/ CB-3a/ N3 dye 24 hrs/ ITO CE

A92- TTIP B98 B-2/ CB-4/ N3 dye 24 hrs/ ITO CE

A93- TTIP B98 B-3/ CB-5/ N3 dye 24 hrs/ ITO CE

A94- TTIP B98 A-2/CB-6/ N3 dye 24 hrs/ ITO CE

A95- TTIP B98 A-2/ CB-7/ N3 dye 24 hrs/ ITO CE

A96- TTIP B98 A-2/ CB-8/ N3 dye 24 hrs/ ITO CE

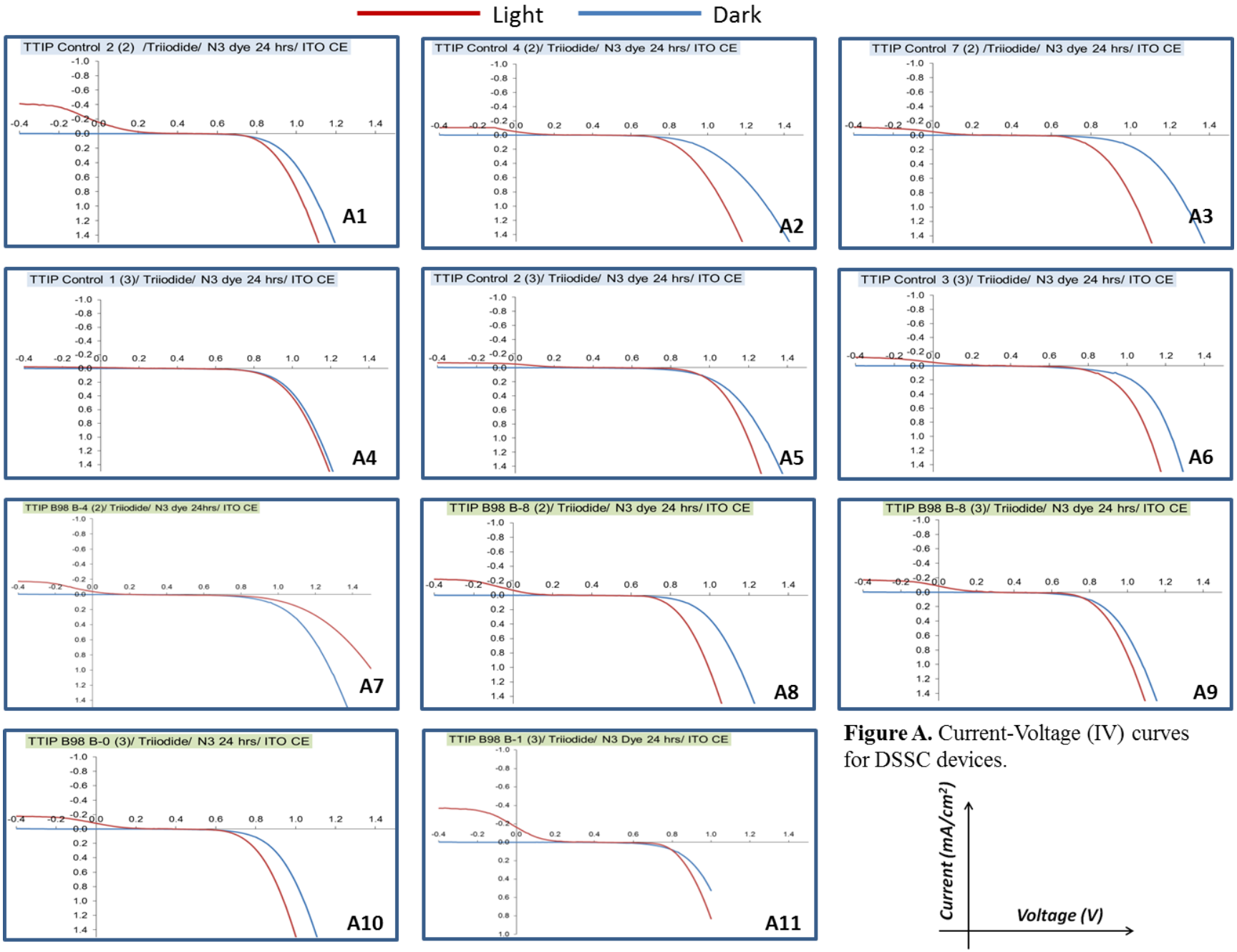

Figure A. Current-Voltage (IV) curves for DSSC devices.

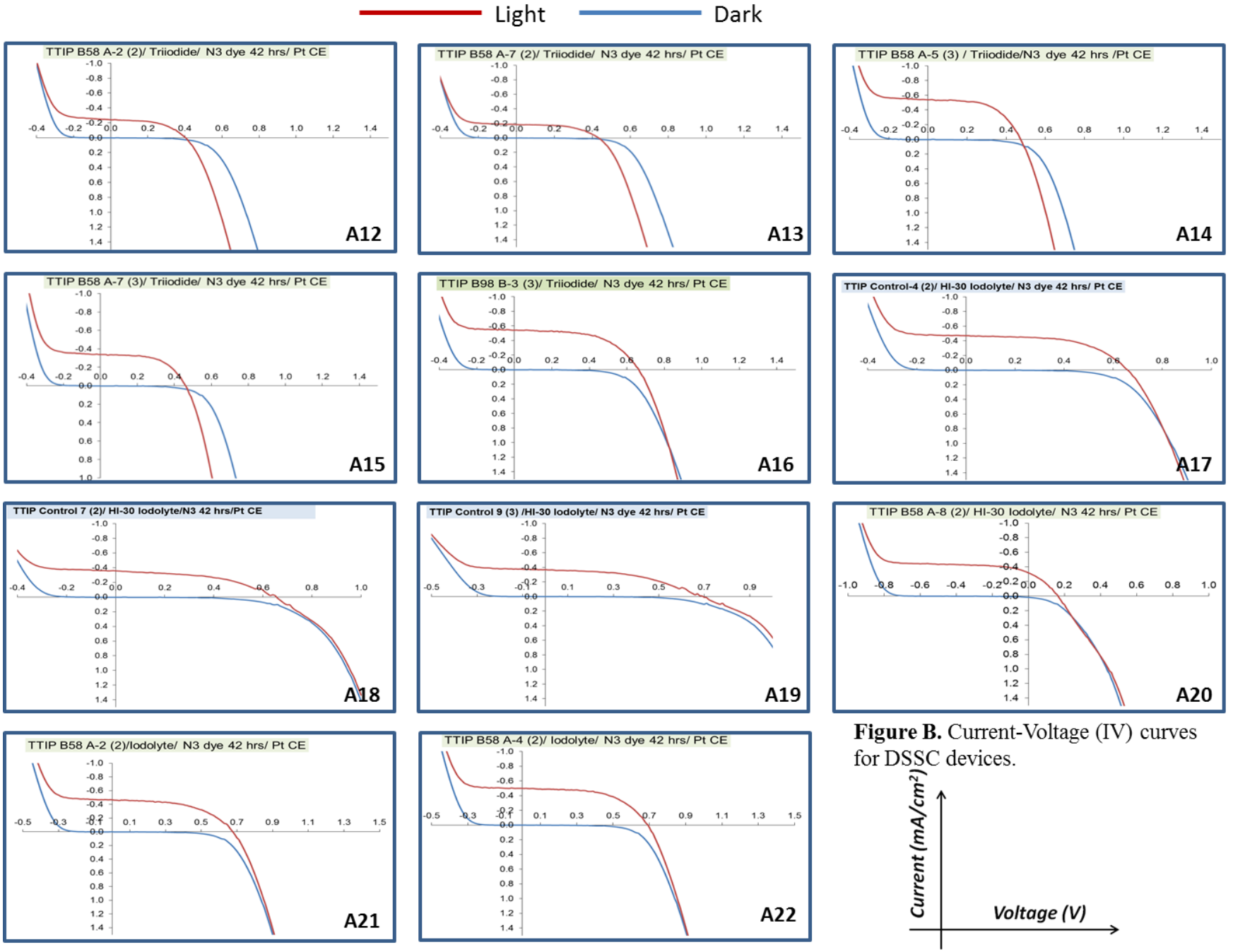

Figure B. Current-Voltage (IV) curves for DSSC devices.

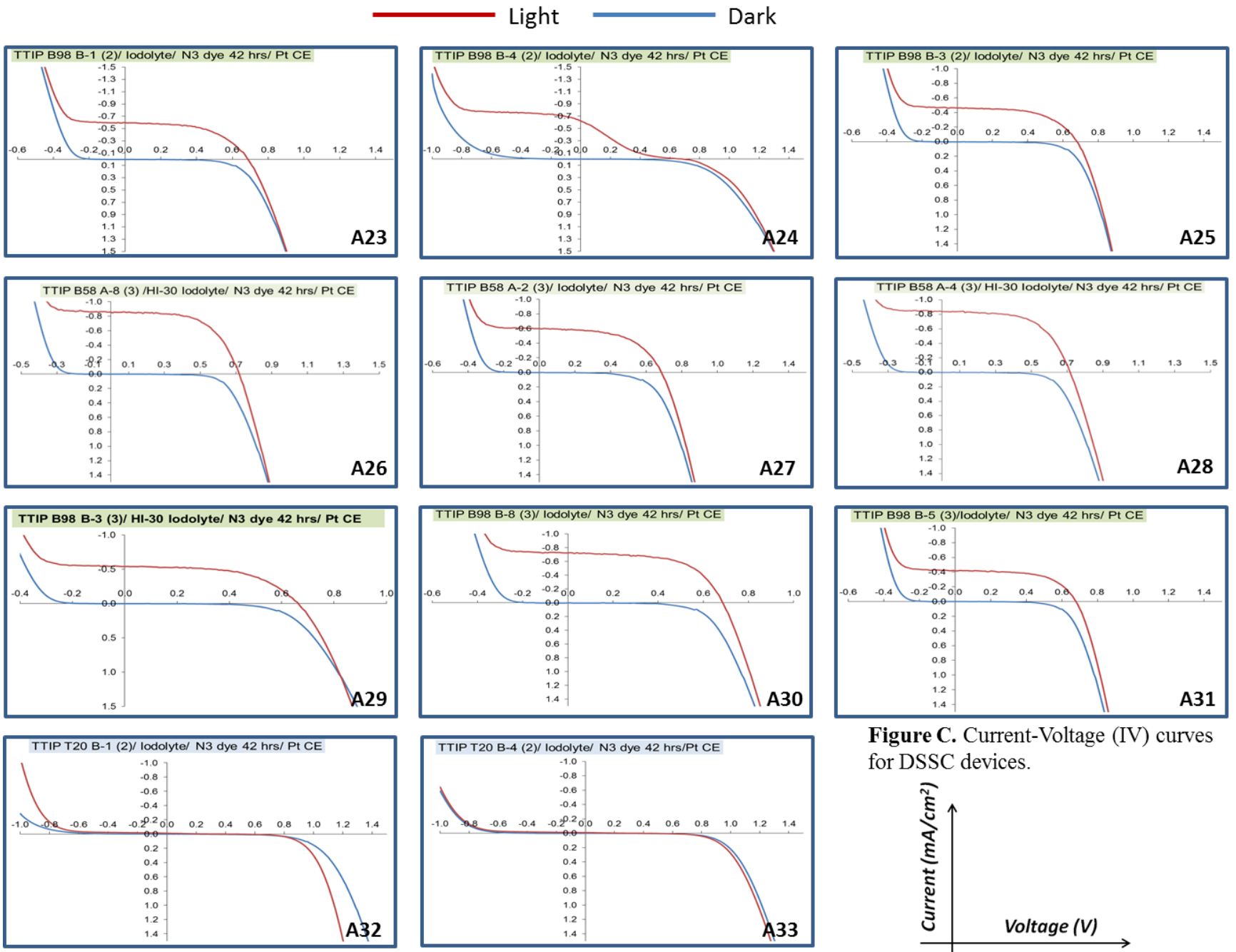

Figure C. Current-Voltage (IV) curves for DSSC devices.

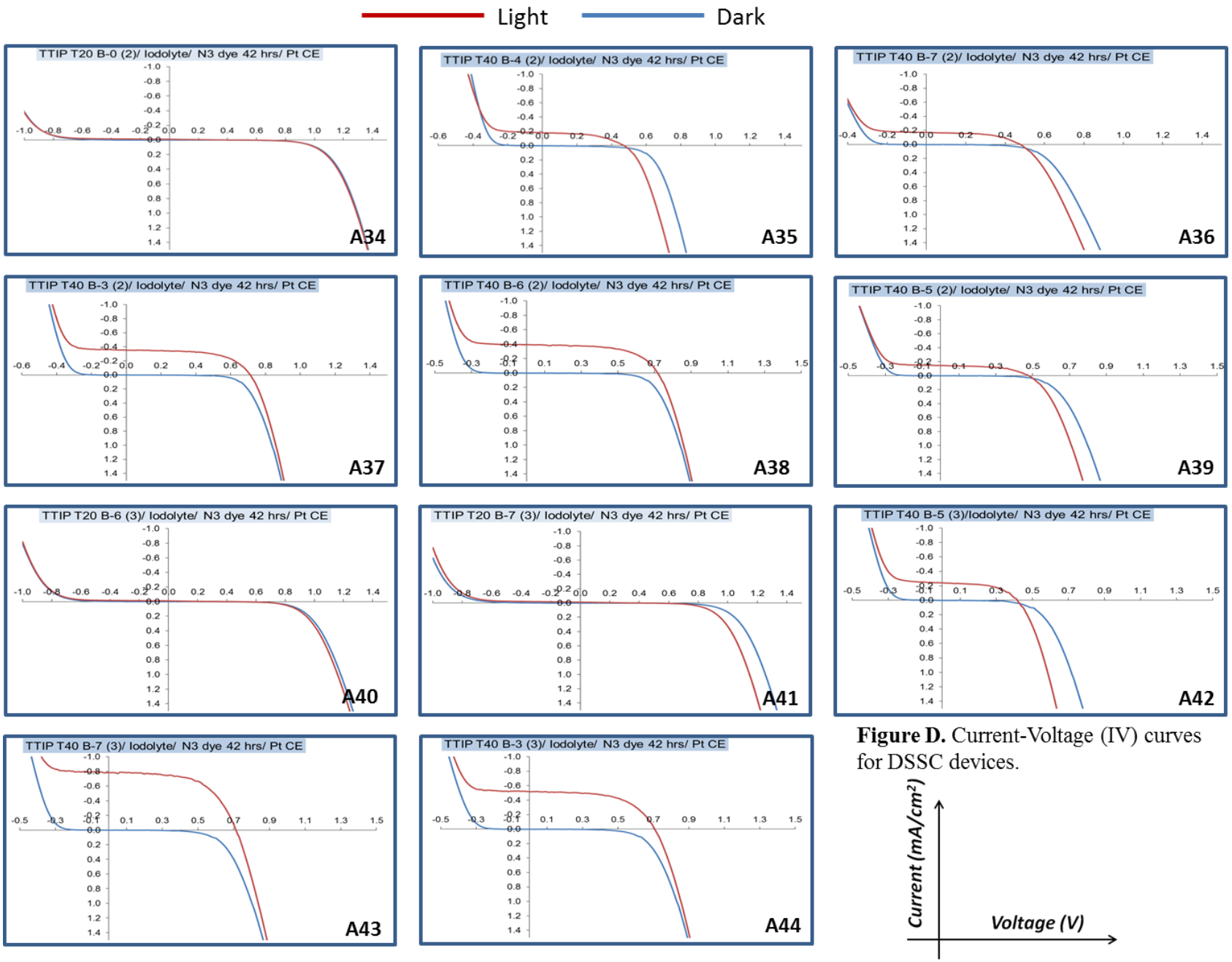

Figure D. Current-Voltage (IV) curves for DSSC devices.

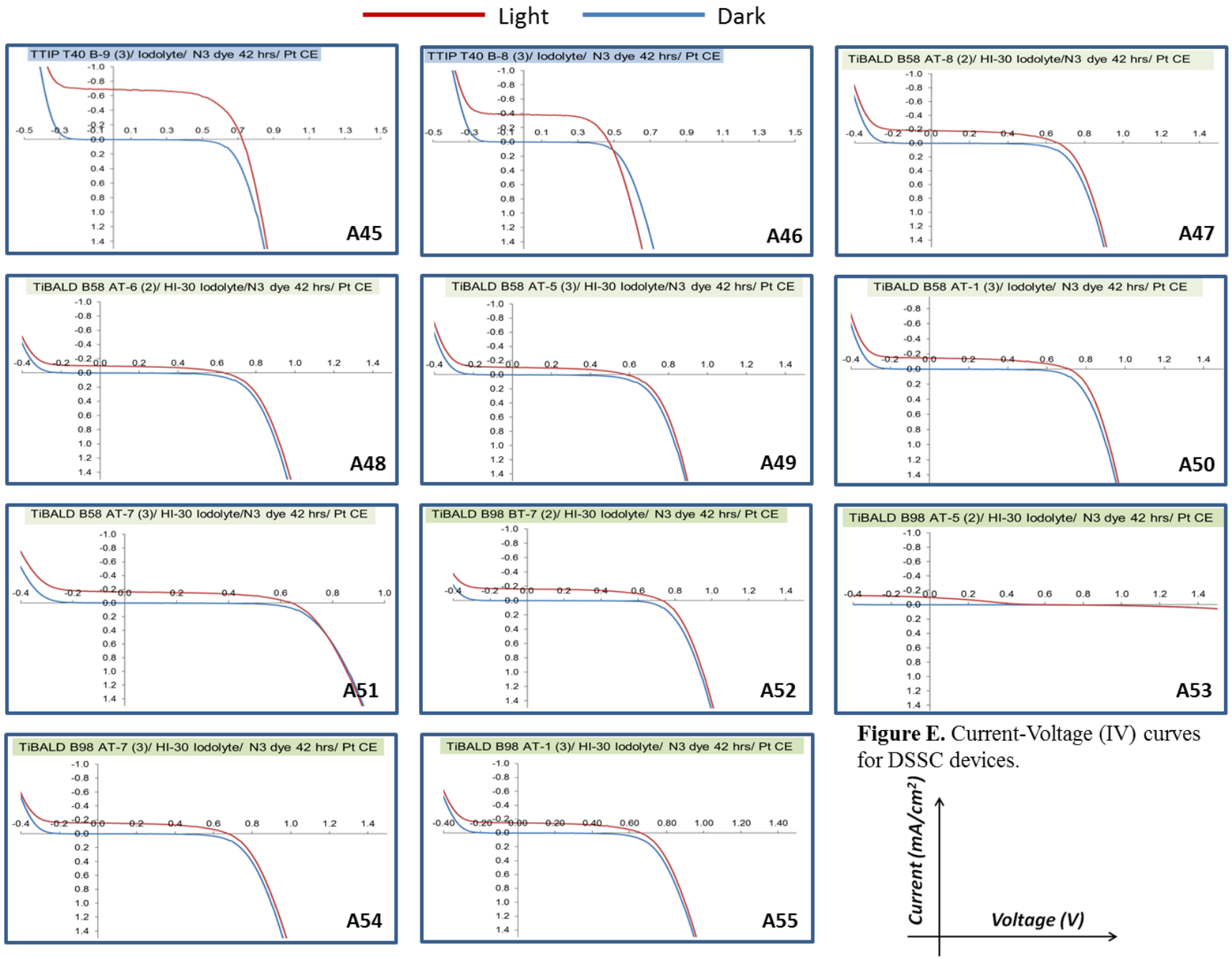

Figure E. Current-Voltage (IV) curves for DSSC devices.

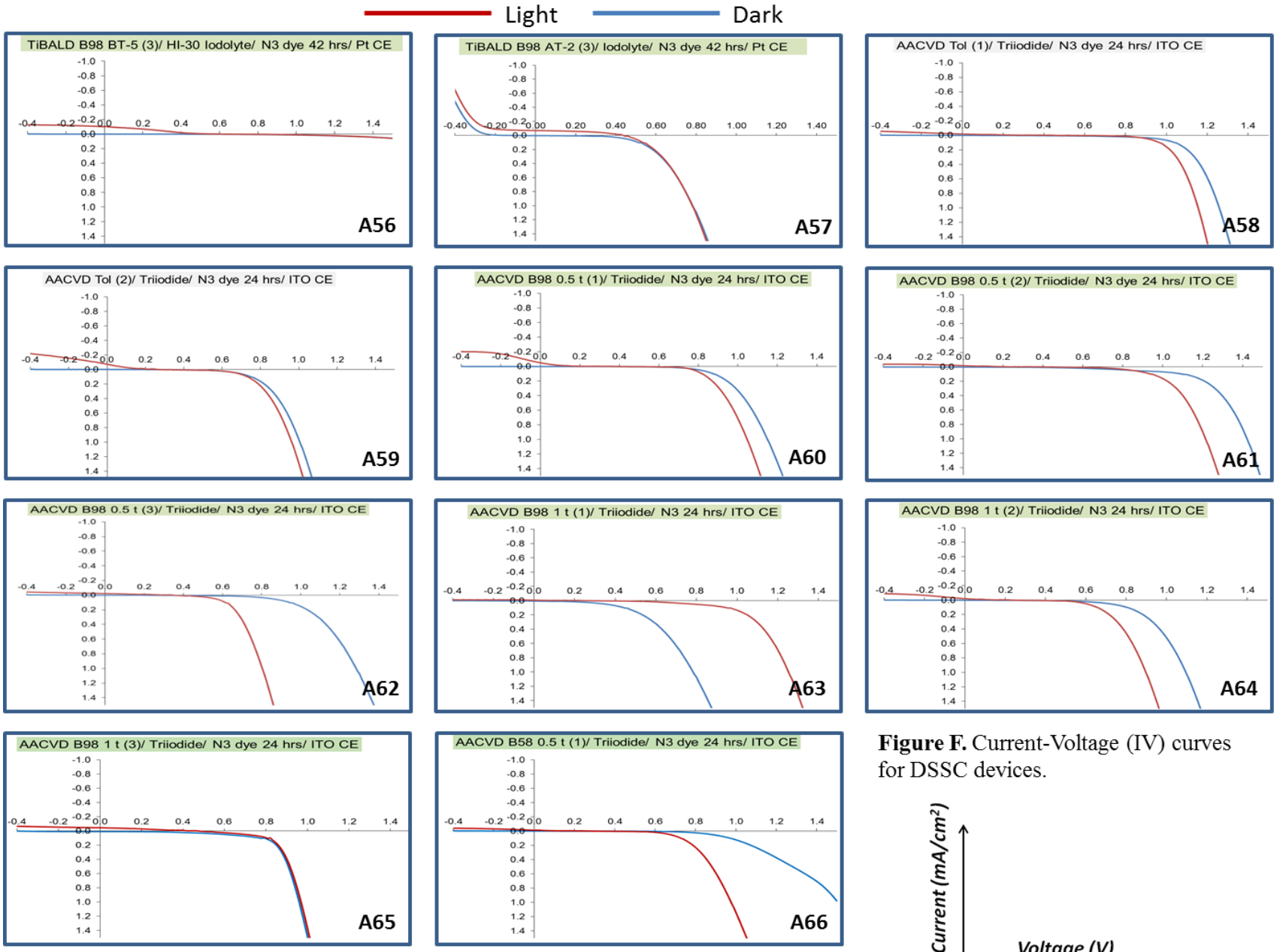

Figure F. Current-Voltage (IV) curves for DSSC devices.

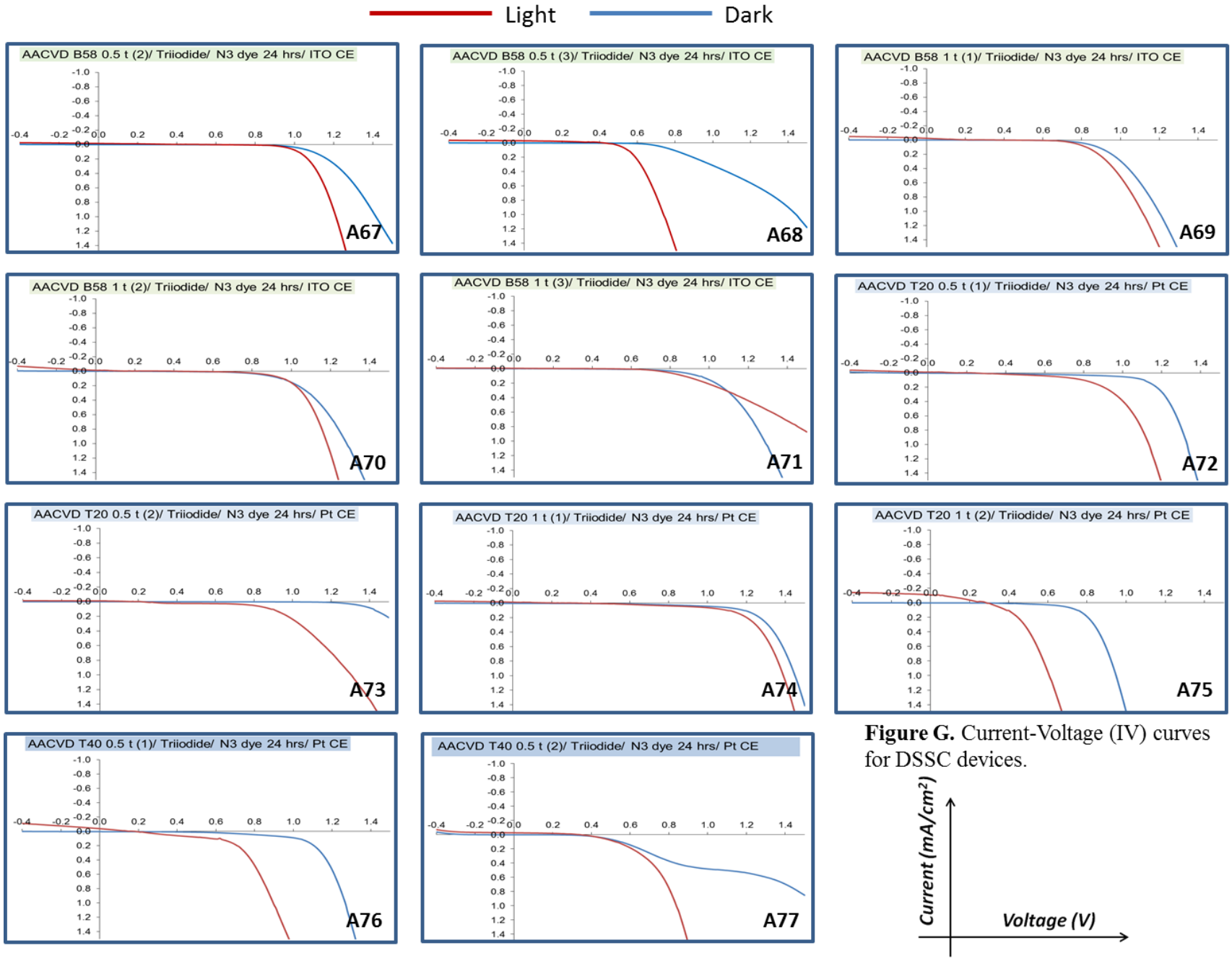

Figure G. Current-Voltage (IV) curves for DSSC devices.

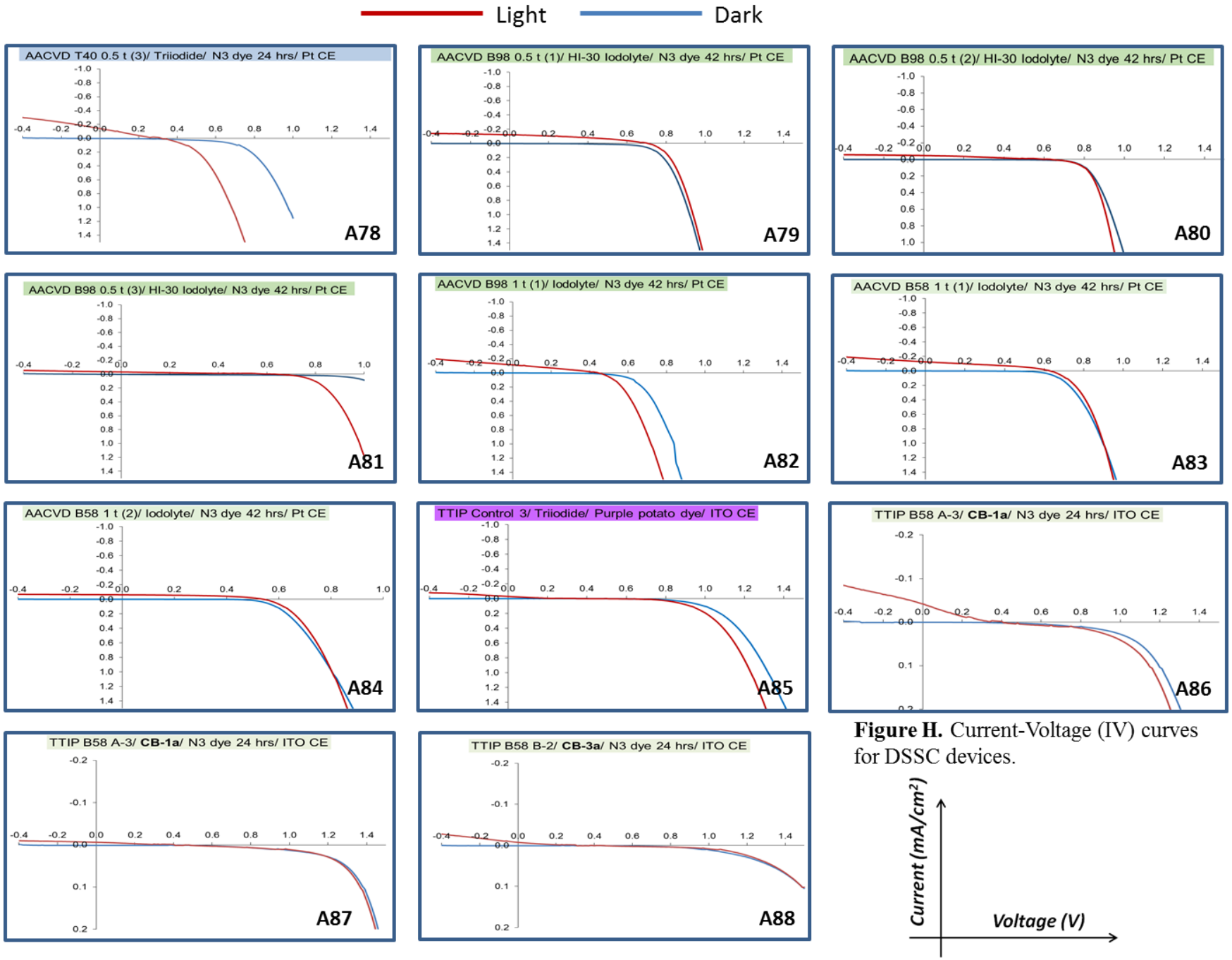

Figure H. Current-Voltage (IV) curves for DSSC devices.

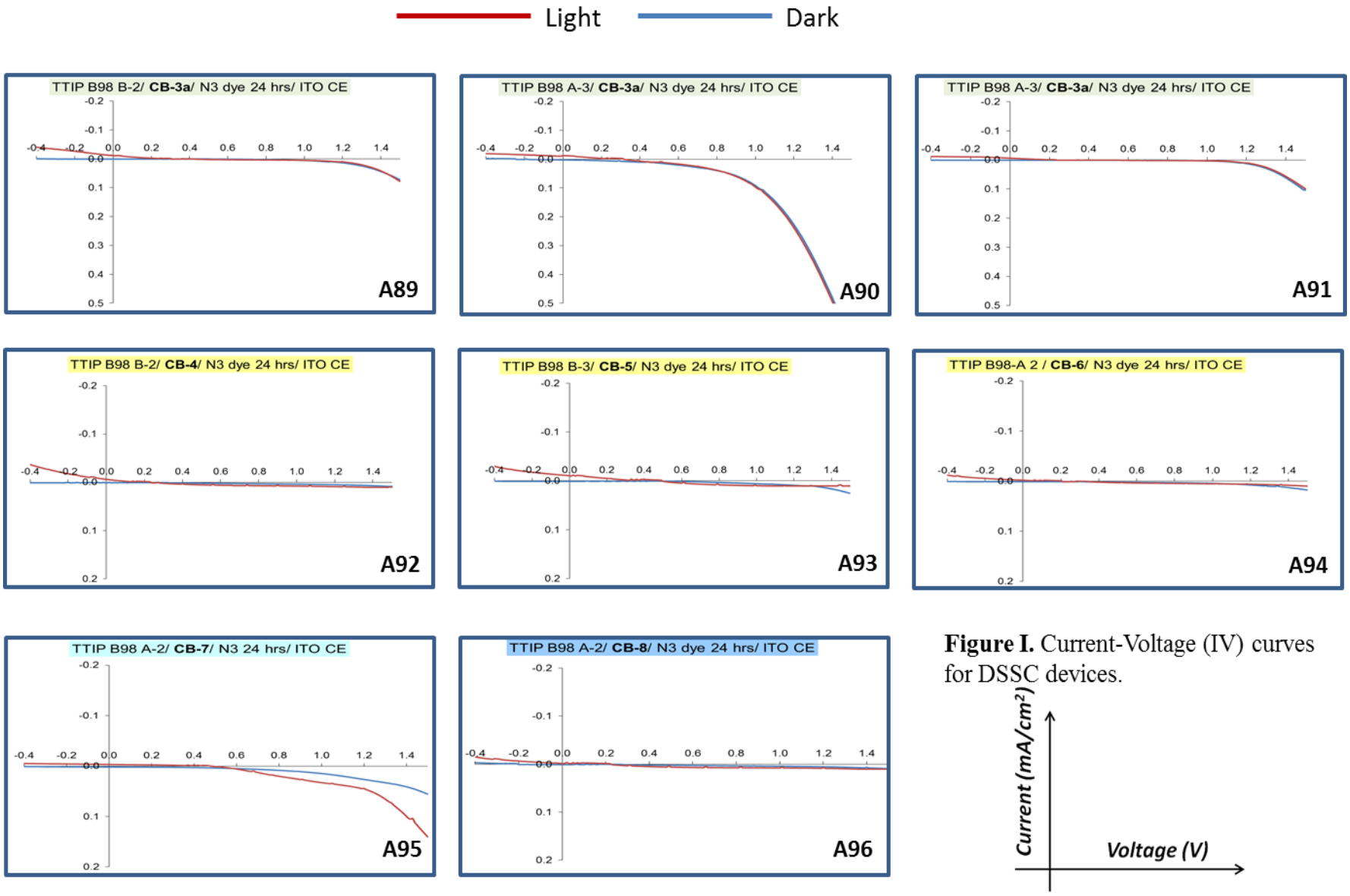

Figure I. Current-Voltage (IV) curves for DSSC devices.